

Matrix Assisted Room Temperature and Vacuum Drying of Functional Proteins and Applications

Thesis submitted for the Degree of Doctor of Philosophy

Yejiong Yu

Exeter College

Hilary Term 2021

Matrix Assisted Room Temperature and Vacuum Drying of Functional Proteins and Applications

Thesis submitted for the Degree of Doctor of Philosophy, Hilary Term 2021
Yejiong Yu, Exeter College, University of Oxford

Abstract

Proteins in aqueous solution are commonly unstable at room temperature and require a cold chain to maintain low temperatures during storage and transportation to minimise degradation. The need for the cold chain limits product distribution and increases the cost of goods. An alternative to prevent degradation and extend the shelf life is to remove water from protein solutions, drying with protective agents. The well-established freeze-drying has prolonged drying processing time and is energy-intensive, potentially increasing the cost of products.

In this work, a novel and cost-effective drying method, Matrix Assisted Room Temperature (MART) drying, was proposed and tested. The technique, initially developed from sugar film drying of vaccines at room temperature, was applied to dry functional proteins. A mathematical model to simulate the simplified MART drying was established to investigate the stabilisation mechanisms of sugar films on proteins. The simulation results showed that capillary bridges of trehalose solution formed on the fibre matrix would not rupture during the drying at a suitable concentration range. Proteins were immobilised in sugar glass to minimise degradation.

The feasibilities of drying proteins with MART drying were also experimentally studied. Two functional proteins, lactate dehydrogenase (LDH) and fibroblast growth factor 2 (FGF-2), were dried on a biocompatible and sterile cellulose fibre matrix at room temperature or even at elevated temperatures. Two sets of drying conditions, drying under low relative humidity conditions (RH<5%) at atmospheric pressure (MART drying) and drying under vacuum (MART-V drying), were investigated. The results showed that MART drying, with or without vacuum, can preserve proteins without any significant activity and functionality loss after drying and one-week storage at 40 °C. More than 80% of the initial activity was maintained for the MART dried LDH after six-month storage at 25 °C. Meanwhile, the activity of dried FGF-2 by both drying conditions was retained after one week of storage at 40 °C. The efficacy of dried FGF-2 after storage did not show a significant difference with FGF-2 solution stored at -80 °C on the proliferation assay of human Mesenchymal Stem Cells.

Another novel drying strategy, vacuum-spin drying, was developed to stabilise the enzymes and other reagents with the supplement of sugars in SARS-CoV-2 rapid detection kits, using the reverse transcription-loop mediated isothermal amplification (RT-LAMP) technique. In the clinical trial, the vacuum-spin dried detection kits demonstrated a sensitivity of 95% and specificity of 99%. As the first attempt of its kind, stabilising the RT-LAMP reagents at room temperature made the storage and transport of the COVID-19 rapid test kits much simpler and more economical, and contributed significantly to its commercial success.

Acknowledgements

First and foremost, I would like to express my gratitude to my supervisor, Professor Zhanfeng Cui, who led me into this remarkable field. It would have been impossible for me to finish the project without his invaluable guidance and constructive feedback throughout my DPhil study.

I am grateful for the financial support from China Regenerative Medicine International Ltd, Department of Engineering Science, University of Oxford and Exeter College, Oxford.

I am sincerely grateful to Dr Julian George for his training and help in designing and constructing the drying apparatus for protein thermostabilisation tests. I would also like to thank Dr Zhi Xu, who helped shape the project and gave me ideas about fibre matrix. I would like to extend my sincerer thanks to Dr Julian Dye, Professor Aidong Yang and Professor Hua Ye for providing tremendous help in modelling and numerical simulation. Also, special thanks to Siqi Dai; your constant advice and support have helped me throughout my DPhil project. Thank you also to our Tissue Engineering Group members for their assistance, friendship, and support, particularly Dr Linh Nguyen, Dr Xin Liu, Dr Di Shen, Dr Robin Nyland, Shuai Ren, and Dr Miren Tamayo Elizalde. I have enjoyed working with you all. You are the ones who made this DPhil unforgettable. I am also grateful to Nicholas Hawkins for his help in DSC measurements and data analysis.

I would like to extend my thanks to members of the COVID-19 detection group. It was a great pleasure for me to work with you all, Professor Zhanfeng Cui,

Professor Wei Huang, Dr Chiachen Hsu, Boon Lim, Dr Hong Chang, Siqi Dai and Shuai Ren. Your patient explanations did help me to understand the LAMP and other techniques. Also, I am grateful for your assistance with the lyophilisation. It was an extraordinary and impressive experience.

I am very thankful for the friendship with many wonderful people in Oxford. I would like to show my gratitude to Yan Tong, Weiyi Gao, Thanishta Mungur, Qian Xu, Xiaohang Fang, Yu Zhou, Pengfei Zhu, Yuanyuan Dai, Sihao Di, Jinfeng Chen, Yun Chen, and Dan Ge for their company and good memories we have shared.

I would like to express my most profound appreciation to Liyiwen Yuan, for her unfailing support and continuous encouragement throughout my DPhil. Thank you for your company and understanding. The delicious food you have made is irresistible to me. Finally, I would like to thank my parents, who encouraged and supported me. Thank you for giving me the chance to pursue my dreams.

Declaration

I declare that this thesis is entirely my own work, except where explicitly stated below:

Chapter 4

The part of retained LDH activity measurement was helped by Siqi Dai.

Chapter 5

The cell cultivation and Cell Count Kit 8 assay were helped by Siqi Dai.

Chapter 6

The residual moisture content analysis and the stability test of the vacuum-spin dried kit were helped by Siqi Dai.

Chapter 7

Statement of Authorship for the joint authored paper was attached at the end of the chapter.

Publications arising from the thesis

The partial work of this thesis is based on the following publications:

Paper 1: **Yu, Y.**, Yang, A., Ye, H., Dye, J. F. & Cui, Z. Numerical study of the formation and drying kinetics of a capillary bridge of trehalose solution between two parallel hydrophilic fibres. *Chem. Eng. Sci.* **226**, 115849 (2020) https://doi.org/10.1016/j.ces.2020.115849.

Paper 2: **Yu, Y.**, Dai, S., Cui, Z. Drying of functional Proteins with Sugar Glass Film on Three-Dimensional Matrices – a study with Lactate dehydrogenase. *To be submitted.*

Paper 3: **Yu, Y.**, Dai, S., Cui, Z. Novel Drying of Fibroblast Growth Factor (FGF-2) Evaluated with Immortalized Mesenchymal Stem Cells (MSC-hTERT) Proliferation, to be submitted.

Paper 4: Huang WE, Lim B, Hsu CC, Xiong D, Wu W, **Yu Y**, Jia H, Wang Y, Zeng Y, Ji M, Chang H, Zhang X, Wang H, Cui Z. RT-LAMP for rapid diagnosis of coronavirus SARS-CoV-2. Microb Biotechnol. 2020 Jul;13(4):950-961. Doi: 10.1111/1751-7915.13586. Epub 2020 Apr 25. PMID: 32333644; PMCID: PMC7264870.

Paper 5: Cui, Z., Chang, H., Wang, H., Lim, B., Hus, C., **Yu, Y.**, Jia, H., Wang, Y., Zeng, Y., Ji, M., Liu, W., Inverarity, C., Huang, WE. Development of a rapid test kit for SARS-CoV-2: an example of product design. *Bio-des. Manuf. 3, 83-86 (2020).* https://doi.org/10.1007/s42242-020-00075-7

Paper 6: **Yu, Y.,** Dai, S., Hsu, C., Lim, B., Ratcliff, J., Ren, S., Huang WE., Cui, Z., Vacuum Drying of RT-LAMP Reagents for Rapid Detection of SARS-CoV-2, to be submitted.

Paper 7: Lim B., Ratcliff J., Nawrot D., **Yu Y.**, Sanghani H., Hsu C., Peto L., Evans S., Hodgson S., Poncin K., Vasudevan S., Dai S., Ren S., Chang H., Cheng W., Pang C.,Siu J., Chan C., Tzang L., Ma M., Cui Z., Simmonds P., Huang WE., Andersson M., Clinical Validation of Optimised RT-LAMP for the Diagnosis of SARS-CoV-2 infection *Sci Rep. 2021 Aug 10;11(1):16193.* doi: 10.1038/s41598-021-95607-1. PMID: 34376716; PMCID: PMC8355225.

Patents:

Y, Yu is an inventor to the following patents:

1. Primer design for SARS-COV-2 detection, Patent Application No. CN202010232072.4, filed on 27th March 2020

2. Molecular switch, Patent Application GB No. 2012480.6, filed on 11 Aug 2020

3. Drying of RT-LAMP reagents, Know-how package, Oxford University Innovation (OUI) project 17733.

The above patents and know-how package have been licensed to Oxsed Limited by the University of Oxford to commercialise the rapid test kits for COVID-19 (commercial name Oxsed RaViD Direct for SARS-CoV-2).

TABLE OF CONTENTS

Abstract ..... **I**

List of Abbreviations ..... **XII**

1 INTRODUCTION **1**

1.1 Background **2**

1.2 Aims and Objectives **5**

1.3 Thesis Outline **6**

2 PRESERVATION OF FUNCTIONAL PROTEINS WITH DRYING **9**

2.1 Protein Degradation **10**

2.1.1 Physical Degradation 11
2.1.2 Chemical Degradation 14

2.2 Current Strategies for Protein Stabilisation **17**

2.2.1 Liquid Formulations – Cryopreservation 18
2.2.2 Cryoprotectants 21
2.2.3 Drying Strategies 22
2.2.4 Stabiliser for Drying Strategies 28

2.3 Novel Drying Formulations **32**

2.3.1 Sugar Film Drying 32
2.3.2 Matrix Assisted Room Temperature (MART) Drying 33

2.4 Scope of Thesis **36**

3 NUMERICAL STUDY OF THE FORMATION AND DRYING KINETICS OF A CAPILLARY BRIDGE OF TREHALOSE SOLUTION BETWEEN TWO PARALLEL HYDROPHILIC FIBRES **38**

3.1 Introduction **39**

3.2 List of Variables **42**

3.3 Geometric Criterion for Forming Capillary Bridge **43**

3.4 Modelling of Drying Dynamics of Capillary Bridge **47**

3.4.1 Mathematical Framework and Assumptions 47

3.4.2 Governing Equations 49
3.4.3 Boundary Conditions 50
3.4.4 Dimensionless Scaling 52
3.4.5 Evaporation Rate 58

3.5 Simulated Results of Drying Dynamics and Discussions 59

3.5.1 Determination of Capillary Shape 59
3.5.2 Simulation Results with Pure Water 60
3.5.3 Simulation Results with Different Solute Concentrations 63

3.6 Conclusions 69

4 DRYING OF FUNCTIONAL PROTEINS WITH MART DRYING – A STUDY WITH LACTATE DEHYDROGENASE 71

4.1 Introduction 72

4.2 Materials and Methods 75

4.2.1 Chemicals and Reagents 75
4.2.2 Fibre Matrix Preparation 75
4.2.1 Scanning Electron Microscopic Imaging 76
4.2.2 Fibre Matrix Characterisation 76
4.2.3 Determination of LDH Activity 79
4.2.4 Protein Formulations 80
4.2.5 MART Drying Process 80
4.2.6 Dried Sample Storage and Reconstitution 82
4.2.7 Differential Scanning Calorimetry 82
4.2.8 LDH-Sugar Solution Preparation 83
4.2.9 The Effectiveness of Fibre Matrix 84
4.2.10 Different Drying Conditions 85
4.2.11 MART Dried LDH Long-Term Storage 85
4.2.12 Effect of Freeze-Thaw Cycle on LDH Activity 86
4.2.13 Statistical Analysis 86

4.3 Results and Discussion 86

4.3.1 Cellulose Fibre Membrane Characterisations 86
4.3.2 Effectiveness of Sugars during Drying 90
4.3.3 Stress Relaxations and Mitigations 92
4.3.4 Effectiveness of Fibre Matrix 95
4.3.5 Retained LDH Activities with Different Drying conditions 98
4.3.6 Long-Term Storage Test 100

4.4 Conclusions 103

5 NOVEL DRYING OF FIBROBLAST GROWTH FACTOR 2 (FGF-2) EVALUATED WITH IMMORTALIZED MESENCHYMAL STEM CELLS (MSC-HTERT) PROLIFERATION 105

5.1 Introduction 106

5.2 Material and Methods 109

5.2.1 Materials 109
5.2.2 Fibre Matrix Preparations 109
5.2.3 Excipients Preparations 109
5.2.4 Protein Adsorption Analysis 110
5.2.5 Effect of LDH Activity with BSA 111
5.2.6 Determination of LDH Activity 111
5.2.7 Matrix Assisted Room Temperature Drying 112
5.2.8 Determination of Moisture Content 113
5.2.9 Scanning Electron Microscopic Imaging 114
5.2.10 FGF-2 Formulation and Stabilization 114
5.2.11 Cultivation of Immortalized Mesenchymal Stem Cells 115
5.2.12 MSC-hTERT Propagation and Fibre Matrix Biocompatibility 116
5.2.13 Statistical Analysis 117

5.3 Results and Discussion 117

5.3.1 Protein Adsorption Resolution 117
5.3.2 Feasibility Test of MART-V Drying 119
5.3.3 FGF-2 Thermostabilisation by MART and MART-V Drying 121

5.4 Conclusions 125

6 FORMULATION AND VACUUM-SPIN DRYING OF RT-LAMP REAGENTS FOR RAPID DETECTION OF SARS-COV-2 126

6.1 Introduction 127

6.2 Material and Methods 131

6.2.1 RT-LAMP SARS-CoV-2 Test Kit Formulation 131
6.2.2 Drying and Preservation of Test Kit 132
6.2.3 RT-LAMP Reaction Setup 133
6.2.4 Detection of Nucleic Acid Amplification 134
6.2.5 Determination of Residual Moisture Content 135
6.2.6 pH Adjustment of Discoloured Kits 135
6.2.7 Sensitivity Test 136

6.3 Results and Discussion 136

6.3.1 Comparison of Vacuum-Spin Drying and Vacuum-Foam Drying 136
6.3.2 Colorimetric Assay of VSD Test Kits 138
6.3.3 Stability of VSD Test Kits 142
6.3.4 Stability of Lyophilized Kits 146
6.3.5 Sensitivity of Dried Kits 148

6.4 Conclusions 150

7 CLINICAL VALIDATION OF OPTIMISED RT-LAMP FOR THE DIAGNOSIS OF COVID-19 151

7.1 Introduction 152

7.2 Materials and Methods 154

7.2.1 Primer Design 154
7.2.2 RT-LAMP Reaction Mix Preparation and Generalized Procedure 154
7.2.3 Full-Length Transcripts 155
7.2.4 Clinical Samples 155
7.2.5 Analytic Stability, Sensitivity, and Specificity 157
7.2.6 Quantitative Detection Methods 159

7.3 Results and Discussion 159

7.3.1 Effectiveness of Temperature-Dependent Oligo Switch 159
7.3.2 Sensitivity and Specificity of Vacuum-Spin Dried Kits 163
7.3.1 Clinical Validation of Vacuum-Spin Dried Kits 166
7.3.2 Quantitative Assessment of Colorimetric Readout 167

7.4 Conclusions 169

8 SUMMARY AND OUTLOOKS 171

8.1 MART Drying 172

8.2 Vacuum-Spin Drying of COVID-19 Detection Kit 176

REFERENCES 178

APPENDICES 203

Appendix 1: Distribution of Protein In the Membrane 203

Appendix 2: Determination of Trehalose Viscosity Equation 206

Appendix 3: The Correlation of BSA to LDH in BCA Assay 208

Appendix 4: The Influence of LDH Activity by Adding Excipients 209

Appendix 5: Effect of Using Diluted UTM and VTM 210

Appendix 6: Vacuum Foam Drying Process 211

Appendix 7: The Switch can Stabilise RT-LAMP Performance 212

Appendix 8: Sensitivity Analysis of Improved RT-LAMP Assay 213

List of Abbreviations

50EP	50% endpoints of detection
θ	Contact angle
AdHu 5	Human adenovirus type 6
AFPs	antifreeze proteins
Asn	Asparagine
Asp	Aspartic acid
BCA Assay	Bicinchoninic Acid Assay
Bo	Bond number
BSA	Bovine serum albumin
Ca	Capillary number
CB	Capillary bridge
CCK-8	Cell counting kit 8
CDER	Centre for Drug Evaluation and Research
COVID-19	Coronavirus disease 2019
CPAs	cryoprotective agents
ctDNA	Circulating tumour DNA
D	Diffusion Coefficient
DEME	Dulbecco's modified Eagle's medium
DMF	Dimethylformamide
DMSO	Dimethylsulphoxide
DNA	Deoxyribonucleic acid
DSC	Differential scanning calorimetry
E	Evaporation rate
Epi-hiPSC	Human episomal iPSCs
FBS	Fetal bovine serum
FD	Freeze drying
FDA	Food and drug administration
FDM	Freeze-drying microscopy
FGF-2/b-FGF	Fibroblast growth factor 2
FM	Fibre matrix
G-CSF	Granulocyte colony-stimulating factor
GF	Glass fibre
h	the half-thickness of capillary bridge neck
HEK293	Human embryonic kidney cell line
IgG	Immunoglobulin G
IL-2	Interleukin-2
ITS-S	Insulin-Transferrin-Selenium-Ethanolamine
K	Boltzmann constant

kDa	Kilo Dalton
LDH	Lactate dehydrogenase
LN	Liquid nitrogen
LoD	Limit of Detection
M	Molar
mM	Milli Molar
Ma	Marangoni number
MART Drying	Matrix Assisted Room Temperature Drying
MART-V Drying	Matrix Assisted Room Temperature Vacuum Drying
MPM	Multiphoton microscopy
MSC-hTERT	Immortalized Mesenchymal Stem Cells
MVA	The attenuated poxvirus modified vaccinia virus Ankara
n	Unit normal vector
NAAT	Nucleic acid amplification tests
NAAT	Nucleic Acid amplification tests
NaCl	Sodium chloride
NCC	Normalized Cell Count
ns	No significant difference
OPA	Overall percentage agreement
P	Pressure
PBS	Phosphate buffered saline
PCR	Polymerase Chain Reaction
PDL	Population doubling level
Pe	Peclet number
PEG	Polyethylene glycol
POCT	Point of Care testing
PVA	Polyvinyl alcohol
qPCR	Quantitative polymerase chain reaction
R	Principal radius
Re	Reynolds number
RH	Relative humidity
rHA	Recombinant human albumin
RNA	Ribonucleic acid
RT	Reverse transcription
RT-LAMP	Reverse transcription loop-mediated isothermal amplification
SEM	Scanning Electron Microscopy
T	Temperature

Chapter 1

Introduction

1.1 Background

Proteins, composed of amino acids, are irreplaceable biological molecules that play a crucial role in most physiological processes within living organisms. Proteins function as catalysts for biochemical reactions, tiny pumps for transporting molecules, receptors and channels in cell membranes, motors in cytoskeleton and switches for regulating biosignals[1–7]. There are more than 84,000 to 200,000 different proteins in the human body[8]. Interactions among these endogenous proteins significantly influence the health of an organism. Any of these active proteins become deficient or abnormal, caused by a mutation or deletion of a protein-coding gene, which could alter the function and activity of proteins and lead to diseases[9–12].

In this case, introducing protein therapeutics, which are proteins either naturally produced in the body or synthesised in the laboratory, is an alternative way of complex gene therapies to treat diseases or improve pathological conditions[5,7,13]. In addition, protein therapeutics are highly specific and have less potential to interfere with other normal biological reactions[14], making protein therapeutics continuously gain significance over the past decades[15–18]. There are nearly 380 protein therapeutics with an overall market value of over 140 billion USD in 2016[19]. However, the benefits of protein therapeutics to human healthcare will not be realised if they cannot be effectively stabilised[20].

One set of essential proteins is enzymes that catalyse biochemical reactions. Enzymes have been used widely in drug metabolism[21–24] and in vitro diagnostics[25–

[28]. Conventional non-invasive diagnoses were based on imaging and endogenous biomarkers assays[29,30]. Such methods suffer from low specificity and require expensive facilities and specialised healthcare workers to conclude the findings [31,32]. Recently, the development of molecular diagnostics increased the specificity for detecting the disease biomarkers. For example, molecular diagnostic techniques such as polymerase chain reaction (PCR) or Loop-mediated isothermal amplification (LAMP) allow detection of a specific nucleic acid sequence[33–35]. They are widely used in diagnosing viral infections[36–39] and cancer at an early stage[40–42]. These accurate, rapid and straightforward molecular tests rely on the activity and functionality of proteins[28].

While proteins in solution are typically functional but marginally stable, some proteins are inherently unstable and liable to denaturation[43–47]. Protein denaturation occurs mainly due to physical denaturation and aggregation, such as surface adsorption, hydrolysis, oxidation and covalent aggregation[48–50]. Protein denaturation can be prevented, thereby maintaining protein functionalities by reducing the likelihood of denaturation from occurring. Two basic strategies to prevent denaturation are cryopreservation and dehydration.

In cryopreservation, proteins are stored at low temperatures to slow down the biochemical reactions[51,52]. A lower temperature is required for the longer storage[53,54]. Cryogenic storage is always required for long-term storage, which has high capital and maintenance costs and is unsuitable for large quantities[55].

The other strategy is dehydrating the protein solutions to minimise the biochemical reaction. Due to the absence of liquid water, most chemical reactions are stopped[56,57]. It is conventionally done by freeze-drying, which sublimates water from a frozen state under vacuum [58,59]. High capital cost, high energy consumption, and prolonged process time potentially increased the cost of final products[60]. Spray drying uses hot air to dry atomised droplets, which contain bioproducts. This technique is commonly used for low-value protein products where some loss in protein activity and functionally can be tolerated (e.g. milk powders)[61].

In addition to freeze-drying and spray drying, matrix-assisted room temperature (MART) drying is a relatively new method for dehydration, using a fibre matrix to support formulated protein samples during the drying process at room temperature. It is characterised as a low energy-intensive process with simple operation. Although the mechanisms of stabilising bioproducts remain unclear, MART drying has been used to preserve viral vaccines[62–64]. However, only glass fibre was shown that have a superior protective function on vaccines than the other seven fibre matrices. Glass fibre (GF) is brittle. The fragments may enter the human body and cause allergy during the vaccine administration[62]. Therefore, the first part of the thesis is to test whether MART drying can be applied to dry functional proteins on a biocompatible fibre matrix for long-term storage.

Except for MART drying, another drying strategy is developed to stabilise enzymes and other reagents in a COVID-19 detection kit, allowing the kit to be transported at room temperature. The COVID-19 pandemic impacted our society expressively and would have a long-lasting effect[65–67]. One of the critical issues to combat

COVID-19 is the need for rapid and accurate testing[68–70]. Nucleic acid amplification tests (NAAT) provide higher accuracy than antigen or antibody tests when testing whether the individual carries the SARS-CoV-2 virus or not[71]. The standard NAAT method, the Polymerase Chain Reaction (PCR), is not suitable for the point of care (POC) testing, as it takes an extended processing time (around 2 hours) and needs sophisticated facilities and instruments[72]. Reverse Transcription-Loop mediated isothermal amplification (RT-LAMP) is performed at a constant temperature, commonly at 65 °C. It only requires 30 min for the reaction, ideal for the Point of Care testing[73,74]. Therefore, a COVID-19 detection kit using RT-LAMP is developed[72]. However, the RT-LAMP enzymes, reverse transcriptase and Bst 2.0 polymerase, should be stored and transported at -20 °C or below, limiting the test distribution and application. The second part of the thesis is to formulate and stabilise the functional enzymes and other reagents in COVID-19 detection kits by vacuum-spin drying, which dry the reagents under vacuum with the assistance of centrifugation.

1.2 Aims and Objectives

The aims of this thesis are:

1. To study the feasibility and mechanisms of Matrix Assisted Room Temperature drying in preserving functional proteins.

2. To study the feasibility and optimise the drying of RT-LAMP enzymes in the rapid test kit for COVID-19 detection.

These aims are accomplished by

- simulating the evaporation kinetics of the capillary bridge of different trehalose concentrations in order to gain insight into protein stabilisation mechanisms (paper 1)
- tailoring MART drying on a cellulose fibre matrix with various sugar concentrations and drying conditions to optimise protein (lactate dehydrogenase) stabilisation for long-term storage (paper 2)
- investigating the feasibility of using MART drying under vacuum (MART-V) to preserve the functionality of formulated proteins such as fibroblast growth factor 2 (FGF-2) (paper 3)
- validating the vacuum-spin dried COVID-19 detection kits, which developed in papers 4 & 5, by synthesised full-lengthed SARS-CoV-2 RNA in the laboratory (paper 6) and clinical samples (paper 7)

1.3 Thesis Outline

The thesis is structured into eight chapters, which are outlined as follows.

In Chapter 2, the primary degradation pathways of proteins are illustrated. The conventional preservation strategies are reviewed, followed by the discussions on the pros and cons of different approaches. In addition, the efficacy of different kinds of stabilisers is discussed.

In Chapter 3, geometric simulation was constructed to analyse the criterion of forming capillary bridges between fibres. Capillary Bridge number was derived to

predict the wetting morphologies. The stabilisation mechanisms of sugar films were investigated by simulating the evaporation dynamics of capillary bridges with trehalose solutions at different concentrations.

In Chapter 4, an inexpensive and biocompatible cellulose membrane was discovered and tested to support Matrix Assisted Room Temperature (MART) drying. The efficacy of this membrane in preserving functional protein was tested with lactate dehydrogenase (LDH), a model protein. The amount of sugar needed was analysed by drying solutions of different LDH/sugar ratios and measuring the activity of LDH after drying and storage. Different drying conditions were investigated to find the optimum condition for preserving LDH. Finally, a long-term storage trial was performed by placing MART dried LDH at 25 °C for six months.

Chapter 5 investigated the effectiveness of bovine serum albumin coating on reducing non-specific adsorption onto the matrix and its effect on protein drying. Meanwhile, the feasibility of Matrix Assisted room temperature drying under vacuum (MART-V) was studied by applying a vacuum to speed up the drying process. Fibroblast growth factor-2 (FGF-2), used as the test protein, was supported by cellulose membrane and dried by MART drying and MART-V drying. The functionality of FGF-2 after one week of storage at 40 °C was analysed by measuring the proliferation of Immortalised Mesenchymal Stem Cells (MSC-hTERT) in response to the preserved FGF-2.

In Chapter 6, a novel drying strategy, vacuum-spin drying, was applied to preserve the enzymes and other reagents in a rapid test kit, which was using reverse

transcription loop-mediated isothermal amplification (RT-LAMP) to detect the SARS-CoV-2 (the COVID-19 virus). The shelf lives of the test kit were studied with different drying conditions. The storage time and sensitivity of the vacuum-dried test kits were investigated and compared to freeze-dried kits and freshly prepared kits.

In Chapter 7, a temperature-dependent molecular switch, an oligonucleotide, was developed to reduce the self- or off-target amplification of the novel COVID-19 test kits, increasing the test kits' accuracy. Vacuum-spin dried test kits were used to test clinical RNA extracted samples and showed high sensitivity and specificity for detecting SARS-CoV-2.

The final Chapter 8 summarises the key findings in this thesis and provide a discussion of the future directions of protein preservation.

Chapter 2

Preservation of Functional Proteins with Drying

This chapter introduces the background of protein preservation and drying techniques to preserve the functionalities of proteins for long-term storage. Initially, the common degradation pathways of proteins are described. To minimise the degradation, the current preservation strategies are either storing protein at low temperature or drying protein to solid state.

TABLE OF CONTENTS

2.1 Protein Degradation 10
2.1.1 Physical Degradation 11
2.1.1.1 Denaturation 11
2.1.1.2 Surface Adsorptions 12
2.1.1.3 Aggregation and Precipiatation 13
2.1.2 Chemical Degradation 14
2.1.2.1 Hydrolysis 14
2.1.2.2 Oxidation 15
2.1.2.3 Covalent Aggregation 16
2.2 Current Strategies for Protein Stabilisation 17
2.2.1 Liquid Formulations – Cryopreservation 18
2.2.2 Cryoprotectants 21
2.2.3 Drying Strategies 22
2.2.3.1 Freeze Drying or Lyophilisation 22
2.2.3.2 Spray Drying 24
2.2.3.3 Spray Freeze Drying 26
2.2.3.4 Vacuum Foam Drying 27
2.2.4 Stabiliser for drying strategies 28
2.2.4.1 Disaccharides 30
2.3 Novel Drying Formulations 32
2.3.1 Sugar Film Drying 32
2.3.2 Matrix Assisted Room Temperature (MART) Drying 33
2.4 Scope of the Thesis 36

2.1 Protein Degradation

Proteins are naturally susceptible to degradation once they leave their native environment, which can cause proteins to lose their potencies and functionalities[43–47]. To maintain the effectiveness of proteins, the molecular structures of proteins need to be preserved and stabilised. Protein structures are determined by inter and intramolecular interactions, including covalent linkage, electrostatic interactions, hydrogen bonding, hydrophobic interactions and van der Waals force[75,76]. Environmental factors, such as pH, temperature, mechanical shear stresses and concentrations of proteins and salts, presence of other molecules could all disturb protein molecular structures and lead to denaturation. Understanding how these extrinsic factors denature proteins is essential for protein stabilisation.

2.1.1 Physical Degradation

Physical degradation changes the conformation of protein molecules without any alternation in the chemical composition[48]. In this work, four physical degradation pathways, denaturation, surface adsorption, aggregation and precipitation, will be illustrated.

2.1.1.1 Denaturation

Denaturation refers to the loss of globular or three-dimensional structures of protein. When protein is in globular structure or the native state, the net free energy of protein is at a minimum state, typically 5-20 kcal/mol[76]. When proteins are exposed to mechanical stresses (cavitation and shear) or heat, the net free energy of protein increases, leading to denaturation or unfolding[77–79]. The manifestation of protein denaturation is losing the tertiary and partially secondary structures[80–82]

Protein denaturation also occurs during dehydration. Water removal reduces the hydrogen bonding interactions between proteins and water molecules, altering the protein's hydration shell. When the deformed hydration shell can no longer support the globular structure, protein molecules will denature[76,83–85].

Temperature is also a key determining factor affecting protein molecular stability. The denaturation of protein could be induced by either thermally or cold denaturation[86–88]. Thermally denaturation is the most common degradation pathway, losing the globular structure at elevated temperatures[89]. The majority of protein molecules are also affected by cold denaturation. Reducing temperature could lower the repulsive forces between nonpolar amino acids of proteins and water molecules, causing stronger hydrogen bonding interactions[90–93]. The

proteins with higher net free energy are prone to unfold partially to release the gained energy[94].

Low temperatures also cause the formation of ice crystals when the temperature of the protein solution is stored below its freezing point. The ice nucleation triggers phase separation and generates the ice-water interface, adversely affecting protein stability[95–98]. The ice-water interface could lower the activation energy for unfolding, which does not require proteins to be adsorbed on the ice crystals[95]. A considerable loss of lactate dehydrogenase activity was observed with the formation of ice crystals. At the same time, no degradation of LDH is detected at the same compositions but without ice crystals[99]. Meanwhile, the volume expansion from ice crystallisation generates mechanical stresses and high local pressure, causing protein denaturation[95].

2.1.1.2 Surface Adsorptions

Protein surface adsorption is unavoidable during bioprocessing and manufacturing and is a highly complex phenomenon[100]. The adsorption involves interactions between protein molecules and different material surfaces[101,102]. For instance, granulocyte colony-stimulating factor (G-CSF)[103] and interleukin-2 (IL-2)[103] in solutions are liable to be adsorbed to glass. Bovine serum albumin (BSA) and immunoglobulin G1 (IgG1) often adsorb to stainless steel[104].

When approaching the surface, proteins in the native state are attracted and bound to some contact sites on the surface. For instance, protein molecules are prone to be adsorbed by hydrophobic surfaces[105,106]. Since water is a polar molecule, water near a hydrophobic surface interacts with neighbouring water molecules rather

than the nonpolar (hydrophobic) surface. It altered water structures around the hydrophobic surface, dehydrating and unfolding proteins. The hydrophobic groups of the partially unfolded protein form interactions with the hydrophobic surface[101,107,108]

Proteins are multi-polar molecules and adsorbed on the hydrophilic surface, although the displacement of water on the hydrophilic surface makes such adsorption less energetically favourable[101]. When protein molecules contact a hydrophilic surface, the free energy of proteins increases compared to that in the liquid, forcing the proteins to expand their footprint via reorganization[109–113]. As a protein forms more interactions with a hydrophilic surface, the structure of protein reorganises, leading to the release of the counterions or solvation molecules (and thereby additional structural rearrangement) as well as a loss of secondary structures[114–116]. There is almost no resistance for adsorbed proteins eluting back to the solution when the protein layer is freshly established. After a specific period, spanning from a few minutes to serval hours, proteins could be irreversibly adsorbed on the surface[116]. In certain cases, some peptides or proteins perform their functions only after adsorption[117,118], while in other cases, adsorption can irreversibly unfold proteins[112,119], leading to aggregation and loss of function[120,121].

2.1.1.3 Aggregation and Precipiatation

When a protein partially or completely unfolds, the uncovered hydrophobic groups form hydrophobic interactions with neighbouring proteins, altering their structures and promoting protein aggregation[85,122,123]. In most cases, aggregation is a kind of irreversible process. Aggregates appear in a soluble state with varied sizes and

grow gradually until no longer being soluble, which result in the precipitation and cloudiness of the solution[124].

Protein aggregation can also be caused by high salt concentration[125]. Low ionic strength increases protein solubility. Conversely, high ionic strength or high salt concentration condition increases the chemical potential of the proteins and can change the protein conformation and render them insoluble. Salted out proteins retain activities, and the process is reversible upon dilution[126].

2.1.2 Chemical Degradation

Chemical degradation of a protein involves a covalent modification. The most frequently described degradation pathways are hydrolysis, oxidation and covalent aggregation[77,127].

2.1.2.1 Hydrolysis

Hydrolysis is a chemical reaction in which water molecules beak chemical bonds of the compunds[128]. Deamidation is the most common hydrolytic reaction in proteins. An amide functional group from asparagine (Asn) or glutamine (Glu) residues on the protein is converted into another functional group via hydrolysis. For Asn residues, the amide is converted to a carboxylic acid group, becoming either aspartic acid (Asp) or iso-aspartic acid (iso-Asp). Iso-Asp contains a methylene group that Asp does not contain. This methylene group can cause a larger disturbance of local protein confirmation when iso-Asp is formed[129,130]. Although glutamine (Gln) deamidation also occurs, the reaction rate is considerably slower than Asn deamidation[128].

Deamidation alters the polypeptide sequence and changes the local conformation of proteins by converting a neutral side chain into an anionic side chain. These negatively charged side chains certainly increase the likelihood of protein aggregation[130–132].

The rate and product of deamidation depend on the protein's primary sequence, pH and temperature[77,128,133,134]. Deamidation occurs in both acidic and basic conditions. In acidic conditions (pH<5), the deamidation of the Asn chain to Asp is favoured. In neutral to basic pH conditions (pH>5), carboxylic acids are generated via the formation of cyclic succinimide intermediate (Asu)[128,135]. The minimum deamidation rate is typically detected in the pH range of 4 to 5. Thus, adding buffers like phosphate, borate, and tris may promote deamidation[128,136,137].

The deamidation could be inhibited by decreasing the temperature[128] and water content[138]. Drying protein solution can decrease the deamidation rate. However, when the water content is lower than a threshold value, the rate of deamidation becomes independent. It means drying protein solution could only decrease the deamidation rate but not eliminate the deamidation[138].

2.1.2.2 Oxidation

Oxidation is the primary protein degradation pathway and can occur by exposing proteins to light, atmospheric oxygen, peroxide, or redox-active metal ions[48,139–142]. Methionine and tryptophan are the most common sites for oxidation. Cysteine, histidine or tyrosine residues can also be oxidised[77]. If a protein contains aromatic rings, oxidisation of methionine and cysteine often results in the formation of

sulphur groups[143]. Such modifications can alter protein conformation and can potentially lead to aggregation. Several proteins, such as parathyroid hormone, human stem cell factor and human growth hormone, have been shown to lose functionality via oxidation[75,128].

Oxidation can still occur in sealed samples (under vacuum) or in samples containing inter gas like nitrogen because any oxygen remaining in the sample can oxidise the sample completely[77,144]. Molecular oxygen is not exceptionally reactive at the ground state, which means the presence of oxygen is not enough for rapid oxidisation. The contamination from excipients carrying transitional metal ions or peroxide might be the major cause of protein oxidation. For instance, peroxide has always been found when adding excipients such as polyethylene glycols and surfactants[145]. When exposed to light or transitional metal ions, molecular oxygen could be activated to superoxide radicals, hydroxyl radicals or hydrogen peroxide[146], oxidising proteins. Therefore, excipient impurities need to be minimised[78]. The addition of antioxidants or reducing agents may bring advent effects, prompting the oxidation[147,148].

Oxidation can be minimised by adding certain sugars, such as dextran[149], mannitol and trehalose[146]. These sugars could hinder oxidisation by interacting with metal ions or stabilising the native conformation of proteins via hydrogen bonding. Such stabilisation does not occur if using reducing sugars, such as glucose[146].

2.1.2.3 Covalent Aggregation

Covalent aggregation normally occurs on proteins with thiol-disulphides[150–152]. The covalent aggregation is caused by the thiol-disulphide interchange. This reaction

commonly occurs on proteins, like bovine serum albumin (BSA) and recombinant human albumin (rHA), containing free thiol and disulphide bonds[153,154]. The mechanism is demonstrated in ***Figure 2.1***. Ionised thiol groups of one albumin molecule can disturb the disulphide linkage of another albumin molecule by a nucleophilic interaction. A new disulphide bond forms between two protein molecules and release a free ionised thiol group. Then, this propagative process could keep adding free albumin molecules and eventually cause insoluble aggregation[150,154,155].

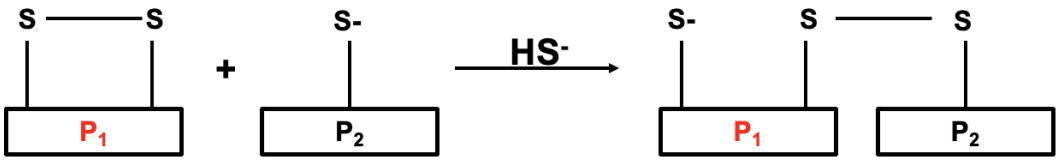


Figure 2.1*: The intermolecular thiol-disulphide interchange reaction.*

The free thiols, catalysts of the interchange, are the limiting reagent in disulphide interchange[156,157]. Some proteins, like insulin, do not contain a free thiol at their native conformation but produce free thiols if the protein undergoes a hydrolysis reaction. Dehydration is still an effective method to minimise aggregation[158].

2.2 Current Strategies for Protein Stabilisation

Cryopreservation is a widely used strategy to slow the rate of protein degradation for long-term storage by storing proteins in solution at -20 °C or even -80 °C[51,52].

Although the formation of ice crystals can denature proteins, the protein molecules are largely immobilised in the frozen state, decreasing the diffusive collisions of molecules and decreasing the likelihood of aggregation. Alternatively, dehydration, removing free water, can also increase protein stability by inhibiting degradations from hydrolysis and isomerization[159].

2.2.1 Liquid Formulations – Cryopreservation

From a clinical point of view, storing protein therapeutics in liquid is preferable, as aqueous protein is ready to use and does not require reconstitution before use [160]. However, as mentioned above, most proteins are unstable even at 4 °C. Therefore, protein solutions are primarily frozen at -20 °C or -80 °C in order to increase stability and extend shelf life. The frozen state also hinders microbial growth and eliminates the formation of bubbles or foam in the solution during transportation[161–163]. In this case, proteins need to be stored and distributed while remaining frozen, requiring low-temperature transportation and storage facilities[164]. What is more, low temperatures and the formulations of ice crystals are the two main factors impacting the stability of products over the cryopreservation, as mentioned above[88,165,166].

The ice-water interface generated by ice crystals is the main issue causing the protein denaturation. The cooling rate decides the size and the surface area of ice crystals. At low cooling rates, larger ice crystals are formed, and on the contrary, plenty of tiny ice crystals are obtained with a high cooling rate[167,168].

Although the lower ice-water interfacial area is generated with a low cooling rate, prolonged exposure to freeze-concentrated solutes and low temperatures

increases protein aggregation[149]. The formation of ice crystals excludes solutes from ice, causing freeze concentration at the ice front[169,170]. Electrolytes, like sodium chloride, may be increased as much as 40 folds. Such high ionic strength in unfrozen water could alter the conformation of the protein, which may consequentially salt out as a precipitate. Moreover, increased solute concentration may cause more chemical reactions[171]. For instance, pH buffers could precipitate and thereby change the pH of the unfrozen solution, which would alter protein structure[172,173]. The difference in concentration drives the diffusion and convection. However, the increased excipient concentrations may increase the viscosity of unfrozen water, reducing the mass transfer rate[174]. The solute distribution depends on the difference between the growth rate of ice crystals and the mass transfer rate[175].

When a solution is cooled quickly, the size of ice crystals decreases, but the quantity increases, resulting in a greater surface area for the ice-liquid interface. This greater surface area of the ice-liquid interface increases protein denaturation[176], as the activation energy of unfolding is lower at the ice-liquid interface.

Putting small samples directly to liquid nitrogen, the ultra-high cooling rate can avoid the formation of ice crystals. This process is known as vitrification. Vitrification results in a glassy matrix with a relatively high viscosity that inhibits the presence of ice nucleation and crystallization[177], increasing the stability of proteins for long term storage[178–180]. However, vitrification cannot be achieved in many fields due to equipment limitations[96]. The required high cooling rate cannot be

achieved. Also, the vitrified state is not stable. Any disturbance in the environment, such as temperature fluctuation or moisture absorption, leads to uncontrolled recrystallisation. Therefore, cryoprotective agents (CPAs) are added to inhibit crystallisation, which will be thoroughly discussed in the following context[181].

Apart from the cooling rate, the thawing rate from the frozen state also affects protein stability. Fast thawing rates, where the temperature is increased faster than 10 °C/min, preserve proteins more effectively than slow thawing rates. This effect is much more pronounced for products frozen with high cooling rates[182]. As mentioned above, plenty of tiny ice crystals are distributed in the samples frozen with high cooling rates. Slight temperature changes can cause ice recrystallisation. Tiny crystals grow into larger ones. The stresses generated from this volume expansion can perturb protein structure and causes degradation. However, ice recrystallisation could be inhibited by fast thawing rates. When the thawing rate was faster than 20 °C/min, the recovery of proteins was expressive improved[176].

An additional difficulty in cryopreservation is maintaining the necessary cold storage temperature. For cryopreservation of protein therapeutics, it is necessary to maintain a cold chain so that the therapeutic never loses its potency by being kept outside the optimum temperature during transport, handling and storage[183–187]. The high cost of maintaining the cold chain can be an economic burden, especially for areas still having a shortage of refrigeration and electricity[188,189]. For instance, the cold chain's financial cost could account for around 80% of the total cost of a vaccination program. Moreover, deficiencies in the cryogenic equipment within a cold chain frequently occur even in developed counties, causing a high

waste rate[190,191]. Loss of temperature control leads to the degradation and waste of approximately half the vaccines produced each year[191,192].

2.2.2 Cryoprotectants

The addition of cryoprotective agents (CPAs), or cryoprotectants, can distort water molecular interactions by disturbing the hydrogen bonding in the solution. Such alternations inhibit or slow down ice crystallisation and mitigate the solute accumulation[167,193–197]. Polyols (Polyethylene glycol), polymer (Dextran), polyvinyl alcohol (PVA), hydroxyethyl starch (HES)[193–195] and non-aqueous solvents, such as dimethylsulphoxide (DMSO), dimethylformamide (DMF), are commonly added to lower the melting point of water and reduce the aggregation[198]. For example, polyethene glycol (PEG) protected phosphofructokinase and lactate dehydrogenase over multiple freeze-thawing cycles[199]. However, PEG cannot provide protection during lyophilisation unless used with other stabilisers, such as glucose or trehalose[200]. Buffers and salt, such as HEPES buffer, citrate buffer and phosphate buffered saline, can also be added to prevent a pH shift during the freezing[201].

Another set of cryoprotective agents, glycerol and antifreeze proteins (AFPs), is used to lower the freezing point and prevent the solution from freezing at -20 °C or lower temperatures[202]. AFPs were initially extracted from fish[203] and applied as cryoprotectants[203]. Currently, AFPs are obtained from a wide range of organisms living in freezing temperatures. AFPs from insects can decrease the solution's freezing point by up to 7°C, which is more effective than AFPs from fish and plants [204]. When AFPs irreversibly bind to ice crystals, the freezing point is depressed to

be lower than the expected melting temperature, preventing the growth of ice crystallization[205]. Although AFPs are over 200 times more effective than ideal solutes[205], the high cost of commercial AFPs production, which requires recombinant protein expression techniques, limits their applications[206].

2.2.3 Drying Strategies

Water removal via drying minimises hydrolysis and immobilises protein molecules in the solid state[207,208]. The dried therapeutics, if appropriately dried, presents excellent stability at room temperature[209]. At present, common drying techniques consist of freeze-drying (FD), spray drying (SD), spray freeze drying (SFD) and vacuum foam drying(SFD)[207].

2.2.3.1 Freeze Drying or Lyophilisation

Lyophilization or freeze-drying (FD) was initially applied in the food and dairy manufacturing processes. With the development of recombinant proteins as therapeutics, freeze-drying started to gain interest in the pharmaceutic industry[207]. Several proteins, such as immunoglobulin G (IgG)[210], lysozyme[211], bovine serum albumin(BSA)[212] and Anti-IgE antibodies[213], are lyophilised to extend their shelf lives151. The lyophilisation process consists of three steps: freezing, primary drying, and secondary drying[181,214–216].

In the freezing step, water is frozen into ice crystals and separated from the solution. As already discussed, the freezing step can potentially alter protein confirmation via a number of mechanisms, including ice crystallisation and freeze concentration of solutes. Additionally, as in cryopreservation, the cooling rate of lyophilisation must also be optimized. The cooling rate in freeze-drying determines the size and

distribution of ice crystals and affects the porosity and surface area of the dried products. The size of ice crystals also links to the efficiency of the process and the final quality[171,217–219]. The ice crystals in large size promote the drying rate in primary drying but require lower temperatures due to the lower collapse temperature (T_c)[168].

Collapse temperature (T_c) is a critical temperature for samples to preserve the shape and microstructure during drying. If drying above collapse temperature, the structure of the cake will collapse. The desired porous structure of the final product will also be lost[220–222]. Meanwhile, ice sublimation in the primary drying step is hindered by the collapsed structure[223,224]. Meanwhile, the requirement of reconstitution is more restrictive, requiring longer reconstitution time or higher reconstitution temperatures[220]. For frozen products, the collapse temperature is determined by freeze-drying microscopy (FDM)[225,226].

The freezing step of lyophilisation ends when the temperature of the sample is lower than T_c. The next step in lyophilisation is primary drying, where the pressure in the chamber is lowered [227]. When the chamber pressure is lower than the water saturation vapour pressure at the temperature of the frozen sample, ice is sublimated from the frozen sample slowly[228]. Energy is required to sublimate the frozen water. Due to the low pressure in the drying chamber, heat transfer to the sample by convection is limited. The majority of heat transmission is conduction from the contact surfaces, mainly from the shelves[228,229]. Increasing the drying temperature to a value but below the collapse temperature can reduce the drying time. Increasing one degree in drying temperature could save around 13% of

primary drying time[230]. The collapse temperature could be increased by adding bulking agents, polymers or polysaccharides, into the freeze-drying formulation to shorten the drying process[231–233].

After primary drying, the free water in the sample is removed[234]. The secondary drying is commencing by elevating the drying temperature to remove the residual water, which was trapped in the glassy solid due to the high viscosity or bonded water. When the moisture content of the product reaches the required standard, the whole freeze-drying process is finished[215].

Although lyophilisation has been extensively studied and optimized, the prolonged drying time leads to high energy use on top of the high capital cost (vacuum equipment). The expenditure of lyophilisation can be six times higher than that of spray drying and two to five times higher than drying by hot air[235]. Meanwhile, each product requires a customised formulation and a typical freeze-drying protocol. After freeze-drying, the stability of the final products cannot be guaranteed[219]. Owing to the high porosity of lyophilised cake (the final product), the large contact surface area makes the final product vulnerable to oxidation in storage. Sealing and packing in an inert gas environment are recommended to increase the stability of the final products[236].

2.2.3.2 Spray Drying

Compared to lyophilisation, spray drying is a single-step process in which solid protein particles are generated by a continuous drying process[237,238]. This faster and more economical process converts aqueous solution into dried powders. Spray drying was initially employed in dairy[239] and food processing industries[239].

While initially used in dehydrating active extracts from plants, spray drying has also become an essential drying process in biopharmaceutics[239]. A variety of proteins, including Influenza vaccine[212], catalase[212], erythropoietin[212], Anti-IgE Mab, rhDNase[212], have been produced by this technique.

The whole drying process is comprised of three steps. The formulated protein solution is first fed into an atomiser and sprayed into the drying chamber as a mist. Upon entering the drying chamber, water quickly evaporates from the mist because of the large contact surface compared to the aqueous sample. Hence, the drying time is significantly shortened for spray drying compared to other drying techniques. After passing through the drying chamber, the dried products are transported into the cyclone and settled in the collector[240–242].

Spray drying is a controllable continuous process, having high batch-to-batch reproducibility and controllable and uniform dry particle sizes. This fast and cheap method is suitable for drying materials with high heat resistance. It would be more challenging to heat-sensitive and unstable materials like proteins. Extensive studies need to be done to optimise the formulations, in order to prevent proteins in the sample from shaking, pumping, shear stresses, dehydration, elevated temperature and aggregations[241,243,244]. The common use of low molecular weight sugars as excipients causes dried products to stick to the walls of the drying chamber and conveying systems, resulting in a low product yield[244]. This adhesion of the product to the system can also decrease protein activity. For instance, only 67% of all spray-dried human growth hormone (hGH) molecules retained activity in the final dried product[245].

Processing variables during spray-drying, such as inlet air temperature, airflow rate, residence time and outlet air temperature, significantly influence the quality and morphology of the dried product. Another limitation of spray-drying is that this technique cannot be used with products sensitive to air or must be processed under aseptic conditions[207].

2.2.3.3 Spray Freeze Drying

Another effective drying method, spray freeze drying (SFD), is the combination of freeze-drying and spray drying. It has been developed for preserving thermolabile active pharmaceutical ingredients, insulin[212], Influenza vaccine[246], and anthrax vaccines[209] as lyophilised microparticles. The formulated protein solution is atomised into tiny droplets, frozen by a cryogenic fluid, typically liquid nitrogen, then dried by sublimating ice under low-pressure condition[237,247–249].

The ultra-low temperature environment generated by cryogenic liquid suppresses ice crystallisation and pH shifts. Since sample droplets are vitrificated, molecules are immobilised rapidly in the amorphous state, where protein crystallisation and phase separation between proteins and excipient is considerably prevented[250]. It is known that the protein powders produced by spray freeze drying are easy to handle and distribute compared to those produced by freeze-drying. The protein particles in different densities and size distributions could be manufactured by tuning the parameters in spray freeze drying, which can fit various pharmaceutical applications[251,252]. However, in spite of its benefits, spray freeze-drying is time-consuming, has high capital and maintenance costs, the products are often fragile

particles, and the safety risks of cryogenic fluids are limitations of this drying technique[253].

2.2.3.4 Vacuum Foam Drying

Vacuum foam drying (VFD) has recently been developed as an alternative approach to spray and freeze-drying for preserving bioproducts. The formulated biopharmaceutic solution with stabilisers is boiling or foaming under reduced pressure conditions at room temperature. Water is evaporated quickly due to the reduced pressure in the drying chamber. This foaming is analogous to when the primary drying step of freeze-drying is performed at temperatures above a sample's collapse temperature[254–256]. Some vaccines have recently been preserved by vacuum foam drying[257–260]. For example, the vaccine against parainfluenza was better preserved when the vaccine was dried with VFD, compared to freeze-drying and spray freeze-drying. With VFD, the vaccine's potency was retained after 20 weeks of storage at 25 °C, with a low titer loss of only0.73 log/week$^{0.5}$ loss in titer. In contrast, vaccines preserved by the other two drying methods had a titer loss of 1 log/week$^{0.5}$ [260].

However, to ensure the quality of the dried product, the drying conditions need to be controlled carefully and precisely. If the pressure dops too quickly, the solution could overflow the containers due to the foaming. Meanwhile, the solution will freeze due to the evaporation[261]. By contrast, the foaming is suppressed, generating a low evaporation rate. Under this circumstance, the stabilisers could form a polymer skin at the surface, further decreasing the evaporation rate[262,263]. In spite of extensive research into how materials foam and boil[264], the drying process is still largely uncontrollable and not robust enough for the industry.

Meanwhile, the non-uniform dried cake generated by vacuum foam drying affects reconstitution time and user acceptance[261].

2.2.4 Stabiliser for Drying Strategies

Lyoprotectants, usually sugars, are added to increase the thermostability of proteins during any drying process[211]. Lyoprotectants were initially discovered in organisms that increase the concentration of sugar or sugar-alcohols to stabilise proteins in dry or frozen conditions[265,266]. Crowe and Carpenter[267] have applied this natural strategy to protein preservation by adding sucrose into the formulation before lyophilisation. When sugars are added to samples that undergo freeze-drying, recovery of protein functions can be over 90%. This promising outcome has facilitated the development of various drying formulations[268].

Two prevalent stabilisation mechanisms are proposed to demonstrate how sugars stabilise proteins during the drying process: the water-substitution hypothesis based on thermodynamics and the glassy matrix hypothesis based on kinetics[78].

The water substitution hypothesis considers thermodynamics[78]. Water plays a significant role in maintaining protein conformation in the aqueous state via hydrogen bonding[269]. Increasing hydrogen bonding density prompts the thermal stability of proteins[270]. When a protein is dehydrated, water is no longer present to facilitate hydrogen bonding, and the protein contains fewer hydrogen bonds. In this case, the protein is less likely to maintain the native state and more likely to degrade. Sugars can act as lyoprotectants because sugars can substitute water molecules during dehydration by forming hydrogen bonds with proteins via the sugar's hydroxyl groups. With sugars, the hydrogen bonds in a protein are

preserved, and thereby the native conformation of the protein is maintained during the drying process[15,167].

The kinetic stabilisation mechanism, or the glassy matrix hypothesis, describes the kinetics of protein degradation processes. The reactivity and degradation of proteins are associated with molecular mobility. Therefore, higher molecular mobility results in a faster degradation rate[167,271,272]. When using sugars or polymers as stabilisers, the viscosity of the unfrozen liquid is increased during the water removal. When the temperature reaches glass transition temperature (T_g), protein with sugars transfers from a rubbery liquid state to a rigid glassy state. After the instant glass transition, the viscosity surges to 10^{13} poise, which expressively hindering protein movement and degradation[273–278]. The glass transition temperature of the product is directly related to the residual moisture content[279,280]. Further water removal in secondary drying of freezing drying allows the lyophilised cake to maintain the glassy state at room temperature or even elevated temperatures and retain the effectiveness of products[281].

In summary, sugar helps stabilize proteins via substitution of water (in maintaining a protein's hydrogen bonds) that maintains the native structure of proteins and the formation of a glassy matrix of sugar polymers that limits the mobility and degradation of protein molecules[212].

The stability of proteins cannot be assured by adding any sugar into the formulation. Sugars with different molecular weights have different stabilising effects. Sugars with low molecular weight, such as glucose, have stronger hydrogen bonding

interactions with proteins[282] but have a relatively low glass transition temperature, around 23 °C[283]. The addition of glucose decreases the glass transition temperature of dried products, which requires a lower storage temperature to maintain the glassy state[284–286]. By contrast, polysaccharides and polymers generally possess high glass transition temperatures[283]. The glass transition temperature of Dextran, a sugar with a molecular weight of 4 kDa, is around 157 °C[287]. In addition to Dextran, Polyvinylpyrrolidone (PVP) and PEG) are often added to samples to increase the final glass transition temperature[288–290]. However, interactions between high molecular weight sugars and proteins are weaker than sugars of low molecular weight. Polysaccharides and polymers have a lower capacity of water substitution than smaller sugars[282].

2.2.4.1 Disaccharides

The ideal stabilizer should be selected by balancing the above mechanisms. That is, ideally, disaccharides with relatively high glass transition temperatures should be used as stabilisers[291]. Disaccharides, sucrose and trehalose, are frequently used as stabilisers in cryopreservation and lyophilisation for this reason[97,292]. Sucrose and trehalose have the same chemical formula ($C_{12}H_{22}O_{11}$), but different configurations (***Figure 2.2***). The trehalose molecule comprises two pyranose rings, while sucrose consists of one pyranose ring and one furanose ring. Since neither contains anomeric hydroxyl groups, both trehalose and sucrose are non-reducing sugars[293].

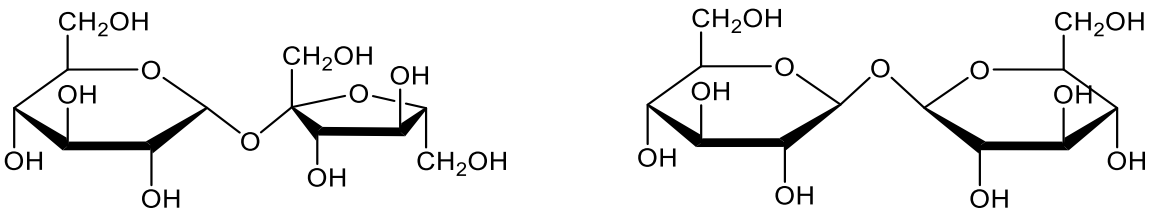


***Figure 2.2**: Structural formula for sucrose(left) and trehalose(right).*

Both disaccharides can replace water molecules to form hydrogen bonds with proteins and immobilise molecules in the glassy state after drying[293]. Sample preservation with trehalose is typically more effective than sucrose[294–297]. One possible explanation for this observation is that the properties of these two similar molecules, such as solubility, viscosity, glass transition temperature, and the interaction with water molecules, are significantly different to explain their different success in preserving proteins[298–303]. For example, trehalose contains (1-1) - α bonding that increases the rigidity of trehalose molecules[304,305], allowing trehalose to resist acid hydrolysis and high temperatures[293]. Additionally, less intramolecular hydrogen bonding in trehalose (=1) compared to sucrose (=2) means that more sites on trehalose are available for forming hydrogen bonds with other molecules, such as water and proteins[293]. Furthermore, hydrogen bonding between trehalose and water disrupts the natural tetrahedral structure of water, thereby inhibiting ice formation during freezing. Therefore, for all these reasons, trehalose is widely used as a protective agent in freeze drying, which can provide the protection functions in the freezing step and dying steps[142,306].

Although the solubility of sucrose (2.14 g/g water) in water is almost twice as much as trehalose (1.1 g/g water)[307], the relatively low glass transition temperature of sucrose (around 60 °C, compared to trehalose which is around 106 °C) limits its applications[283,308]. Moreover, the viscosities of trehalose solutions are always higher than sucrose solutions with identical sugar concentrations and temperatures[309]. These differences allow trehalose to materialise a homogeneous

matrix much easier than sucrose[310,311] and has a more extensive concentration range to achieve virtrification[300].

In the formulation, disaccharide concentration should be well considered. There needs to be a high enough concentration of disaccharides to form a monomolecular layer on the protein surface. However, excessive disaccharides may lead to crystallisation in freezing or dehydration conditions, reducing the hydrogen bonding with protein and causing aggregation[294]. For the sample that requires a higher glass transition temperature, polysaccharides are typically added to the formulation[312].

2.3 Novel Drying Formulations

2.3.1 Sugar Film Drying

Apart from the established drying methods mentioned above, new drying strategies for biopharmaceutics are being developed. Sugars are often involved in these new techniques. One such method to improve the thermostability of bioproducts is the sugar membrane technique. This technique relies on the protective ability of disaccharides to preserve biopharmaceutics. The sugar membrane technique is relatively simple and has low energy intensity. First, biopharmaceutics in an aqueous solution is mixed with a sugar solution throughout and transferred into Eppendorf tubes or on plastic plates. Then, the solution is dried overnight in a biosafety cabinet and forms thin sugar films, trapping the biopharmaceutic molecules. Since such samples are kept at room temperature, reconstitution is the only step before use[63,64,313,314].

In the previous work[314], various vaccines, including enveloped DNA (Herpes Simplex Virus type 2) and RNA (Influenza A virus) viral vaccines, were dried in the Eppendorf tubes using the sugar film drying method with trehalose and pullulan. The results showed that the potency of both vaccines is largely retained after being stored for 12 weeks at 40 °C. The loss of potency or functions was mainly dropped during the first 4-week storage, then remained relatively stable after 4 weeks. These observations suggested that multiple stages of degradation occurred in sugar film preservation.

In another study, formulated bacteria phage was dried on a well-plate to increase the drying efficiency[315]. The activity loss was reduced compared to the products dried in the tube. The phage activity could be retained after drying for three months at room temperature, showing great potential for drying other bioproducts. However, the drying process required over one day to be dried. This is because the sugar film formed on the surface and became a barrier for water removal[262].

2.3.2 Matrix Assisted Room Temperature (MART) Drying

Pawan[316] and Rebert[64] put forward another way to perform the sugar film drying, i.e. to dry vaccines on fibre matrices at room temperature, which was the preliminary studies of Matrix Assisted Room Temperature (MART) drying. The process of MART drying is relatively straightforward. The formulated protein or bioproduct solution is loaded onto fibre membrane matrices and dried overnight in a low relative humidity (RH) environment at room temperature. The dried products

are stabilised at room temperature or elevated temperatures and reconstituted with water or buffer solution before use.

MART drying showed promising results in vaccine preservation. For example, two recombinant vaccine vectors, the attenuated poxvirus modified vaccinia virus Ankara (MVA) and human adenovirus type 5 (AdHu5), were stabilised on Whatman Standard 14 glass fibre matrices. The efficacies of dried vaccines could be retained for up to six months at 45 °C[64,316]. However, glass fibre is brittle, and the fragments may enter the human body during vaccine administration, causing allergic reactions. Therefore, the application in pharmaceutics is limited[317].

Seven alternative porous membranes (Table A1 in Appendix 1) have been tested to replace glass fibres. The porosity, loading capacity and hydrophilicity of these membranes were diversed[62]. The adenoviral vaccine vectors (AdHu5) supplemented with sugars were dried on these seven fibre membranes. After storing at 45 °C for one week, the efficacy of dried vaccines was measured by cell infection assay. The reconstituted vaccine solutions were incubated with Human Embryonic Kidney cell (HEK293) lines at 37 °C, 5% CO_2 for 48 hours, and fixed 100% methanol. After immunostaining, the number of infected cells was counted to indicate the potency of vaccines. Comparing the positive controls stored at -80 °C for one week, the loss of vaccines dried on glass fibre after storage was minimal[62]. Scanning electron microscopy (SEM) showed that only glass fibre contained ultra-thin sugar films (***Figure 2.3***). For other tested fibre matrices, no sugar film was detected after drying. It is related to the surface properties of this unique glass fibre[64,316].

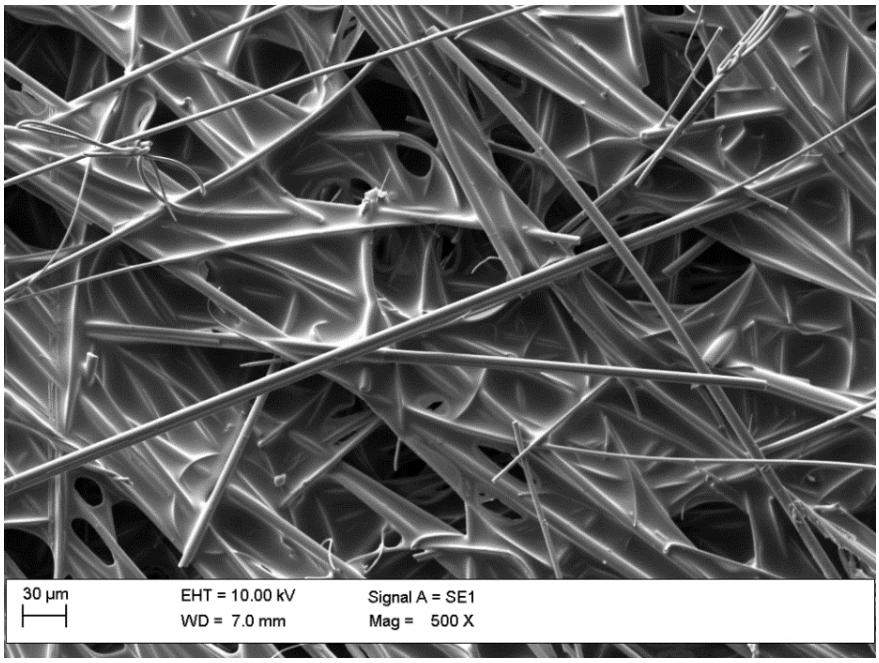


***Figure 2.3**: Scanning electron microscopy image of sugar films formed on a glass fibre matrix at 500X magnification.*

Since scanning electron microscopy cannot locate vaccine particles within the fibre membrane, fluorescently tagged antibodies were formulated with the same sugar solution and loaded on these seven fibre membranes. The fluorescent signal of each membrane was scanned after drying by multiphoton microscopy (MPM) layer by layer, generating a three-dimensional fluorescence image eventually (Figure A1 in Appendix 1). The fluorescent signal is mainly localised in the sugar films in the glass fibre matrix, showing the viral particles were trapped within the sugar film. Drying with other membranes, such localisation of fluorescence was not observed, and the fluorescent signal has a uniform distribution[64,316].

There is a clear indication that the sugar film formation on the fibre matrix is essential for preserving dried bioproducts. However, how sugar films formed the fibre matrix after drying and the stabilisation mechanisms of sugar film were

unclear. The current best option, glass fibre, was not suitable for clinical use. It is noted that these preliminary conclusions are based on the tests using viral vaccines, and less attempt has been made to use the matrix to support drying functional proteins at room temperature. In addition, overnight drying is required owing to the low drying efficiency. Hence, it is proposed to conduct a thorough study on MART drying of proteins at room temperature and supported with a three-dimensional porous matrix.

2.4 Scope of Thesis

The overall aim of the thesis is to study advanced drying methods for proteins, which have clinical relevance and benchmark with the common freeze-drying. With MART drying as the primary target, mathematical modelling and experimental study are carried out to identify and optimise the critical design and operational parameters. The formation of sugar film and its stabilisation mechanisms will be studied by numerical simulation. The feasibility of MART drying will be investigated by the potencies of functional proteins after MART drying and storage. Enzyme and human growth factor, as examples, are stabilised by standard MART drying and also under vacuum (MART-V drying). Compared to cryogenic storage and freeze-drying, the MART dried proteins reserved their functionality, showing this fast and low-cost MART drying is effective and a promising alternative to freeze-drying.

Responding to the COVID-19 pandemic, a research effort was directed to develop an RT-LAMP rapid test kit to detect SRAS-COV-2 during the lockdown. On top of

the molecular probe design and testing, drying of formulated enzymes and other reagents to improve the thermostability of test kits was an important step contributing to the field deployments at airports and point of care testing. Spin-vacuum drying, again at room temperature, with optimised parameters, was developed and successfully applied to the manufacture of the rapid test kits, Oxsed RaViD Direct, which was also benchmarked with industrial freeze-drying.

Chapter 3

Numerical Study of the Formation and Drying Kinetics of a Capillary Bridge of Trehalose solution between two Parallel Hydrophilic Fibres

MART drying proved to be effective to preserve some vaccines for long term storage. The mechanism of how biologics and their functions are preserved in the sugar film during MART drying is unclear. Electron microscopic study indicated vaccine particles need to be trapped within the vitrified sugar structure to preserve their functions. Capillary bridging is essential to form the sugar films. This chapter aims to develop mathematical models to predict the formation of capillary bridges of sugar solutions and their stability during drying.

This chapter is based on the paper:

Yu, Y., Yang, A., Ye, H., Dye, J. F. & Cui, Z. Numerical study of the formation and drying kinetics of a capillary bridge of trehalose solution between two parallel hydrophilic fibres. *Chem. Eng. Sci.* **226**, 115849 (2020).

As the main author, Y Yu's contribution in this paper is developing the numerical models, simulating the results analysing the data and drafting the paper.

TABLE OF CONTENTS

3.1 Introduction 39

3.2 List of Variables 42

3.3 Geometric Criterion for Forming Capillary Bridge 43

3.4 Modelling of Drying Dynamics of Capillary Bridge 47

3.4.1 Mathematical Framework and Assumptions 47
3.4.2 Governing Equations 49
3.4.3 Boundary Conditions 50
3.4.4 Dimensionless Scaling 52
3.4.5 Evaporation Rate 58

3.5 Simulated Results of Drying Dynamics and Discussions 59

3.5.1 Determination of Capillary Shape 59
3.5.2 Simulation Results with Pure Water 60
3.5.3 Simulation Results with Different Solute Concentrations 63
3.5.3.1 Initial Trehalose Concentration=1 M 63
3.5.3.2 Initial Trehalose Concentration=0.5 M 65
3.5.3.3 Initial Trehalose Concentration=2 M 68

3.6 Conclusions 69

3.1 Introduction

The capillary bridge, also called the liquid bridge, is a volume of liquid spanning two or more solid surfaces by surface tension and capillary pressure[317–319], typically recognized in granular flows[320,321], microfluidic dynamics[322,323], oil recovery[318] and pattern formation of solidified materials[319]. Since Young studied the surface tension of the capillary bridge in 1805[320], much work has been done to investigate the shape and stability of capillary bridges between surfaces with differences in wettability, rugosity and geometry, principally focusing on spherical particles[321–329]. Less attention has been paid to the capillary bridge in fibre matrices, and the majority of these studies have analysed the wetting morphologies experimentally[330–334]. Boulogen et al.[335] presented experimental results on evaluating the viscose liquid evaporation at the cross point of two nylon fibres aligned with different angles (column, drop and mixed) and compared the evaporation rate with a simplified predication.

Capillary bridge structure in fibre matrices determines the wetting, the degree of liquid retention and the drying rate[330,336]. The bridge geometry is a principal parameter in the drying dynamic defining either the break point or solidification point. Several experiments have studied the rupture of a pure water capillary bridge due to the evaporation[337–340]. However, the drying kinetics of a solution capillary bridge, such as a sugar solution, is still poorly understood. In this chapter, we seek to model these two processes.

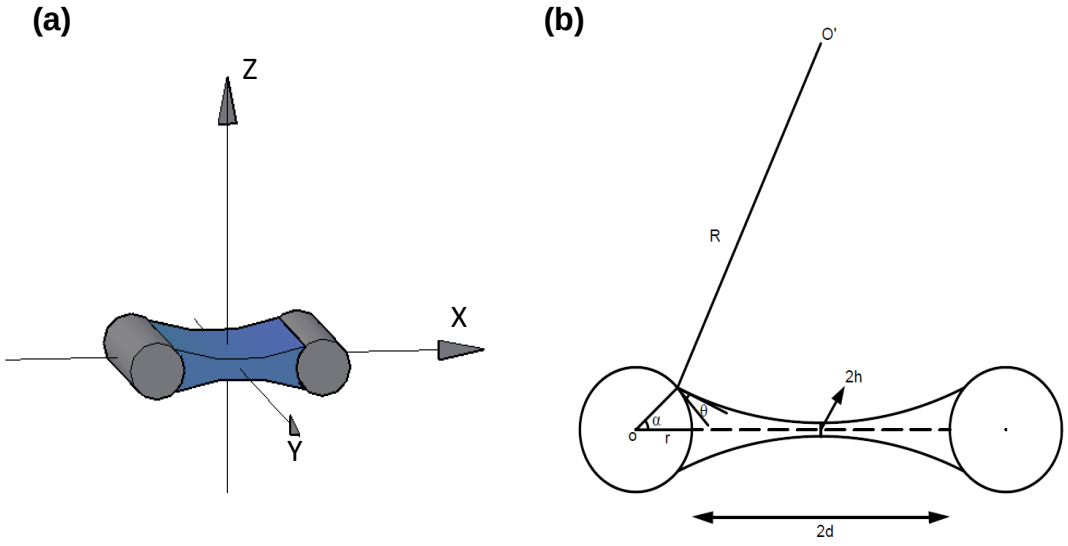


***Figure 3.1**: **(a)** The three-dimensional diagram of a capillary bridge between two hydrophilic fibres and **(b)** the cross-sectional illustration of a capillary bridge for detailed analysis.*

Developing a mathematical model of capillary bridge drying in three-dimensional fibre matrices presents a complex problem due to the loss of axisymmetric structure[333,341]. The problem is simplified by considering the capillary bridge on two parallel hydrophilic fibres. The axial symmetry of the capillary bridge along the Y-axis (***Figure 3.1** (a)*) and the absence of gravity reduce the difficulty of the geometry determination and drying dynamic simulation.

For a submillimetre system, the Bond number (Bo) describing the ratio of gravitational force against surface tension is less than 1, indicating that gravitational force may be neglected[342,343]. Therefore, the shape of the capillary bridge is governed by liquid surface tension, which is expressed by the Young-Laplace Equation (Eq. 3.1)[343–346],

$$\sigma\kappa = \sigma\left(\frac{1}{R_1}+\frac{1}{R_2}\right) = \Delta p, \qquad \textit{Eq. 3.1}$$

where σ is surface tension of the loaded solution and Δp is capillary pressure. δ is the curvature and R_1 and R_2 are the two principal radii of curvature. In this case, the principal radius in the Y direction is infinite, $R_1 = \infty$. R_2 is the principal radius of the curvature for the middle point at the gas-liquid interface, shown as R in ***Figure 3.1 (b)***. The curvature (κ) of the capillary bridge is expressed as $\kappa = \frac{1}{R}+\frac{1}{\infty} = \frac{1}{R}$, which is constant along the surface. Constant curvature, namely nodoid geometry, makes the surface a perfect arc.

To our knowledge, the theoretical prediction of capillary bridge formation and the simulation of drying kinetics of the capillary bridge have not been described previously, despite the established theories of the geometry and wetting morphology[331,332]. Therefore, this study starts with a geometric analysis to find the criterion for capillary bridge formation between two paralleled fibres. Then, a mathematical model is constructed to explore the flow within the capillary bridge driven by evaporation of either pure water or sugar solution. Notably, the varying physical properties of a solution with different initial concentrations increase the mathematical model's complexity.

3.2 List of Variables

Table 3.1: List of the variables used in the simulation and their units.

Symbol	Description	Units
c	Solute Concentration	M
Ca	Capillary number	-
d	Halved separation distance between two fibres	m
D	Diffusion coefficient of the solute	m^2/s
E	Evaporation rate	m/s
H	Thickness of capillary bridge neck	m
K	Boltzmann constant	$m^2\ kg/(s^2\ K)$
Ma	Marangoni number	-
$\boldsymbol{n}$	Unit normal vector	
$\boldsymbol{p}$	Pressure vector	
Pe	Peclet number	-
T	Temperature in Kelvin unit	K
$\boldsymbol{T}$	Stress Tensor	
t	Time	s
$\boldsymbol{t}$	Unit tangential vector	
R	Principal radius of the curvature	m
Re	Reynolds number	-
RH	Relative humidity	
$\boldsymbol{U}$	Velocity vector	
$\boldsymbol{U_s}$	Interfacial velocity vector	
u	Velocity in x direction	m/s
$\bar{u}$	Mean horizontal velocity	m/s
w	Velocity in z-direction	m/s
x	Distance in x-direction	m
z	Distance in z-direction	m
V	Volume	m^3
V_m	Molecular volume	m^3/mol
α	half-filling angle	rad
θ	Contact angle of liquid and solid surface	rad
σ	Surface tension	N/m
κ	Curvature	1/m
μ	Viscosity	Pa • s
φ	Weight percentage	
γ	Surface tension coefficient	N/(m• M)

3.3 Geometric Criterion for Forming Capillary Bridge

A cross-sectional diagram of the capillary bridge formed between two parallel hydrophilic fibres with mathematical parameters was constructed (***Figure 3.1*** *(b)*) based on the previous work[347,348], where d is the halved separation distance between two fibres, α represents the half-filling angle, θ stands for contact angle of liquid and solid surface, H is the thickness of capillary bridge neck. The two equations Eq. 3.2 and Eq. 3.3 were established in the literature:

$$\frac{H}{2} = h = rsin\alpha - [R - Rsin(\alpha + \theta)] \qquad \textit{Eq. 3.2}$$

$$\frac{R}{r} = \frac{1 + \frac{d}{r} - cos\alpha}{cos\,(\alpha + \theta)} \qquad \textit{Eq. 3.3}$$

However, the criterion for capillary bridge formation, the maximum distance between two fibres that could sustain a capillary bridge, has not been previously derived.

A capillary bridge is assumed to be formed between two fibres if the half-thickness of the capillary bridge neck (h) is greater than zero. Namely, the result of Eq. 3.2 must be greater than zero with given fibre properties. However, the half-filling angle cannot be directly measured but may be substituted by four other measurable parameters (Eq. 3.3). Rearranging the equation above gives the value of half-filling angle (α) based on the liquid and solution properties (Eq. 3.4), which must be located between zero and pi/2:

$$\alpha = arcsin\left(\frac{-(r+d)}{\sqrt{r^2 + 2Rr \cdot cos\theta + R^2}}\right) + acrtan\left(\frac{\frac{r}{R} + cos\theta}{sin\theta}\right)$$

Eq. 3.4

Substituting the half-filling angle into Eq. 3.2, the criterion of forming a capillary bridge, $h > 0$, could be expanded to:

$$h = \frac{C_2 \cdot C_3 - R^2 sin\,(\theta)\sqrt{-\frac{C_3}{C_1}}}{Rsin\,(\theta)\sqrt{-\frac{R^2 + 2Rr\,cos(\theta) + r^2}{C_1}}} > 0$$

Eq. 3.5

where

$$C_1 = -R^2 sin^2(\theta)$$

$$C_2 = \sqrt{-\frac{-R^2 - 2Rr\cos(\theta) + d^2 + 2rd}{C_3}}$$

$$C_3 = R^2 + r^2 + 2Rr \cdot \cos(\theta).$$

Eq. 3.6 is obtained after simplifying the equation Eq. 3.5.

$$h = \frac{C_2 \cdot C_3 - R^2 \sin\,(\theta)\sqrt{-\frac{C_3}{C_1}}}{\sqrt{C_3}} > 0$$

Eq. 3.6

Since the contact angle (θ) of liquid on hydrophilic surface is located between 0 and $\frac{\pi}{2}$, the denominator, $\sqrt{C_3}$, must be greater than 0. Eq. 3.6 could convert to Eq. 3.7.

$$C_2 \cdot C_3 > R^2 \sin\,(\theta)\sqrt{-\frac{C_3}{C_1}}$$

Eq. 3.7

After dividing by $\sqrt{C_3}$ and expanding the equations, the further simplifications were presented from Eq. 3.8 to Eq. 3.11.

$$\sqrt{R^2 + 2Rr\cos(\theta) - d^2 - 2rd} > R^2 \sin(\theta) \sqrt{\frac{1}{R^2 sin^2(\theta)}} \quad \textit{Eq. 3.8}$$

$$\sqrt{R^2 + 2Rr\cos(\theta) - d^2 - 2rd} > R \quad \textit{Eq. 3.9}$$

$$R^2 + 2Rr\cos(\theta) - d^2 - 2rd > R^2 \quad \textit{Eq. 3.10}$$

$$CB = 2Rr\cos(\theta) - d^2 - 2rd > 0 \quad \textit{Eq. 3.11}$$

We call this criterion the Capillary Bridge number (CB number). If the CB number is greater than zero, the fibre matrix can maintain a capillary bridge structure based on the geometry of fibre and liquid properties. If the CB number is less than zero, only a droplet conformation of liquid could exist. The maximum distance between parallel fibres with given properties that could sustain a capillary bridge is deduced. The maximum distance is derived from the condition $h = 0$. After rearranging Eq. 3.3 by the substitution of Eq. 3.2 and Eq. 3.4, the expression of maximum distance could be derived Eq. 3.12.

$$d_{max} = -C_4 R \cdot sin\left[arctan\left(\frac{-1}{C_5}\right) - arctan(C_5) + arcsin\left(\frac{1}{C_4}\right)\right] - r \quad \textit{Eq. 3.12}$$

where,

$$C_4 = \sqrt{sin^2(\theta) + [cos(\theta) + r/R]^2} \ , \ C_5 = \frac{sin\,(\theta)}{cos(\theta) + r/R}$$

Since $arctan\left(\frac{-1}{C_5}\right) - arctan(C_5) = -\frac{\pi}{2}$, Eq. 3.12 could be simplified into

$$D_{max} = 2d_{max} = 2c_1R \cdot cos\left[arcsin\left(\frac{1}{c_4}\right)\right] - 2r$$

$$= 2c_1R \cdot \sqrt{1 - \left(\frac{1}{c_4}\right)^2} - 2r$$

$$= 2\sqrt{r^2 + 2Rrcos(\theta)} - 2r.$$

Eq. 3.13

The main challenge in determining the Capillary Bridge number is to find a value of the principal radius of the curvature (R), which is related to the Laplace pressure through the Youngs-Laplace equation. The Kelvin equation (Eq.3.14) gives a relationship between Laplace pressure and relative humidity (RH).

$$KTln(RH) = V_m\Delta P$$

Eq.3.14

where K is Boltzmann constant, T is the temperature in Kelvin unit, RH is relative humidity, V_m is the molecular volume of liquid. Combining those two equations, the Kelvin radius is defined as

$$R_k(Kevin\ radius) = \frac{\sigma \cdot Vm}{KTln(RH)}$$

Eq. 3.15

At 20 °C, the value of $(\sigma \cdot V_m)/KT$ is 0.54 nm for pure water with surface tension of 72.8 x 10^{-3} N/m[349,350]. Although the Kelvin radius has been applied to calculated as a principal radius of curvature, this is only relevant in the nanometre range. For larger scale, observed values are several orders of magnitude greater than kelvin radius[351–353].

The principal radius could be calculated if the unit volume (V) of the capillary bridge is obtained. The combination of Eq. 3.4 and Eq. 3.16 can eliminate the half-filling angle, the relationship between principal radius (R) and unit volume (V) with other three measurable parameters (r, d, θ) can be found. The function expressed this relationship is too long to be shown here.

$$V = 4rsin\alpha \cdot (r - rcos\alpha + d) - R^2[\pi - 2(\alpha + \theta)] - 2\alpha r^2 + 4R^2 \sin(\alpha + \theta) \cdot \cos(\alpha + \theta)$$

Eq. 3.16

3.4 Modelling of Drying Dynamics of Capillary Bridge

A mathematical model for capillary bridge drying with either pure water or solution has been made based on previous works involving droplet drying simulations[354,355]. A disaccharide, trehalose, regarded as a surfactant, is used in the system. It is widely used as cryoprotectant[356–358].

The mathematical framework of drying the capillary bridge with pure water overlaps with the same model for a sugar solution. Therefore, only the mathematical framework of evaporating capillary bridge with trehalose is presented here.

3.4.1 Mathematical Framework and Assumptions

A Cartesian coordinate system (***Figure 3.2***) is applied to simulate the drying process in the capillary bridge structure, in which x and z symbolize the horizontal and vertical coordinates. Since the gravitational force is ignored, the geometry of

the capillary bridge is symmetric in both x and z directions. For simplicity, the top-right corner of the capillary bridge is taken to represent the whole capillary bridge for detailed analysis (***Figure 3.2*** *(b)*).

There are several assumptions made to ease the calculations. The mixture is regarded as an incompressible, Newtonian liquid and the solute was considered as evenly distributed over the capillary bridge at the starting point. Dry air is assumed to flow at a constant velocity. The relative humidity and temperature of dry air during drying were assumed to be constant. The density of the solution is regarded as constant throughout drying[355,358,359].

The contact angle between liquid and fibre surface does not change with solution concentration[360]. The right-side were simplified as a straight and rigid wall. Therefore, the dynamics of the contact line during evaporation is not included in this work.

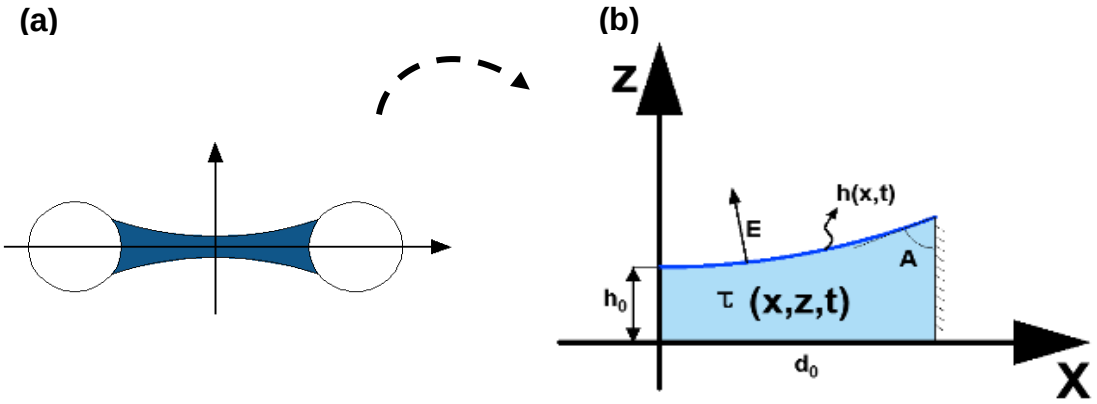


Figure 3.2*: Schematic diagram of the Capillary bridge model (a) and mathematical model of the capillary bridge for simulation (b).*

3.4.2 Governing Equations

Since the mixture is regarded as incompressible and Newtonian liquid, the continuity and momentum conservation equations in the bulk mixture are expressed as:

$$(\nabla \cdot \boldsymbol{U}) = 0 \qquad \textit{Eq. 3.17}$$

$$\rho \boldsymbol{U}_t + \rho(\boldsymbol{U} \cdot \nabla)\boldsymbol{U} = -\nabla \boldsymbol{p} + \mu(\tau)\nabla^2 \boldsymbol{U} \qquad \textit{Eq. 3.18}$$

where the subscripts denote the derivative. ∇ is the differential operator. $\boldsymbol{U}$ is the velocity vector in the system, which has two components (u, w) in x and z directions. ρ and $\boldsymbol{P}$ stand for liquid density and pressure, respectively.

Viscosity (μ) of the mixture is dependent on the concentration (c) of trehalose measured in M. An empirical equation of the viscosity and concentration of trehalose was described previously[309]:

$$\mu(\tau) = A_0 e^{A_1 \psi} \qquad \textit{Eq. 3.19}$$

where,

$$\varphi(weight\ percentage) = \frac{c \cdot M_{Tre}}{\rho} \qquad \textit{Eq. 3.20}$$

The empirical parameters A_0 and $A_1$are relevant to the temperatures, which were obtained in Appendix 2. M_{Tre} is the molar mass of trehalose.

Trehalose is a non-volatile and non-reducing solute[361], whose mass is conserved during drying. A standard convective-diffusion equation governs the concentration in the bulk solution:

$$\frac{\partial c}{\partial t} + \nabla \boldsymbol{U} c = D(c)\nabla^2 c \qquad \textit{Eq. 3.21}$$

where D refers to the diffusion coefficient of the solute in the units of m^2/s which is also subject to the concentration (φ) [362]:

$$D(c) = \frac{5 \cdot 10^{-8}}{e^{-13} \cdot \varphi^{1.1}} \cdot \exp\left(\frac{-1500 \cdot e^{1.9\varphi}}{T}\right) \qquad \textit{Eq. 3.22}$$

where T represents the temperature in Kelvin.

3.4.3 Boundary Conditions

To resolve the governing equations above, several boundary conditions are set. At the substrate ($z = 0$), no solute flux is assumed due to symmetry[363,364]. Due to the symmetry, it is also a moving boundry condition, which makes the simulation unsovable. In this case, this moving boundary condition was simpilifed as a wall boundary condition.

$$\frac{\partial c}{\partial z}_{|z=0} = 0 \qquad \textit{Eq. 3.23}$$

$$\boldsymbol{U}_{|z=0} = 0 \qquad \textit{Eq. 3.24}$$

The solute accumulated at the interface due to drying diffuses back to the bulk solution (Eq. 3.25). The kinematic boundary conditions (Eq. 3.26) associated with evaporation rate are involved:

$$c(\boldsymbol{U} - \boldsymbol{U}_s) \cdot \boldsymbol{n} - D(c)\nabla \mathrm{c} \cdot \boldsymbol{n} = 0, \qquad \textit{Eq. 3.25}$$

$$E = (\boldsymbol{U} - \boldsymbol{U}_s) \cdot \boldsymbol{n}$$

Eq. 3.26

where $\boldsymbol{U_s}$ is the interfacial velocity and $\boldsymbol{n}$ is the unit normal vector along the interface. E refers to the evaporation rate, which will be discussed later.

The extension and rearrangement of the interfacial kinematic boundary condition (Eq. 3.27) show the relationship between the changing rate of surface height with time($\partial h/\partial x$) and horizontal velocity component (u):

$$E = \frac{1}{\Pi}\left(w - u\frac{\partial h}{\partial x} - \Pi \cdot \frac{\partial h}{\partial t}\right)$$

Eq. 3.27

where,

$$\Pi = \sqrt{1 + \left(\frac{\partial h}{\partial x}\right)^2}$$

In the meantime, the stresses in normal and tangential directions are balanced at the interface, where involves the capillary flow (Eq. 3.28) and Marangoni flows (Eq. 3.29). Capillary flow is driven by capillary pressure, which is related to surface tension (σ) and curvature (κ) of the interface.

At the tangential direction of the interface, the Marangoni effect is considered, which pull the liquid from the low surface tension region to the high surface tension region. Therefore, the tangential stress should be balanced by the surface tension difference along the interface, the right-hand side of Eq. 3.29.

Since the scale of bulk properties in the gas phase is much smaller than those of liquid, the system can be viewed as a one-sided model. In the one-sided model, the descriptions of the normal and tangential stress balance are presented as:

$$(\boldsymbol{T}\cdot\boldsymbol{n})\cdot\boldsymbol{n}=p_{cap}=\sigma\cdot\kappa=\frac{\sigma\cdot\frac{\partial^2 h}{\partial x^2}}{\left(\sqrt{1+\left(\frac{\partial h}{\partial x}\right)^2}\right)^3} \qquad \textit{Eq. 3.28}$$

$$(\boldsymbol{T}\cdot\boldsymbol{n})\cdot\boldsymbol{t}=\boldsymbol{t}\cdot\nabla_s\sigma \qquad \textit{Eq. 3.29}$$

where $\boldsymbol{T}$ is the stress tensor and ∇_s is surface gradient operator. $\boldsymbol{n}$ and $\boldsymbol{t}$ are the unit normal vector and tangential vector, respectively, along the interface, respectively.

Surface tension of the solution is involved in both normal and tangential stresses, which is dependent on temperature and solute concentration. As the system temperature is assumed to be constant, the solute concentration becomes the determining factor. For trehalose, surface tension increases with trehalose concentration and the relationship are illustrated by the surface tension coefficient (γ_{tre})[61]:

$$\gamma_{tre}=\frac{\partial\sigma}{\partial c}=4.11\times10^{-8}\ \mathrm{N/(m\cdot M)} \qquad \textit{Eq. 3.30}$$

3.4.4Dimensionless Scaling

The governing equations and boundary conditions are non-dimensionalised consistent with the following scalings. The tildes represent the dimensionless variables.

$$x = d_0\check{x} \qquad z = h_0\check{z} \qquad u = U_0 \cdot \check{u} \qquad h = h_0\check{h} \qquad c = c_i\check{c}$$

$$w = \frac{h_0}{d_0}U_0 \cdot \check{u} \qquad \mu = \mu_0\check{\mu} \qquad D = D_0\check{D} \qquad t = \frac{d_0}{U_0}\check{t}$$

μ_0 and D_0 are the initial viscosity and diffusion coefficient based on the initial concentration. The velocity scale is based on the balance of capillary force and viscous.

$$U_0 = \frac{{h_0}^3}{\mu_0 {d_0}^3}\sqrt{\sigma_0}$$

Thus, the continuity and momentum conservation equations are scaled to:

$$\check{u}_{\check{x}} + \check{w}_{\check{z}} = 0 \qquad \textit{Eq. 3.31}$$

$$Re \cdot \epsilon\left(\check{u} \cdot \frac{\partial \check{u}}{\partial \check{x}} + \check{w} \cdot \frac{\partial \check{u}}{\partial \check{z}}\right) = -\frac{\partial \check{p}}{\partial \check{x}} + \check{\mu}(\check{c}) \cdot \epsilon^2 \frac{\partial^2 \check{u}}{\partial \check{x}^2} + \check{\mu}(\check{c})\frac{\partial^2 \check{u}}{\partial \check{z}^2} \qquad \textit{Eq. 3.32}$$

$$Re \cdot \epsilon\left(\check{u} \cdot \frac{\partial \check{w}}{\partial \check{x}} + \check{w} \cdot \frac{\partial \check{w}}{\partial \check{z}}\right) = -\frac{\partial \check{p}}{\partial \check{z}} + \epsilon^2\check{\mu}(\check{c})\left(\epsilon^2 \frac{\partial^2 \check{w}}{\partial \check{x}^2} + \frac{\partial^2 \check{w}}{\partial \check{z}^2}\right) \qquad \textit{Eq. 3.33}$$

where,

$$Re = \frac{\rho U_0 D}{\mu_0}, \epsilon = h_0/d_0$$

The boundary condition at the substrate was nondimensionalised to

$$\check{u} = \check{w} = 0\,, \quad \textit{at} \;\; z = 0 \qquad \textit{Eq. 3.34}$$

The boundary conditions at the interface are nondimensionalised as follows:

i) Normal stress balance:

$$\frac{2\epsilon^2}{\Omega^2}\left[\epsilon^2 \frac{\partial \check{u}}{\partial \check{x}}\left(\frac{\partial \check{h}}{\partial \check{x}}\right)^2 - \frac{\partial \check{h}}{\partial \check{x}}\left(\frac{\partial \check{u}}{\partial \check{z}} + \epsilon^2 \frac{\partial \check{w}}{\partial \check{x}}\right) + \frac{\partial \check{w}}{\partial \check{z}}\right] - p = \frac{\epsilon^3}{Ca} \cdot \frac{\partial^2 \check{h}}{\partial \check{x}^2} \qquad \textit{Eq. 3.35}$$

where,

$$\Omega = \sqrt{1 + \left(\epsilon \frac{\partial \check{h}}{\partial \check{x}}\right)^2} \qquad \text{and} \qquad Ca(Capillary\ number) = \frac{\mu_0 U_0}{\sigma}$$

ii) Tangential stress balance:

$$-2\epsilon^2\frac{\partial\check{h}}{\partial\check{x}}\cdot\frac{\partial\check{u}}{\partial\check{x}}-\frac{\partial\check{u}}{\partial\check{z}}+\epsilon^2\frac{\partial\check{w}}{\partial\check{x}}-\epsilon^2\left(\frac{\partial\check{h}}{\partial\check{x}}\right)^2\left(\frac{\partial\check{u}}{\partial\check{z}}+\epsilon^2\frac{\partial\check{w}}{\partial\check{x}}\right)+2\epsilon^2\frac{\partial\check{h}}{\partial\check{x}}\frac{\partial\check{w}}{\partial\check{z}}$$

$$=\frac{Ma}{Pe}\left[\frac{\partial\check{c}}{\partial\check{x}}+\frac{\partial\check{h}}{\partial\check{x}}\frac{\partial\check{c}}{\partial\check{z}}\right]$$

Eq. 3.36

where,

$$Ma(\text{Marangoni number})=\frac{\gamma c_0 h_0}{\mu_0\cdot D}$$

iii) Kinematic boundary condition

$$E=\frac{d_0}{h_0U_0}(\check{w}-\check{u}\cdot\frac{\partial\check{h}}{\partial\check{x}}-\frac{\partial\check{h}}{\partial\check{t}})$$

Eq. 3.37

The dimensionless convective diffusion equation governs the evolution of trehalose mass fraction,

$$\frac{\partial\check{c}}{\partial\check{t}}+\check{u}\cdot\frac{\partial\check{c}}{\partial\check{x}}+\check{w}\cdot\frac{\partial\check{c}}{\partial\check{z}}=\frac{1}{Pe\epsilon^2}(\epsilon^2\cdot\frac{\partial^2\check{c}}{\partial\check{x}^2}+\frac{\partial^2\check{c}}{\partial\check{z}^2})$$

Eq. 3.38

with the boundary condition at substrate and interface, respectively.

$$\frac{\partial\check{c}}{\partial\check{z}}_{|z=0}=0$$

Eq. 3.39

$$\epsilon^2Pe\ \cdot\check{c}\cdot\left(\check{w}-\check{u}\cdot\frac{\partial\check{h}}{\partial\check{x}}-\frac{\partial\check{h}}{\partial\check{t}}\right)=-\epsilon^2\frac{\partial\check{h}}{\partial\check{x}}\frac{\partial\check{c}}{\partial\check{x}}+\frac{\partial\check{c}}{\partial\check{z}}\ ,at\ z=h$$

Eq. 3.40

Peclet number ($Pe=\frac{U_0d_0}{D}$) is a parameter to evaluate the prioritization of convective against diffusive transportation during drying. In this work, rapid vertical diffusion is imposed. In this case, the mass fraction could be expanded as follows[354,365]:

$$\check{c}(x,z,t) = \check{c}_0(\check{x},\check{t}) + \epsilon^2 Pe \cdot \check{c}_1(\check{x},\check{z},\check{t}) \qquad \textit{Eq. 3.41}$$

Then, the convective diffusion equation (Eq. 3.41) is substituted as

$$\frac{\partial \breve{c_0}}{\partial \check{t}} + \epsilon^2 Pe \cdot \frac{\partial \breve{c_1}}{\partial \check{t}} + \breve{u} \cdot \left(\frac{\partial \breve{c_0}}{\partial \check{x}} + \epsilon^2 Pe \cdot \frac{\partial \breve{c_1}}{\partial \check{x}}\right) + \breve{w} \cdot \epsilon^2 Pe \cdot \frac{\partial \breve{c_1}}{\partial \check{z}} = \frac{1}{Pe}\frac{\partial^2 \breve{c_0}}{\partial \check{x}^2} + \frac{\partial^2 \breve{c_1}}{\partial \check{z}^2}$$

Eq. 3.42

with the boundary conditions

$$\frac{\partial \check{c}_1}{\partial \check{z}} = 0 \; at \; z = 0 \qquad \textit{Eq. 3.43}$$

$$(\check{c}_0 + \epsilon^2 Pe \cdot \check{c}_1) \cdot \left(\breve{w} - \breve{u} \cdot \frac{\partial \check{h}}{\partial \check{x}} - \frac{\partial \check{h}}{\partial \check{t}}\right) = \frac{-\frac{\partial \check{h}}{\partial \check{x}} \cdot \left(\frac{\partial \breve{c_0}}{\partial \check{x}} + \epsilon^2 Pe \cdot \frac{\partial \breve{c_1}}{\partial \check{x}}\right)}{Pe} + \frac{\partial \breve{c_1}}{\partial \check{z}}$$

$$at \; z = h$$

Eq. 3.44

Owing to $\epsilon = h_0/d_0 \ll 1$, the lubrication approximation is applied to simplify the system to the leading orders of all above dimensionless equations. The leading order of continuity, momentum conservation and trehalose diffusion equations are yielded.

$$\frac{\partial \breve{u}}{\partial \check{x}} + \frac{\partial \breve{w}}{\partial \check{z}} = 0 \qquad \textit{Eq. 3.45}$$

$$\frac{\partial \check{p}}{\partial \check{x}} = \breve{\mu}(\check{\tau}) \cdot \frac{\partial^2 \breve{u}}{\partial \check{z}^2} \qquad \textit{Eq. 3.46}$$

$$\frac{\partial \check{p}}{\partial \check{z}} = 0 \qquad \textit{Eq. 3.47}$$

From the x-component of the Navier-Stokes equation (Eq. 3.46), the horizontal velocity depends on the pressure, which is not varied along the vertical direction (Eq. 3.47). Hence, to solve this second derivate momentum equation (Eq. 3.46), two boundary conditions are applied, no-slip wall condition (Eq. 3.48) and scaled tangential stress balance (Eq. *3.49*).

$$\check{u} = \check{w} = 0 \qquad \textit{Eq. 3.48}$$

$$\check{\mu}(\check{c})\frac{\partial \check{u}}{\partial \check{z}} = \frac{Ma \cdot \check{D}}{Pe}\left(\frac{\partial \check{c}}{\partial \check{x}} + \frac{\partial \check{h}}{\partial \check{x}} \cdot \frac{\partial \check{c}}{\partial \check{z}}\right) \qquad \textit{Eq. 3.49}$$

After solving the momentum conservation equation, the horizontal velocity profile was expressed as:

$$\check{u} = \frac{1}{\check{\mu}(\check{c})}\left[\frac{\partial \check{p}}{\partial \check{x}}\left(\frac{\check{z}^2}{2} - \check{h}\check{z}\right) + \frac{Ma \cdot \check{D}}{Pe} \cdot \left(\frac{\partial \check{c}}{\partial \check{x}} + \frac{\partial \check{h}}{\partial \check{x}} \cdot \frac{\partial \check{c}}{\partial \check{z}}\right)\check{z}\right] \qquad \textit{Eq. 3.50}$$

According to the simplified normal stress balance (Eq. 3.51), the pressure could be substituted, and the velocity was reviewed as the function of surface and height and local concentration (Eq. 3.52).

$$-\check{p} = \frac{\epsilon^3}{Ca} \cdot \frac{\partial^2 \check{h}}{\partial \check{x}^2} \qquad \textit{Eq. 3.51}$$

$$\check{u}(\check{h}, \check{c}) = \frac{1}{\check{\mu}(\check{c})}\left[\frac{\epsilon^3}{Ca} \cdot \frac{\partial^3 \check{\mathrm{h}}}{\partial \check{x}^3}\left(\frac{\check{z}^2}{2} - \check{h}\check{z}\right) + \frac{Ma \cdot \check{D}}{Pe} \cdot \left(\frac{\partial \check{c}}{\partial \check{x}} + \frac{\partial \check{\mathrm{h}}}{\partial \check{x}} \cdot \frac{\partial \check{c}}{\partial \check{z}}\right)\check{z}\right] \qquad \textit{Eq. 3.52}$$

Then, the convective diffusion equation was scaled as

$$\frac{\partial \breve{c_0}}{\partial \check{t}} + \breve{u} \cdot \left(\frac{\partial \breve{c_0}}{\partial \check{x}}\right) = \frac{\check{D}}{Pe}\frac{\partial^2 \check{c}}{\partial \check{x}^2} + \check{D} \cdot \frac{\partial^2 \breve{c_1}}{\partial \check{z}^2} \qquad \textit{Eq. 3.53}$$

with boundary conditions:

at the substrate, $z = 0$

$$\frac{\partial \check{c}_1}{\partial \check{z}}_{|z=0} = 0 \qquad \textit{Eq. 3.54}$$

at the interface, $z = h$

$$\frac{E}{\epsilon \cdot \check{D} U_0} \cdot \check{c}_0 = \frac{-\frac{\partial \check{\mathrm{h}}}{\partial \check{x}} \cdot \frac{\partial \breve{c_0}}{\partial \check{x}}}{Pe} + \frac{\partial \breve{c_1}}{\partial \check{\mathrm{z}}} \qquad \textit{Eq. 3.55}$$

To get the dynamic equation of trehalose liquid bridge, the cross-sectional averaging technique was applied[365]. The diffusion equation (Eq. 3.53) could be reformed as:

$$\frac{\partial \breve{c_0}}{\partial \breve{t}} + \breve{\bar{u}}\frac{\partial \breve{c_0}}{\partial \breve{x}} = \frac{\breve{D}}{Pe}\frac{\partial^2 \breve{c_0}}{\partial \breve{x}^2} + \frac{1}{\breve{\bar{h}}}\left[\frac{\partial \breve{c_1}}{\partial \breve{z}}\right]_0^{\breve{h}} \qquad \textit{Eq. 3.56}$$

where the last term could be extended with the boundary conditions Eq. 3.54 and Eq. 3.55. Thus, the governing equation of local concentration along the drying was stated as

$$\frac{\partial \check{c}_0}{\partial t} = -\bar{u}\cdot\frac{\partial \breve{c_0}}{\partial \check{x}} + \frac{\breve{D}}{Pe\cdot\check{h}}\cdot\frac{\partial\left(\breve{h}\cdot\frac{\partial \breve{c_0}}{\partial \check{x}}\right)}{\partial \check{x}} + \frac{\check{c}_0}{hU_0\epsilon}\cdot E \qquad \textit{Eq. 3.57}$$

The concentration distribution was used to simplify the velocity profile equation.

$$\check{u}(\check{h},\check{c}_0) = \frac{1}{\check{\mu}(\check{\tau})}\left[\frac{\epsilon^3}{Ca}\cdot\frac{\partial^3 \breve{h}}{\partial \check{x}^3}\left(\frac{\check{z}^2}{2} - \check{h}\check{z}\right) + \frac{Ma\cdot\breve{D}}{Pe}\cdot\left(\frac{\partial \check{c}_0}{\partial \check{x}}\right)\check{z}\right] \qquad \textit{Eq. 3.58}$$

As the other objective of this work, solving the evolution of surface height along the drying is also an essential part, which could be illustrated by the kinematic boundary condition.

$$E = \frac{d_0}{h_0 U_0}(\breve{w} - \breve{u}\cdot\frac{\partial \breve{h}}{\partial \check{x}} - \frac{\partial \breve{h}}{\partial \breve{t}}) \qquad \textit{Eq. 3.59}$$

The mean horizontal velocity ($\bar{u}$) simplified the kinematic boundary condition to eliminate the vertical velocity component calculations by Leibniz's Rule.

$$-\frac{\partial \breve{h}\bar{u}}{\partial \check{x}} = \breve{w} - \breve{u}\cdot\frac{\partial \breve{h}}{\partial \check{x}} \qquad \textit{Eq. 3.60}$$

Thus, the evolution of surface height could be substituted and expressed as

$$\frac{\partial \breve{h}}{\partial \check{t}} = -\frac{h_0 U_0}{d_0}E - \frac{\partial(\breve{h}\bar{u})}{\partial \check{x}} \qquad \textit{Eq. 3.61}$$

where the mean velocity is integrated as:

$$\bar{u} = \frac{1}{\check{h}(\check{x})}\int_0^{\check{h}(\check{x})} \check{u}\, d\check{z} \longrightarrow \bar{u} = \frac{1}{\check{\mu}(\check{c})}\left[\underbrace{\frac{\epsilon^3}{Ca}\frac{\check{h}^2}{3}\cdot\frac{\partial^3\check{h}}{\partial\check{x}^3}}_{\text{Capillary Effect}} + \overbrace{\frac{Ma\cdot\check{D}}{Pe}\cdot\left(\frac{\partial\check{c}_0}{\partial\check{x}}\right)\frac{\check{h}}{2}}^{\text{Marangoni Effect}}\right]$$

Eq. 3.62

Surface evolution (Eq. 3.61) demonstrates the relationship between the convection flux and evaporation rate. In terms of concentration variation with time, Eq. 3.57 shows that the concentration is related to convection flux, diffusion flux and solute accumulation by evaporation.

Both Eq. 3.61 and Eq. 3.57 cannot be resolved without knowing the average velocity cross z-direction ($\bar{u}$). From the boundary conditions of surface stress balances, the velocity is illustrated by the Capillary Effect and the Marangoni effect (Eq. 3.62). As mentioned above, Capillary Effect is raised by the surface curvature while the surface tension differences raise Marangoni Effect.

3.4.5 Evaporation Rate

The evaporation rate is the mass transfer rate of water across the gas-liquid interface, with units of (m/s). The gas is assumed to obey the ideal gas law.

$$E_i = \frac{M_w \cdot N_A}{\rho} = \frac{M_w \cdot k_c(c_s - c_\infty)}{\rho} = \frac{M_w \cdot k_c}{\rho}\left(\frac{p_s(\tau)}{RT_s} - \frac{p_\infty}{RT_\infty}\right) \quad \textit{Eq. 3.63}$$

where k_c is mass transfer coefficient. p_w, p_∞ are the partial pressure at the interface and in the gas phase.

The ambient temperature (T_∞) is 25 °C, with 5% relative humidity. According to the psychometric chart, the wet-bulb temperature (T_s) at the liquid surface is 9 °C. The partial vapour pressure of water in the gas phase (p_∞) and the ambient temperature are assumed as constant all the time. The partial vapour pressure at the interface (p_s) is dependent on trehalose concentration, and the relationship complies with Raoult's Law.

3.5 Simulated Results of Drying Dynamics and Discussions

3.5.1 Determination of Capillary Shape

As mentioned above, the initial shape of the interface is an arc. Therefore, the surface profile along the x-direction is expressed in dimensionless terms as:

$$\check{h}(\check{x}, \check{t} = 0) = \frac{R}{h_0} + 1 - \frac{1}{h_0}\sqrt{R^2 - {d_0}^2 \check{x}^2} \quad \textit{Eq. 3.64}$$

where the contact angle (θ) of liquid on fibre was set to $\pi/6$, and the distance of two fibres (D) was 1 μm. The diameter of the fibre is 3 μm. The principal radius of curvature was set to 0.7 μm as arbitrary values representative of a typical system.

The variables following are all scaled except for trehalose weight percentage. The distance is scaled by the half distance between two fibres ($\breve{x} = x/d_0$), where $\breve{x} = 0$ means the centre of the capillary bridge and $\breve{x} = 1$ stands for the end of the capillary bridge. The height is scaled by the half of the initial neck thinness ($\breve{h} = h/h_0$).

3.5.2 Simulation Results with Pure Water

Since the structure at the centre ($x = 0$) is symmetric, there is no flux across the symmetry line, which means the horizontal velocity and the derivative of concentration with the respect of x at the centre were both zero.

$$\breve{u}(\breve{x} = 0, \breve{t}) = \bar{u}(\breve{x} = 0, \breve{t}) = 0 \qquad \textit{Eq. 3.65}$$

The surface evolution could be numerically simplified to an ordinary differential equation by a finite difference approximation with the above boundary conditions. There are a third derivative ($\frac{\partial^3 \breve{h}}{\partial \breve{x}^3}$) was involved in the simulation, giving a high stiffness of the equations, changing drastically on different time scale unless the step size of calucluation to be extremely small. ODE 15s of Matlab is a first choice for stiff ODE equations, recommended by Matlab[366]. Therefore, it is calculated by ODE 15s. The derivative uses the centred difference approximation for the continuous parts and a one-sided difference for the endpoints.

The surface evolution of the top-right part of the capillary bridge is presented in ***Figure 3.3*** *(a)*. The coloured curves represent the top-right part of the capillary bridge surface as shown in the schematic diagram in the dashed box and are shown in the drying time course.

Generally, the surface shape of the capillary bridge with pure water is not significantly transformed, still maintaining the curved shape. The surface height around $x = 0$ is reduced slowly while the height at the end section increases in the drying condition.

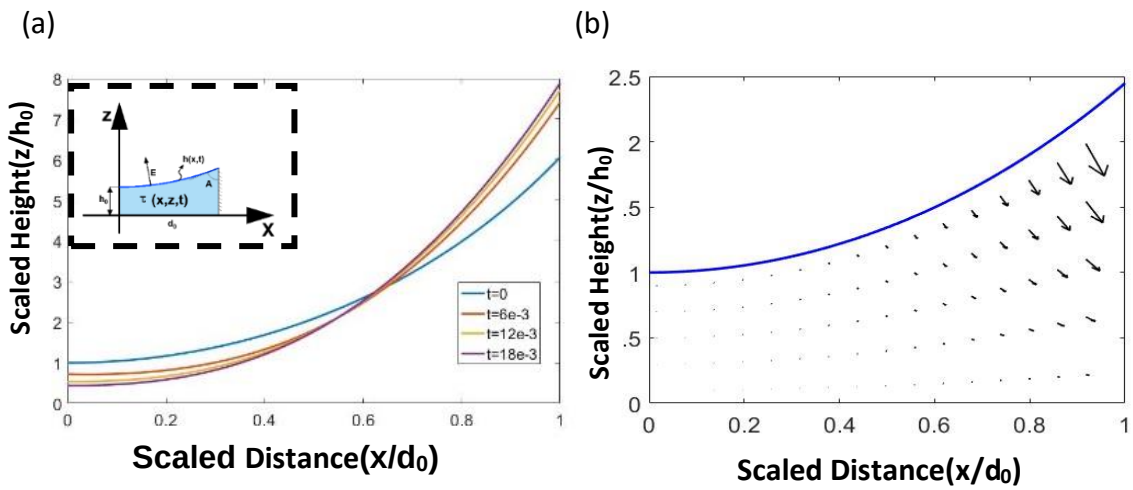


***Figure 3.3**: (a) Surface evolution of the capillary bridge surface with pure water. The coloured curve represents the top-right part of the capillary bridge surface, as shown in the schematic diagram in the dashed box. The mass transfer coefficient (k_p) used is 1e-3 with scaled time interval of 6e-3. (b) The velocity profile during drying. The direction and length of the arrow indicate the inner flow trend and magnitude. The distance and height presented in the figures are all scaled.*

This could be easily explained by the inner flow velocity profile (***Figure 3.3** (b)*). Since there is no solute concentration gradient, the latter part of the inner flow velocity is removed (Eq. 3.66). In other words, Marangoni Effect is not involved in this scenario. The velocity is governed by Capillary Effect only (Eq. 3.66). The magnitude and direction of velocity are only dependent on the surface height and third derivative. The third derivative ($\frac{\partial^3 \tilde{h}}{\partial \tilde{x}^3}$) is the leading order in this equation, which

increases from $\breve{x}$=0 to $\breve{x}$=1. Therefore, the length of arrow in ***Figure 3.3*** *(b)* indicates magnitude of velocity increases from $\breve{x}$=0 to $\breve{x}$=1.

$$\bar{u} = \frac{1}{\breve{\mu}(\breve{c})} \frac{\epsilon^3}{Ca} \frac{\breve{h}^2}{3} \cdot \frac{\partial^3 \breve{\mathrm{h}}}{\partial \breve{x}^3} \qquad \textit{Eq. 3.66}$$

Based on the velocity profile, it can be seen that liquid is pushed from $\breve{x} = 0$ to the end $\breve{x} = 1$ (***Figure 3.3*** *(b)*), which results in the upsurge of surface height at the sides ($\breve{x} = 1$) even in the drying environment.

At the central point ($\breve{x} = 0$), the curvature of the surface equals zero, leading to the third derivative of height ($\frac{\partial^3 \breve{\mathrm{h}}}{\partial \breve{x}^3}$) in Eq. 3.66 is equal to zero. It means the surface height of the central point ($\breve{x}$=0) is only governed by the evaporation rate.

However, owing to the curvature, the region next to the central point generates the capillary flow towards the side when evaporation commences and consequently reduces the surface height. Then, the area near the centre of the liquid bridge ($\breve{x}$=0) transforms from the initial curve to a flat line gradually. In the course of drying, the flattening of the surface spreads from the centre and continues until the capillary bridge rupture at the centre. This simulation results are in agreement with the experiment result from the previous work[337–340].

3.5.3 Simulation Results with Different Solute Concentrations

Unlike the case for pure water, the mathematical construction of the capillary bridge with a trehalose solution is much more complex. The boundary condition of no-flux flow through the plane of symmetry mentioned above (Eq. 3.65) is insufficient to solve all the equations. The initially uniform trehalose concentration distribution and non-penetration substrate are applied.

$$\widetilde{\frac{\partial c}{\partial \check{x}}}(\check{x}=0,\check{t})=0 \qquad \textit{Eq. 3.67}$$

$$\check{c}(\check{x},\check{t}=0)=constant \qquad \textit{Eq. 3.68}$$

3.5.3.1 Initial Trehalose Concentration=1 M

After relating all the conditions above into the numerical solution, the evolution of surface height and bulk concentration of the capillary bridge through the drying process are calculated (***Figure 3.4***). The coloured curves represent the top-right part of the capillary bridge surface.

The initial capillary bridge curve (***Figure 3.4*** *(a)*) is flattened when drying commences (***Figure 3.4*** *(a-c)*). After a 12e-5 scaled time, liquid accumulates at the centre point (***Figure 3.4*** *(d)*), which is entirely opposite to the situation with the pure water capillary bridge.

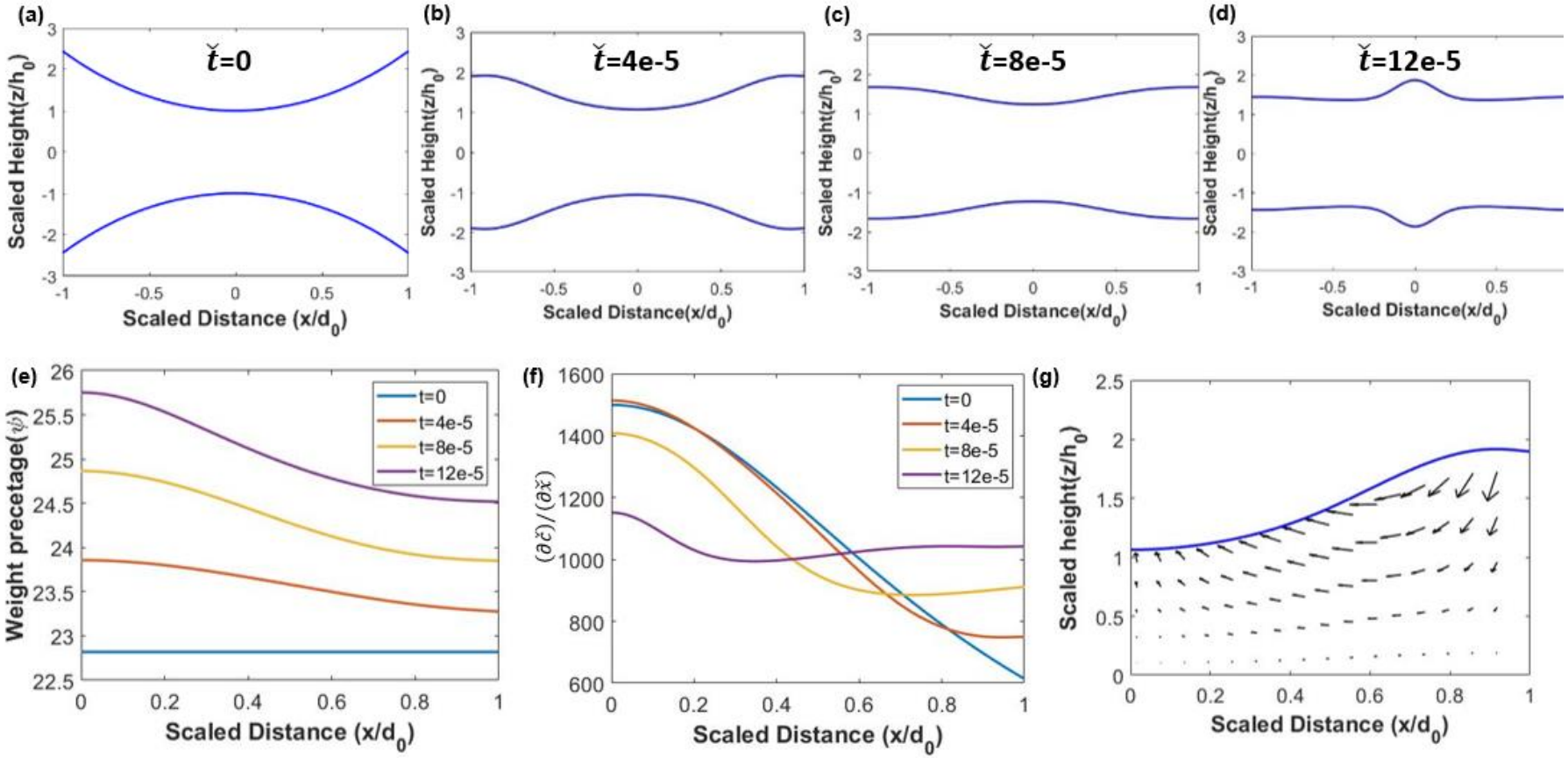


Figure 3.4*: The evolution of capillary bridge surface with the Marangoni effect with 1M initial solution. The mass transfer coefficient (k_p) used is 1e-3 with a scaled time interval of 4e-5. (a-d) Evolution of surface height over scaled time, (e) Evolution of trehalose concentration (f) Changing rate of concentration with the respect of time ($\widetilde{\partial c}/\widetilde{\partial t}$), (g)Velocity profile of inner flow at the second time interval(t=4e-5). The direction and length of the arrow indicate the inner flow direction and magnitude. The distance and height presented in the figures are all scaled.*

This phenomenon is driven by the trehalose concentration gradient along the surface (***Figure 3.4*** *(e)*). Trehalose concentration is identical at the start, leading to the same drying rate. Owing to different volumes at different points along the concave surface, the changing rate of concentration with respect to time varies along the X-axis (***Figure 3.4*** *(f)*), decreasing from $\check{x}$=0. Then, the concentration of trehalose at the centre ($\check{x}$=0), the thinnest part, would be the greatest and a concentration gradient along the surface is thus established.

Due to the properties of trehalose, the increasing concentration would increase the surface tension of the solution. The liquid in the area of low surface tension is pulled to an area of high surface tension by the Marangoni effect (***Figure 3.4*** *(g)*).

The thickness of the central area is increased by Marangoni flow, causing the concentration at that point is still the highest point across the bridge. In the course of drying, high concentration trehalose increases the viscosity of the capillary bridge and halt the inner flow. In the meantime, high sugar concentration also could impede the drying according to Raoult's law. Therefore, at the end of evaporation, the solute will be gathered and vitrified at the central area, which prevents bridge rupture.

3.5.3.2 Initial Trehalose Concentration=0.5 M

For low initial trehalose concentration (0.5 M), the evolution of the right-top surface height has been presented in ***Figure 3.5*** *(a)*. Up to $\check{t}$=8e-5, the tendency could be similar as the situation in 1M trehalose drying. Liquid accumulates at the centre due to the Marangoni flow. However, the volume of the central area, increased by

Marangoni flow, hinders trehalose accumulation at the central area shown in ***Figure 3.5*** *(b)*.

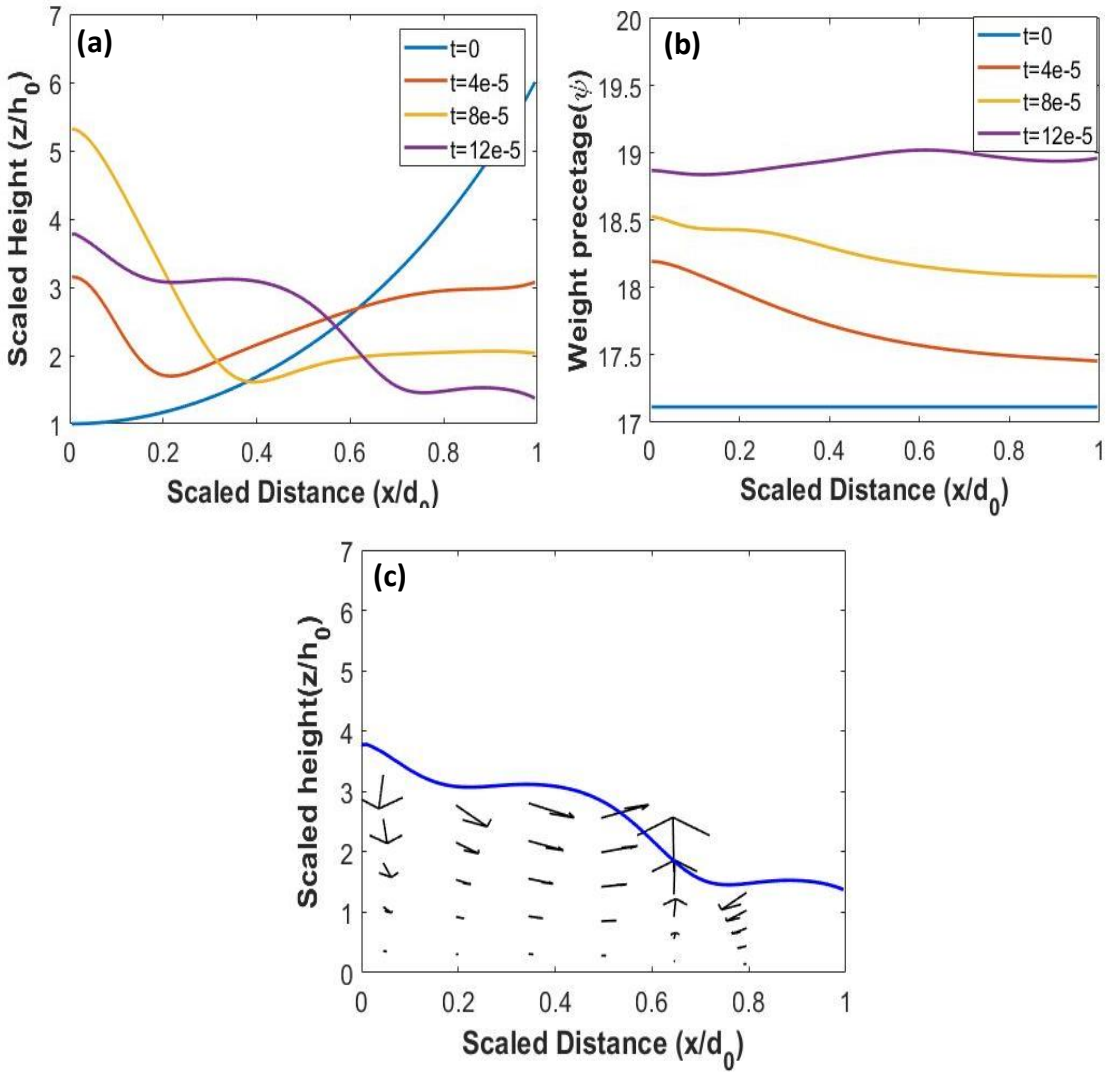


Figure 3.5*: (a) The evolution of the right-top surface height of capillary bridge with 0.5M initial concentration. The coloured curve denotes the surface height of the capillary bridge. The legend was attached. (b) trehalose concentration along the surface during the drying. The mass transfer coefficient (k_p) used is 1e-3 with scaled time interval of 4e-5. Different coloured curves indicate the surface height at the different time slots. The legend was attached. (c) The velocity profile of inner flow at* $\check{t}$*=12e-5. The distance and height presented in the figures are all scaled.*

At some point after $\check{t}$= 8e-5, the concentration at the centre, or the first point, volume of which is compensated by the Marangoni flow, is the same as the concentration of the point next to the centre, the second point. Owing to the concentrations being equal, the drying rates during the following time interval are identical. Since the volume of the first point is greater than the second point, the concentration of the second point is greatest in the next time interval. Another Marangoni flow is driven from the centre ($\check{x}$=0) to the second point.

At some point afterwards, the same situation will occur between the second point and third point. This 'chain reaction' mechanism pushes liquid away from the central area, which is seen from the velocity profile at t=12e-5 shown in ***Figure 3.5*** (c). At the point with the greatest trehalose concentration, the liquid is gathered from both sides.

Depending on the drying rate, there are two possible conformations of the final state. In the first condition, the glassy state of trehalose is formed somewhere between the centre ($\check{x}$=0) and the end ($\check{x}$=1). Then, the glassy matrix spreads from that point to the whole capillary bridge. If the drying rate was relatively low, the reverse Marangoni flow would flatten the capillary bridge and form a glassy matrix at the edge ($\check{x} = 1$).

Another situation could occur at lower sugar concentration (<0.5M). The concentration gradient created by the drying at the start cannot initiate sufficient Marangoni flow to overcome capillary flow. The surface instability would be similar

to a pure water capillary bridge. The liquid is pushed to the end ($\check{x}$=1) and the capillary bridge may rupture in this scenario.

3.5.3.3 Initial Trehalose Concentration=2 M

Using 2M trehalose solution, almost the saturation point of trehalose at room temperature, the surface evolution progresses more simply (***Figure 3.6*** *(a)*). The amorphous state with large viscosity, weight percentage over 70%, rapidly appears at the centre (***Figure 3.6*** *(b)*) and spreads out to form an even bridge structure.

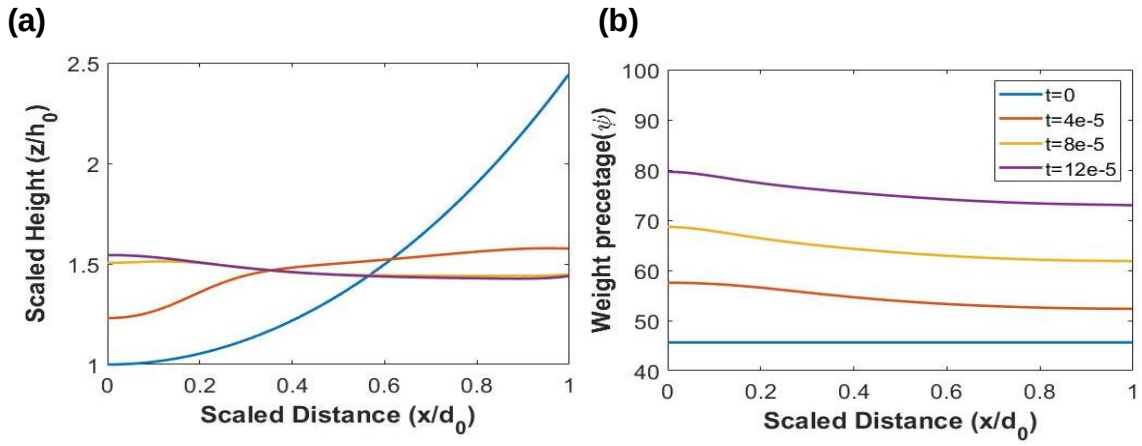


Figure 3.6*: (a) The evolution of the right-top surface height of capillary bridge with 2M initial concentration. The coloured curves denote the surface height of the capillary bridge. (b) Trehalose concentration along the surface during the evaporation. The mass transfer coefficient (k_p) used is 1e-2 with a scaled time interval of 4e-5. Different coloured curves mean the surface height at different time intervals. The distance and height presented in the figures are all scaled.*

However, this simulation above is oversimplified because high concentration trehalose would form a skin layer at the surface rapidly, which has a very high viscosity. Thus, the assumption of rapid vertical diffusion is no longer valid. Also, this skin layer could significantly cut the drying rate to prolong the drying process significantly. The skin layer movement is related to the Stefan problem, which is not considered in this work.

3.6 Conclusions

The wetting morphology of fibres can be predicted by the Capillary Bridge number (CB number), which is obtained from structure geometry. When CB number is greater than zero for given fibre matrix properties, a capillary bridge can be formed between fibres. However, the unknown nature of the relationship between principal radius and ambient environment limits the application of Capillary Bridge number but is related to the volume.

The surface instability of the capillary bridge formed by pure water or sugar solution of different concentrations was simulated numerically using MATLAB. In the pure water situation, the liquid is driven from the centre ($\check{x}$=0) to the end ($\check{x}$=1) by capillary pressure, which leads to the surface of the central area becoming flat. Then, the flatness is retained until the capillary bridge rupture due to evaporation. The simulation result agrees with the experimental observations based on the previous work[337–340].

A surface tension gradient introduces Marangoni flow in a sugar solution-loaded capillary bridge. Marangoni flow overcomes the capillary flow and pushes liquid towards the centre($\check{x} = 0$) regardless of the sugar concentrations. The thickness of the central area is increased by Marangoni flow. The drying rate reduces with the increase of trehalose concentration and is stopped by the sugar skin formed on the surface. Therefore, a trehalose-loaded capillary bridge will not rupture

except at extremely low initial trehalose concentration with a relatively high drying rate.

This model can be extended to any solution, where there are known relationships between solute concentration and viscosity, diffusion coefficient, and surface tension. Also, the drying rate influences the outcome through the rate of changing concentration during the drying process. It is quite similar to changing the initial concentration.

The modelling and simulation results revealed the complexity of capillary bridge formation for trehalose-fibre combination and its dynamics during drying. Given a set of physical, thermodynamic and transport properties, it is possible to predict whether the capillary bridges can be formed and not break during drying, which is essential to the MART drying of biological therapeutics.

Chapter 4

Drying of Functional Proteins with MART drying – a Study with Lactate Dehydrogenase

In the last chapter, the formation and drying kinetics of capillary bridges with various trehalose concentrations have been studied by simulation, which illustrated the stabilisation mechanisms of sugar films on fibre matrix. In this chapter, lactate dehydrogenases (LDH), as a model protein, is dried at room temperature with the support of a cellulose fibre matrix. The protein functionalities after drying and storage are investigated with enzyme activity assays and so the effect of different drying parameters. Stress relaxation, which could deteriorate the protein, is detected after the short-term storage and is mitigated by higher sugar concentration in the formulation. The potency of MART dried LDH with the modified formulation was evaluated after long-term storage, six months at 25 °C.

This chapter is based on the paper:

Yu, Y., Dai, S., Cui, Z. Drying of Functional Proteins with Sugar Glass Film on Three-dimensional Matrices – a Study with Lactate Dehydrogenase. Submitted.

As the main author, Y Yu's contribution to this paper is designing and experimenting, collecting and analysing data, deriving conclusions and drafting the paper.

TABLE OF CONTENTS

4.1 Introduction 72

4.2 Materials and Methods 75

4.2.1 Chemicals and Reagents 75
4.2.2 Fibre Matrix Preparation 75
4.2.1 Scanning Electron Microscopic Imaging 76
4.2.2 Fibre Matrix Characterisation 76
4.2.2.1 Fibre Diameter Measurements 76
4.2.2.2 Water Absorption 76
4.2.2.3 Protein Adsorption on Fibre Matrices 77
4.2.2.4 The Effect of LDH Activity on the Fibre Matrix 79
4.2.3 Determination of LDH Activity 79
4.2.4 Protein Formulations 80
4.2.5 MART Drying Process 80
4.2.6 Dried Sample Storage and Reconstitution 82
4.2.7 Differential Scanning Calorimetry 82
4.2.8 LDH-Sugar Solution Preparation 83
4.2.9 The Effectiveness of Fibre Matrix 84
4.2.10 Different Drying Conditions 85
4.2.11 MART Dried LDH Long-Term Storage 85
4.2.12 Effect of Freeze-Thaw Cycle on LDH Activity 86
4.2.13 Statistical Analysis 86

4.3 Results and Discussion 86

4.3.1 Cellulose Fibre Membrane Characterisations 86
4.3.2 Effectiveness of Sugars during Drying 90
4.3.3 Stress Relaxations and Mitigations 92
4.3.4 Effectiveness of Fibre Matrix 95
4.3.5 Retained LDH Activities with Different Drying conditions 98
4.3.6 Long-Term Storage Test 100

4.4 Conclusions 103

4.1 Introduction

Enzymes are biological catalysts accelerating the biochemical reactions within cells[367,368]. As a greener alternative to chemical catalysts, enzymes also have higher specificity and activity[369]. However, enzymes will lead to unfolding, structural changes and reducing the activities once leaving their native conditions. To maintain the activities, enzymes were commonly cryopreserved or dehydrated, which requires high energy-intensity machines, like the -80 °C freezer and freeze dryer. In addition, both preservation methods have high operational and maintenance costs, potentially increasing the cost of final products.

An alternative drying strategy, Matrix Assisted Room Temperature (MART) drying, has been put forward. MART drying has a straightforward process with low energy intensity and cost. The formulated protein (and other bioproducts) solution was loaded onto a fibre membrane matrix and dried at room temperature in a low relative humidity environment. The mechanism of the offered protection to the protein molecules by the matrices, particularly capillary bridging, has been studied in the previous chapter. In this chapter, lactate dehydrogenase (LDH), which is vulnerable to freeze[97,176,370], was selected as the model protein to investigate the effectiveness of MART drying.

Trehalose was used as the primary protective agent while dextran was added to increase the glass transition temperature (T_g), improving the thermostability of the dried product. The ratio of trehalose and proteins was evaluated by the retained activity of proteins after MART drying and short-term storage. At low sugar concentrations, although the activity of the enzyme was largely retained after drying, the enzyme activity was reduced over the short-term storage even at temperatures lower than T_g. The decreasing of enzyme activity was caused by stress relaxation or polymer ageing.

Three different stress relaxations, which are α, β and γ relaxations, are involved in the sequence, from the rubbery state into the glassy state. The relaxation, α relaxation, takes place in the glass transition and immobilises molecules. β and γ relaxations, are detected when storage temperature is lower than the glass transition temperature[371]. It has been reported that α relaxation was related to the difference of glass transition temperature and storage temperature ($T_g - T$) but not

affecting the protein stability in the glassy state. Addition of cryoprotectants, such as DMSO or glycerol to maltitol, which could decrease the glass transition temperature and lower ($T_g - T$), but increases the protein stability in the glassy state[372,373]. After testing over 100 formations, it has been shown that using ($T_g - T$) to predict the protein stability and degradation could cause a 1000-fold error. Therefore, α relaxation may not be the significant parameter for deciding the protein stability in glassy state[374].

In contrast to α relaxation, β relaxation is significantly correlated with the stability of the protein in the glassy state[375–377]. Since the crystalline state is the only state of thermodynamic equilibrium below the melting temperature, a glassy solid in an amorphous state is not an equilibrium state[378,379]. The glassy solid tends to approach a more stable and ordered structure to lower the enthalpy even at temperatures lower than the glass transition temperature, which is β relaxation[380,381]. β relaxation is described as the motion of specific chemical groups or a short sequence of molecules in the regime of low local density and intermolecular forces[382].

This motion could result in the internal rotations of large molecules, like polymer and proteins, to lower the energy by adjusting the hydrogen-bonding interactions and chemical structures, which could unfold proteins[371,383]. Although the mechanisms of how β relaxation denatures proteins in the glassy state are not clear, inhibiting β relaxation indeed increases the stability of proteins over the storage[375–377]. γ relaxation occurs at lower temperatures and is much weaker than the above

two relaxations[384]. Meanwhile, there was no report indicating the correlation between protein denaturation in the glassy state and γ relaxation.

In this chapter, β relaxation was successfully mitigated by adjusting the formulations, improving the stability of enzymes over the storage. Meanwhile, different drying parameters, such as drying temperatures, relative humidity and drying duration, were investigated. An optimal set of conditions was derived, and a long-term storage study was conducted to show the effectiveness of MART drying compared to cold storage at -20 °C and -80 °C.

4.2 Materials and Methods

4.2.1 Chemicals and Reagents

L-lactate dehydrogenase (LDH) solution from Rabbit muscle, D-(+)-trehalose dihydrate for microbiology (90210), ammonium sulphate, Dextran (MW= 40,000) and bovine serum albumin (A7906) were all purchased from Sigma-Aldrich, UK. Sterile cellulose fibre membranes were obtained from Merlin Medical, UK. Both kits used for measuring LDH activity (MAK066) and protein concentration (BCA assay kit, QPBCA) were purchased from Sigma-Aldrich, UK.

4.2.2 Fibre Matrix Preparation

A large fibre membrane was randomly torn into small pieces. Then, 20 mg of torn fibre matrix was placed in a well of the 48-well plate (Corning, UK) and compressed into a disc with a uniform thickness of 0.8 mm. This process ensured that all the fibre matrices applied in the experiments had a similar mass (approximately 20 mg)

and dimensions. The compressed fibre matrices were then carefully taken out of the well and placed on a Petri dish (Corning, UK).

4.2.1 Scanning Electron Microscopic Imaging

The scanning electron microscopy was used to image the fibre matrices. Fibre matrices were placed onto aluminium mounts with conductive copper tape. After coating with gold, the fibre matrices were imaged by Zeiss Sigma 300 Field Emission Gun Scanning Electron Microscope (FEG-SEM) under vacuum with accelerating voltage of 2 kV.

4.2.2 Fibre Matrix Characterisation

4.2.2.1 Fibre Diameter Measurements

The Image J software, a public domain open-source software, was used to analyse the SEM images of the unloaded cellulose fibre matrix to measure the fibre diameter. The number of pixels between fibres' edges was measured and compared to the scale. A magnified image was used to increase the accuracy. More than 40 measurements have been taken to reduce human errors.

4.2.2.2 Water Absorption

To investigate the amount of water absorbed on fibre matrices, fibre matrices in different weights, ranging from 10 to 35 mg, were prepared and placed into the loading tubes of centrifuge tube filters with 0.45 µm pore size (Thermo-fisher, UK). The centrifuge tube filter consists of two parts, the loading tube with the filter at the bottom and the collection tube to collect the liquid after filtration. The mass of each loading tube after loading fibre matrix was measured and recorded.

Two ml of MilliQ water was added into each loading tube to immerse the fibre matrix. After incubating at room temperature for 5 min, the centrifuge tube filter, containing the loading tube and collection tube, was centrifuged in the Sigma 1-14 centrifuge (Sigma-Aldrich, UK) with 5,000 rpm for 10 min. An empty filter with two ml water was placed as the background measurement. After discarding the collection tubes, the masses of the loading tubes with fibre matrices after centrifugation were measured and recorded. The mass difference of each sample subtracted the mass difference of background measurement was the amount of water absorbed on the fibre matrix.

4.2.2.3 Protein Adsorption on Fibre Matrices

The extent of protein adsorption was determined by measuring the amount of protein released from the fibre matrix and comparing it to the initial amount. Fibre matrices (around 20 mg) were individually placed into the loading tubes of centrifuge tube filters (0.45 µm pore size). 50 µl of protein solutions with different concentrations, ranging from 0 to 2.4 mg/ml, were dripped onto fibre matrices and the loading tubes directly without fibre matrix, which served as the positive control group.

LDH was suspended in 3.2 M ammonium sulphate solution with a concentration of 5 mg/ml. To eliminate the interface from ammonium sulphate in the protein concentration measurement, background solutions containing the same amount of ammonium sulphate in protein solutions were added to the fibre matrix in the loading tubes (negative control of fibre matrix) and the loading tubes directly (negative control).

After adding 2 ml of MilliQ water, all samples were incubated at room temperature for 5 min and then were centrifuged in Sigma 1-14 centrifuge at 5,000 rpm for 10 min. The total protein concentrations of the solutions in the collection tubes were measured using QuantiPro Bicinchoninic Acid (BCA) protein assay kit. Bovine serum albumin solutions (BSA) were used to plot the standard curve. For protein concentrations greater than 0.8 mg/ml, further dilution was required to make the results laid in the validated and accurate range of the BCA assay. For protein concentrations of 0.8 to 1.6 mg/ml, 2X dilution was used, while 3X dilution was applied for concentrations greater than 1.6 mg/ml.

After dilution, 50 µl of the sample from the collection tube was transferred into a 96-well plate. The reaction reagents were mixed with the sample in a 1:1 stoichiometric ratio and incubated at 37 °C for 2 h, then measured the absorbance at 562 nm by a SpectraMax i3X plate reader (Molecular Devices, UK). The temperature of the reading chamber was set to 25 °C according to the protocol. Eq. 4.1 illustrates the calculation of the amount of protein adsorbed in fibre matrices in the unit of mg BSA

$$Amount\ of\ Adsrobed\ Proteins = \Big(\big(c_{pc} - c_{nc}\big) - \big(c_{fm} - c_{nc_fm}\big)\Big) \times V$$

Eq. 4.1

where c_{pc} andc_{nc} are the protein concentrations of the positive control group and the negative control group, respectively, which do not have the fibre matrix. c_{fm} and c_{nc_fm} are the protein concentrations of the released solution from fibre matrices and its negative control group; V stands for the protein realising volume, which is 2.2 ml.

4.2.2.4 The Effect of LDH Activity on the Fibre Matrix

Proteins are prone to be adsorbed on the solid surface. To determine the effects of adding fibre matrix, the activity of LDH on fibre matrix was compared with the initial activity. The L-LDH solution (5 mg/ml) was diluted by water to the concentration of 2 mg/ml. Background solutions containing the same amount of ammonium sulphate in protein solutions were also prepared.

50 µl of the protein solutions or background solution were added to fibre matrices in the loading tubes and the loading tubes directly without the fibre matrix. Then, two ml of MilliQ water was added to each tube. After mixing by pipetting, centrifuge tube filters were centrifuged by the Sigma 1-14 centrifuge at 5,000 rpm for 10 min. Then, the activity of LDH solution in the collection tube was measured following the procedure in Section 4.2.3. All measurements were performed in triplicates.

4.2.3 Determination of LDH Activity

LDH solutions on fibre matrix or in the tubes were first mixed with 2 ml MillQ water. For measuring the LDH activity in the collection tube of the centrifuge tube filter, this 2 ml MilliQ water was not needed. Then, 10X further dilution with MilliQ water was applied before measuring activity. The lactate dehydrogenase activity assay kit (MAK066) was used for this aim. Following the protocol provided by the manufacturer, 2 µl of each diluted sample solution was added into a 96-well plate (Corning, UK) and mixed with 48 µl LDH assay buffer. After adding 50 µl reaction mix, the plate was incubated at 37 °C for 2 min. The plate was then transferred to a plate reader. The absorbances were acquired every 1.5 min at 480 nm at 37 °C. The activity of LDH was calculated as follows,

$$\frac{Amont\ of\ NADH\ genretaed\ during\ the\ incubation}{incubation\ time\ \times\ sample\ volume\ added\ into\ well} \times dilution\ factor,$$

where the volume added into the well was 2 µl, and the dilution factor was 10. All measurements were done in triplicate.

4.2.4 Protein Formulations

For sugar stabilisation, two parts of the LDH solution (5 mg/ml) were diluted by three parts of sugar solution (trehalose and dextran), which was previously filtered by a 0.22 µm syringe filter (Millipore, Sigma-Aldrich, UK). Sugar solutions in different concentrations were used. The formulated solution was prepared freshly before each experiment.

4.2.5 MART Drying Process

The whole drying process is demonstrated in ***Figure 4.1***. 50 µl of formulated enzyme solution was evenly dripped onto each prepared three-dimensional fibre matrix (***Figure 4.1*** *(a)-i)*. For the background measurements, ammonium sulphate in 3.2 M was mixed with excipients in the same ratio of the protein solution.

For the drying process, step (ii), the loaded matrices were placed on the sample station in the specially designed experimental apparatus, as depicted in ***Figure 4.1*** *(b)*. Drying was driven by the vapour pressure difference between the samples and circulated air. The circulating air was driven by the electric fan heater. At the sample station, the airflow velocity is constant at 0.12 m/s, measured by ATP Thermoanemeter AVM-888 (Rapid Electronics, UK).

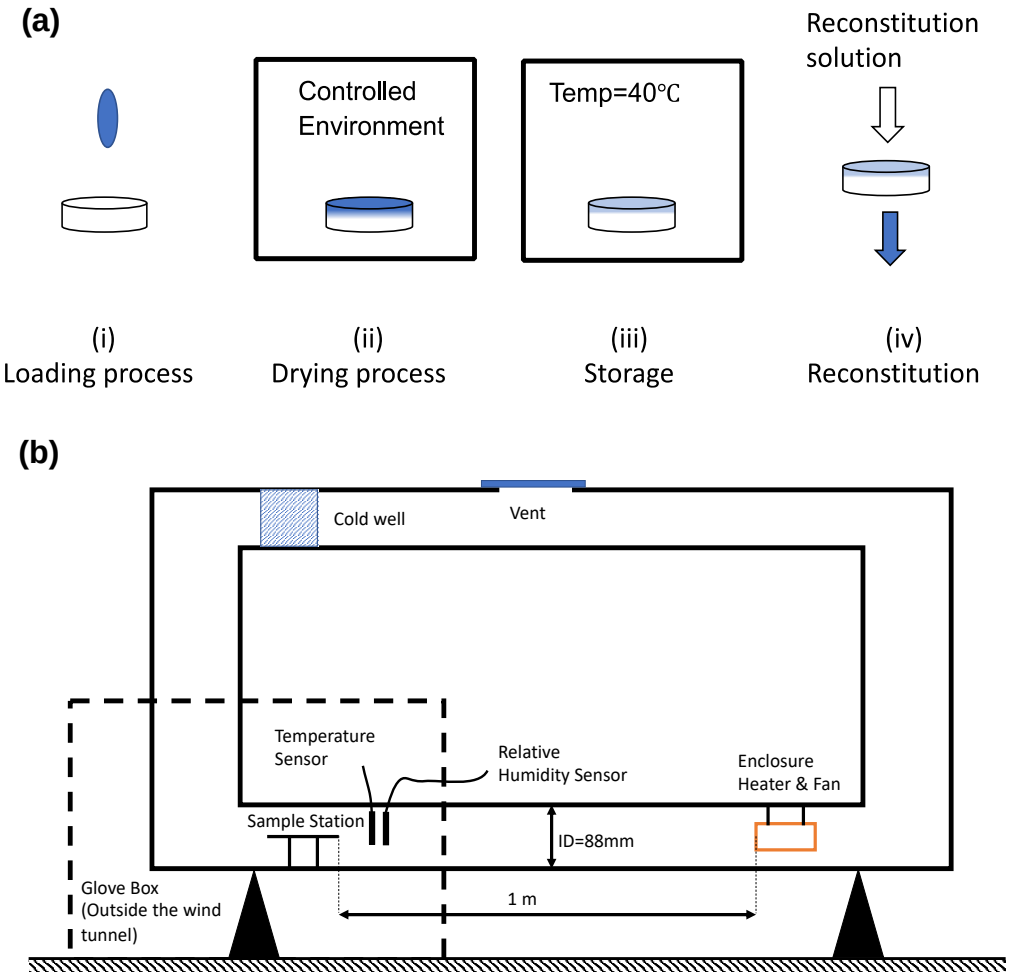


***Figure 4.1**: (a)Schematic demonstration of the protein stabilization process. (b)Schematic diagram of the drying equipment. Samples were placed on the sample station and dried by conventional drying. The temperature of dehydration is maintained to 28 °C by a PID controller. The cold well controlled relative humidity of the system.*

A PID controller was installed to control the air temperature. The humidity of circulated air was controlled by applying a 'cold well', which used a Peltier module (RS component, UK) to remove moisture in the circulating air. The temperature difference between the hot side (outside) and the cold side (inside the apparatus) of the Peltier module is constant, based on the voltage. A DC30-K20 digital control bath (Thermo-fisher, UK) was connected to the hot side to remove the heat by

circulating 4 °C water. With this 'cold well' setup, relative humidity of the circulating air in the apparatus could be maintained at 3% at 30 °C. The drying experiments usually ran overnight for 18 h.

4.2.6Dried Sample Storage and Reconstitution

After drying, the matrices were transferred into lyophilisation vials and sealed in moisture barrier bags (SCS, RS components) within the glove box. The temperature in the glove box was controlled to be the same as that in the drying apparatus. Relative humidity in the glove box was controlled by moisture absorbents (MiniPax, Sigma-Aldrich, UK) to the same as or lower than that in the drying apparatus. After heat sealing, the sample bags were stored at certain temperatures for stability tests.

After storage, samples were taken out from the incubators. After cooling to room temperature, dried matrices were taken out from vials, transferred into a 12-well plate, and reconstituted with 2 ml of MilliQ water.

4.2.7 Differential Scanning Calorimetry

Differential scanning calorimetry (DSC) was applied for measuring glass transition temperature (T_g) of dried protein-sugar samples immediately after drying and after storage. All the measurements were done by DSC Q2000 from the TA instrument, US.

The size of the Tzero DSC pan (TA instrument, US) used for DSC measurements was smaller than the size of the fibre matrix of 20 mg. After drying or storage, a

small piece of LDH-loaded matrix was cut off and transferred into Tzero DSC Pan. The sample was hermetically sealed with an aluminium lid (TA instrument, US) in the glove box. An empty pan was sealed in the same condition as the reference.

After placing the pan on the sensor with the reference pan at room temperature, the machine was precooled to 0 °C. After equilibrating at 0 °C, the sample was heated up to 105 °C at a rate of 10 °C/min. Heat flow (W/g) was recorded with the temperature of the machine. The glass transition temperature (T_g) was acquired by Universal Analysis software (TA instrument).

When stress relaxation was involved in standard DSC measurement, modulate DSC measurement was applied to separate the glass transition and stress relaxation. When the sample reached thermal equilibrium at 0°C, the machine temperature was set to be modulated at $\pm$ 0.6 °C every 1 min. After stabilising for 5 min, the temperature gradually increased at the rate of 1 °C/min to 105 °C with the modulation. The heat flows (W/g) along the heating were recorded with the machine temperatures. Universal Analysis software (TA instrument) was applied to calculate stress relaxation.

4.2.8 LDH-Sugar Solution Preparation

Lactate dehydrogenase (5 mg/ml) were mixed with sugar solution. The final protein concentration was 2 mg/ml, while the final sugar concentration was 1 M trehalose and 10%w/v dextran. The solutions were mixed thoroughly using a vortex shaker (Cole-Parmar, UK).

4.2.9 The Effectiveness of Fibre Matrix

LDH-sugar was dripped directly on fibre matrix and Petri dish. The initial activity was measured before drying. After drying under the same condition, 30 °C with 3% RH, the LDH activity of samples was measured.

The effectiveness of fibre matrix thickness on the LDH stabilisation was evaluated. Torn cellulose fibres with the same mass were pressed into the different thicknesses using pressers of different sizes, as depicted in ***Figure 4.2***. After placing the pressers, heavy objectives were placed on the pressers' top. After one hour, the fibre matrices were carefully taken out by tweezer from the wells and placed on a Petri dish.

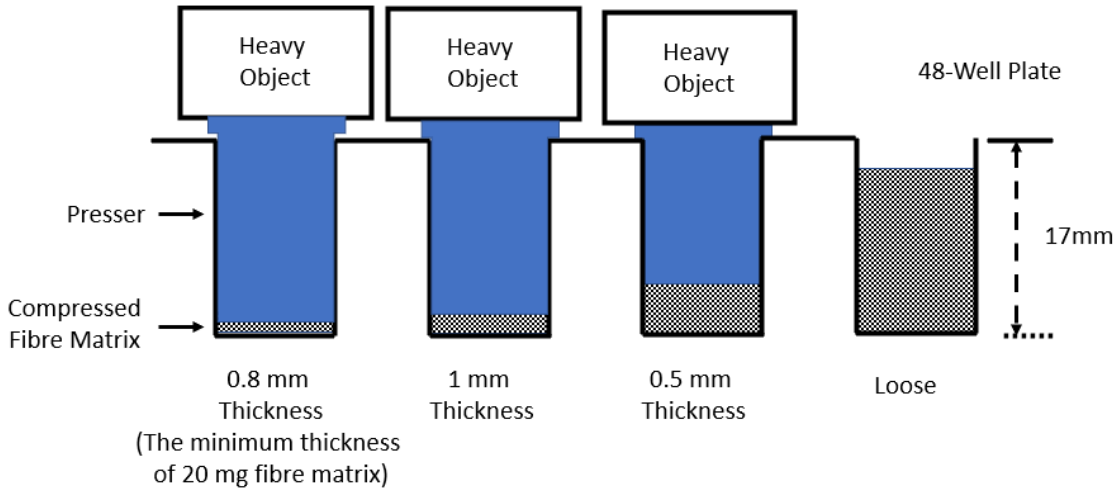


Figure 4.2*: Schematic demonstration of pressing cellulose fibres into different thicknesses.*

After the drying apparatus reached stable drying conditions (30 °C and RH=3%), 50 µl of LDH-sugar solution was dripped on fibre matrices with different thicknesses. The enzyme activity was measured before drying as the initial enzyme activity. The

other loaded matrices were placed on the sample station in the drying apparatus. After 18-hour drying, the samples were stored at 40 °C for one week. The LDH activity was measured after reconstitution. All measurements were performed in triplicate.

4.2.10 Different Drying Conditions

The drying apparatus was switched on for 2 hours before experimenting. After the drying condition reached a steady state, 50 µl of LDH-sugar solutions were dripped onto compressed fibre matrices. After 18-hour drying, the samples were stored at 40 °C.

To find the effect of different drying times, three samples were taken out at each time point and stored at 40°C. After one week of storage, the activity of dried samples was measured. All the measurements were performed in triplicate.

4.2.11 MART Dried LDH Long-Term Storage

To test the long-term stability of the MART dried LDH, the same batch of LDH-sugar formulation (1 M trehalose and 10%w/v dextran) were prepared and aliquot into four groups, two drying groups and two liquid control groups. For two drying groups, 50 µl of LDH-sugar solutions were added to compressed fibre discs and dried in the drying apparatus, which was set to 30 °C with relative humidity of 3%. After 18-hour drying, samples were stored at 25 °C and 40 °C, respectively. The other two liquid control groups stored the same batch of LDH solution as the liquid phase at -80 °C and -20 °C, respectively. After six months, the LDH activities were measured. All the experiments were done in triplicate.

4.2.12 Effect of Freeze-Thaw Cycle on LDH Activity

One batch of LDH-sugar solution was divided into three groups. 50 µl of LDH solutions were dripped on fibre matrices and measured the activities immedicably as initial LDH activities. Meanwhile, the other two groups were stored at -20 °C and -80 °C, respectively. After 1-week storage, frozen samples were taken out and thawed at room temperature. After mixing by vortex, 50 µl of LDH-sugar solutions were dripped on fibre matrices. Then, 2ml MilliQ water was added to release LDH before measuring the activities. All the experiments were done in triplicate.

4.2.13 Statistical Analysis

Statistical differences of the data from the same time point but different conditions were analysed by t-tests. Differences between groups with various time points were analysed by analysis of variance (ANOVA). The P values between groups less than 0.05 was considered as a significant difference. The statical analysis was performed with GraphPad Prism 6.0.

4.3 Results and Discussion

4.3.1 Cellulose Fibre Membrane Characterisations

The microstructure of the cellulose fibre membrane was presented by scanning electron microscopy (SEM), and the impact of adding fibre matrix on the activity of LDH was studied.

The compressed fibre matrix without sugar solution loading was observed by scanning electron microscopy (***Figure 4.3*** *(a)*). The fibre diameter was 12.84 ± 2.86 µm, analysed by ImageJ. According to the figure, the fibres are randomly orientated, and nothing is spanning between fibres.

Less liquid volume has been observed for the samples with fibre matrices after reconstitution than those without fibre matrices. It might be caused by the hydrophilic property of cellulose, where the structure of the water molecule was changed[385]. To increase measurement accuracy, centrifugation was applied to reduce the absorbed water. From (***Figure 4.3*** *(b)*), it could be seen that almost all water could be excluded from fibre matrices after centrifugation. Only around 7.726 µl of reconstitution water was bound to 20 mg fibre matrix and cannot be rereleased. Compared to 2 ml of reconstitution water, the volume of absorbed water was negligible. In the meantime, the proportional relationship between fibre matrix mass and the amount of bound water has been discovered, which was in the slope of 0.3863 µl/mg fibre.

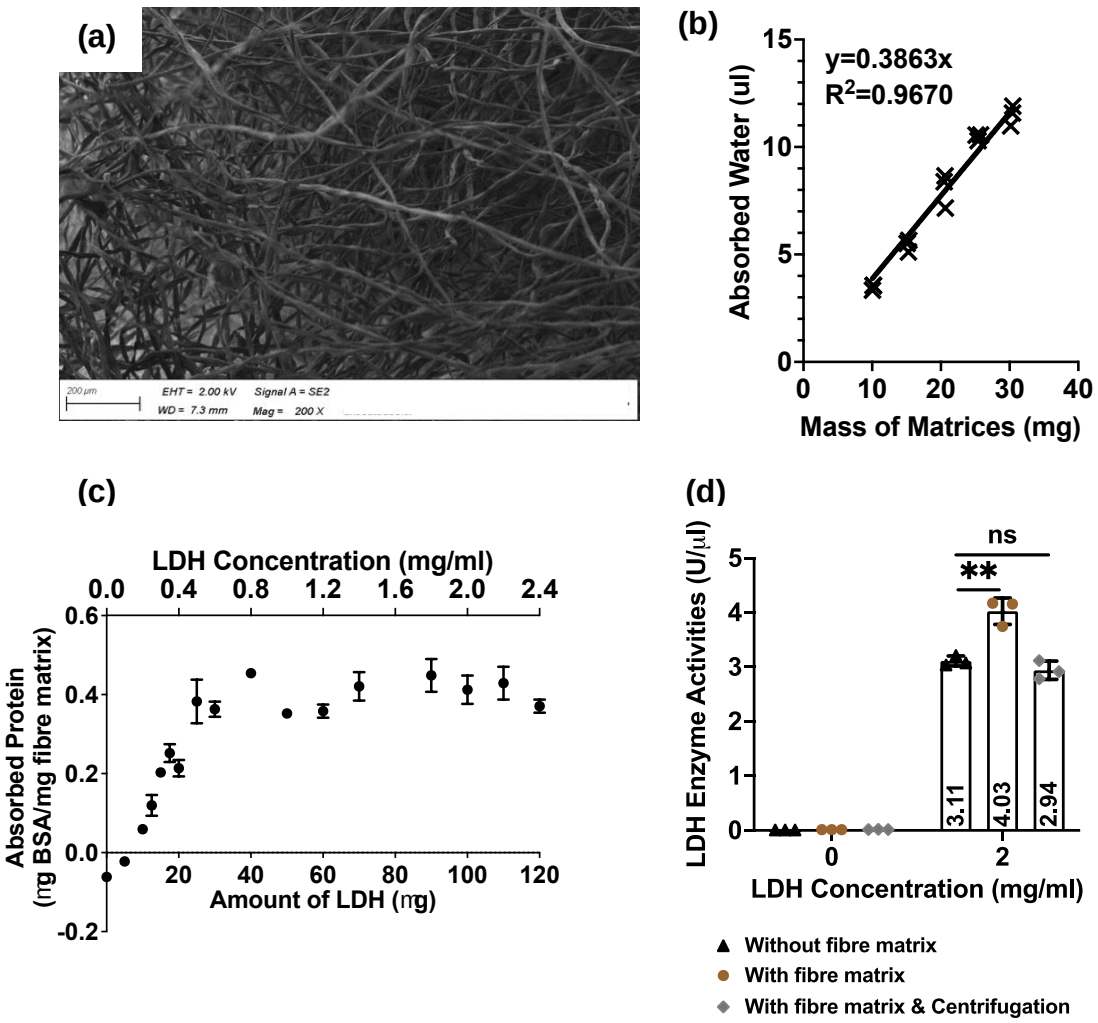


Figure 4.3*: (a) Scanning electron microscopy of unloaded cellulose fibre matrix. (b) The relationship between the mass of fibre matrix and the amount of bound water after centrifugation. Every point in the figure is represented as a measurement with one fibre matrix. (c) The amount of absorbed protein, in the unit of µg BSA/mg fibre, was plotted against the amount of LDH added to the matrix. The upper x-axis showed the corresponding concentration of LDH, ranging from 0 to 2.4 mg/ml. (d) The activities of LDH at the concentration of 2 mg/ml were measured without and with fibre matrices. In the meantime, the LDH activities of the samples with and without centrifugation was investigated. 0 mg/ml of LDH was measured as background. Results were presented as Mean±SEM. n=3, ns=no significant difference, **=P<0.01.*

Meanwhile, proteins are unavoidably adsorbed on solid surfaces[100,141] due to energetic interactions between protein molecules and different material surfaces[101,102]. In this study, the amount of protein molecules adsorbed on the

fibres was also measured with centrifugation (***Figure 4.3*** *(c)*). Some proteins have been eluted from fibre matrices after adding water but did not have LDH activity (***Figure 4.3*** *(d)*). After adding water, the samples were incubated at room temperature for 5 min. The amount of absorbed proteins was increased with the protein concentrations and reached a plateau when the protein concentration was over 0.8 mg/ml.

Since different concentrations of bovine serum albumin (BSA) solutions were applied as standards, the amount of absorbed proteins was presented in 'µg BSA/mg fibre'. The relationship between LDH and BSA in the bicinchoninic acid assay (BCA assay) was presented as $m_{BSA} = 1.036 m_{LDH}$ (Figure A3 in Appendix 3) where m_i indicted the mass of substance i. Therefore, around 0.4 µg of BSA was absorbed per mg of fibre matrices or 0.39 µg LDH/mg fibre. Approximately 7.8 µg of LDH would be absorbed on 20 mg fibre matrices.

Although some protein was absorbed on fibre matrix, the LDH activity with fibre matrix was higher than the LDH solution without fibre matrix (***Figure 4.3*** *(d)*). Therefore, the addition of fibre matrix reduced free liquid volume significantly, leading to a higher concentration of LDH. Based on the activity difference, around 500 µl of water was attached to the fibre matrix if ignoring the protein adsorption. After centrifuging the reconstituted samples with fibre matrices, the activity of LDH (2.94 U/ml) was slightly lower than the activity of samples without fibre matrix (3.11 U/ml), which might cause by protein adsorption. However, there was no significant difference in statistics.

Therefore, the addition of fibre matrices could reduce the volume of free water after reconstitution and increase the concentration of LDH, leading to higher initial LDH activity. The impact of protein adsorption might be ignored when using a relatively high initial protein concentration. The activity of LDH with fibre matrix before drying was regarded as initial activity in the following context. Then, centrifugation was not required, which simplified the activity measurement.

4.3.2 Effectiveness of Sugars during Drying

To acquire the optimum trehalose concentration, the retained activities of LDH after drying with different trehalose concentrations were evaluated. Moreover, the protective function of sugars by combining trehalose with dextran was investigated.

The original LDH (5 mg/ml) is stabilised in 3.2 M ammonium sulphate as a suspension mixture. Therefore, diluting LDH by different solutions, water or 3.2 M ammonium sulphate, to required concentrations (2 mg/ml) could result in different liquid phases, solution or suspension, respectively. The retained activities of LDH were measured after drying without any other excipients (***Figure 4.4*** *(a)*). It could be seen that almost all LDH were denatured, whether in the solution phase or the suspension phase. Neither water nor ammonium sulphate can stabilise LDH over the drying process.

Trehalose was selected as a stabiliser to stabilise LDH over MART drying. The addition of sugar did not affect the activity of LDH (Figure A4 in Appendix 4). The retained activities of LDH after MART drying with different trehalose concentrations were investigated. As indicated in ***Figure 4.4*** *(b)*, the protective function of trehalose was generally increased with the growth of concentration. When

trehalose concentration was over 500 mM, the retained activity of LDH reached a plateau, around 87% of the initial LDH activity.

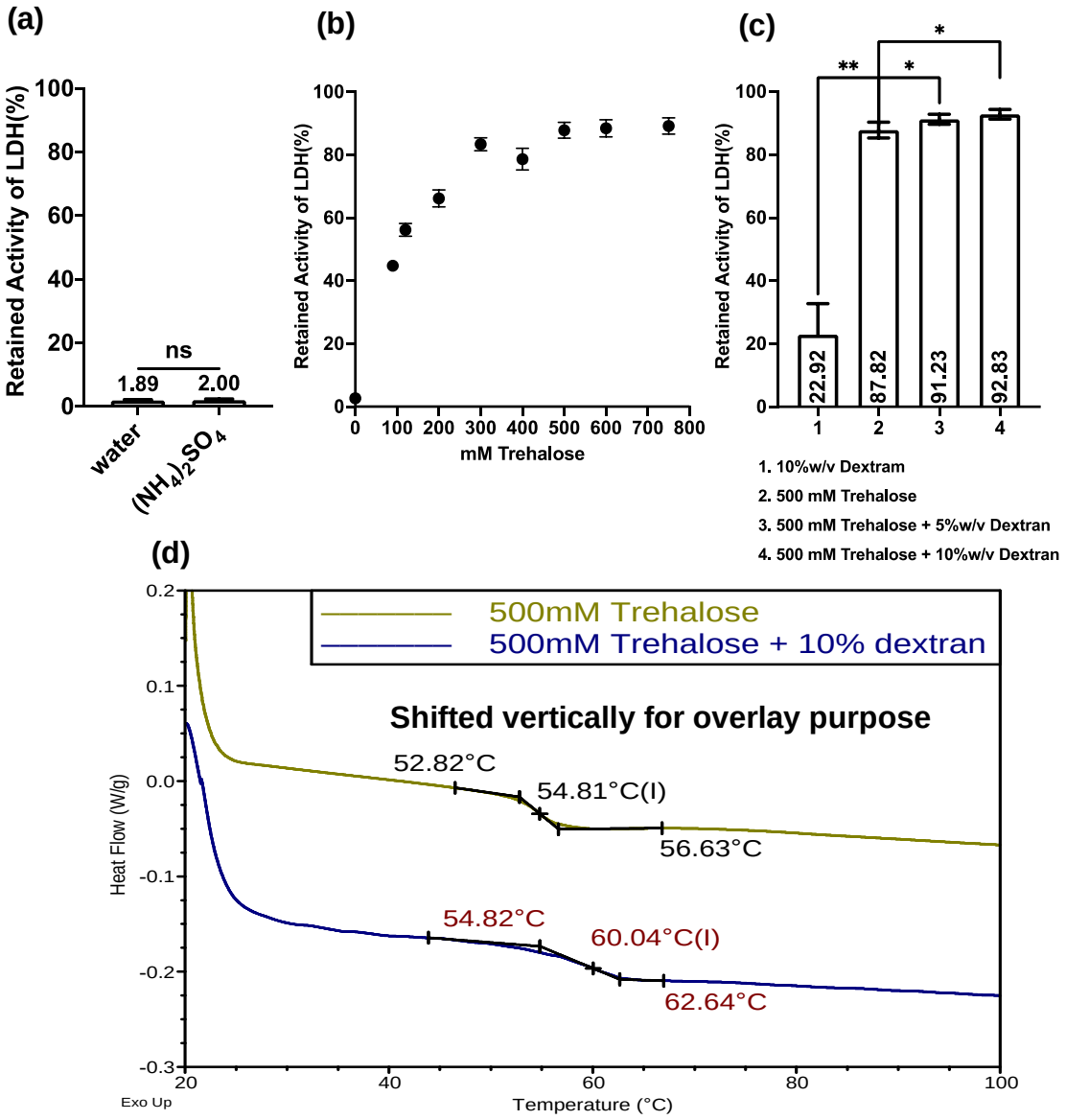


Figure 4.4: *(a) The retained activity of LDH after drying with different liquid phases, solution and suspension. The results were shown in percentage, which was compared with the initial LDH activity. (b) The retained activities of lactate dehydrogenase formulated with trehalose in different concentrations, ranging from 0 to 800 mM. At 0 mM trehalose condition, water was used for the dilution. (c) The retained activities of LDH after drying with dextran alone or with trehalose and dextran were shown in the percentage of the activity before drying. (d) Glass transition temperatures of MART dried LDH. LDH was formulated with different sugars and dried on the fibre matrix. All samples were dried in the low relative humidity condition (3%) at 30°C. Results are presented as Mean±SEM for (a), (b), and (c). n=3, ns=no significant difference, *=P<0.05, **=P<0.01.*

Polysaccharides are usually added to increase the glass transition temperature and improve the thermostability of the dried products. Therefore, the retained activity of LDH after drying with trehalose and dextran were also studied. As depicted in ***Figure 4.4*** *(c)*, 10% w/v dextran only gave minor protection for LDH. Only 22.92% of initial activity was preserved. However, combining dextran with 500 mM trehalose improved the retained activity of LDH. 92.83% of LDH activities were retained after MART drying with 10% w/v dextran and 500 mM trehalose. Meanwhile, the addition of 10% dextran into 500 mM trehalose increased T_g from 54.81 °C to 60.04 °C, as shown in ***Figure 4.4*** *(d)*.

4.3.3 Stress Relaxations and Mitigations

The enzymatic activity of MART dried LDH, supplemented with 500 mM trehalose and 10% w/v dextran, was reduced significantly after one-week storage, even though most of the initial activity was preserved after drying. β relaxation was detected by differential scanning calorimetry (DSC) for MART dried LDH after storing at 40 °C for one week. It could be the primary degradation pathway during the storage. The relaxation could be mitigated by modifying the formulation.

As presented in ***Figure 4.5*** *(a)*, there was no significant decrease in enzyme activities after drying with 500 mM trehalose and 10%w/v dextran, 93.28% of initial LDH activity (3.41 U/ml) left. Nevertheless, after 1-week storage, the retained enzyme activity dropped to 75% at 25 °C and almost halved at 40 °C storage. Although both storage temperatures were lower than the glass transition

temperature (60.78 °C), the degradation of enzyme activity was still observed, which was also found in the previous works[314,315].

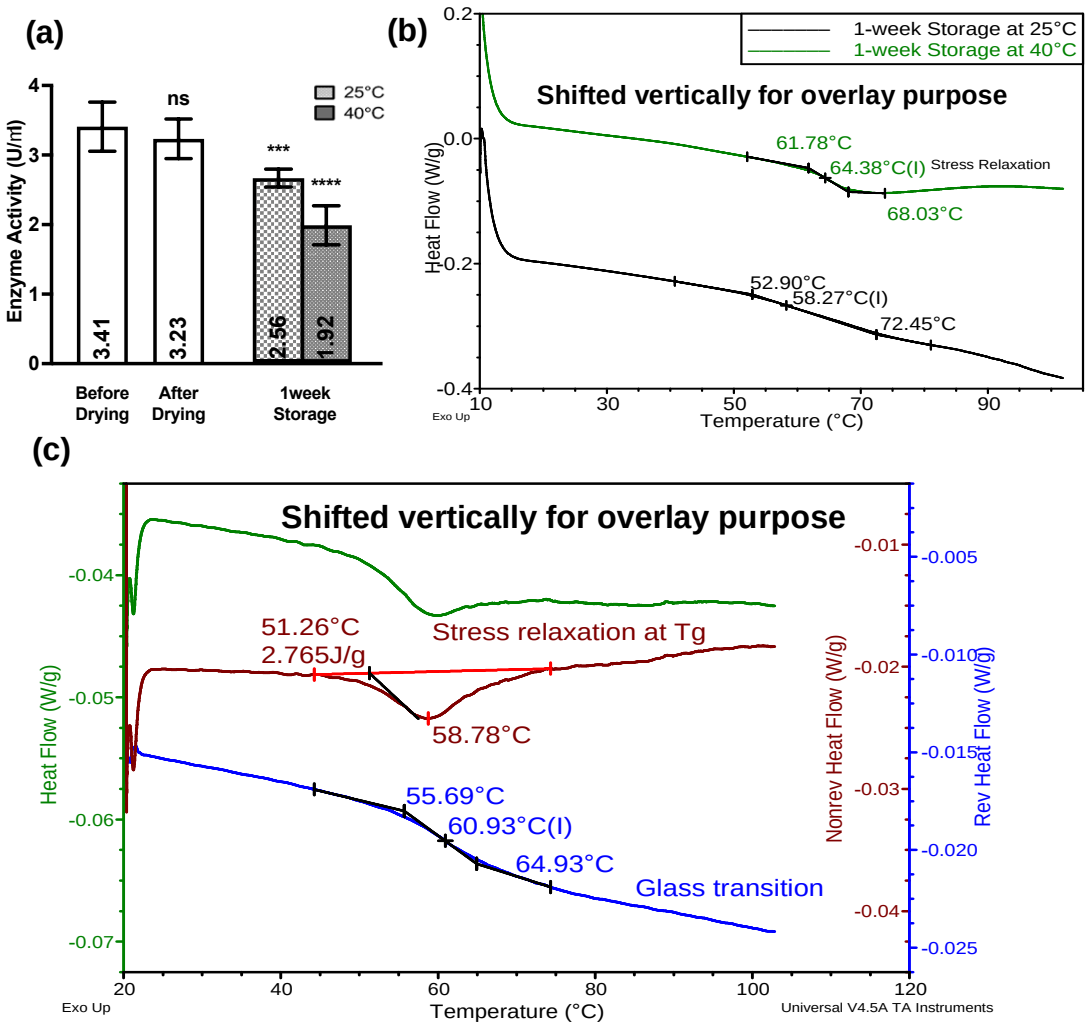


***Figure 4.5**: (a) The activities of LDH formulated with 500 mM trehalose before drying, after drying and after 1-week storage at different temperatures (25 °C and 40 °C). Same formulation, 500 mM trehalose with 10%w/v dextran, and the same drying condition were used. Results are presented as Mean±SEM, n=3. (ns=no significant difference, ***=P<0.001, ****=P<0.0001). (b) The glass transition temperatures of dried LDH with sugar after 1-week storage at 25 °C (black line) and 40 °C (green line). Stress relaxation was detected in dried samples stored at 40 °C for one week. (c) Modulate DSC analysis was applied for the dried sample, which was stored at 40 °C for one week. The overall heat flow profile (green line) was separated into glass transition (blue line) and stress relaxation (brown line). In the stress relaxation profile, the surface area under the horizontal line (red line) was integrated with time to get the activation energy. The integration was calculated by the Universal Analysis software provided by TA Instrument.*

According to differential scanning calorimetry (***Figure 4.5*** *(b)*), the glass transition temperatures of both formulations were quite similar. However, the stress relaxation was detected after storing the sample at 40 °C for one week. The modulate DSC measurement separated the heat flow curve (in green colour) into standard glass transition curve (in blue colour) and stress relaxation curve (in brown colour) by modulating the heating rate (***Figure 4.5*** *(c)*). Except for glass transition, an extra endothermal process was presented at the glass transition temperature, which illustrated that the energy required for breaking stress relaxations had been done over the storage. After integrating the peak of the stress relaxation curve with the time, recorded by the machine but not shown in the figure, the activation energy for stress relaxation was estimated via Universal Analysis software (TA instrument), which was around 2.765 J/g.

As mentioned in the introduction, although the mechanisms of how stress relaxation denatures proteins in the glassy state are unclear, protein stability over the storage could be increased by inhibiting the β relaxation[375–377]. It has been reported that the β relaxation can be mitgated by increasing the trehalose concentration[386].

Therefore, LDH solutions were drying with elevated concentrations of trehalose and stored at 40 °C for one week. As shown in ***Figure 4.6*** *(a)*, the retained activities of LDH after 1-week storage at 40 °C was improved by increasing the trehalose concentrations. Over 90% initial activity was retained when 1 M trehalose was formulated. Further increase of trehalose concentration would raise the difficulty of liquid handling and not significantly improve the retained activity.

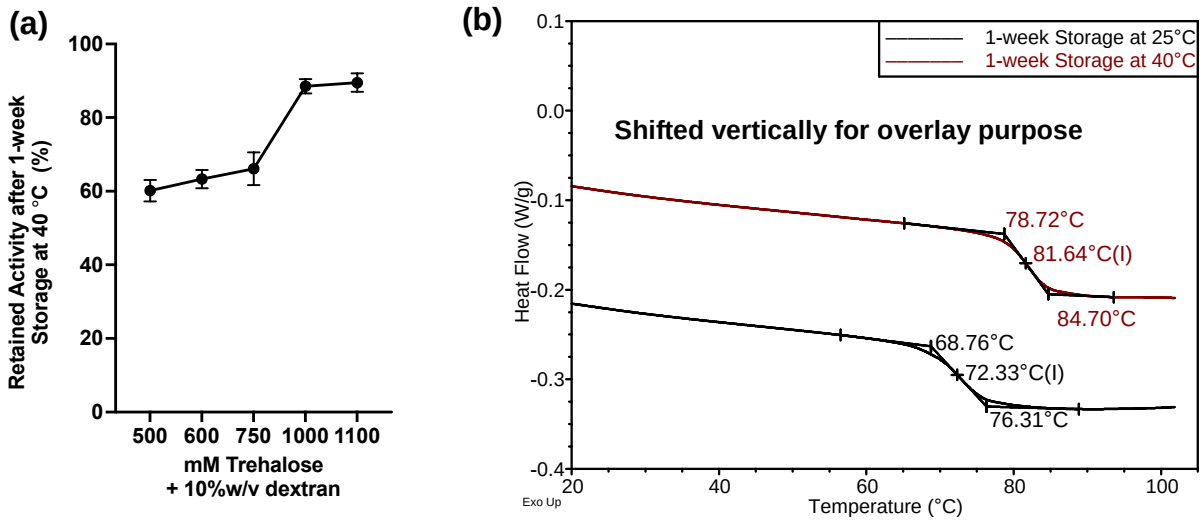


***Figure 4.6**: (a) Percent retained activities of MART dried LDH formulated with elevated trehalose concentrations after 1-week storage at 40 °C. (b)The glass transition temperatures of MART dried LDH with 1 M Trehalose and 10%w/v dextran after one-week storage at 25 °C and 40 °C. In (a), results are presented as Mean ±SEM, n=3.*

The glass transition temperatures were measured after storing the MART dried LDH formulated with 1 M trehalose and 10%w/v dextran at 25 °C and 40 °C for one week (***Figure 4.6** (b)*). Clear glass transitions were found in both sample measurements. There was no sign of stress relaxation. Then, the formulation in the following experiments was changed to 2 mg/ml LDH solution with 1 M trehalose and 10%w/v dextran (LDH-sugar solution).

4.3.4 Effectiveness of Fibre Matrix

The retained activities of LDH dried on compressed fibre matrice and Petri dishes were measured to assess the effectiveness of using fibre matrix to support drying. At the same time, the retained activities of LDH dried on fibre matrix with different

thicknesses were investigated. The sugar films formed on the fibre matrices in different thicknesses were also imaged.

The LDH-sugar solution was dried on the fibre matrices and Petri dishes under the same drying conditions. Without fibre matrix, formulated LDH solution was dried on Petri dishes as droplet structure. The retained activities were measured immediately after 18-hour drying (***Figure 4.7*** *(a)*). The retained activity of LDH dried on the fibre matrices was around 89%, higher than that on the Petri dish (80%).

The retained activity of LDH was not related to the thickness of the fibre matrix. As shown in ***Figure 4.7*** *(b)*, samples dried with varying thicknesses of fibre matrices were all retained over 80% of their initial activities. There was no significant difference in statistics. Since the softness of fibres, the liquid weight would drag the fibre downside during the dripping step. It might be the reason that the fibre density difference was not evident for different thicknesses of fibre matrices based on the images taken by SEM (***Figure 4.7*** *(c-f)*. The most compressed fibre matrix with 0.8 mm thickness would be preferred for economic and logistical reasons.

According to scanning electron microscopy, sugar films were found in a compressed fibre matrix (***Figure 4.7*** *(c-f)*). To maintain sugar films after drying, capillary bridges need to be spanned among fibres before drying[263]. The capillary formation increases the air-liquid interface, improving the mass transfer efficiency and reducing the protein hydrolysis. Due to the shape of the capillary bridge, enzyme molecules could be gathered and immobilised in the sugar films, which was fully discussed in Chapter 3.

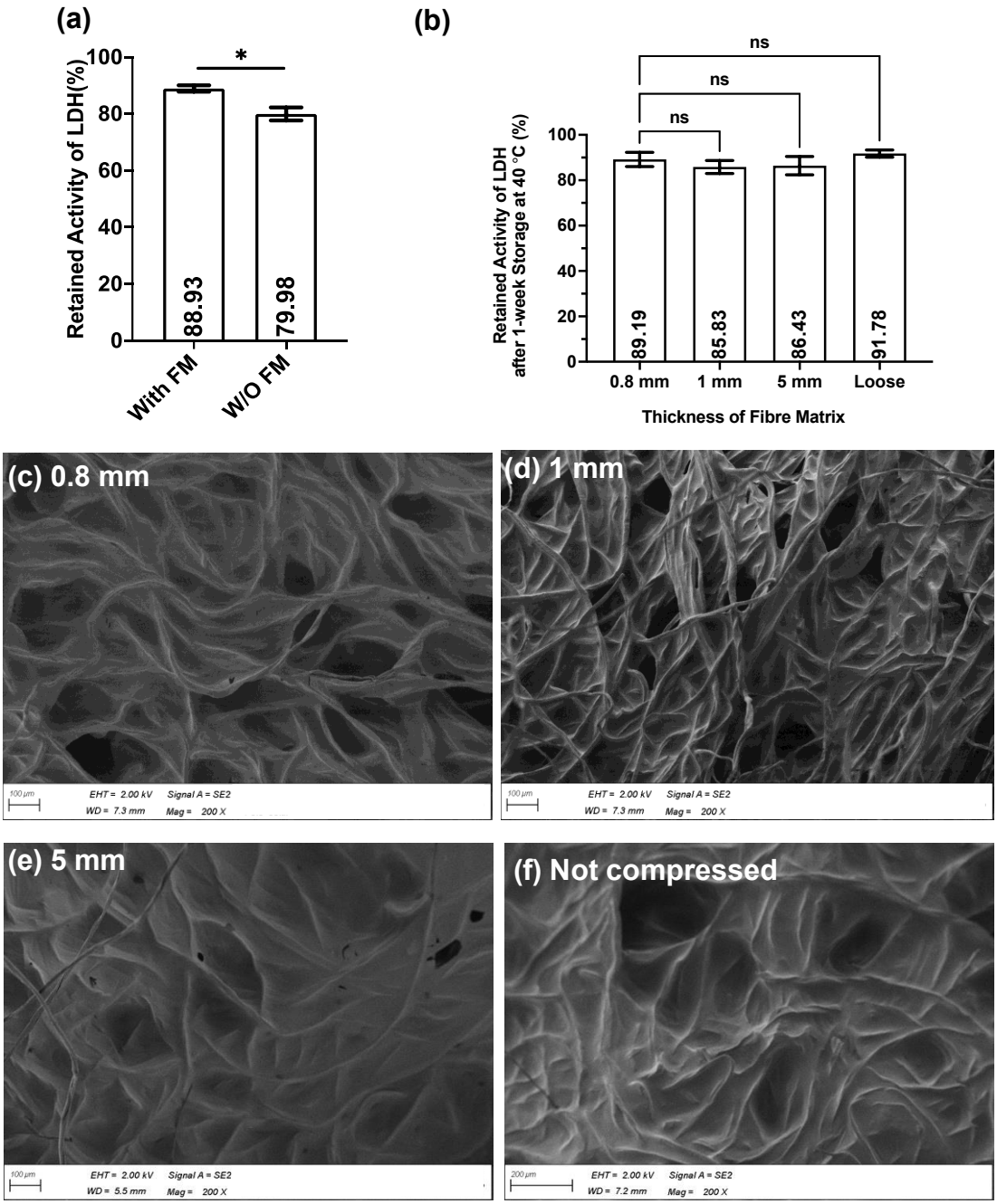


***Figure 4.7**: (a) The retained activity of LDH drying with and without compressed fibre matrix after drying. FM denotes a fibre matrix. (b) The retained activity of LDH drying with fibre matrix with different thicknesses. (c-f) The scanning electron microscopy of formulated LDH dried on cellulose matrix with different thicknesses, which were (c)0.8 mm, (d)1.0 mm, (e)5 mm, and (f)not compressed. Sugar films were deposited among the fibres. The scale bar was shown at the left-down part of the figure. Results in (a) and (b) were presented as Mean±SEM, n=3. T-test has been applied for (a) and (b), where ns=no significant difference, *=P<0.05.*

4.3.5 Retained LDH Activities with Different Drying conditions

Different MART drying conditions could result in different evaporating rates and final moisture contents, affecting the protein stability over the storage. Different drying conditions, including drying temperature, relative humidity and drying time, were investigated. After drying, matrices loaded with LDH-sugar solution were stored at 40 °C for one week before measuring their enzymatic activities.

LDH-sugar solutions were MART dried for 18 hours at different drying temperatures. The constant temperature of the cold well ensured a consistent partial vapour pressure of the air inside the system. However, this led to different initial relative humidity values for the different drying temperatures, 5%, 4% and 3% at 22 °C, 26 °C and 30 °C, respectively. According to the psychrometric chart, the sample temperatures, or wet-bulb temperatures, in these conditions are all above 0 °C, which prevent samples from freezing.

After 1-week storage at 40 °C, all MART dried LDH samples retained over 80% of their initial activities, regardless of drying temperatures (***Figure 4.8*** *(a)*). There was no significant difference in retained activity between drying at ambient temperature (22 °C) and elevated temperature (30 °C). Although MART drying at 26 °C produced slightly inferior results, the retained activities of the LDH samples were still over 80%. Therefore, this drying method was quite robust for varying temperatures.

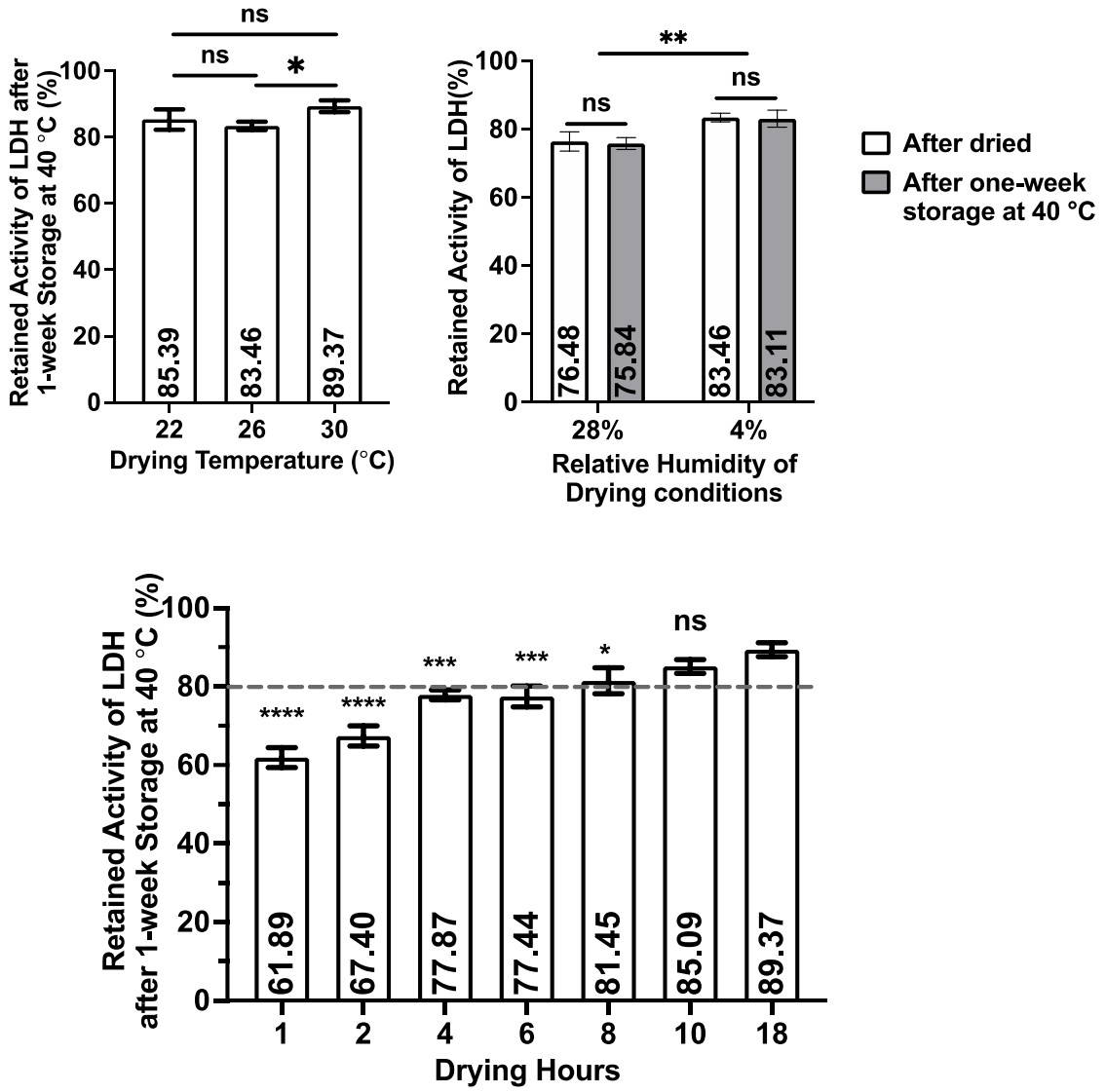


Figure 4.8*: Percent retained activities of MART dried LDH desiccated in different drying conditions, temperature (a), relative humidity (b), and drying time (c), after 1-week storage at 40°C. Results are presented as Mean±SEM, n=3. T-test has been applied for (a) and (c). 2way ANOVA was applied for (b). (ns=no significant difference, *=P<0.05, **=P<0.01, ***=P<0.001, ****=P<0.0001).*

With temperature kept unchanged at 26 °C, drying with different initial relative humidity resulted in significant differences in the retained LDH activity (***Figure 4.8 (b)***). The initial relative humidity was controlled by turning the cold well on and off. Around 77% initial activity was preserved after drying at ambient conditions (RH =

28%) and 1-week storage at 40 °C. The retained activity improved to 83.11% by drying the samples in a low relative humidity condition (RH= 4%).

The higher relative humidity at drying conditions led to more residual moisture contents in the dried products. It might cause a greater extent of trehalose crystallisation. The crystallisation of trehalose could reduce hydrogen bonding between sugar and proteins, decreasing protein stability[294]. Therefore, the moisture content of the drying air should be controlled as low as possible to preserve the activity of LDH optimally.

The drying duration was also investigated for its influence on the retained LDH activity. We tested a range of drying durations, from 1 hour to 18 hours, and measured the retained activities of the dried LDH after storing at 40 °C for one week (***Figure 4.8*** *(c)*). A positive correlation between the retained activity of LDH and the drying time was observed. After storing at 40 °C for one week, the retained activity of MART dried LDH was over 80% when the drying duration was longer than 8 hours. By stretching the length of drying to 18 hours, 90.33% of the LDH activity was preserved after storage. Longer drying time with low RH drying conditions led to lower residual moisture content, increasing the glass transition temperature and thus the stability of the product.

4.3.6 Long-Term Storage Test

Formulated LDH was desiccated at 30 °C with 3% RH and placed in 25°C and 40 °C for long term storage after drying. MART dried LDH showed promising retained activities after 6-month storage at 25 °C but were significantly deteriorated at 40 °C.

In this case, LDH was formulated with 1 M trehalose and 10%w/v dextran and stored at -20 °C and -80 °C as the control groups. As shown in **Figure 4.9** *(a)*, for enzymatic activity, storing LDH-sugar solution at -20 °C did not exhibit a significant difference from storing at -80 °C. The relatively lower retained activity of LDH and higher variation at -20 °C storage might be caused by the solute precipitation[176] (**Figure 4.9** *(b)*), while the solution kept clear at -80 °C storage.

The precipitates were re-dissolved when the samples returned to room temperature but dissolved after mixing. We speculate that the precipitate might be ammonium sulphate, enriched and precipitated due to ice crystallisation at -20 °C. After placing the sample at -80 °C, the LDH-sugar solutions were vitrificated. The solution transit into the glassy state instantly without ice crystal formation. All molecules were immobilised in the glassy state. There was no solute enrichment and precipitation.

Meanwhile, LDH was thermostabilised after MART drying. The retained activity of dried products after storing at 25 °C for six months did not show a statistical difference with the -80 °C control group. Specifically, MART dried LDH has preserved around 96.47% activity compared to the -80 °C control group. However, 6-month storage at 40 °C expressively reduced the activity of MART dried LDH, with only around 35.03% left compared to the -80 °C control group. An acceptable degree of thermo-stabilisation was achievable for one-week storage at 40 °C, enough for transportation across continents.

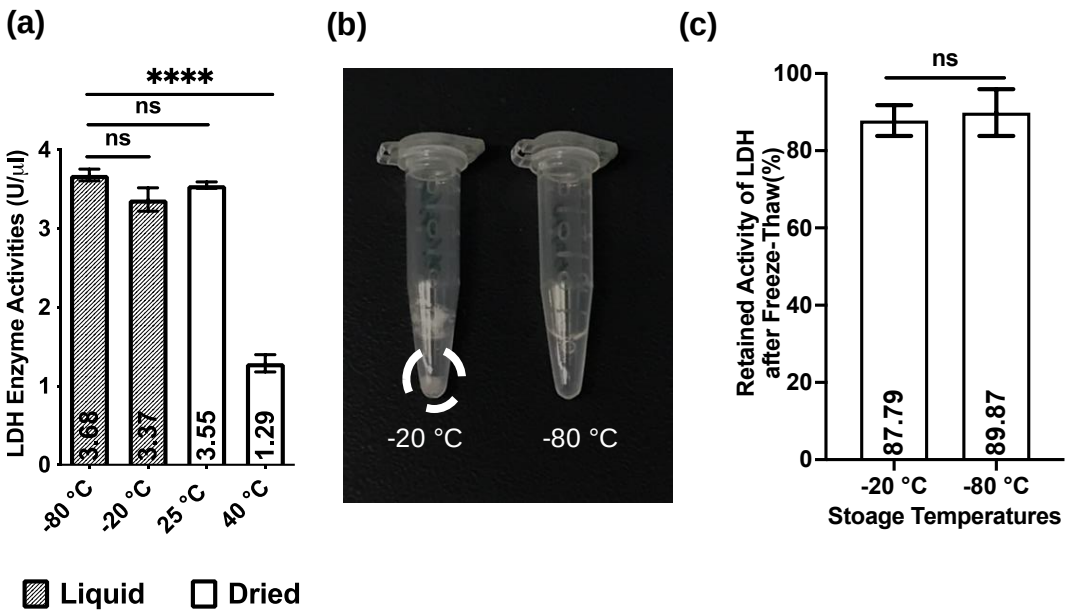


Figure 4.9*: (a) The activities of enzyme LDH after 6-month storage with different storage conditions: liquid form at -80 °C; liquid form at -20 °C; MART dried and stored at 25 °C; MART dried and stored at 40 °C. (b)The solute was precipitated after 6-month storage at -20 °C, while the LDH-sugar solution was kept clear after storage. (c) The retained activity of LDH after one freeze-thaw cycle at -20 °C and -80 °C. In (a) and (c), results were presented as Mean±SEM, n=3. 'ns' = no significant difference (P>0.05) and ****=P<0.0001.*

The control groups underwent a freeze-thaw cycle, which was not involved in the drying groups. The effect of a freeze-thaw cycle on the activity was tested (**Figure 4.9** *(c)*). With the formulation of 1 M trehalose and 10%w/v dextran, 89.87% of initial LDH activity was retained after one freeze-thaw cycle at -80 °C, while 87.79% was preserved at -20 °C. There was no significant statistical difference between those two groups. Consequently, MART drying could preserve around 86.69% of initial LDH activity after 6-month storage at room temperature.

Therefore, this Matrix Assisted Room Temperature drying (MART drying) technique can thermostabilise LDH in the solid state for at least six months at room temperature and get rid of the cold chain during storage and transportation.

4.4 Conclusions

This chapter applied an inexpensive and biocompatible cellulose fibre membrane to support Matrix Assisted Room Temperature (MART) drying of lactate dehydrogenase (LDH). The activity of MART dried LDH was retained after 6-month room temperature storage by using trehalose and dextran as stabilisers.

The protective function of sugar increased with the increase of trehalose concentration. It reached a plateau at around 500 mM. The addition of dextran further improved the protective function and increased the glass transition temperature. However, stress relaxation was detected after 1-week storage at 40 °C. The activity of LDH was considerably reduced.

The stress relaxation was inhibited when the trehalose concentration was doubled to 1000 mM while keeping the dextran concentration of 10% w/v. After storing at 40 °C for one week, MART dried LDH could maintain over 80% of the initial activity. In addition, the glass transition temperature was higher than 70 °C.

The stability of LDH dried on fibre matrix was higher than LDH dried on a hydrophilic surface. The fibres formed capillary bridge structures within the fibre matrix, which could gather and stabilise bioproducts in solid glassy sugar films.

Sugar films were also detected in different thicknesses of fibre matrix, resulting in the similar retained activity of LDH after one-week storage at 40 °C.

The effectiveness of preservation was tested with different drying conditions. The retained activity of LDH was not affected by varying drying temperatures. However, the higher retained activity of the enzyme was found after drying with lower relative humidity and longer drying time. It was found that 30 °C and 3% RH for 18 hours could be a suitable set of operational parameters for LDH MART drying. LDH dried on fibre matrix with the above conditions could preserve around 86.69% of initial LDH activity after 6-month storage at room temperature.

In conclusion, Matrix Assisted Room Temperature (MART) drying is a simple and cost-effective method for long-term protein preservation. Unlike freeze-drying and many other drying techniques, the process is not energy-intense as it does not rely on refrigeration or vacuum conditions. During the process, sample temperature, or wet-bulb temperature, was consistently above 0 °C, eliminating the risk of freeze damage to protein. Moreover, the softness of the membrane allows it to be compressed into any shape, which potentially extends its applications.

Chapter 5

Novel Drying of Fibroblast Growth Factor 2 (FGF-2) Evaluated with Immortalized Mesenchymal Stem Cells (MSC-hTERT) Proliferation

MART drying using cellulose fibre matrix with different drying parameters was studied in the last chapter. MART drying is further studied by applying BSA coating to reduce the non-specific binding and the feasibility of combining vacuum with MART drying, i.e. drying under vacuum state (Matrix Assisted Room Temperature Vacuum drying, or MART-V drying). Fibroblast growth factor 2 (FGF-2) is formulated and stabilised by MART and MART-V drying. Any functionality loss of FGF-2 after drying and storage is analysed by the proliferation assay of immortalised mesenchymal stem cells (MSC-hTERT), compared to the conventional storage condition, -80 °C storage.

This chapter is based on the paper:

Yu, Y., Dai, S., Cui, Z. Novel Drying of Fibroblast Growth Factor 2 (FGF-2) and Evaluated with Immortalized Human Mesenchymal Stem Cells (hMSC) Proliferation, to be submitted.

As the main author, Y Yu's contribution to this paper is designing and experimenting, collecting and analyzing data, deriving conclusions and drafting the paper.

TABLE OF CONTENTS

5.1 Introduction 106

5.2 Material and Methods 109

5.2.1 Materials 109
5.2.2 Fibre Matrix Preparations 109
5.2.3 Excipients Preparations 109
5.2.4 Protein Adsorption Analysis 110
5.2.5 Effect of LDH Activity with BSA 111
5.2.6 Determination of LDH Activity 111
5.2.7 Matrix Assisted Room Temperature Drying 112
5.2.7.1 Matrix Assisted Room Temperature Vacuum (MART-V) Drying 112
5.2.7.2 Normal Matrix Assisted Room Temperature (MART) Drying 112
5.2.8 Determination of Moisture Content 113
5.2.9 Scanning Electron Microscopic Imaging 114
5.2.10 FGF-2 Formulation and Stabilization 114
5.2.11 Cultivation of Immortalized Mesenchymal Stem Cells 115
5.2.12 MSC-hTERT Propagation and Fibre Matrix Biocompatibility 116
5.2.13 Statistical Analysis 117

5.3 Results and Discussion 117

5.3.1 Protein Adsorption Resolution 117
5.3.2 Feasibility Test of MART-V Drying 119
5.3.3 FGF-2 Thermostabilisation by Matrix Assisted Drying 121

5.4 Conclusions 125

5.1 Introduction

Fibroblast growth factors are a family of protein mitogens regulating cell proliferation, differentiation and migration[387,388]. Among this family, fibroblast growth factor 2 (FGF-2), or basic fibroblast growth factor, is commonly found in wound fluids, especially at the earliest stage[389–393]. The expression of FGF-2 was highest at the centre of the wound and progressively decreased toward the periphery[392]. In wounds, FGF-2 stimulated the proliferation and differentiation of cells and their derivates, including fibroblast, endothelial cell and derivates of mesodermal and neuroectodermal, and participated in the early activation of macrophages, augmenting the secretion of extracellular matrix components, angiogenesis and reepithelialisation[389,394–397].

FGF-2 was a therapeutic agent for repairing damaged tissue and has been widely studied in clinical trials. The use of FGF-2 spray or FGF-2 soaked gauze could considerably reduce the healing time of burns, donor sites, chronic wounds, sutured wounds after surgery and aphthous ulcers[398].

However, the FGF-2 solution was unstable at ambient temperature. The efficacy of FGF-2 could be significantly reduced after one day at room temperature. Therefore, FGF-2 was recommended to be stored at -20 °C for long-term storage. The shelf life of the FGF-2 solution was around one week as the storage temperature was 4 °C[399,400].

Lyophilization, or freeze-drying, was applied to produce commercial FGF-2 powder, which possesses a longer shelf life. FGF-2 was formulated with cryoprotectants, such as human serum albumin, mannitol, polyethene glycol or glucose, to maintain stability. However, the stresses raised from freezing, temperature ramps, vacuum and drying could potentially change the structure of FGF-2 and cause aggregation, reducing the potency of final products[400,401].

In our previous work, Matrix Assisted Room Temperature (MART) drying was established as an alternative drying strategy to stabilise protein at room temperature or elevated temperature (30 °C), which did not require refrigeration and vacuum. However, the protein was unavoidably absorbed on the fibre matrix. Proteins of low concentration could be absorbed entirely on fibre matrix and not be released after reconstitution. In the meantime, the efficiency of the cold well was

insufficient. More than 10 hours of drying was required to stabilise LDH throughout the storage.

In this work, bovine serum albumin (BSA) was coated on the same fibre matrix to minimise non-specific adsorption. BSA coating passivate surfaces and reduce the non-specific adsorption[402]. Therefore, BSA coating was widely used in antifouling applications[403–405] and biological assays, such as enzyme-linked immunosorbent assays (ELISA)[406] and western blot[407].

Furthermore, we developed another MART drying, which dry formulated bioproduct on fibre matrix at room temperature under vacuum. We call this alternative MART drying as the Matrix Assisted Room Temperature Vacuum (MART-V) drying, which could significantly shorten the drying time. The feasibility of MART-V drying was firstly examined by stabilising the thermolabile enzyme, lactate dehydrogenase (LDH).

After knowing the feasibility, formulated FGF-2 was thermostabilised on cellulose fibre matrix by regular MART drying and MART-V drying. Based on the previous studies[408,409], 100 ng/ml FGF-2 could significantly increase the proliferation of Mesenchymal Stem Cells. To emphasise the efficacy of FGF-2 on cell proliferation, cells were cultured in a medium with low nutrition. After 1-week storage at 40 °C, the effectiveness of FGF-2 was investigated by the proliferation of Immortalised Mesenchymal Stem Cells (MSC-hTERT), which did not reduce growth and proliferation due to the ageing in vitro[410].

5.2 Material and Methods

5.2.1 Materials

Animal-Free Recombinant Human FGF-Basic (AF-100-18C) was purchased from PeproTech. Bovine serum albumin (A9647), L-Lactate dehydrogenase (101278760001), D-(+)-trehalose dihydrate (90210) and dextran with M_r~ 40,000 (31389) were obtained from Sigma-Aldrich, UK. Sterile cellulose fibre membranes were got from Merlin Medical, UK.

Phosphate buffered saline (PBS) of pH=7.4 was purchased from Thermo Fisher, UK. Dulbecco's Modified Eagle Medium with 1 g/l glucose (Gibco™), Insulin-Transferrin-Selenium-Ethanolamine (ITS-X) (Gibco™) and fetal bovine serum (Gibco) were purchased ThermoFisher Scientific, UK.

5.2.2 Fibre Matrix Preparations

A large fibre membrane was randomly torn into small pieces. 20 mg of torn fibre matrix was placed in each well of a 48-well plate and compressed into a disc with a uniform thickness of 0.8 mm. This process ensured that all the fibre matrices applied in the experiments had similar mass (approximately 20 mg) and dimensions. The compressed fibre matrices were then carefully taken out of the well and placed onto a flat plate.

5.2.3 Excipients Preparations

Bovine Serum Albumin (BSA) solution with the concentration of 10 mg/ml was prepared as an excipient by dissolving 0.20 g BSA into 20 ml PBS solution and

filtered by a 0.22 µm syringe filter (Millex, Sigma-Aldrich). The prepared solution was stored at 4 ℃ fridges and used up within 1 week.

For the sugar solution, 18.92 g of D-(+)-trehalose dihydrate and 5 g of dextran was dissolved in MillQ water with the final volume of 30 ml. Heating is required for dissolution. The final sugar concentration was 1.66 M trehalose and 16.66%w/v of dextran and filtered by a 0.22 µm syringe filter. After aliquoting, sugar solutions were stored at 40 °C to avoid crystallisation.

5.2.4 Protein Adsorption Analysis

Since the amount of BSA added as excipient was much higher than desired bioproducts, the protein adsorption cannot be analysed by the protein concentration differences with QuantiPro Bicinchoninic Acid (BCA) assay. The activity of FGF-2 cannot be measured directly except for involving cell culture. Therefore, lactate dehydrogenase (L-LDH) with the same amount was used to replace FGF-2. To analyse the effectiveness of adding bovine serum albumin, the activity of LDH was measured within seven different samples. The formulation was 10 µl of 10 mg/ml BSA mixed with 10 µl of 100 µg/ml FGF-2 and 30 µl sugar solution. Since BSA and FGF-2 were dissolved in PBS, the control groups added PBS in the same amount. When sugar solution is involved, the final concentration of sugar was 1 M trehalose and 10%w/v dextran.

For the samples without fibre matrix, the solution was added into wells of 24 well-plate. For the sample with fibre matrix, the solution was added to the fibre matrix in the loading tube of centrifuge tube filters with 0.45 µm pore size(Thermo-fisher, UK). 2 ml water was added to the fibre matrix. After incubating at room temperature

for 5 minutes, the centrifuge tube filter, containing the loading tube and the collection tube, was centrifuged by Sigma 1-14 centrifuge (Sigma-Aldrich, UK) with 5,000 rpm for 10 min. The LDH activity of the solution in the collection tube was analysed. For the samples without fibre matrix, the LDH activity was measured after adding 2 ml water and mixing by pipetting.

5.2.5 Effect of LDH Activity with BSA

LDH solution (120 µg/ml) was mixed with BSA solution (2.5 mg/ml) to prepare the sample solutions, the amount of LDH of which are ranging from 0.4 µg to 1.2 µg. Then, 50 µl of those diluted solutions were added to the well plate. Then, the activities of LDH were measured. All the measurements were done in triplicate.

5.2.6 Determination of LDH Activity

LDH solutions on fibre matrix or in the tubes were first mixed with 2 ml MillQ water. For measuring the LDH activity in the collection tube of the centrifuge tube filter, this 2 ml MilliQ water was not needed. Then, 10X further dilution with MilliQ water was applied before measuring activity. The lactate dehydrogenase activity assay kit (MAK066) was used for this aim. Following the protocol provided by the manufacturer, 2 µl of each diluted sample solution was added into a 96-well plate (Corning, UK) and mixed with 48 µl LDH assay buffer. After adding 50 µl reaction mix, the plate was incubated at 37 °C for 2 min. The plate was then transferred to a plate reader. The absorbances were acquired every 1.5 min at 480 nm at 37 °C. The activity of LDH was calculated as follows,

$$LDH\ activity = \frac{Amont\ of\ NADH\ genretaed\ during\ the\ incubation}{incubation\ time\ \times\ sample\ volume\ added\ into\ well}$$

All measurements were performed in triplicate.

5.2.7 Matrix Assisted Room Temperature Drying

5.2.7.1 Matrix Assisted Room Temperature Vacuum (MART-V) Drying

After loading desired proteins, fibre matrices were transferred into lyophilisation vials and placed into drying bottles. Here, we used the freeze dryer only to create a vacuum condition. After attaching the drying bottles to the freeze dryer (Genesis, SP Scientific), the valve was turned 180 degrees to connect drying bottles to the drying chamber. Manually start the vacuum pump. After 3-hour drying, the drying bottles were isolated from the drying chamber by turning 90 degrees of the valves. The vacuum state in the drying chamber was released by importing ambient air. After the pressure in the drying chamber back to atmospheric pressure, the drying bottles were detached from the freeze dryer and placed into a glove box. After turning an additional 90 degrees in the same direction of the valves, the vacuum state in drying bottles was released by filling dry air. After closing the caps, the vials were sealed into moisture barrel bags and stored at incubators (25 °C or 40 °C). The control group, using the same formulation but without desired protein, was dried on fibre matrices with the same procedure and stored at the same condition. Each test was done in triplicate.

5.2.7.2 Normal Matrix Assisted Room Temperature (MART) Drying

The drying apparatus was switched on 2 hours before experimenting. The temperature and relative humidity of the drying apparatus was stabilised at 30 °C with relative humidity of 3%. Then, fibre matrices were loaded with desired proteins and placed on the sample station. After 18-hour drying, dried matrices were placed

into lyophilisation vials and sealed into moisture barrel bags in the glove box. Then, the bags were placed into incubators for 1 week. The same drying procedure was applied to the control group, using the same formulation but without desired protein on fibre matrices. The control group was stored in incubators (25 °C or 40 °C) for 1 week. Each test was done in triplicate.

5.2.8 Determination of Moisture Content

The moisture content of the dried matrix was estimated by the mass difference before and after burning the bioproduct-loaded fibre matrices. The masses of fibre matrices were recorded before loading formulated bioproduct (m_{fi}). After loading, the fibre matrices were desiccated in a low relative humidity environment, either by MART drying or MART-V drying. Then, each fibre matrix was transferred into one 1.5-ml Eppendorf tube, which recorded the previous mass (m_t). The total mass of tube and dried fibre matrix was recorded as (m_{fd}). Then, the tube containing fibre matrix was placed into a heat block with the cap open. The temperature of the heat block was 120 °C. After overnight burning, close the tubes' caps and measure the tube's final mass with fibre matrix (m_{final}).

Moreover, Fibre matrices without loading were also desiccated and burnt at the same condition. The mass difference was regarded as references, which R_1 was the mass change after drying and R_2 was the mass change after burning. The moisture content could be calculated as:

$$Moisture\ content = \frac{the\ mass\ of\ water\ lost\ during\ the\ burning}{the\ mass\ of\ dried\ product}$$

$$= \frac{m_{fd} - m_{final} - R_2}{m_{fd} - m_t - m_{fi} + R_1}$$

Eq. 5-1

5.2.9 Scanning Electron Microscopic Imaging

The dried fibre matrices with formulated bioproduct were imaged by Scanning electron microscopy. Fibre matrices were mounted onto aluminium mounts with conductive copper tape. After coating with gold, the fibre matrices were imaged by Zeiss Sigma 300 Field Emission Gun Scanning Electron Microscope (FEG-SEM) under vacuum with the accelerating voltage of 2 kV.

5.2.10 FGF-2 Formulation and Stabilization

The FGF-2 powder was spined down by centrifugation (Sigma 1-14 centrifuge, Sigma-Aldrich, UK) at 5,000 rpm for 10 min. Then, the powder was reconstituted by 1 mg/ml BSA solution in PBS. It was Inverted 20 times for mixing. The final concentration of FGF-2 solution was 50 µg/ml. After aliquoting, the FGF-2 solutions were stored at -80 °C.

The liquid formulation was used as a control group, which was consisted of 30 µl sugar solution, 10 µl FGF-2 solutions and 10 µl BSA solution. After mixing by pipetting, the liquid formulation was stored at -80 °C for one week. The solution with the same formulation but added 10 µl PBS instead of FGF-2 was stored at -80 °C for one week. All experiments were done in triplicate.

For the drying formulation, 20 µl of the sugar solution was first evenly dripped onto the compressed fibre matrix. Then, 10 µl BSA solution was added to the same position. After the solution was absorbed by the matrix, 10 µl FGF-2 was dripped on the same position before adding the final 10 µl sugar solution. The same procedure was applied to the drying control group but using 10 µl PBS instead of FGF-2 solution. Two different drying methods, Matrix Assisted Room Temperature Vacuum (MART-V) Drying and Matrix Assisted Room Temperature (MART) Drying, were used for stabilising FGF-2 loaded fibre matrices with the drying control group. The drying procedure was mentioned above.

5.2.11 Cultivation of Immortalized Mesenchymal Stem Cells

Human bone marrow mesenchymal stem cells transduced with telomerase reverse transcriptase (MSC-hTERT) were cultured for seven days for cellular experiments. The cells were seeded in tissue culture-treated T-25 flasks (Falcon, UK) and 96-well plates at a seeding density of 5000 cells/cm^2 with low glucose DMEM (Gibco, UK) supplemented with 1% fetal bovine serum (Gibco, UK) and 1% ITS -X (Gibco, UK).

MART-V dried, MART dried and -20 °C freezer stored FGF-2 samples were mixed with the media to prepare experimental media containing 100 ng/ml FGF-2 (concentration before preservation). Control group experimental media were prepared in the same way without FGF-2. Medium change was performed on the day after seeding and then every other day to introduce FGF-2 to the cells cultured in 96-well plates. A nitrocellulose fibre matrix was carefully added to cultures in T-

25 flasks without disturbing the cells on the day after seeding. Control group cells were cultured without the fibre matrix. Medium change was performed every other day.

5.2.12 MSC-hTERT Propagation and Fibre Matrix Biocompatibility

Proliferation rates of MSC-hTERT cells cultured with different experimental media were assessed with Cell Counting Kit-8 (CCK-8) purchased from Dojindo, UK. The manufacturer provides a detailed protocol for the assay. Briefly, for each well of a 96-well plate, 10 µl of the assay reagent was added to 100 µl culture medium, followed by incubation at 37 °C for two hours. During incubation, the assay reagent reacts with live cells to produce formazan dye, which absorbs light at 450 nm wavelengths. The plate was then read for light absorbance at 450 nm with a SpectraMax i3x plate reader (Molecular Devices, UK). A standard calibration curve was plotted for optical density against live cell count. The assay was performed on day 1 (the day after seeding), day 3, day 5 and day 7 to determine the proliferation rates of the different cultures.

The propagation of MSC-hTERT was analysed by Normalized Cell Count (NCC) and Cell Population Doubling Level (PDL). The cell number was normalised by dividing the respective cell number determined at Day1. Cell Population Doubling Level refers to the times of the population of cells have been doubled, which was calculated as follows:

$$PDL = \frac{log(Cell\ population\ of\ Day\ n) - log\ (Cell\ population\ of\ Day\ 1)}{log\ (2)}$$

Eq. 5-2

Sterile cellulose fibre matrix was carefully added to cells cultured in T-25 flasks. The cells were observed every other day. Images were captured with a Nikon Eclipse Ti widefield fluorescent microscope and adjusted for contrast with NIS Elements AR software (Nikon, UK).

5.2.13 Statistical Analysis

The statistical differences between groups at various time points were analysed by analysis of variance (ANOVA). The P values between groups that were less than 0.05 were considered as a significant difference. The statistical analysis was performed with GraphPad Prism 6.0.

5.3 Results and Discussion

5.3.1 Protein Adsorption Resolution

Protein adsorption on fibre matrix was resolved by coating BSA on fibre matrix before adding excipients. No LDH activity was detected for the excipients, sugar or BSA (Sample 1 in ***Figure 5.1*** *(a)*). However, even without a fibre matrix, LDH could be absorbed on the well plate and lost activity (Sample 2). Adding BSA and sugar could significantly decrease the adsorption and restore the initial LDH activity (Sample 4). Since the addition of sugar only slightly increased the activity (Sample 3), BSA played a key role to protect LDH from adsorption. Based on the serial dilution of LDH with BSA (***Figure 5.1*** *(b)*), the intersection point of the regression line with the x-axis was the absorbed amount of LDH in this scenario. In this case, only 0.02 µg of LDH was absorbed with the addition of BSA. In other words, the

addition of BSA in high concentrations was preserved on almost all the LDH added into the well plate.

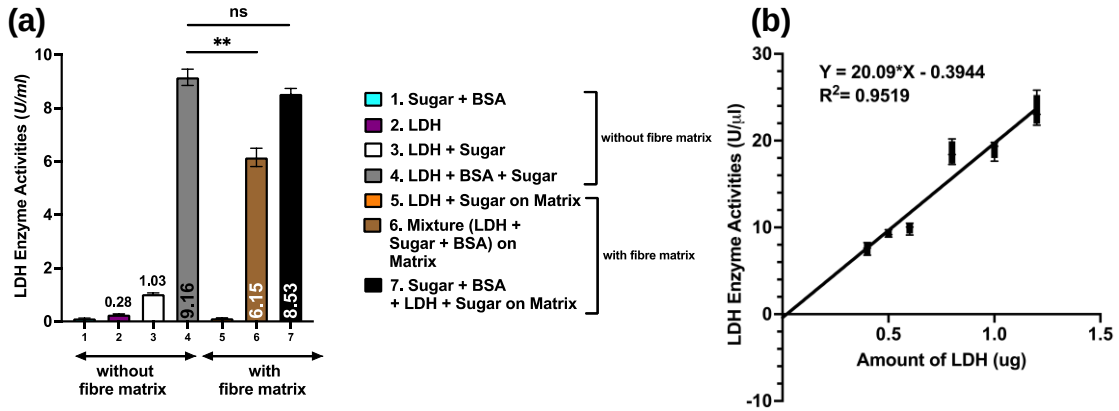


***Figure 5.1**: (a)The LDH activity with different excipients without and with fibre matrix (Sample1-7). The first four samples were added to the well plate before adding water. The last three samples were added to the fibre matrix in the well plate before adding water. Sample 1: The sugar solution was mixed with BSA. Sample 2: The LDH solution. Sample 3: The LDH solution was mixed with sugar. Sample 4: The LDH solution was mixed with sugar and BSA. Sample 5: LDH solution was mixed with the sugar solution and dripped on the fibre matrix. Sample 6: The LDH solution was mixed with sugar and BSA and dripped on the fibre matrix. Sample 7: First, a half volume of the sugar solution was dripped on the fibre matrix. Then, the BSA solution was dripped, followed by adding LDH. Finally, the other half volume of the sugar solution was added. The results presented in Mean±SEM, n=3 ns=no significant difference (P>0.05), **=P<0.01. (b)The relationship between the amount of LDH and the LDH activity. BSA with high concentration was added as an excipient.*

When LDH was formulated with sugar only and added to the fibre matrix, no LDH activity was detected after release (Sample 5), following the previous results in MART drying. LDH was absorbed on the fibre matrix. Although mixing LDH with BSA before dripping to fibre matrix could reduce the adsorption, the activity of the released solution was still much lower compared to Sample 4. Nevertheless, coating BSA on fibre matrix before adding desired proteins could maintain the protein activity, which was not significantly different with Sample 4. Sugar was

added first to protect BSA from degradation over the drying. Therefore, coating the fibre matrix with BSA before adding desired proteins could reduce the non-specific binding and preserve the effectiveness of desired proteins.

5.3.2 Feasibility Test of MART-V Drying

Since negative pressure may cause liquid bubbling and freezing if pressure drops too quickly, the stresses generated by those conditions could degrade the bioproducts and lose their effectiveness. Therefore, the feasibility of using MART-V drying to preserve bioproduct was investigated. Thermolabile protein, LDH, which is also sensitive to freezing, was used as a model protein.

In MART-V drying, fibre matrices could be placed into lyophilisation vials before drying (***Figure 5.2*** *(a)*). Moreover, the caps of lyophilisation vials also could be automatically pressed by typical freeze dryers after releasing the vacuum by importing nitrogen gas. This process was much more straightforward than MART drying. In MART drying, a bioproduct-loaded fibre matrix needed to be collected and transferred into vials after drying. The fibre matrix should be exposed to circulated dry air to ensure drying efficiency.

Since residual moisture content affects the glass transition temperature[234,411,412], this suggests the storage temperature[273]. Therefore, the relationship of MART-V drying time with residual moisture content was studied. The residual moisture content of MART dried fibre matrices with formulated bioproducts after 18-hour drying was around 4.8% of the dried mass (***Figure 5.2*** *(b)*). Owing to much more significant vapour pressure differences, MART-V drying only needed 3 hours to

reach a similar moisture content. Although the involvement of the vacuum pump increased the energy intensity of the drying process, the significantly shortened drying period indeed improved the cost-effectiveness of MART-V drying.

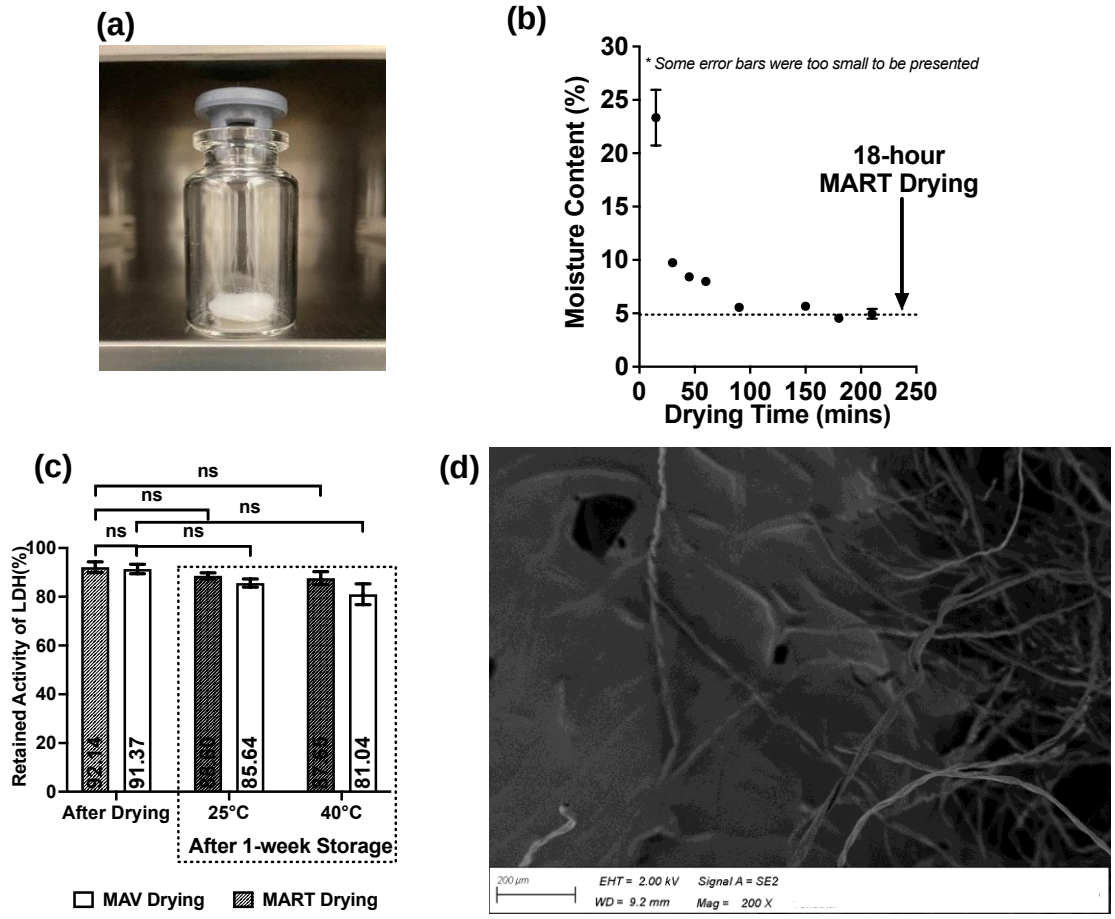


***Figure 5.2**: (a) The presentation of stabilising bioproducts by Matrix Assisted Room Temperature Vacuum drying. After loading bioproducts, the fibre matrices were transferred into lyophilisation vials and desiccated in the freeze dryer. (b) The relationship of the MART-V drying period against the residual moisture content of the final product. (c) The retained activities of dried LDH, which was stabilised by MART drying and MART-V drying. The measurements were conducted after drying and after one week of storage at 40°C. The results were presented as a Mean ±SEM. n=3, ns=no significant difference(P>0.05). (d)The scanning electron microscopy image of formulated LDH on cellulose fibre matrix after MART-V drying. The left part of the figure showed the sugar films deposited on the membrane, while the right part was the fibre matrix without sugar film.*

As mentioned above, reducing the ambient pressure by vacuum pump may lead to liquid bubbling, like vacuum foam drying. The stresses generated by bubbling could

denature proteins. Therefore, the retained activity of LDH after MART-V drying was measured and compared with MART drying. As presented in ***Figure 5.2*** *(c)*, MART-V drying could preserve approximately 91.37% of initial LDH activity after drying, which was not significantly different from MART drying (92.14%).

After 1-week of storage, the activity of MART-V dried LDH was retained over 80% for both storage temperatures, 85.64% for 25 °C and 81.04% for 40 °C, respectively, which there was no statistical difference with MART drying. Therefore, thermostabilised LDH by MART-V drying could be stored at 40°C for at least one week.

The dried morphology of the final product was also detected by scanning electron microscopy (SEM). As shown in ***Figure 5.2*** *(d)*, sugar films were spanned among fibres, which required the formation of capillary bridges before drying. Due to the shape of the capillary bridge and the property of trehalose, bioproducts could be gathered by the Marangoni effect and stabilised in glassy sugar film after drying[263]. The flat and smooth surface of the sugar film implied that the bubbling was inhibited.

5.3.3 FGF-2 Thermostabilisation by MART and MART-V Drying

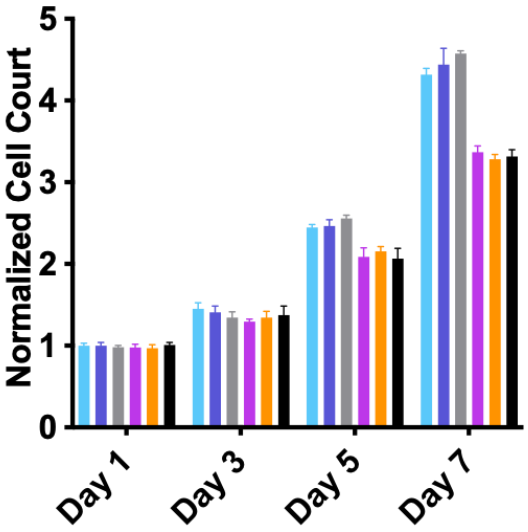
Formulated FGF-2 was stabilised on fibre matrices by MART-V drying and MART drying. Following 1-week storage at 40 °C, the efficacies of thermostabilised FGF-2 in solid-state was investigated by the proliferation of Immortalized Mesenchymal Stem Cells (MSC-hTERT). FGF-2 in frozen state at -80 °C, the standard storage condition, was applied as the control group.

Figure 5.3(a) showed the proliferation of MSC-hTERT, which was accessed by the CCK-8 assay. With the reference of cell number on day 1, the proliferation of cells in various culture media was normalised. It could be seen that the proliferation of MSC-hTERT with FGF-2 was significantly increased compared to the samples without FGF-2. The cell numbers of the samples A-C, which were with FGF-2, were increased more than 4 times by Day 1. In contrast, the cell number in the control samples(D-E) without FGF-2 was only increased around 3 times.

Within the samples with FGF-2, the reconstituted FGF-2 from MART drying and MART-V drying were improved by the proliferation of MSC-hTERT at the same level as FGF-2 in the frozen state, which did not have significant differences in statistics.

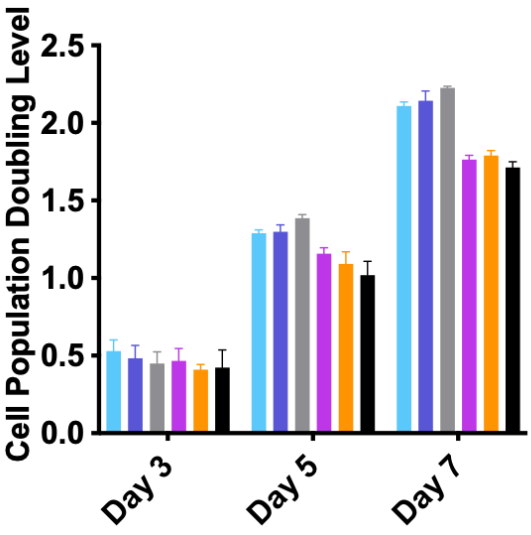
The same trend was also found in Cell Doubling Level. Cell cultured with FGF-2 (Sample A-C) was doubled more than 2 times within seven days while only 1.5 times for control samples (Sample D-E). Meanwhile, there was no significant difference between the samples with FGF-2. Therefore, MART drying and MART-V drying could stabilise FGF-2 for one week at 40°C.

(a)



	A. FGF-2 (MAV)	B. FGF-2 (MART)	C. FGF-2 (-80°C)	D. Control (MAV)	E. Control (MART)	F. Control (-80°C)
A. FGF-2 (MAV)		NS	NS	****	****	****
B. FGF-2 (MART)			NS	****	****	****
C. FGF-2 (-80°C)				****	****	****
D. Control (MAV)					NS	NS
E. Control (MART)						NS
F. Control (-80°C)						

(b)



	A. FGF-2 (MAV)	B. FGF-2 (MART)	C. FGF-2 (-80°C)	D. Control (MAV)	E. Control (MART)	F. Control (-80°C)
A. FGF-2 (MAV)		NS	NS	**	*	***
B. FGF-2 (MART)			NS	**	*	***
C. FGF-2 (-80°C)				***	**	****
D. Control (MAV)					NS	NS
E. Control (MART)						NS
F. Control (-80°C)						

Figure 5.3: *CCK-8 assay on MSC-hTERT proliferation, presented in (a)normalized cell count and (b)cell population doubling level. Six different culture media, Sample A-E, shown in the table, were used to culture cells. The statistical relationships between samples were presented in the table next to the figure. The results in the bar chart were presented as Mean ±SEM. n=3, ns=no significant difference(P>0.05), *=P≤ 0.05, **=P≤ 0.01, ***=P≤ 0.001, ****=P≤ 0.0001.*

Since the freeze dryer was not aseptic, FGF-2 loaded fibre matrices cannot be put directly into the cell culture flask. To assess the potential of applying FGF-2 loaded fibre matrix into cell culture, the biocompatibility of fibre matrix was analysed with MSC-hTERT cell line. As presented in ***Figure 5.4***, the addition of fibre matrices did not change the morphology of the cells. In the meantime, the cell growth and cell density were not affected by the addition of fibre matrix. Therefore, this cellulose fibre matrix is biocompatible.

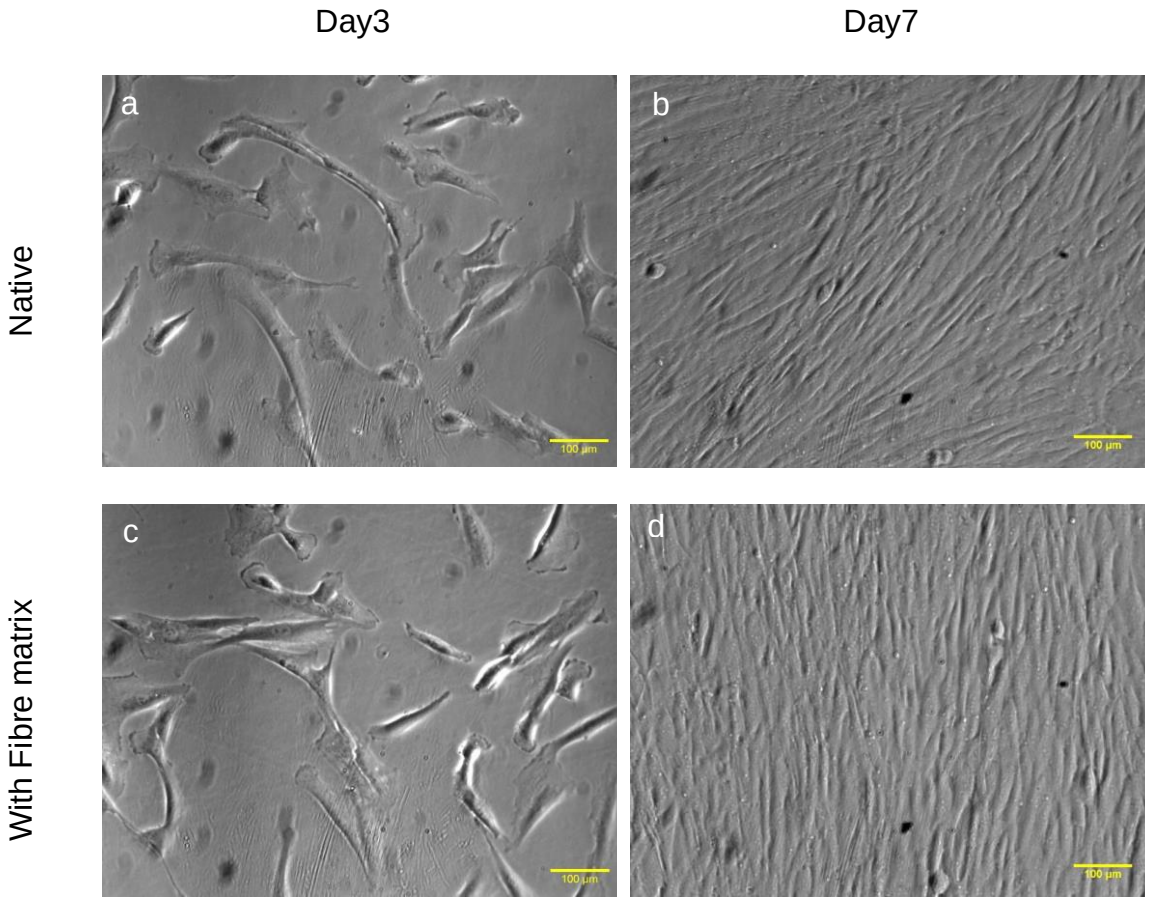


Figure 5.4*: The morphology of cells after culturing three days without (a) and with (c) fibre matrix. The morphology of cells after culturing seven days without(b) and with fibre matrix(d). The scale bar showed a length of 100 µm.*

If the whole process is processed in an aseptic condition, the stabilised bioproduct could be used directly to cell cultivation or even to humans as the materials are all

biocompatible. Since bioproducts were supported by fibre matrix, the handling could be much easier than the lyophilised powder. Bioproducts loaded with fibre matrix could be applied to cell cultivation directly, which do not require reconstitution before application.

5.4 Conclusions

In this work, coating BSA on the fibre matrix before adding desired proteins was proved as an effective method to minimise the non-specific binding. The functionality of preserved protein on the cellulose fibre matrix was maintained. The application of both MART drying and MART-V drying were demonstrated and can be extended to stabilise proteins at low concentrations.

Meanwhile, the feasibility of MART-V drying was investigated by LDH. With the assistance of the vacuum pump, drying 50 µl formulated bioproducts on fibre matrix only required 3 hours. The activities of LDH after MART-V drying was not significantly different from MART drying. Then, FGF-2 was thermostabilised on a biocompatible cellulose fibre matrix by both MART drying and MART-V drying. After one-week storage at 40 °C, the reconstituted FGF-2 increased the proliferation of MSC-hTERT to the same extent as frozen FGF-2 at -80 °C.

We developed two alternative drying strategies for stabilising FGF-2. The effectiveness of solidified FGF-2 could be preserved at least for one week at 40 °C. Moreover, since materials were all biocompatible, FGF-2 loaded fibre matrix could be applied to the wound directly if manufactured in aseptic conditions.

Chapter 6

Formulation and Vacuum-Spin Drying of RT-LAMP Reagents for Rapid Detection of SARS-CoV-2

In this chapter, Enzymes and other reagents in a rapid COVID-19 detection kit have been stabilised by a novel drying strategy, Vaccum-Spin drying (VSD). In chapters 4 and 5, proteins were stabilised on fibre matrix by MART drying and MART-V drying to extend the shelf life. However, the addition of fibre matrix into PCR tube increases the difficulty of reading results, either in colorimetric or florescent. Therefore, another drying strategy, vacuum-spin drying, is introduced. Formulated enzymes are stabilised under vacuum with the assistance of centrifugation to control the foaming. The stabilization of dried enzymes and reagents in the test kit is achieved, which can be stored and transported at ambient temperature without the need for the cold chain.

This chapter is based on the paper:

Yu, Y., Dai, S., Hsu, C., Lim, B., Ratcliff, J., Ren, S., Huang WE., Cui, Z., Vacuum-Spin Drying of RT-LAMP Reagents for Rapid Detection of SARS-Cov-2, to be submitted.

As the main author, Y Yu's contribution to this paper is designing and conducting the experiment, collecting and analyzing data, deriving conclusions and composing the paper.

TABLE OF CONTENTS

6.1 Introduction 127

6.2 Material and Methods 131

6.2.1 RT-LAMP SARS-CoV-2 Test Kit Formulation 131
6.2.2 Drying and Preservation of Test Kit 132
6.2.2.1 Vacuum-spin drying 132
6.2.2.2 Vacuum-foam drying 132
6.2.2.3 Freeze drying 133
6.2.3 RT-LAMP Reaction Setup 133
6.2.4 Detection of Nucleic Acid Amplification 134
6.2.5 Determination of Residual Moisture Content 135
6.2.6 pH Adjustment of Discoloured Kits 135
6.2.7 Sensitivity Test 136

6.3 Results and Discussion 136

6.3.1 The Comparison of Vacuum-Spin Drying and Vacuum-Foam Drying 136
6.3.2 Colorimetric Assay with Dried Test Kits 138
6.3.3 Fluorometric Assay for the Stability Test of Dried Test Kits 142
6.3.4 Stability of Lyophilized Kits 146
6.3.5 Sensitivity of Dried Kits 148

6.4 Conclusions 150

6.1 Introduction

Since the global outbreak of the COVID-19 pandemic, social distancing and lockdown were implemented in many cities, which expressively disturbed the living and working conditions of billions of people across the world[413–415]. At the same time, the spreading of coronavirus disease has critically challenged many healthcare systems[416–418]. One of the challenges of controlling the spreading is the identification of asymptomatic cases, which were still carrying the virus. Having effective, accurate, and rapid diagnostic methods for detecting SARS-CoV-2 could aid in eliminating this silent spreading and allow physicians to provide timely treatments to patients who are at high risk at an early stage[419,420].

Nucleic acid amplification for detecting viral RNA was considered a feasible and effective screening method. Real-time polymerase chain reaction (qPCR) is the standard laboratory method for detection with high sensitivity and reliability.

However, it requires a specific instrument and takes a relatively long processing time, around 2 hours, which lead to the limited capacity of detection[72].

To resolve this challenge, we developed a test kit[72] employing reverse transcription loop-mediated isothermal amplification (RT-LAMP)[421], a thermal polymerisation reaction, for SARS-CoV-2 RNA and was able to produce lengthened copies as DNA. The pre-mixed reagents include enzymes for the reverse transcription of viral RNA and the polymerisation of DNA, primers to initiate the polymerisation reaction, dNTP molecules to build up the length of the DNA, phenol red pH indicator and other chemicals to stabilise the mixture. When the viral RNA templates were added, the pH indicator in the test kit changed from pink to yellow, signalling the lengthening of the acidic RT-LAMP product.

Unlike real-time polymerase chain reaction (qPCR), RT-LAMP elongates nucleic acids at a constant temperature, commonly at 65 °C, and does not require thermal cycles[422]. Without the requirement of expensive equipment for quick thermal cycles, RT-LAMP testing can be conducted at the point of care or even at home. Furthermore, phenol red or other pH-sensitive dyes can be added to the reaction mix to visually report the amplification process, as the protons released during RT-LAMP reaction acidify the solution[423](**Figure 6.1**).

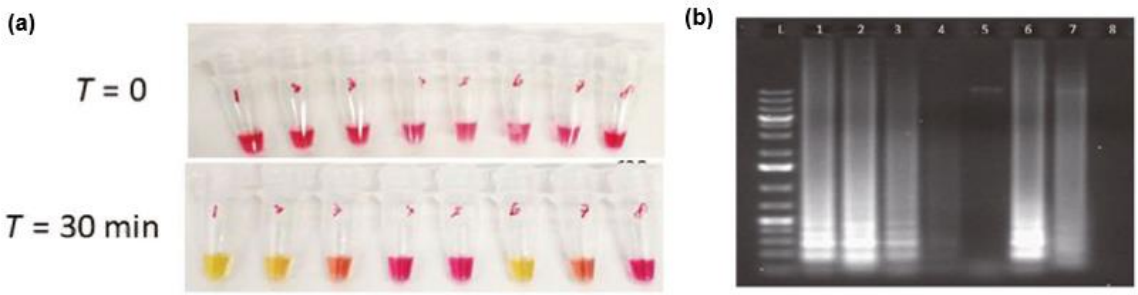


***Figure 6.1**: The colorimetric RT-LAMP assay developed Huang et al. [72]. (a)The upper figure showed the colour of reaction mixtures before RT-LAMP, while the lower figure presented the colour after the reaction. (b) Gel electrophoresis of (1) N15 primers + N gene RNA (200k copies); (2) N15 primers + N gene RNA (200 copies); (3) N15 primers + N gene RNA (20 copies); (4) N15 primers + N gene RNA (2 copies); (5) N15 primers + human genome; (6) human primers + human genome; (7) human primers + whole human RNA; (8) Colorimetric Master Mix Only;*

Although the advantage of RT-LAMP in COVID-19 testing, such as in the previous work reported by Huang *et al.* [72]., makes it applicable in underdeveloped regions, delivering the test kits may not be as easy. To minimize the degradation of the enzymes, the kits were recommended to be stored at low temperatures. Therefore, the cold chain is required to maintain the temperature, -20 °C, from the manufacture to the point of care, which potentially increase the cost of test kits.

By drying the reagents, they can be stored for much longer without losing enzymatic activity, so the test kits can be dispatched to further distances from the manufacturer at lower costs. Therefore, stabilising the proteins and other reagents, including dNTPs and salts, in the reaction mix is crucial for efficient transport and storage. Many preservation techniques for biomedical products include drying and storage at low temperatures. However, conventional drying strategies, such as freeze-drying and spray drying, can be too expensive for the intention to make COVID-19 testing more affordable and ubiquitous.

In Chapters 4 and 5, proteins were stabilised on cellulose fibre matrix by MART drying and MART-V drying. Although the non-specific binding could be minimized by BSA coating, the addition of fibre matrix had the difficulty of interpreting results, either by colorimetric or fluorescent.

Therefore, we put forward an alternative, low energy consumption drying strategy, Vacuum-spin drying, developed from Vacuum foaming drying (VFD). Vacuum foaming drying is a single-step drying technique that desiccates the boiling or foaming liquid formulation into a solidified foam structure near ambient temperature (15-25 °C) with reduced pressure. The performance of vacuum foaming drying was considerably related to pressure control. If the pressure drops too quickly, the solution is prone to freezing, leading to insufficient foaming. Nevertheless, foaming could also be insufficient if pressure is decreased too slowly. Moreover, the non-uniform morphology of dried foam structure was difficult for product characterization, reproduction and quality control and less acceptable for patients and health care workers[207,254,261].

In the meantime, betaine was formulated in the LAMP reagents[423] to improve DNA amplification[424]. However, betaine was a foaming agent, making the drying process more uncontrollable. Vacuum-spin drying used centrifugation to suppress the foaming of reagent and evaporate water under vacuum conditions. Since the drying temperature was maintained at room temperature or even higher, the evaporation rate was much higher than lyophilization. The drying time could be reduced.

Moreover, owing to the centrifugation, dried reagents were settled at the button of tubes, giving a uniform dried morphology. In this chapter, the impact of adding lyoprotectants on enzyme activity was studied. Then, the residual moisture contents of kits with different drying times were estimated. Meanwhile, the stability of kits with different drying times was studied.

6.2 Material and Methods

6.2.1 RT-LAMP SARS-CoV-2 Test Kit Formulation

All pipettes and laminar flow hood were wiped with 70% w/v ethanol (Sigma-Aldrich) and PCR clean (Cambio) before placing under UV lights for 1 hour. The regents were thawed and placed on ice to minimize the degradation. Since there were fewer mutations in the Orf1ab region, the O117 primer set was used. The sequences of O117 primers are listed in ***Table 6.1***.

Table 6.1: *Primer sequences for the detection of SARS-CoV-2.*

O117 Primer	Sequence (5'-3')
FIP	GGTTTTCAAGCCAGATTCATTATGGATGTCACAATTCAGAAGTAGGA
BIP	TCTTCGTAAGGGTGGTCGCAGCACACTTGTTATGGCAAC
F3	CCCCAAAATGCTGTTGTT
B3	TAGCACGTGGAACCCAAT
LF	TCGGCAAGACTATGCTCAGG
LB	TTGCCTTTGGAGGCTGTGT

Vacuum-Spin Drying and Vacuum Foam Drying

12.5 µl of Warmstart colorimetric master mix (New England Biolabs, UK) was mixed with 2.5 µl of 10X O117 primer mix and 4 µl drying protective agent, OSD-D1™ (Oxsed, UK) containing sucrose, lactose and trehalose. After mixing by vortex, the solution was added to a PCR tube. The prepared tubes were placed on ice.

Freeze Drying

12.5 µl of Warmstart colorimetric master mix was mixed with 2.5 µl of 10X O117 primer mix and 7.5 µl drying protective agent, OSD-D2™ (Oxsed, UK) containing sucrose, dextran, lactose, polyvinyl alcohol and trehalose. After mixing by vortex, the solution was added to a PCR tube. The prepared PCR tubes were placed on ice.

6.2.2 Drying and Preservation of Test Kit

6.2.2.1 Vacuum-spin drying

After formulation, PCR tubes with caps open were dried with a concentrator (Concentrator Plus, Eppendorf, UK) at 30 °C. After drying, the caps of PCR tubes were closed immediately, and the dried reaction mixes were stored at -20 °C. Different drying times were evaluated by the moisture content of the dried product and the activity of dried enzymes.

6.2.2.2 Vacuum-foam drying

After formulation, PCR tubes with caps open were placed into a freeze dryer (Genesis, SP Scientific, UK). The vacuum pump was manually turned on. The drying process was taken place at room temperature. After drying, ambient air was imported to break the vacuum. After the pressure of the drying chamber back to

atmospheric pressure, the PCR tubes were taken out and capped immediately. The dried products were stored at -20 °C.

6.2.2.3 Freeze drying

After aliquoting the formulated solution, PCR tubes with caps open were placed into a freeze dryer. The shelf temperature was reduced to -40 °C at the rate of 1 °C/min. After stabilising the reagent temperature at -40 °C, the vacuum pump was switched on to lower the chamber pressure, commencing water sublimation. After the sample temperature back to around -40 °C, the secondary drying was initiated. The shelf temperature was raised to 25 °C at the rate of 1 °C/min. The vacuum state was maintained for the secondary drying. After secondary drying, nitrogen gas was imported to break the vacuum. After the pressure returned to atmospheric pressure, the PCR tubes were taken out and capped immediately. The dried products were stored at -20 °C.

6.2.3 RT-LAMP Reaction Setup

For wet formulated reagents, 1 µl of RNase/DNase Free water and 5 µl of sample solution with either targeted RNA as positive control or human genome cDNA as negative control were added before reaction. Synthetic RNA Control 2 - MN908947.3 (Twist Bioscience, US) was used as the positive control.

Human genome cDNA was reverse transcribed from the whole RNA extracted from human bone marrow-derived MSC line (Lonza, UK), followed as previously described[425,426]. The QuantiTect Reverse Transcription kit (Qiagen, Manchester, UK) was used to reverse transcript RNA. The procedure followed the manufacturer's instructions, including a genomic DNA wipe-out step. The final

cDNA sample was diluted to 0.2 µg/ml in RNase/DNase free water and stored at -20 °C.

For dried formulation, 20 µl of RNase/DNase Free water and 5 µl of the sample solution containing either viral RNA or human genome cDNA were added before reaction. For the non-formulated control group, only 12.5 µl of Warmstart colorimetric master mix and 2.5 µl of 10X O117 Primer mix were added into the PCR tube. 5 µl of RNase/DNase Free water and 5 µl of sample solution with either targeted RNA or human genome were added before reaction. 1000 copies of viral RNA were added into each positive control.

6.2.4 Detection of Nucleic Acid Amplification

The amplification of nucleic acid could be detected by colorimetric and fluorescence. For detecting the growth of florescence over the amplification, SYTO9 green (Thermo Fisher, UK) was added into the reagent before heating as the final concentration of 0.5 µM per reaction. The fluorescence of SYTO9 was read by the FAM channel every 20 seconds in the qPCR machine (Qiagen, Rotor3000, UK).

Instead, the amplification also could be detected by the concentration of nucleic acid concentration after reactions. The Qubit dsDNA HS Assay kit (Invitrogen, UK) was used to do the measurement. 5 µl of reagent after the reaction was mixed with 195 µl buffer in the Qubit dsDNA HS Assay Kit and read by a Qubit 2.0 fluorometer (Thermo Fisher Scientific, UK).

6.2.5 Determination of Residual Moisture Content

The mass difference estimated the moisture content of dried mass before and after burning the dried mass. The masses of PCR tubes were recorded before loading formulated bioproduct (m_t). After loading reagents, PCR tubes were dried in a concentrator. After drying, the total mass of the tube and the dried product was recorded as (m_{dried}). Then, PCR tubes containing dried reagents were placed into a heat block with the cap open. The temperature of the heat block was set to 120 °C. After overnight burning, the mass of PCR tubes containing burnt reagent (m_{burnt}) was measured after capping. In the meantime, PCR tubes without loading were also dried and burnt at the same condition. The mass difference was regarded as references, which R_1 was the mass change after drying and R_2 was the mass change after burning. The moisture content could be calculated as:

$$Moisture\ content\ (\%) = \frac{the\ mass\ of\ water\ lost}{the\ mass\ of\ dried\ product} = \frac{m_{dried} - m_{final} - R_2}{m_{dried} - m_t + R_1}$$

6.2.6 pH Adjustment of Discoloured Kits

Discoloured kits were reconstituted by 20 µl RNase/DNase Free water. The solution was homogenised by pipetting. Then, 0.5 µl of 100 mM potassium hydroxide (KOH) was added each time and followed by mixing with pipetting. A fresh prepared wet kit was prepared as a colour reference. When the colour of discoloured kits changed to the same colour as the reference, water was added to bring the final volume to 24 µl. 1 µl of sample solution, which has targeted RNA or non-targeted RNA, was added before heating at 65 °C for 30 min.

6.2.7 Sensitivity Test

To estimate the analytic sensitivity, the 50% endpoint of the LAMP assay was evaluated with the Twist full-length SARS-CoV-2 transcripts. Different concentrations of viral RNA were added into the wet or reconstituted reagent. The concentration has five replicates. The LAMP assay was run as described above and assessed via colour change. The 50% endpoint was calculated using the Reed-Muench method.

6.3 Results and Discussion

6.3.1 Comparison of Vacuum-Spin Drying and Vacuum-Foam Drying

The reaction mixture was supplemented with drying protectants to maintain the enzyme stability over the drying process. Before drying, the effects of adding drying protectants on the colorimetric assay and the enzyme activity were evaluated. As shown in (**Figure 6.2** *(a)*), the addition of excipients kept pink colour for negative samples and turned to yellow when full-length COVID-19 viral RNA was added. Based on the fluorescence, the amplifications were only detected in positive controls and started around 10 min after heating, whether drying protectants were added or not (**Figure 6.2** *(b)*). Therefore, the addition of drying protectants did not affect the activities of enzymes in test kits.

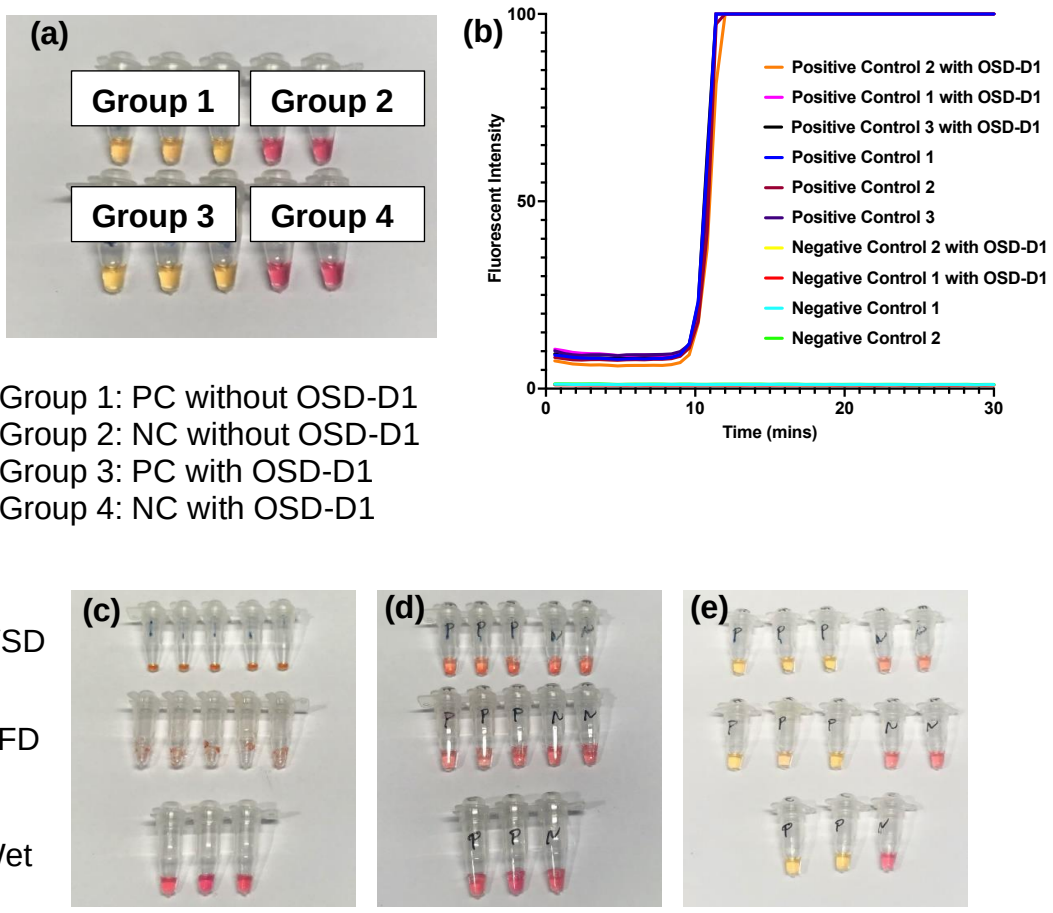


Figure 6.2: *(a)The colorimetric results for positive and negative samples with and without drying protectants. It implied that the addition of drying protectants did not affect the colourimetry of the test kits. PC: positive control. NC: negative control. (b) The fluorescence results of positive and negative samples with and without drying protectants. (c) The reagent mixtures were vacuum-spin dried (top row), or vacuum-foam dried (middle row) for 2.5 hours before (d) being reconstituted with RNase-free water to the same volume as the undried reagents (bottom row). NIBSC SARS-CoV-2 RNA standard and RNase-free water were added to the tubes marked with P (positive) and N (negative), respectively, before incubating the tubes at 65 °C for 30 min to allow RT-LAMP reactions to happen. (e) The colour of the negative samples did not change, while the initially pink contents in all of the positive tubes turned yellow, implying successful amplification of the genetic material.*

The same formulation was applied for Vacuum-Spin Drying (VSD) and Vacuum Foam Drying (VFD). The reagents, preserved by both drying methods, VFD and VSD, were able to amplify the viral RNA. However, the drying process of VFD was

quite uncontrollable. Reagents were easily erupted from tubes due to the foaming. One of the samples was frozen, which may reduce the kits' effectiveness due to the ice crystal (Figure A6 in Appendix 6). After drying, the dried morphologies of final products were not uniform, which could cause difficulty in quality control and reproduction. In contrast, the drying process of VSD was easy to control, and the dried morphologies were uniform.

6.3.2 Colorimetric Assay of VSD Test Kits

Since residual water content in dried bioproduct is usually a dominating factor for its stability over prolonged storage[427,428], the moisture content test kits were determined after different drying periods, from 0 to 15 hours (***Figure 6.3*** *(a)*). As the graph demonstrates, a decreasing relationship was found between the moisture content and the length of drying. The mixture of reagents started with around 85% water content (with the rest of the mass being the enzymes, primers, nucleotides and other molecules). It was reduced to only 9.1% and 6.7% water after 8-hour and 15-hour drying, respectively.

The potency of the dried kits was assessed by detecting viral RNA before and after storing at ambient conditions (25 °C with 30% relative humidity) for up to 31 days. Immediately after drying, the test kits retained their original pink colours after reconstitution, except for those that dried for 8 and 15 hours (***Figure 6.3*** *(b)*). However, all dried reagents were discoloured after 31-day storage at 25 °C (***Figure 6.3*** *(c)*). The samples were incubated at 65 °C for 30 min to allow the RT-LAMP reaction. Before prolonged storage, test kits dried for up to 5 hours were able to detect SARS-CoV-2 RNA with their pH indicator, as the positive samples turned

yellow and the negative samples stayed pink (***Figure 6.3*** *(f)*). However, all undried and dried test kits failed to report RT-LAMP reaction colourimetrically after 31 days of storage.

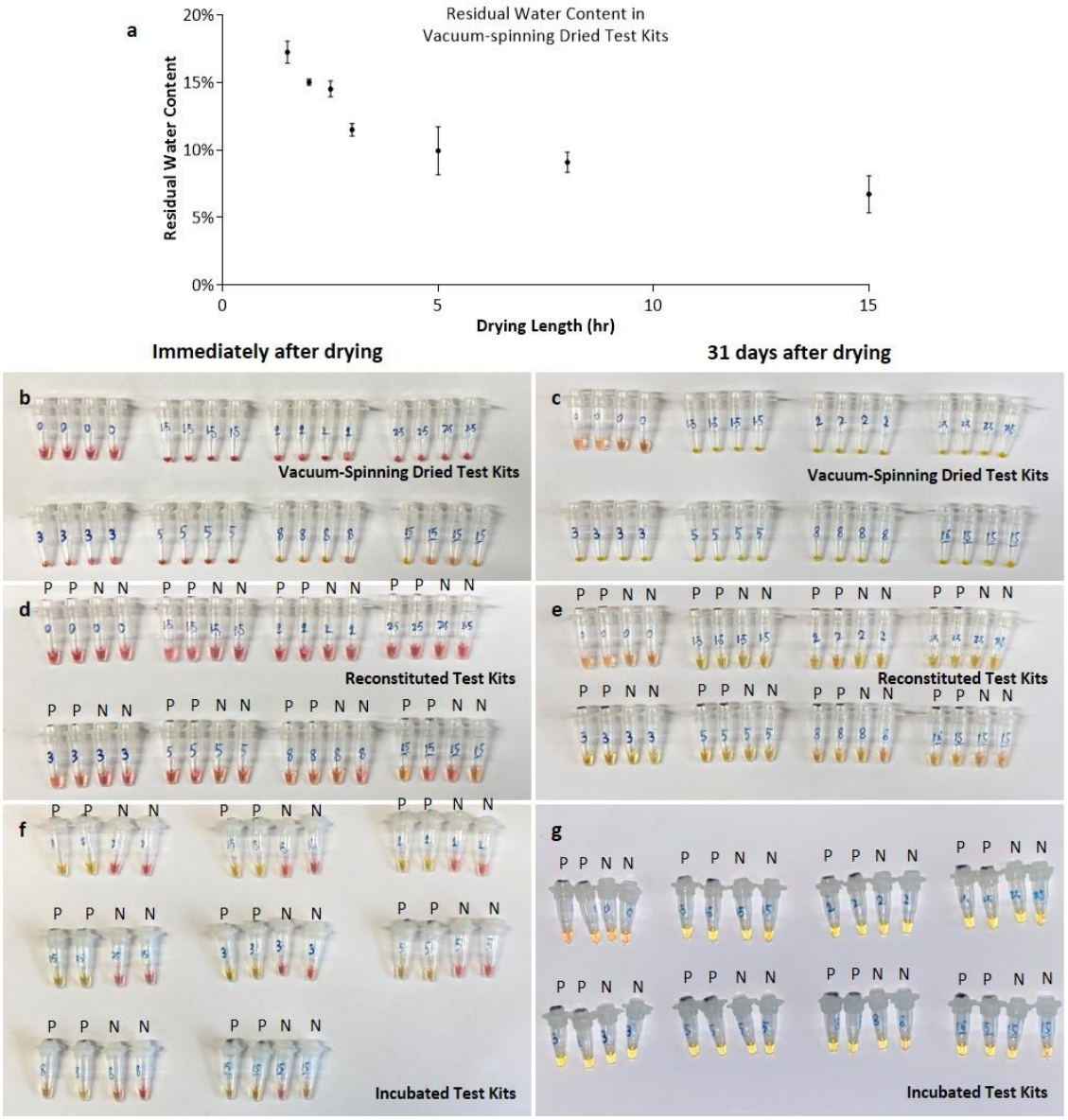


Figure 6.3: (a) *Residual water content in test kits vacuum-spin dried for 1.5 to 15 hours.* ***(b, c)*** *RT-LAMP COVID-19 test kits in solution form (undried, marked as 0-hour drying) and vacuum-spin dried for 1.5, 2, 2.5, 3, 5, 8 and 15 hours.* ***(d, e)*** *The dried test kits were reconstituted with RNase-free water to the same volume as the undried ones. SARS-CoV-2 RNA was added to the positive tubes, while RNase-free water was added to the negative tubes.* ***(f, g)*** *All tubes were incubated at 65°C for 30min to undergo RT-LAMP reactions. The photos illustrate experiments conducted* ***(b, d, f)*** *immediately after drying and* ***(c, e, g)*** *31 days after storing the dried test kits at 25 °C.*

RT-LAMP primers were prone to self-amplification[429,430], which could increase the acidity of the reagent. To investigate this hypothesis, reagent mixtures dried without primers for 15hr showed the same discolouring result as well (***Figure 6.4*** *(a)*). Furthermore, we dried complete test kits, with primers, for 15hr (***Figure 6.4*** *(b)*) and loaded them to a polyacrylamide gel for electrophoresis (***Figure 6.4*** *(c)*). The sole bands in lanes 1, 2 and 3 depict the presence of the primers, and no DNA with other sizes was found in the dried test kits. Therefore, the colour change prior to RT-LAMP incubation was not because of the self-polymerisation of the primers. The colours of reconstituted discoloured samples were kept as yellow (***Figure 6.4*** *(d), (e)*). However, after adding KOH solution, the colour of the sample was back to pink, which meant the functionality of the pH indicator, phenol red, was not affected by drying. Reagents were acidified through drying, leading to colour change.

The acidification might be caused by surfactant, Tween 20. Tween 20 could be degraded to free fatty acid. The degradation rate was increased by the growth of temperature and concentration[431–433]. Tween 20 was concentrated and accumulated at tube bottom during vacuum-spin drying at 30 °C. The high concentration and elevated temperature considerably increased the degradation rate.

Although the colour of the reagent was changed to yellow, the activity of enzymes in the kit was effectively preserved (***Figure 6.4*** *(g)*). After adjusting the pH by adding KOH, the colour of discoloured samples was changed back to pink. After

adding targeted or non-targeted RNA, kits were heated at 65 °C for 30 min. The colour of positive samples was changed to yellow, while negative samples were kept in pink.

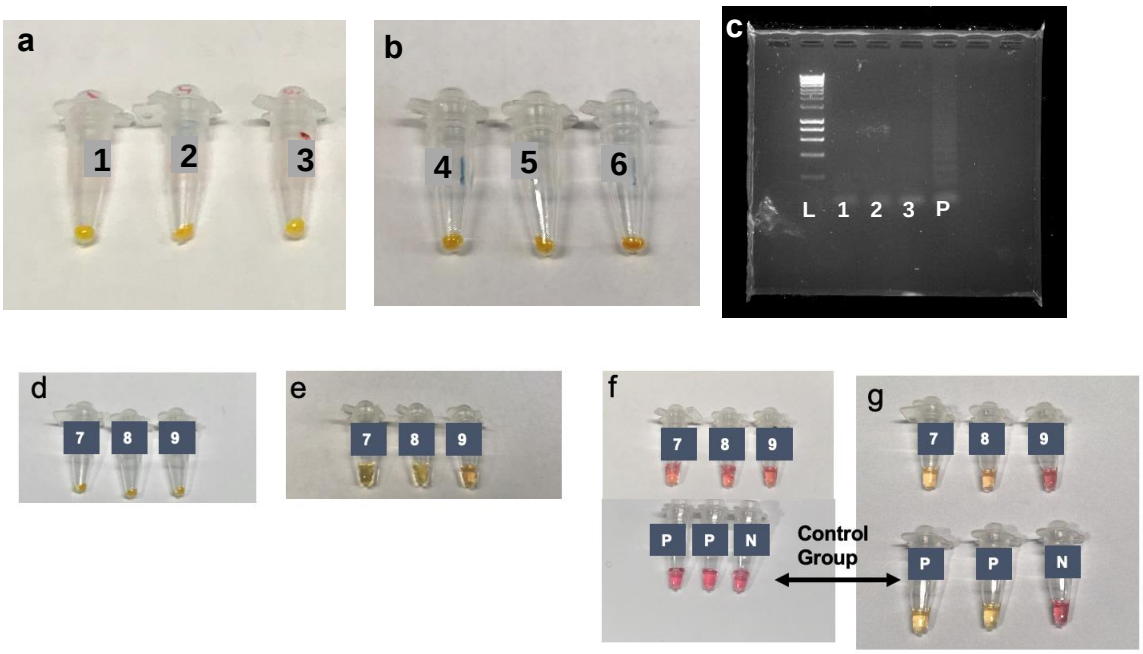


***Figure 6.4**: **(a)** Reagent mixtures prepared without primers turned yellow after vacuum-spin drying for 15 hours. It indicated that the reagents were acidified without the polymerisation of nucleic acid. **(b)** Test kits with primers turned yellow after 15-hour vacuum-spin drying. The reconstituted solutions were loaded to a polyacrylamide gel for electrophoresis **(c)**. The samples were compared against a DNA ladder on the left and a positive RT-LAMP product on the right. The primers were not found to have self-looped in the discoloured test kits. **(d)** Discoloured sample after drying. **(e)**The colour of the kits was maintained as yellow after reconstitution. **(f)**The pH of the kits can be adjusted by adding KOH. The colour of the adjusted reagents was changed to a similar colour to the original fresh mixes. The control group was prepared freshly. (**g**)The pH colour-corrected mixes can perform colorimetric detection of Synthetic RNA Control 2 - MN908947.3 (Twist Bioscience) at 200 copies in the final reaction solution. Sample 7 and 8: pH adjusted mixes with viral RNA. Sample 9: pH adjusted mix with human genome as the negative control. P: fresh reagents with viral RNA. N: fresh reagents with human genome as the negative control.*

Therefore, nuclear acid amplification was still occurring in the discoloured sample, which was not caused by non-specific amplification. After pH adjustment, the colour of the discoloured samples could be titrated back to pink and could turn to yellow in the presence of targeted RNA. In the meantime, the results could also be read out by fluorescence and DNA concentration after amplification.

6.3.3 Stability of VSD Test Kits

The previous results suggested that the pH indicator in the test kit may not produce a consistent result for the amplification of viral RNA. Fluorescent dye, SYTO 9, was used to determine the presence with higher repeatability since it emitted fluorescence only when specifically bound to DNA molecules[434–436].

With SYTO 9, we were able to plot the real-time fluorescence change in the positive and negative samples as we ran RT-LAMP reactions with a qPCR device at a constant 65 °C. Test kits were immediately reconstituted after drying and assessed for their efficiency in viral RNA detection (***Figure 6.5*** *(a)*). As expected, all positive samples had a growth in fluorescence, reaching 100% normalised fluorescence within 30 mins, and no sign of nucleic acid polymerisation was found in any negative samples. The undried test kits with viral RNA were the first to reach 100% normalised fluorescence, followed by the positive kits that had been dried for 1.5, 2, 2.5, 3, 5, 8 and 15 hours, respectively. It implies a decline in testing efficiency as the reagents were dried for longer. Nevertheless, the presence of viral RNA triggered RT-LAMP reaction in all positive samples.

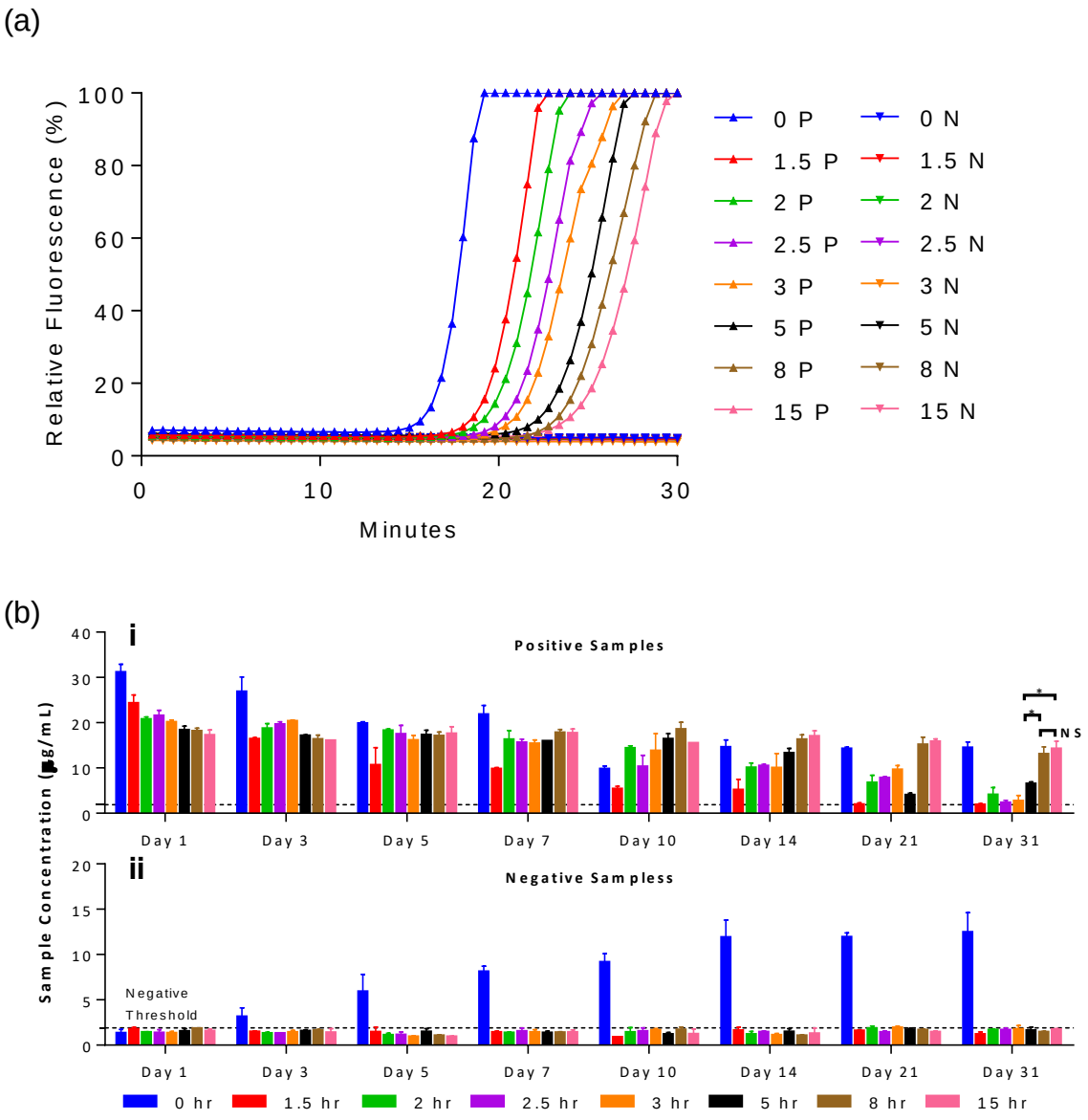


Figure 6.5: (a) Real-time fluorescence of SYTO 9-supplemented test kits run with positive and negative samples at 65°C with a qPCR machine. The legend indicates the number of hours of drying and whether positive (P) or negative (N) samples were prepared with the test kits. There was no thermal change during the experiment, and the time taken for 50 cycles was around 30 min. (b) RT-LAMP product concentration in the undried and dried test kits stored for up to 31 days after incubating with positive and negative samples at 65 °C for 30 min with a heat block. The negative threshold, represented as dashed lines, was defined as the mean plus standard deviation of the RT-LAMP product concentration in 16 undried test kits without storage after incubation with negative controls.

The concentrations of RT-LAMP products were determined with a Qubit assay kit to explore the effect of prolonged storage on the undried and dried test kits. The result of the test kits before storage (day 1) was consistent with that obtained in the real-time fluorescence experiment: the amount of RT-LAMP product produced in the positive samples within the 30 min incubation decreased with the length of drying (***Figure 6.5*** *(b)-i).*

The undried test kits became invalid after only three days of ambient storage. The amount of DNA produced in the negative control tubes after 30min incubation at 65 °C exceeded the threshold of 1.9 ug/ml (***Figure 6.5*** *(b)-ii*). The DNA concentrations in negative controls using undried kits increased over the storage and reached a plateau after two weeks. It suggests that the non-specific binding and amplification occurred during ambient storage.

With vacuum-spin drying applied, the test kits maintained their efficacy for as long as 31 days at ambient conditions. All dried test kits showed valid performance for negative controls throughout the storage. However, there was a severe deterioration in the activity of the 1.5-hour dried test kits, as the amount of DNA produced in RT-LAMP reactions became undetectable after two weeks of storage. It was improved by increasing the drying time to at least 5 hours. Our evidence demonstrates that test kits dried for 5-15 hours could produce detectable RT-LAMP products in positive samples. Moreover, 8hr and 15hr drying both exhibited statistically significant enhancement in the stability of the test kits after 31 days of storage.

Since initial clinic validation was processed in the UK domestically, the shipping time cannot be prolonged. 2.5-hour vacuum-spin drying was selected to stabilise kits, which could vastly decrease the processing time to reduce the cost and maintain the kits' effectiveness. In the meantime, the colorimetric assay was also retained after 5-day storage at room temperature (***Figure 6.6*** *(a-c)*).

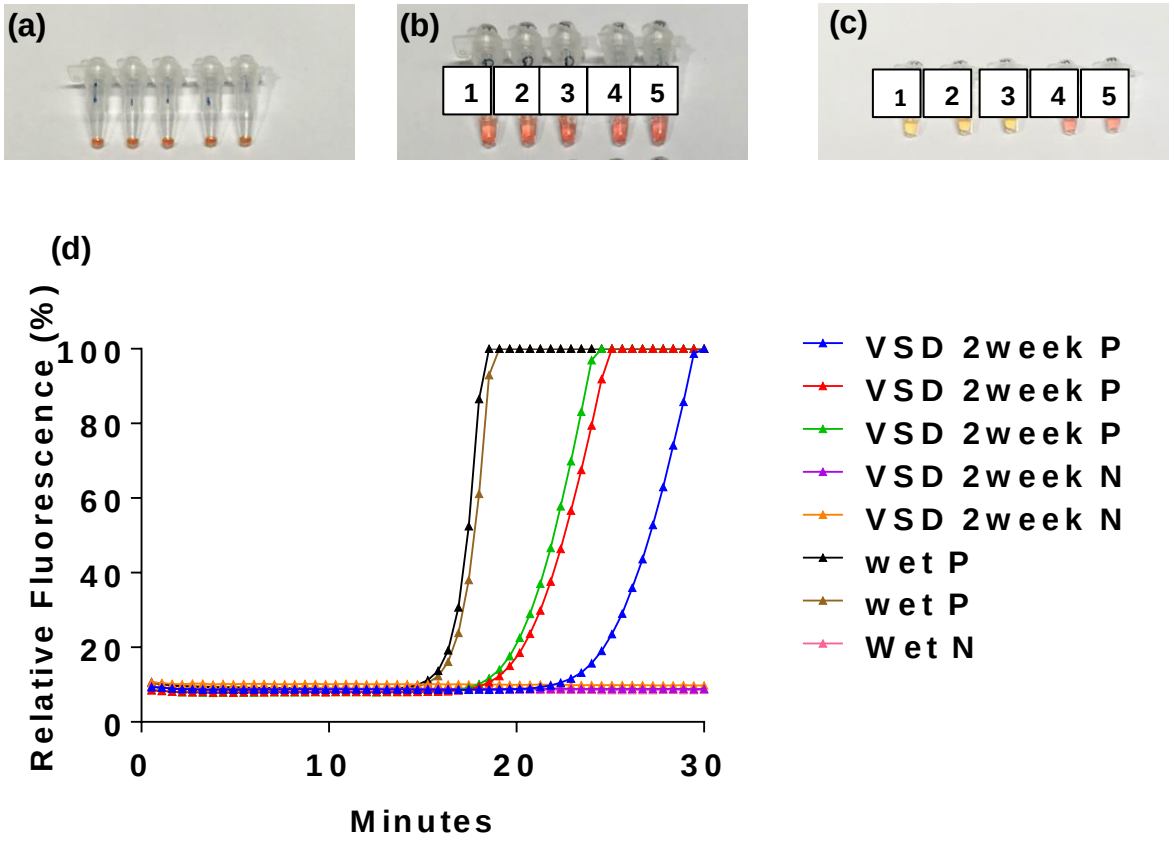


Figure 6.6*: (a) Kits after 2.5-hour vacuum-spin dried were stored at 25 ℃ for five days. (b) Test tubes 1,2, and 3 were reconstituted by positive samples containing Twist viral RNA and samples 4,5 reconstituted water as negative controls. (c)After heating at 65 ℃ for 30 min, the colour of positive controls was changed while still pink of negative controls. (d) After 2.5-hour vacuum-spin dried, kits were stored at 25°C for 14 days. The discolour samples were reconstituted by either positive samples containing Twist viral RNA or water as negative controls. The freshly prepared reagent was used as the control group. SYTO 9 was added before heating. The final concentration of SYTO 9 was 0.5 μM..*

After 2.5-hour vacuum-spin drying, the kits were stored at 25 °C with 30% relative humidity for two weeks. Although the reagent colour was changed to yellow, the enzymes inside were retained (***Figure 6.6*** *(d)*). The fluorescence of positive samples in kits was increased after 15 min of incubation at 65 °C. Although the starting point in fluorescence was slightly later than the freshly prepared reagent, the kits can still amplify sufficient DNA to reach 100% fluorescence in 30 minutes.

6.3.4 Stability of Lyophilized Kits

Reagents were also lyophilised to retain enzymes' activity and extend the shelf life. The master mix was formulated with sugar solution and freeze-dried over 20 hours. After lyophilisation, kits were stored at 25 °C for 15 days to investigate the stability of the kits. As shown in ***Figure 6.7***, the dried reagent was maintained as an elegant lyophilised cake after storage, which was the same morphology and colour as the kits just after lyophilisation.

The colour changing in the vacuum-spin dried kit did not occur in this scenario. Since the water was sublimated at low temperatures, around -40 °C, the degradation of Tween 20 was significantly decreased. Meanwhile, Tween 20 was dispersed with lyophilised cake, lowering the local concentration.

The first four dried kits in each row were reconstituted by viral RNA solution as the positive controls. In comparison, the last four kits were reconstituted by non-targeted DNA, human genome cDNA as the negative controls (***Figure 6.7***). The colours of reconstituted kits were maintained as pink. There was no colour variation between reconstituted samples. After placing at 65 °C for 30 min, the results were read out by colour. The colour of positive samples all changed to yellow, while the

colours of negative samples were kept in pink. Therefore, the activities of enzymes in dried kits were retained after 15-day storage at 25 °C.

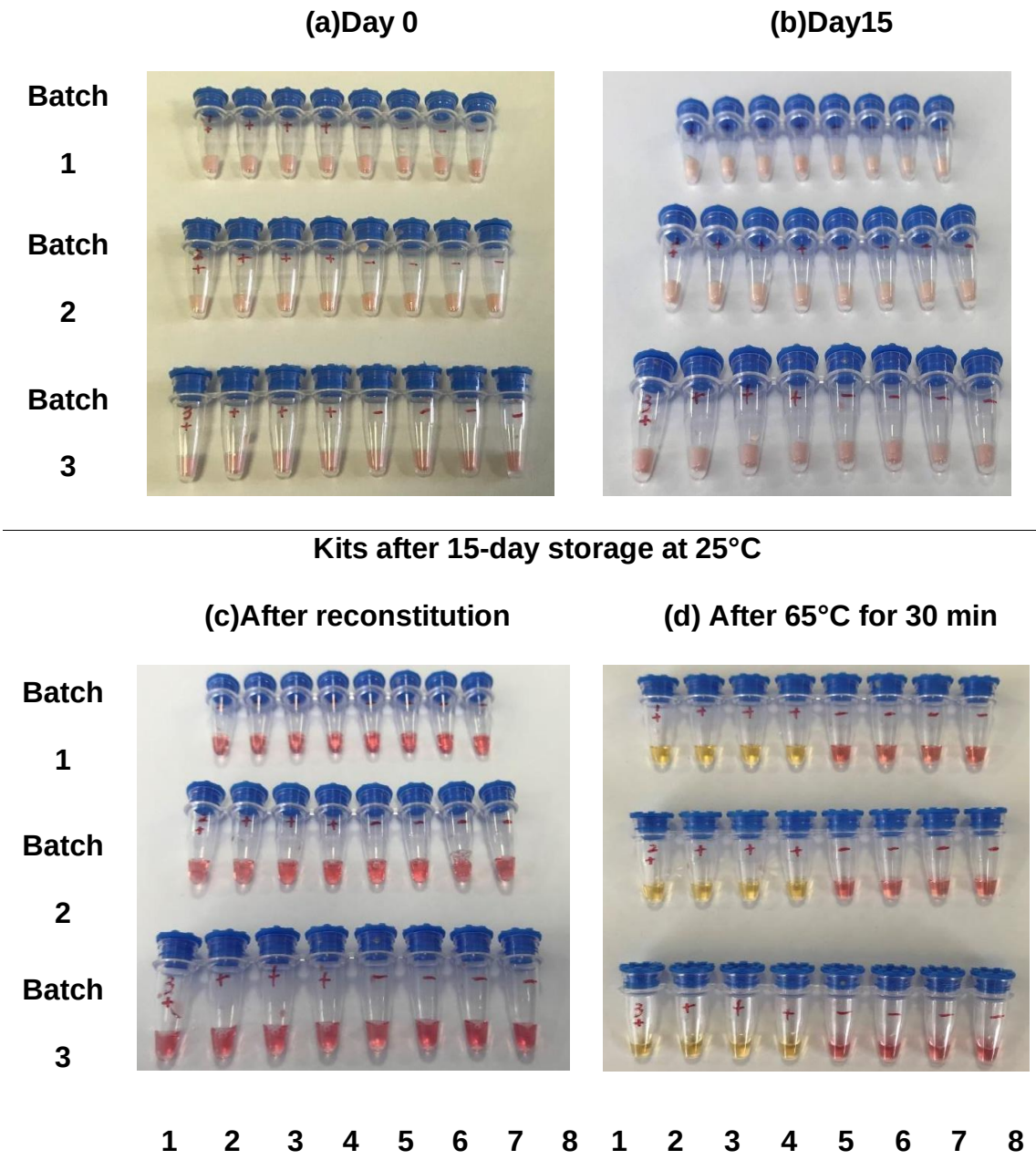


***Figure 6.7**: (a)The dried morphology of dried reagent after lyophilisation. (b) The dried morphology of the lyophilised kit after 15-day storage at 25 °C. (c)Dried mixes were reconstituted with 20 µl DNase/RNase free water followed by adding 5 µl of Synthetic RNA Control 2 - MN908947.3 (40 copies/µl, Twist Bioscience) or human genome DNA as negative samples. (c) Tubes were incubated at 65 °C for 30 min. Three different batches of lyophilised kits were tested for stability. (+) in figure stood for positive samples while (-) represented as negative samples.*

6.3.5 Sensitivity of Dried Kits

50% endpoints of detection (50EP) were applied to evaluate dried kits' sensitivity. Full-lengthed synthetic RNA Control 2 was used with different concentrations. The sensitivities of 2.5-hour VSD kits and lyophilised kits were investigated with fresh prepared wet reagent as the control group.

All of these three different kits could detect RNA with 100 copies. VSD kits with O117 had the highest sensitivity of around 13 copies per reaction (***Figure 6.8***), while the lyophilised kits could reach 56 copies (***Figure 6.9***). The sensitivity of freshly prepared wet reagents was around 42 copies per reaction (***Figure 6.10***).

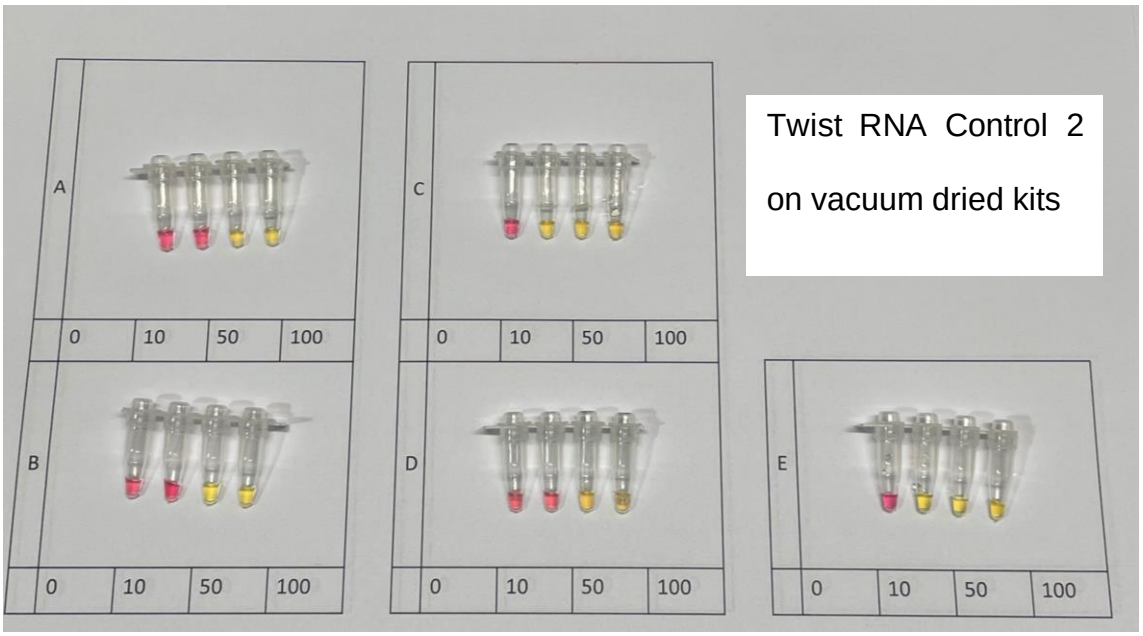


Figure 6.8: Sensitivity analysis of 2.5-hour vacuum-spin dried kit using Synthetic RNA Control 2.

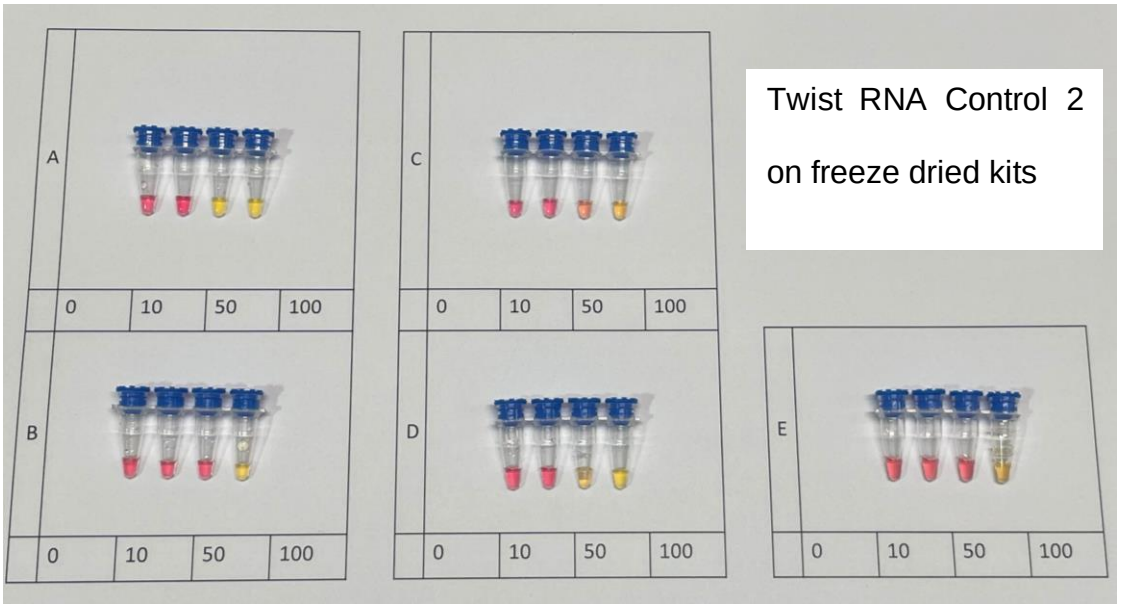


***Figure 6.9**:* Sensitivity analysis of lyophilised kit using Synthetic RNA Control 2.

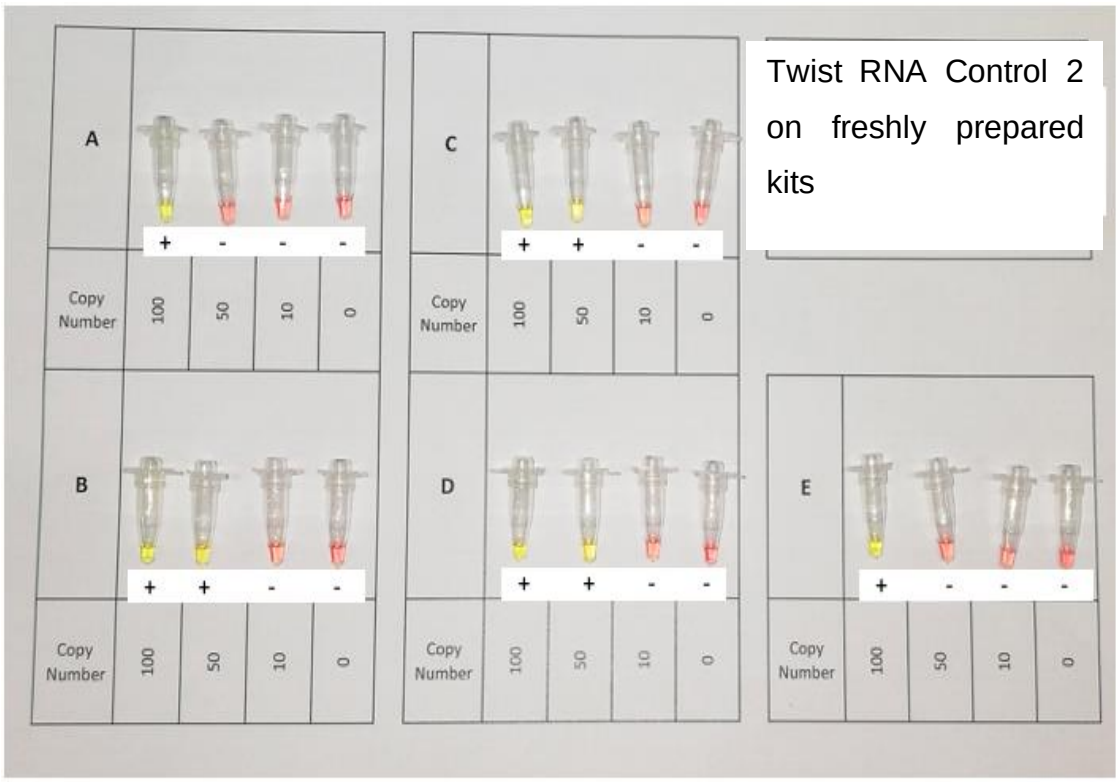


***Figure 6.10**:* Sensitivity analysis of freshly prepared wet kits using Synthetic RNA Control 2.

6.4 Conclusions

This chapter introduced a cost-effective and straightforward drying strategy to preserve bioproducts at ambient temperature. The reagents in the RT-LAMP-based SARS-CoV-2 detection kit were stabilised by this drying method. The efficacy and stability after drying were also investigated.

The SARS-CoV-2 test kit was supplemented with trehalose and other reagents, which did not affect the activity of enzymes in reagents before vacuum-spin drying. To find the optimal conditions for preserving reagents, varying drying times were conducted. Evidence was shown that test kits dried for 8 hours at 30 °C had sufficient activity after 31-day storage to react with RNA templates of the SARS-CoV-2 virus and produce RT-LAMP products. In balance, 2.5-hour vacuum-spin drying was selected for stabilising reagents, which could maintain the colorimetric assay for up to 5 days and be used in fluorescence assay for more than two weeks. Although the lyophilised kit has a longer shelf life, more than 15 days, the prolonged processing time (around 23 hours) and high energy intensity drying process had largely increased the cost. Moreover, the sensitivity of the lyophilised kit was relatively lower than the vacuum-spin dried kits.

It has been shown that dried test kits with long shelf life at ambient temperature are significantly advantageous, especially for regions with limited storage facilities or transportation networks.

Chapter 7

Clinical Validation of Optimised RT-LAMP for the Diagnosis of COVID-19

In the last chapter, vacuum-spin drying was used to preserve the efficacy of kits, which only required a small concentrator and a much shorter drying period than lyophilization. In this chapter, 2.5-hour vacuum-spin dried test kits are evaluated by clinical samples. Moreover, a temperature-dependent oligo will be designed as a switch to minimise the false positive during the diagnosis.

This chapter is based on the paper:

Lim B., Ratcliff J., Nawrot D., **Yu Y.**, Sanghani H., Hsu C., Peto L., Evans S., Hodgson S., Poncin K., Vasudevan S., Dai S., Ren S., Chang H., Cheng W., Pang C.,Siu J., Chan C., Tzang L., Ma M., Cui Z., Simmonds P., Huang WE., Andersson M., Clinical Validation of Optimised RT-LAMP for the Diagnosis of SARS-CoV-2 infection *Sci Rep. 2021 Aug 10;11(1):16193.* doi: 10.1038/s41598-021-95607-1. PMID: 34376716; PMCID: PMC8355225.

As a key author, Y Yu's contribution to this paper is conducting the experiments, drying the RT-LAMP reagents, scaling up the production, and reporting the results.

TABLE OF CONTENTS

7.1 Introduction 152

7.2 Materials and Methods 154

7.2.1 Primer Design 154
7.2.2 RT-LAMP Reaction Mix Preparation and Generalized Procedure 154
7.2.3 Full-Length Transcripts 155
7.2.4 Clinical Samples 155
7.2.5 Analytic Stability, Sensitivity, and Specificity 157
7.2.6 Quantitative Detection Methods 159

7.3 Results and Discussion 159

7.3.1 Effectiveness of Temperature-Dependent Oligo Switch 159
7.3.2 Sensitivity and Specificity of Vacuum-Spin dried Kits 163
7.3.1 Clinical validation of Vacuum-Spin Dried Kits 166
7.3.2 Quantitative Assessment of Colorimetric Readout. 167

7.4 Conclusions 169

7.1 Introduction

The rapid spread of SARS-CoV-2 has challenged the testing capacity of many countries. In the United Kingdom, the testing strategy early on in the outbreak prioritized identifying and protecting essential workers and vulnerable patients. During the height of the outbreak, only symptomatic patients were tested[437]. However, to effectively control localized outbreaks as governments begin to ease lockdown policies, a wider testing strategy achieved by decentralised and rapid testing capacity will be of the utmost importance. Currently, reverse transcription, real-time quantitative polymerase chain reaction (RT-qPCR) detection of SARS-CoV-2 RNA remains the gold standard for diagnosing COVID-19[438]. Whilst largely reliable and able to evaluate samples through high-throughput processes, RT-qPCR requires trained personnel, RNA extraction, and sophisticated instrumentation, all of which limit the use of RT-qPCR tests for decentralized testing.

In addition, the rapid rise in the global demand for RT-qPCR testing has resulted in a global shortage in necessary supplies, particularly in kits for RNA extraction[439].

We propose a reverse transcription loop-mediated isothermal amplification (RT-LAMP) assay to detect SARS-CoV-2 RNA. The RT-LAMP assay is a colorimetric nucleic acid amplification assay - successful amplification of the target sequence results in a colour change from pink to yellow. The reaction takes place in a single-tube format and simply requires heating at 65 °C for 30 min for the reaction to take place. The RT-LAMP assay is rapid, single-step, and ideal for point-of-care-testing (POCT) as the only equipment required is a heating platform. The assay endpoint can be assessed using a variety of outputs, including colour change, fluorescence and absorbance[440]. By shortening the sample collection, testing, and readout to 45 min, the POCT RT-LAMP assay is particularly suited to settings where real-time results would directly impact patient care, including mobile testing centres, emergency departments, primary care facilities, residential homes, and airports[441].

Several groups have reported RT-LAMP assays for detecting SARS-CoV-2 RNA[442–446]. Our RT-LAMP assay method has been previously presented[72]. There, we demonstrated the ability of our O117 primer set to reliably detect 20 copies of an Orf1ab RNA transcript. In this project, we have extended our previous formulation in several ways to further streamline and stabilise the performance of this assay as a POCT outside of standard diagnostic laboratories. We validate the new formulation using several commercial SARS-CoV-2 transcripts and residual clinical samples.

7.2 Materials and Methods

7.2.1 Primer Design

Primers were designed as previously described in Huang et al. [72]. The primer set O117 targeting Orf1ab of SARS-CoV-2 was designed using PrimerExplorer (http://primerexplorer.jp/e/) and each primer was synthesised by Integrated DNA Technologies (IDT, UK). The Switch was synthesised by Integrated DNA Technologies (IDT, UK) with an Iowa Black Dark Quencher at the 3' end (See Supplementary Table 1).

10X O117_N primer mix was prepared by mixing equal volumes of 16 µM FIP, 16 µM BIP, 2 µM F3, 2 µM B3, 4 µM LF and 4 µM LB.

10X O117_Q primer mix was prepared by mixing equal volumes of 16 µM FIP, 16 µM BIP, 2 µM F3, 2 µM B3, 4 µM LF, 4 µM LB and 24 µM Switch.

7.2.2 RT-LAMP Reaction Mix Preparation and Generalized Procedure

All equipment, laminar-flow cabinets, and working benches were sprayed with 70% w/v ethanol (Sigma-Aldrich, UK) and RnaseZap™ (Sigma-Aldrich, UK) prior to reaction mix preparation. All reagents and PCR tubes were kept on ice during kit preparation.

For wet reaction mix, 12.5 µl of WarmStart™ Colorimetric LAMP 2x Master Mix (DNA & RNA) from New England Biolabs (NEB, UK), 5 µl of DNase & RNase-free

molecular grade water (Thermo Fisher Scientific, UK), and 2.5 µl of 10X O117_N or 10X O117_Q primer mix was added into PCR tubes and mixed homogeneously.

For dried reaction mix, 12.5 µl 2X Master Mix was supplemented with 4 µl drying protective agent, OSD-D1™ (Oxsed, UK) containing bovine serum albumin, dextran, lactose and trehalose. 2.5 µl of 10X O117_N or 10X O117_Q primer mix was then added into the PCR tubes. The PCR tubes with caps open were dried with a concentrator (Concentrator Plus, Eppendorf, UK). After drying, PCR tubes were capped immediately and stored at -20 °C.

The RT-LAMP reaction was run by adding 5 µl of the sample of interest to a 20 µl wet reaction mix or a dried reaction mix resuspended in 20 µl of DNase/RNase-free water and heating the reaction at 65 °C for 30 min. A positive result is confirmed through a pH-dependent colorimetric change or confirmation of the production of LAMP product using absorbance or fluorescence.

7.2.3 Full-Length Transcripts

Three full-length SARS-CoV-2 RNA transcripts were used in this study. Research reagent 19/304 (NIBSC, UK) was the kind gift of Giada Mattiuzo. Synthetic RNA Control 1 - MT007544.1 (Twist Bioscience, US) and Synthetic RNA Control 2 – MN908947.3 (Twist Bioscience, US) were the kind gifts of John Taylor (Oxford Medical Genetics Laboratories).

7.2.4 Clinical Samples

The informed consent was obtained from all subjects or, if subjects are under 18, from a parent and/or legal guardian**.** All methods were carried out following relevant

guidelines and regulations. All experimental protocols were approved by the University of Oxford licensing committee.

RT-qPCR

Briefly, oro-nasopharyngeal swabs were stored in Universal Transfer Medium (COPAN Diagnostic, US) or 0.9% saline and extracted using the QIAsymphony system (Qiagen, Hilden Germany). 200 µl of sample solution was mixed with 430 µl of Buffer OBL and carried into the extraction phase. RNA was eluted into 60 µl of buffer AVE, and 10 µl of the elution was carried into the RT-qPCR amplification using the Rotor-Gene Q (Qiagen, UK). RT-qPCR reactions were set up using an RNA-dependent RNA polymerase (RdRP) gene target validated by Public Health England (PHE, UK) and the Altona RealStar SARS-CoV-2 RT-PCR Kit targeting the E and S genes. The eluted RNA sample of 5 µl was added to a wet reaction mix containing O117Q for RT-LAMP assay.

Deep-throat saliva (DTS) was taken from 527 patients. To each sample, DTS was diluted by PBS in a 1:1 ratio. Diluted DTS of 200 µl was added to the binding buffer of MagMAX Viral/Pathogen Nucleic Acid Isolation Kit (Thermo Fisher Scientific, UK, Cat. No. A48310). Viral RNA extraction was carried out according to the manufacturer protocol with the exception that RNA was eluted in 60 µl RNase-free water instead of the elution buffer. The entire isolation process was done in Kingfisher Flex automated system (Thermo Fisher Scientific, UK, Cat. No. 24074431). RT-PCR for detecting extracted RNA of SARS CoV-2 was carried out according to the US CDC 2019-Novel Coronavirus (2019-nCoV) Real-Time RT-PCR Diagnostic Panel Instruction for Use. RT-PCR targeted N1, N2 of SARS-CoV-

2 genes and human RNase P gene. Briefly, 5 µl of extracted RNA or control, 1.5 µl combined primer/probe mix (IDT, UK), 5 µl 4X TaqMan™ Fast Virus 1-Step Master Mix (Thermo Fisher Scientific, UK) and 8.5 µl RNase-free water were mixed (total volume 20 µl) and loaded into real-time PCR system (Applied Biosciences ViiA7, Thermo Fisher Scientific, UK). The data were analysed using the QuartStudio Real-Time PCR software (Thermo Fisher Scientific, UK).

RT-LAMP

RT-LAMP for detecting SARS CoV-2 was carried out according to the manufacturing protocol (Oxsed RaViD Direct SARS-CoV-2 Test, UK). Briefly, 5 µl of extracted RNA was mixed with 20 µl RNase-free water to reconstitute the vacuum-spin dried detection kit. The reaction was incubated at 65 °C for 30 min, and the colour was recorded.

7.2.5 Analytic Stability, Sensitivity, and Specificity

The stability of the wet reaction mix containing O117_N or O117_Q was assessed. 5 µl of 40 copies/µl of Synthetic RNA Control 2 was added as a positive control, and 5 µl of 0.2 µg/µl human genome cDNA was added as a negative control. Human genome cDNA was reverse transcribed from the whole RNA extracted from the human bone marrow-derived MSC line (Lonza, UK). RNA extraction was performed as previously described[425,426] and reverse transcribed using the QuantiTect Reverse Transcription kit (Qiagen, Manchester, UK). 0.5 – 1 µg the whole RNA was converted into cDNA per manufacturer's instructions, including a genomic DNA wipe-out step. The final cDNA sample was diluted to 0.2 µg/µl in RNAse/DNAse free water and stored at -20 °C until used for RT-LAMP assay as

the negative control. The reaction was run as described above, and the colour change was assessed at 0, 30, and 60 min.

To obtain an estimate of analytic sensitivity, the 50% endpoint of the LAMP assay was assessed using the three full-length SARS-CoV-2 transcripts. 19/304 was extracted using the viral RNA mini kit (Qiagen) and eluted in buffer AVE. Serial dilutions of 5 µl of RNA in buffer AVE were used to spike 20 µl of the solution from a 50 µl negative throat swab resuspended in 450 µl of RNAse-free water. 25 µl of the solution was added to a dried kit containing O117_N or O117_Q primers and were tested in parallel and with five replicates. The LAMP assay was run as described above and assessed via colour change and confirmed via UV-Vis of LAMP product on a 2% agarose gel stained with Sybr-Safe (Thermofisher, UK). The 50% endpoint was calculated using the Reed-Muench method.

The specificity of the LAMP assay for SARS-CoV-2 RNA against other human-infective coronaviruses was assessed. RNA was extracted from biobanked respiratory samples positive for OC43, HKU1, NL63, and 229E (matched samples were previously collected and processed as described in Gaunt et al.[447]) using the QIAamp Viral RNA Mini Kit (Qiagen, UK) according to the manufacturer's instructions. 20 µl of solution from a 50 µl negative throat swab resuspended in 450 µl of RNAse-free water was spiked with 5 µl of the RNA eluate. 25 µl was added to a dried kit containing O117_N or O117_Q primers and were tested in parallel. The LAMP assay was run in duplicate at 65 °C for 40 min and assessed via colour change.

7.2.6 Quantitative Detection Methods

Three methods for converting the qualitative colour change output of RT-LAMP reactions into a quantitative output were assessed. The absorbance spectrum of negative and positive samples was read using a BMG Labtech Fluorostar Omega microplate reader, and the reaction outcome was assessed using the ratio of 430/560 nm. Detection of the LAMP product was also performed using an intercalating fluorescent dye, SYTO 9, at a final concentration of 3 µM (Thermofisher, UK), added to the reaction mix once the 30 min RT-LAMP reaction was completed. Excitation and emission were performed at 485 nm and 500 nm, respectively (BMG Labtech Fluorostar Omega microplate reader). Alternatively, 5 µl of the reaction product was carried into the Qubit dsDNA BR Assay Kit (Invitrogen). The assay was performed according to the manufacturer's instructions and read using a Qubit 2.0 fluorometer. Cutoff for positive results for absorbance and SYTO 9 quantitative assays were determined to be 3x standard deviations above the negative controls. For Qubit, 3x standard deviation was calculated using negative samples and negative controls.

7.3 Results and Discussion

7.3.1 Effectiveness of Temperature-Dependent Oligo Switch

Several reports have indicated that carryover contamination and off-target amplification can result in false positives when conducting RT-LAMP assays[430,448,449]. To address the problem of self- and off-target amplification, we introduced a short oligonucleotide designated as a switch, whose sequence is

complementary to one of the primers used in the LAMP reaction, and 3'-end was modified by a dark quencher molecule - Iowa Black® RQ (IBRQ). The switch serves as a temperature-dependent switch to bind an essential primer of LAMP (e.g. FIP), limiting non-specific amplification and the formation of primer dimers. When the temperature is below the working temperature of LAMP (e.g. 65 °C), the switch binds the FIP primer to prevent unspecific dimer amplification. At the working temperature, the switch dissociates from the primer, allowing it to bind target RNA/DNA for reverse transcription and amplification of target nucleic acids.

The O117 primer set[72] was used to evaluate the performance of the switch. Two preparations of the primer mix were used throughout this study: O117_N contains the original six LAMP primers, and O117_Q contains the six LAMP primers and a switch oligonucleotide (**Table 7.1**). The blank controls without target template have been previously shown to result in false-positive due to non-template amplification. In this study, a 12-bp switch with 3'-end modification with IBRQ (IDT, UK) was designed to bind FIP and block self or off-target amplification when the temperature is below the RT-LAMP working temperature. O117_N or O117_Q primers were used to test Synthetic RNA Control 2 - MN908947.3 (Twist Bioscience, US) and human cDNA (Sigma-Aldrich UK) through a prolonged incubation of up to 1 hour. WarmStart Colorimetric Master Mix (New England Biolabs, UK) was used for the RT-LAMP assay.

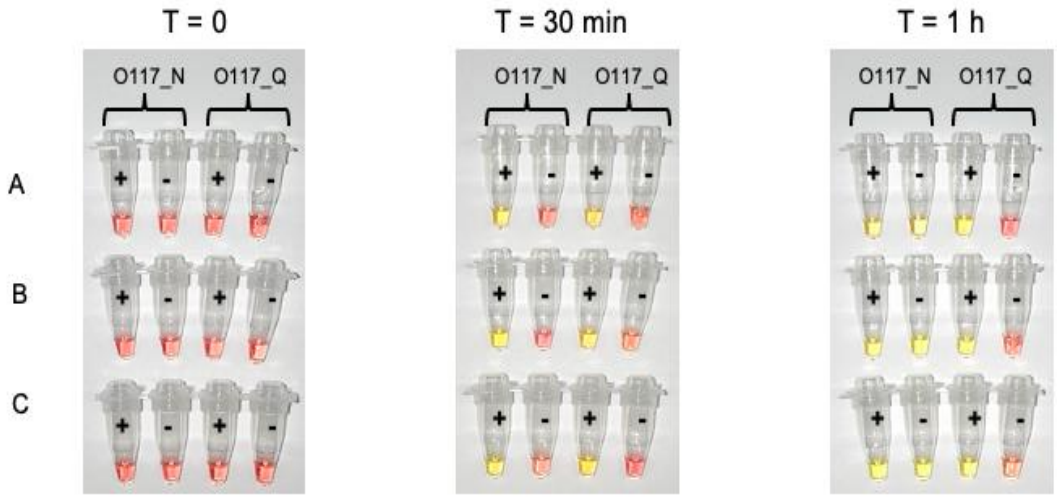
Table 7.1: *Primer sequences used in O117_N and O117_Q primer mix.*

O117 Primer	Sequence (5'-3')
FIP	GGTTTTCAAGCCAGATTCATTATGGATGTCACAATTCAGAAGTAGGA
BIP	TCTTCGTAAGGGTGGTCGCAGCACACTTGTTATGGCAAC
F3	CCCCAAAATGCTGTTGTT
B3	TAGCACGTGGAACCCAAT
LF	TCGGCAAGACTATGCTCAGG
LB	TTGCCTTTGGAGGCTGTGT
Switch	GGCTTGAAAACC-IBRQ

*IBRQ: Iowa Black Dark Quenchers

After incubating at 65 °C for 30 min, both O117_N and O117_Q LAMP primers showed positive results (yellow) for 200 copies of Synthetic RNA Control 2 and negative results (pink) for the human cDNA control (***Figure 7.1*** *(a)*). However, the O117_N primer mix turned yellow within one hour of heating, representing a false positive, while the O117_Q mix maintained a pink colour throughout the experiment (***Figure 7.1*** *(a)*). We also showed that the O117_N primer set could generate up to 60% false-positive result, whilst O117_Q can perform reliably after incubating at 65 °C for one hour (Figure A7 in Appendix 7). The results suggest that a switch in O117 primers should not only prevent off-target amplification at lower temperature but also stabilise the LAMP assay at reaction temperature 65 °C for SARS-CoV-2 and generate reliable results without false positive.

(a)



(b)

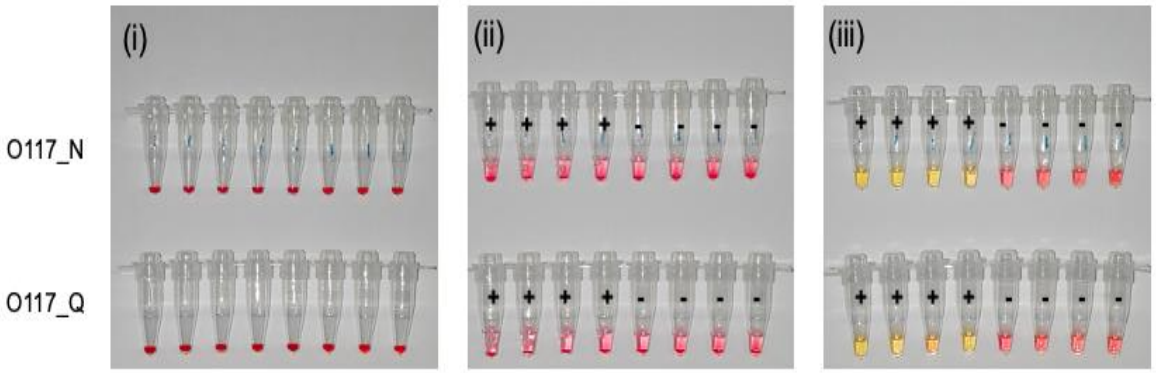


***Figure 7.1**: **Stability test of the improved RT-LAMP reaction mix**. **(a)**, Stability test of RT-LAMP reaction mix containing O117_N and O117_Q. Tubes were added with Synthetic RNA Control 2 - MN908947.3 ('+') or human genome cDNA ('-') followed by heating at 65°C for the time indicated by T. A, B, and C represent three technical replicates. **(b)(i)** Dried reaction mixes stored at room temperature for up to 3 days. **(ii)** Dried reaction mixes reconstituted with 20 µL DNase/RNase free water followed by the addition of Synthetic RNA Control 2 - MN908947.3 ('+') or human genome cDNA ('-'). **(iii)** Tubes incubated at 65 °C for 30 min. Top row: Dried reaction mixes containing O117_N; Bottom row: Dried reaction mixes containing O117_Q.*

7.3.2 Sensitivity and Specificity of Vacuum-Spin Dried Kits

One limitation of the deployability of RT-LAMP to developing countries and rural areas is the need for cold-chain transport of reagents. In the last chapter, the reagents in the COVID-19 detection kit, including Bst2.0 DNA polymerase, WarmStart reverse transcriptase, colorimetric indicator, dNTPs, primers, and buffer, were vacuum-spin dried into one PCR tube. The efficacy of the vacuum-spin dried kits was retained after 3-day storage at room temperature(***Figure 7.1*** *(b)*-iii).

The 50% endpoints of detection (50EP) of vacuum-spin dried kits of the RT-LAMP assay containing O117_N and O117_Q were determined using three full-length transcripts serially diluted in buffer AVE (**Table 7.2**). The RNA templates were research reagent 19/304 (NIBSC), Synthetic RNA control 1 - MT007544.1 and Synthetic RNA control 2 MN908947.3 (Twist BioScience). The testing results are summarised in **Table 7.2**, ***Figure 7.2*** *(a)* and Figure A8 in Appendix 8.

Table 7.2*: The 50% end-point of detection (50 EP) of vacuum-spin dried kits using full-length transcript standards.*

Full-length transcript	Dried Kit with O117_Q*	Dried Kit with O117_N*
19/304	71	89
RNA Control 1	131	224
RNA Control 2	60	13
RNA Control 2 (Wet kit)	71	42

*the total copy number per 25 μl reaction

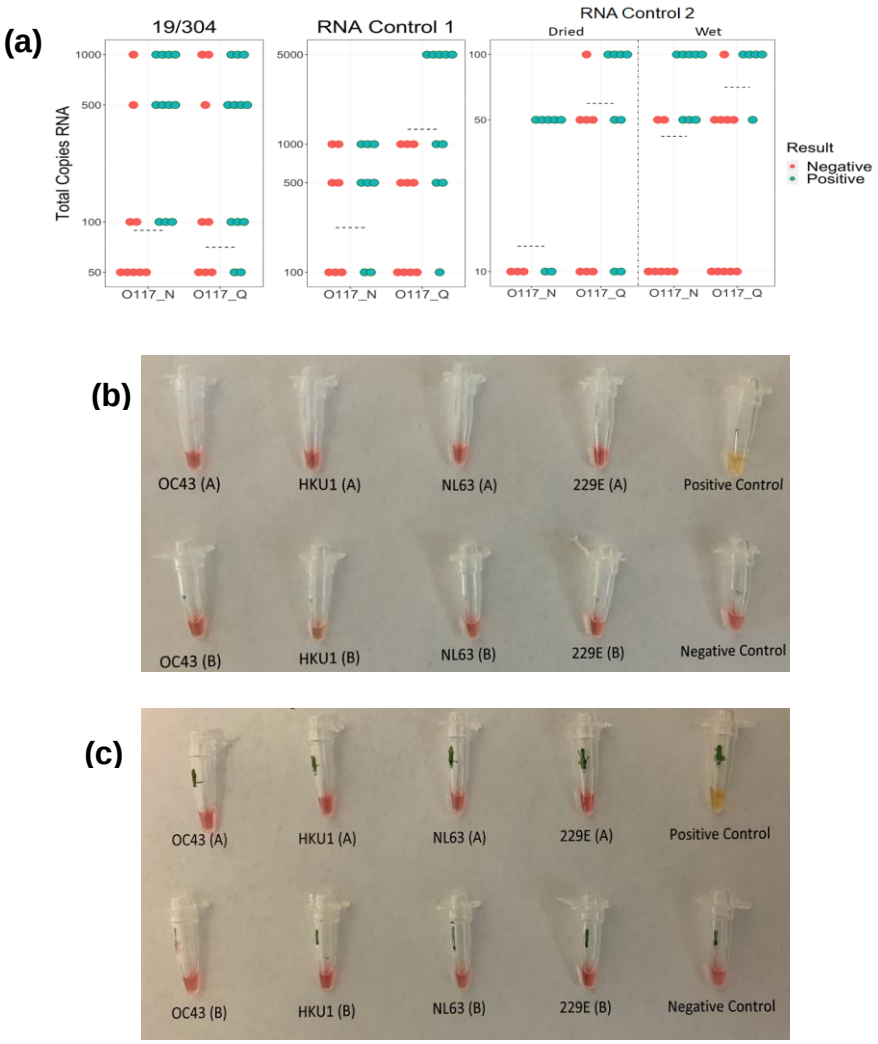


***Figure 7.2**: **Sensitivity and specificity of improved RT-LAMP assay. (a)** Determination of 50% endpoints for O117_Q and O117_N preparations of RT-LAMP assay. Full-length transcripts were serially diluted in buffer AVE to achieve the total RNA input/reaction indicated on the y axis. Each dot represents one experimental replicate. Dashed lines indicate 50% endpoint as calculated by the Reed-Muench method. Kits were dried except where indicated for RNA Control 2. Full-length transcript indicated on the figure. Dried reaction mix containing O117_N **(b)** and O117_Q **(c)** were tested against non-SARS human-infective coronaviruses. A and B represent two technical replicates.*

It shows that 50EP against research reagent 19/304 was 71 (O117_Q) and 89 (O117_N) copies per reaction (25 μl). The 50EP of Synthetic RNA Control 1 was 131 and 224 copies per reaction for O117_Q and O117_N, respectively. Synthetic

RNA Control 2 demonstrated 50EP of 60 and 13 copies per reaction for O117_Q and O117_N, respectively. The 50EP of wet reaction mixes was tested with Synthetic RNA control 2. The level of detectable RNA for O117_Q and O117_N in the wet reaction mix were 71 and 42 copies. The 50EP for dried reaction mixes containing O117_Q targeting 19/304 and Synthetic RNA Control 2 had a mean of 65 copies (95% CI: 57.3 – 72.9). The 50EP for dried reaction mixes containing O117_N and targeting 19/304 and Synthetic RNA control 2 had a mean of 51 copies (95% CI: -1.6 – 104.0). These results suggest that the oligo switch in O117 primers has a minimal impact on the LAMP sensitivity for viral RNA detection and 50EP is 60-131 RNA copies per 25 μl reaction.

The ability of the optimised RT-LAMP assay to discriminate SARS-CoV-2 from other human-infective seasonal coronaviruses was assessed using RNA extracted clinical samples, which were previously demonstrated to be infected with various respiratory pathogens. The RNA samples from infected patient samples positive for beta- coronaviruses (OC43 and HKU1) and alpha-coronaviruses (229E and NL63) were used for specificity testing of O117_Q LAMP assay. Neither replicate of any of the seasonal coronaviruses tested by O117_Q produced a positive result, even using an extended reaction time (40 instead of 30 min) (***Figure 7.2*** *(b)* and *(c)*). It suggested that the O117_Q primer set had a high specificity for SARS-CoV-2, failing to produce false-positive results for related human-infective coronaviruses.

7.3.1 Clinical Validation of Vacuum-Spin Dried Kits

The dried detection kits containing O117_Q were evaluated by RNA extracts from 72 nasopharyngeal swab samples and 527 saliva samples, which were assessed by both RT-qPCR and RT-LAMP in parallel. Compared to RT-qPCR, RT-LAMP demonstrated a sensitivity of 95% (94/99 SARS-CoV-2 positive samples; 95% CI: 91 – 99) and specificity of 99% (495/500 SARS-CoV-2 negative samples; 95% CI: 98 – 100) for the total of 599 clinical samples (**Table 7.3**), demonstrating an overall percentage agreement (OPA) of 98% (589/599 matching samples).

Table 7.3*: Summary of Clinical testing results.*

	Clinical RNA testing (Swab and Saliva)
Total samples	599 (99 Positive + 500 Negative)
Sensitivity (95% CI)	95% (91 – 99)
Specificity (95% CI)	99% (98 – 100)
Detection time	15-30 min

However, over 7 samples with high Ct values (Ct >34), our assay was able to detect 4 of them, and thus it may miss identifying patients with low viral loads. This suggests that the detection limit of O117_Q is equivalent to Ct = ~34 in an RT-qPCR assay.

7.3.2 Quantitative Assessment of Colorimetric Readout

Reading the colorimetric RT-LAMP assay has an element of subjectivity. To overcome any ambiguity and potential for inter-user and inter-lab variation when using a visually-assessed colorimetric readout, we sought to establish quantitative measurements for differentiating positive and negative samples, as seen in ***Figure 7.3***. The first method uses the absorbance ratio at 430 nm and 560 nm to quantitatively assess the colour change of the same 72 clinical samples (Figure A7 in Appendix 7). The result is consistent with the colorimetric readout by the naked eye (***Figure 7.3*** *(a) and (b)*). Fluorescent dyes SYTO 9 and Qubit were also used to detect the products of the RT-LAMP reaction. Specifically, RT-LAMP products were stained with SYTO 9 and read using a microplate reader (***Figure 7.3*** *(c)* and *(d)*) or stained with Qubit BR DNA dye and read with a Qubit fluorometer (***Figure 7.3*** *(e)* and *(f)*). Positive samples are defined as having values greater than three times the standard deviation of negative samples (n=18).

As the Qubit is portable, compact, and gives an accurate readout of fluorescence, we randomly selected a set of 10 positive and negative samples as identified previously using RT-qPCR to verify its applicability for POCT. We established a cutoff value for the Qubit reading. Overall, all three methods demonstrated good agreement with the pH-dependent colorimetric RT-LAMP readout, validating their use as a quantitative measurement to indicate RT-LAMP outcomes. Specifically, absorbance, SYTO 9, and Qubit revealed a 2.1, 2.1 and 9.4 fold change between

SARS-CoV-2 positive and negative patient samples, respectively. Qubit reagents and fluorometer reading demonstrated good performance.

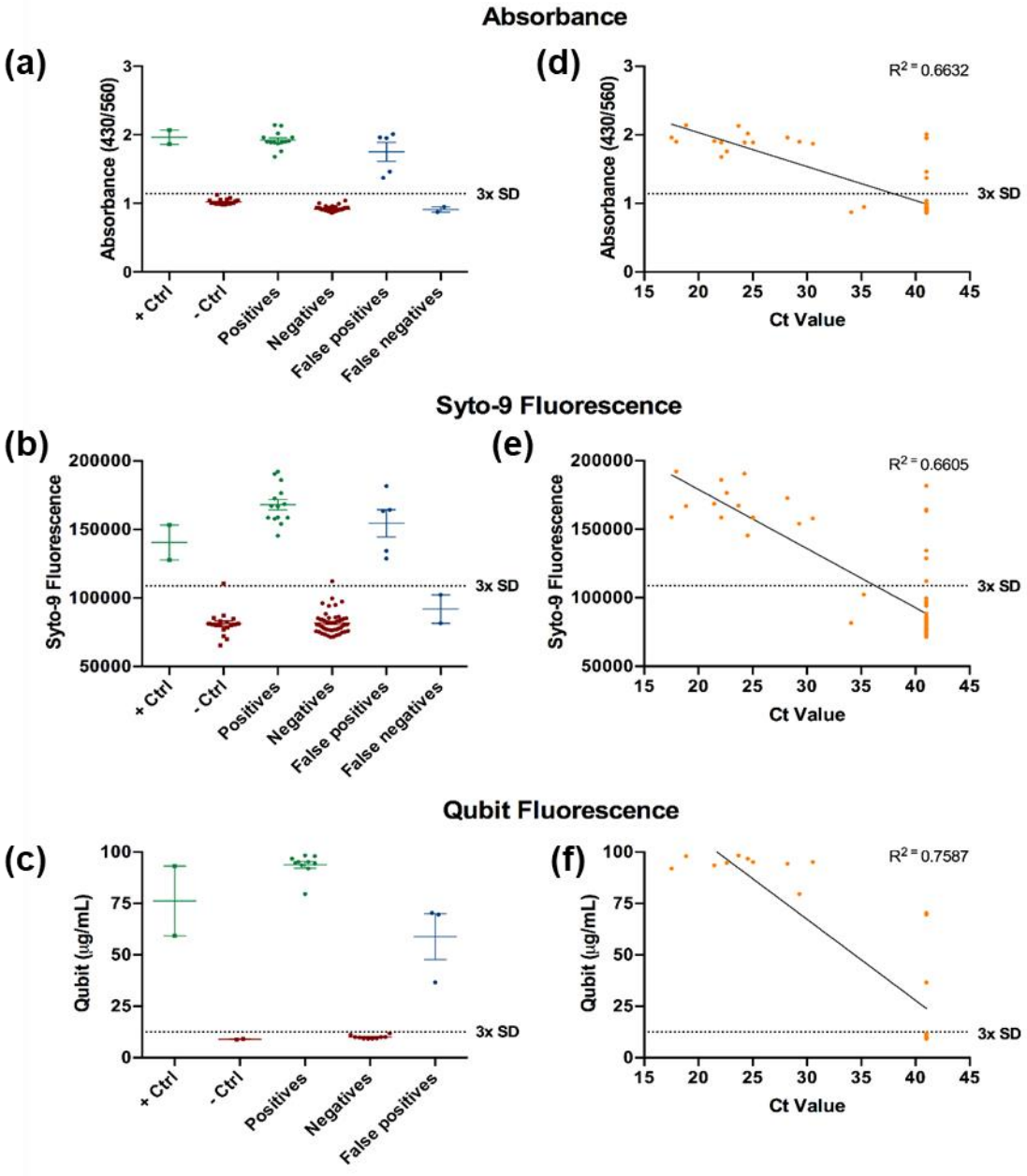


Figure 7.3*:Quantitative evaluation of pH-dependent colorimetric RT-LAMP readout.** *Three quantitative methods* ***a*, Absorbance using 430/560 nm ratio;* ***b,*** *SYTO 9 fluorescence using 485 nm (excitation) and 500 nm (emission); and* ***c****, Qubit fluorescence using Qubit 2.0 fluorometer were used to assess the RT-LAMP result.* ***d****,* ***e****, and* ***f*** *are the correlation analysis between RT-qPCR and the three quantitative evaluations, respectively. Each dot represents one experimental replicate. Dotted lines indicate 3x standard deviations above the negative controls.*

7.4 Conclusions

Several adaptations have been applied to improve the performances of the previously reported RT-LAMP assay[72]. The risk of false-positive results in RT-LAMP was minimised by adding a short temperature-dependent oligo switch. This oligo switch 'locked' FIP from random self-amplification when the temperature was lower than the working temperature and did not demonstrably impair the sensitivity. The 50% endpoint values of vacuum-spin dried kits demonstrated that the RT-LAMP assay could readily detect the samples containing less than 100 copies of SARS-CoV-2 RNA. Meanwhile, the detection kit is highly specific to SARS-CoV-2. No false-positive result was detected when testing the samples containing the four seasonal coronaviruses.

559 RNA extracted clinical samples validated the vacuum-spin dried detection kits. The results gave a high level of overall percentage agreement (90.3%) compared to RT-qPCR and showed the detection limit of O117_Q was equivalent to Ct = ~34 in an RT-qPCR assay. As the visual interpretation of experimental results could be subjective, three different quantitative methods have been established to overcome these limitations. These readouts can be performed accurately using relatively inexpensive equipment that is readily available to many laboratories.

This vacuum-spin dried COVID-19 detection kit shows high accuracy, acceptable sensitivity and rapid turnaround time. It potentially provides a strategic and affordable way to manage surveillance of the SARS-COV-2 public health crisis.

Statement of Authorship for joint/multi-authored papers for PGR thesis

Title of Paper	Clinical Validation of Optimised RT-LAMP for the Diagnosis of COVID-19
Publication Status	☐ Published ☒ Accepted for Publication ☐ Submitted for Publication ☐ Unpublished and unsubmitted work written in a manuscript style
Publication Details	Lim B., Ratcliff J., Nawrot D., **Yu Y.**, Sanghani H., Hsu C., Peto L., Evans S., Hodgson S., Poncin K., Vasudevan S., Dai S., Ren S., Chang H., Cheng W., Pang C.,Siu J., Chan C., Tzang L., Ma M., Cui Z., Simmonds P., Huang WE., Andersson M., Clinical Validation of Optimised RT-LAMP for the Diagnosis of COVID-19. *Scientific Reports. Revised.*

Student Confirmation

Student Name:	Yejiong Yu
Contribution to the Paper	As a key author, Y Yu's contribution to this paper is conducting the experiments, drying the RT-LAMP reagents, scaling up the production, and reporting the results.
Signature & Date	

Supervisor Confirmation

By signing the Statement of Authorship, you are certifying that the candidate made a substantial contribution to the publication, and that the description described above is accurate.

Supervisor name and title:	Zhanfeng Cui Donald Pollock Professor of Chemical Engineering
Supervisor comments	Yejiong is a key contributor to this paper. His contributions are: 1. Design and testing of the enzyme formulation 2. Vacuum drying and testing of the test kits 3. Stability and shelf-life testing 4. A lab Sensitivity study on the test 5. Result discussions 6. Manuscript proofreading
Signature & Date	 10 Mar 2021

Chapter 8

Summary and Outlooks

In this thesis, two novel drying strategies, Matrix Assisted Room Temperature (MART) drying and Vacuum-spin drying (VSD), are applied to stabilise functional proteins for room temperature storage and transportation. For MART drying, the stabilisation mechanisms have been identified, and the critical importance of capillary bridging was illustrated by numerical simulation. The feasibility of MART drying of LDH on a biocompatible and low-cost cellulose fibre matrix has been analysed with different drying parameters. Using the optimal drying conditions, MART drying could stabilise LDH for long-term room temperature storage. MART drying was applied under vacuum conditions as MART-V drying to shorten the drying time. The efficacy of dried FGF-2 by MART drying and MART-V drying was studied by cell proliferation of Immortalized Mesenchymal Stem Cells (MSC-hTERT). Another drying strategy, vacuum-spin drying, was developed to stabilise the enzymes in the SARS-CoV-2 detection kit to enable ambient temperature storage. The dried kit with the correct formulation presented high sensitivity and specificity via clinical trials.

8.1 MART Drying

Similar to sugar film drying of vaccines, forming capillary bridges during drying to trap proteins within the vitrified sugar film is critical to preserve the functionality of proteins. The criterion of forming capillary bridges is derived using Capillary Bridge number (CB number), which is based on the physical properties of fibre matrix and solution. If the CB number is greater than 0, the liquid is structured as capillary bridges on this fibre matrix. Otherwise, a droplet structure is formed and no

capillary bridge formation. In MART drying of proteins formulated with sugar, it is important to ensure CB is greater than zero for the system.

To validate MART drying of protein, LDH was used as the test protein for its easy detection of activity loss. A biocompatible and cheap cellulose fibre matrix is selected. A special drying apparatus with humidity control is fabricated for the test. After drying, sugar films containing bioproducts were observed among fibres using scanning electron microscopy. The enzyme activity after MART drying showed no significant loss, demonstrating the feasibility of MART drying of proteins.

The retained activity of LDH after drying was affected sugar concentrations. Although 500 mM trehalose and 10%w/v dextran could maintain over 90% of initial LDH activity after drying, LDH was slowly degraded over time in storage. Higher storage temperatures could lead to higher degradation rates, owing to stress relaxation. After doubling the concentration of trehalose (1 M) and keeping the concentration of dextran (10%w/v) in formulation, the glass transition temperature of dried products was increased to over 70 °C, and stress relaxation was inhibited. The stability of bioproducts over the storage period was improved. After MART drying LDH at 30 °C with 3% RH, the activity of LDH could be retained for at least six months at 25 °C, preserving over 85% of initial activity.

The driving force to remove water in MART drying is limited. Since the wet-bulb temperature of 30 °C with 3% relative humidity is around 11.39 °C, the drying rate was limited, leading to typically over 10 hours of drying time. To reduce the drying time, MART drying was combined with vacuum, here referred to as Matrix-Assisted

Room Temperature Vacuum (MART-V) drying. 3-hour MART-V drying could reach the same residual moisture content of dried LDH as 12-hour MART drying and even gave a similar retained activity after drying. MART-V is faster but with the complexity of the process and equipment.

Although MART drying is characterized as a simple and low energy-intensity drying strategy compared to lyophilization, it is unavoidable to lose a certain amount of protein molecules due to the matrix surface adsorption. Coating fibre matrix with BSA in high concentration was tested and proved as an effective way to reduce this non-specific binding.

Preloading a cheap protein on the matrix to reduce surface adsorption of the target protein proved effective to reduce target protein loss and to maintain its functions. This point was demonstrated with MART drying of FGF-2 at a low concentration. After coating the fibre matrix with a high concentration BSA solution, FGF-2 of low concentration formulated with trehalose and dextran was loaded onto the cellulose fibre matrix. The dried FGF-2 on fibre matrices were stored at 40 °C for 1 week. The efficacy of dried FGF-2 after storage was assessed by cell proliferation assays using hMSC, as FGF-2 promotes cell proliferation. There was no significant difference between liquid FGF-2 stored at -80 °C and the reconstituted solution from MART dried and MART-V dried matrices. In other words, FGF-2 was stabilised by both MART and MART-V drying

Using LDH and FGF-2, the feasibility of using MART drying with or without vacuum to dry proteins without significant functionality loss was demonstrated. Future work can be directed to explore this promising new technology:

(i) Increase drying rate and controllability of the process by altering the air circulation velocity. By increasing the convection, both the heat transfer rate and the mass transfer rate can be increased. This will shorten processing time to minimise protein hydrolysis, especially at elevated temperatures.

(ii) Develop new equipment for efficient MART drying and MART-V drying. There is no existing equipment for this new process, and hence new apparatus with control flexibility are needed for research and industrial application.

(iii) Study the desired properties of the matrix and design such a matrix with the specific purpose for MART drying.

(iv) Apply to therapeutic protein drying for clinical application. An example would be the development of bioactive would dressing, where growth factors are dried onto the matrix and the latter is used directly to treat wounds.

(v) Apply MART drying to the vaccine, e.g., the non-enveloped vaccine like the Oxford AstraZeneca COVID-19 vaccine. A similar adenovirus vector, which only has a protein shell, has been thermostabilised on glass fibre. Now, an alternative cellulose fibre matrix, which is biocompatible, might potentially replace glass fibre to thermostabilise vaccines, which could expressively enlarge vaccination coverage, especially in Africa.

8.2 Vacuum-Spin Drying of COVID-19 Detection Kit

Another drying strategy, vacuum-spin drying, was applied to stabilise enzymes in SARS-CoV-2 detection kits, which could diagnose SARS-CoV-2 by nucleic acid amplification using Reverse Transcription Loop-mediated Isothermal Amplification (RT-LAMP). The test is quite simple and does not involve special equipment. This test kit has been used in major UK airports and contributed to combat the COVID-19 pandemic.

However, the enzymes in kits need to be stored at low temperatures to maintain the potency, limiting the application coverage of test kits. Here, drying RT-LAMP reagents was attempted for the first time and proved successful. Vacuum-spin drying was applied to stabilise the enzymes, Bst 2.0 polymerase, reverse transcriptase, and other reagents. A formulation is developed to protect the enzymes and reagents over the drying process. The formulated reagents were dried in vacuum condition with the assistance of centrifugation. Owing to the centrifugation, the foaming of reagents was suppressed, which gave a uniform morphology after drying.

The efficacy of the dried kit was analyzed with different drying times after successful drying at 30 °C for 8 hours. The dried product was still effective after 31-day storage. The process was optimized. A 2.5-hour vacuum-spin drying protocol was selected for stabilising reagents, which could maintain the colorimetric

assay for up to 5 days and be used in fluorescence assay for more than 2 weeks. This time frame, although not long, is sufficient to transport to the test sites. Compared to the lyophilized reagents, although the shelf life of vacuum-spin dried kits was shorter, the sensitivity of vacuum-spin dried kits was much higher. Moreover, vacuum-spin drying only requires a small concentrator and a much shorter drying period than lyophilization. The clinical trials showed the high sensitivity and specificity of the vacuum-spin dried kits.

The following topics related to this part of the work are identified:

(i) Quantification of RT-LAMP: RT-LAMP at the moment gives qualitative results – yes or no, and it could not provide the viral load if yes. It would be interesting to quantify RT-LAMP, for example, link to the reaction time.

(ii) Detection of other infectious diseases: Applying the RT-LAMP approach to design detection of other known infectious diseases, apart from COVID-19. Obvious examples are other respiratory diseases, such as influenza, human parainfluenza virus and human metapneumovirus.

(iii) Process scales up: To scale up the production, a larger piece of equipment could be designed to increase the production rate. Reagents could be stabilised into PCR plates for high throughput reading. The feasibility of drying fluorescence dye with reagents could be investigated, simplifying the testing process and quantifying the results.

(iv) Home test device: With the dried test reagents, it is feasible to manufacture home/self-test kits for Covid-19 or other infectious diseases. It would be welcoming if such a device could be developed.

References

1. Chi, Y. H. *et al.* The physiological functions of universal stress proteins and their molecular mechanism to protect plants from environmental stresses. *Front. Plant Sci.* **10**, 1–13 (2019).
2. Zhang, L., Li, Y., Ying, Y. & Fu, Y. Recent advances in fabrication strategies and protein preservation application of protein-nanomaterial hybrids: Integration and synergy. *TrAC - Trends Anal. Chem.* **118**, 434–443 (2019).
3. Suprun, E. V. Protein post-translational modifications – A challenge for bioelectrochemistry. *TrAC - Trends Anal. Chem.* **116**, 44–60 (2019).
4. Ansari, S. & Masoum, S. Molecularly imprinted polymers for capturing and sensing proteins: Current progress and future implications. *TrAC - Trends Anal. Chem.* **114**, 29–47 (2019).
5. Leader, B., Baca, Q. J. & Golan, D. E. Protein therapeutics: A summary and pharmacological classification. *Nat. Rev. Drug Discov.* **7**, 21–39 (2008).
6. Bruce Alberts, A. J. J. L. M. R. K. R. and P. W. *Molecular biology of the cell (4th ed.)*. *Biochemistry and Molecular Biology Education* **31**, (2003).
7. Kanwar, M., Wright, R. C., Date, A., Tullman, J. & Ostermeier, M. Chapter Seventeen - Protein Switch Engineering by Domain Insertion. in *Methods in Protein Design* (ed. Keating, A. E.) **523**, 369–388 (Academic Press, 2013).
8. Vaishya, R., Khurana, V., Patel, S. & Mitra, A. K. Long-term delivery of protein therapeutics. *Expert Opin. Drug Deliv.* **12**, 415–440 (2015).
9. Gonzalez, M. W. & Kann, M. G. Chapter 4: Protein interactions and disease. *PLoS Comput. Biol.* **8**, e1002819–e1002819 (2012).
10. Herrero, E. P., Alonso, M. J. & Csaba, N. Polymer-based oral peptide nanomedicines. *Ther. Deliv.* **3**, 657–668 (2012).
11. Sevimoglu, T. & Arga, K. Y. The role of protein interaction networks in systems biomedicine. *Comput. Struct. Biotechnol. J.* **11**, 22–27 (2014).
12. Ryan, D. P. & Matthews, J. M. Protein–protein interactions in human disease. *Curr. Opin. Struct. Biol.* **15**, 441–446 (2005).
13. Falconer, R. J. Advances in liquid formulations of parenteral therapeutic proteins. *Biotechnol. Adv.* **37**, 107412 (2019).
14. Leader, B., Baca, Q. J. & Golan, D. E. Protein therapeutics: a summary and pharmacological classification. *Nat. Rev. Drug Discov.* **7**, 21–39 (2008).
15. Mensink, M. A., Frijlink, H. W., van der Voort Maarschalk, K. & Hinrichs, W. L. J. How sugars protect proteins in the solid state and during drying (review): Mechanisms of stabilization in relation to stress conditions. *Eur. J. Pharm. Biopharm.* **114**, 288–295 (2017).
16. Walsh, G. Biopharmaceutical benchmarks 2014. *Nat. Biotechnol.* **32**, 992–1000 (2014).
17. Bajracharya, R., Song, J. G., Back, S. Y. & Han, H. K. Recent Advancements in Non-Invasive Formulations for Protein Drug Delivery. *Comput. Struct. Biotechnol. J.* **17**, 1290–1308 (2019).
18. Lagassé, H. A. D. *et al.* Recent advances in (therapeutic protein) drug development. *F1000Research* **6**, 113 (2017).
19. An, Y.-H. *et al.* Recent Advances in the Transdermal Delivery of Protein Therapeutics with a Combinatorial System of Chemical Adjuvants and Physical Penetration Enhancements. *Adv. Ther.* **3**, 1900116 (2020).
20. Bailey, R. Physical education and sport in schools: A review of benefits and

outcomes. *J. Sch. Health* **76**, 397–401 (2006).
21. Testa, B., Pedretti, A. & Vistoli, G. Reactions and enzymes in the metabolism of drugs and other xenobiotics. *Drug Discov. Today* **17**, 549–560 (2012).
22. Xiang, Q. *et al.* The influence of genetic polymorphisms in drug metabolism enzymes and transporters on the pharmacokinetics of different fluvastatin formulations. *Asian J. Pharm. Sci.* **15**, 264–272 (2020).
23. Nishiya, Y. *et al.* Identification of non-P450 enzymes involved in the metabolism of new drugs: Their significance in drug interaction evaluation and prodrug disposition. *Drug Metab. Pharmacokinet.* **35**, 45–55 (2020).
24. Chiang, T.-Y. *et al.* Effects of Shengmai San on key enzymes involved in hepatic and intestinal drug metabolism in rats. *J. Ethnopharmacol.* **271**, 113914 (2021).
25. Pérez, J. A. C. *et al.* Bioinspired biomaterials and enzyme-based biosensors for point-of-care applications with reference to cancer and bio-imaging. *Biocatal. Agric. Biotechnol.* **17**, 168–176 (2019).
26. Kumari, P. *et al.* Potential diagnostics and therapeutic approaches in COVID-19. *Clin. Chim. Acta* **510**, 488–497 (2020).
27. Lan, T., Zhang, J. & Lu, Y. Transforming the blood glucose meter into a general healthcare meter for in vitro diagnostics in mobile health. *Biotechnol. Adv.* **34**, 331–341 (2016).
28. Soleimany, A. P. & Bhatia, S. N. Activity-Based Diagnostics: An Emerging Paradigm for Disease Detection and Monitoring. *Trends Mol. Med.* **26**, 450–468 (2020).
29. Li, J. *et al.* Non-Invasive Biomarkers for Early Detection of Breast Cancer. *Cancers (Basel).* **12**, 2767 (2020).
30. Jamshidi, N. *et al.* The Radiogenomic Risk Score: Construction of a Prognostic Quantitative, Noninvasive Image-based Molecular Assay for Renal Cell Carcinoma. *Radiology* **277**, 114–123 (2015).
31. Team, T. N. L. S. T. R. Reduced Lung-Cancer Mortality with Low-Dose Computed Tomographic Screening. *N. Engl. J. Med.* **365**, 395–409 (2011).
32. Metlay, J. P. *et al.* Diagnosis and Treatment of Adults with Community-acquired Pneumonia. An Official Clinical Practice Guideline of the American Thoracic Society and Infectious Diseases Society of America. *Am. J. Respir. Crit. Care Med.* **200**, e45–e67 (2019).
33. Yamashige, R., Kimoto, M., Okumura, R. & Hirao, I. Visual Detection of Amplified DNA by Polymerase Chain Reaction Using a Genetic Alphabet Expansion System. *J. Am. Chem. Soc.* **140**, 14038–14041 (2018).
34. Österdahl, M. F. *et al.* Detecting SARS-CoV-2 at point of care: preliminary data comparing loop-mediated isothermal amplification (LAMP) to polymerase chain reaction (PCR). *BMC Infect. Dis.* **20**, 783 (2020).
35. Khodakov, D., Wang, C. & Zhang, D. Y. Diagnostics based on nucleic acid sequence variant profiling: PCR, hybridization, and NGS approaches. *Adv. Drug Deliv. Rev.* **105**, 3–19 (2016).
36. Faye, O. *et al.* Quantitative real-time PCR detection of Zika virus and evaluation with field-caught mosquitoes. *Virol. J.* **10**, 311 (2013).
37. Shirato, K. *et al.* Detection of Middle East respiratory syndrome coronavirus using reverse transcription loop-mediated isothermal amplification (RT-LAMP). *Virol. J.* **11**, 139 (2014).
38. Caipang, C. M. A., Haraguchi, I., Ohira, T., Hirono, I. & Aoki, T. Rapid detection of a fish iridovirus using loop-mediated isothermal amplification

(LAMP). *J. Virol. Methods* **121**, 155–161 (2004).
39. Soliman, H. & El-Matbouli, M. Reverse transcription loop-mediated isothermal amplification (RT-LAMP) for rapid detection of viral hemorrhagic septicaemia virus (VHS). *Vet. Microbiol.* **114**, 205–213 (2006).
40. Heitzer, E., Haque, I. S., Roberts, C. E. S. & Speicher, M. R. Current and future perspectives of liquid biopsies in genomics-driven oncology. *Nat. Rev. Genet.* **20**, 71–88 (2019).
41. Khan, A. H. & Sadroddiny, E. Application of immuno-PCR for the detection of early stage cancer. *Mol. Cell. Probes* **30**, 106–112 (2016).
42. Bernard, P. S. & Wittwer, C. T. Real-time PCR technology for cancer diagnostics. *Clin. Chem.* **48**, 1178–1185 (2002).
43. Modarres, H. P., Mofrad, M. R. & Sanati-Nezhad, A. Protein thermostability engineering. *RSC Adv.* **6**, 115252–115270 (2016).
44. Frokjaer, S. & Otzen, D. E. Protein drug stability: a formulation challenge. *Nat. Rev. Drug Discov.* **4**, 298 (2005).
45. Ghosh, K. & Dill, K. Cellular Proteomes Have Broad Distributions of Protein Stability. *Biophys. J.* **99**, 3996–4002 (2010).
46. Brown, L. R. Commercial challenges of protein drug delivery. *Expert Opin. Drug Deliv.* **2**, 29–42 (2005).
47. Sykes, C. Time- and Temperature-Controlled Transport: Supply Chain Challenges and Solutions. *P T* **43**, 154–170 (2018).
48. Manning, M. C., Chou, D. K., Murphy, B. M., Payne, R. W. & Katayama, D. S. Stability of protein pharmaceuticals: An update. *Pharm. Res.* **27**, 544–575 (2010).
49. Mensink, M. A., Frijlink, H. W., van der Voort Maarschalk, K. & Hinrichs, W. L. J. How sugars protect proteins in the solid state and during drying (review): Mechanisms of stabilization in relation to stress conditions. *Eur. J. Pharm. Biopharm.* **114**, 288–295 (2017).
50. Patel, J., Kothari, R., Tunga, R., Ritter, N. M. & Tunga, B. S. Stability considerations for biopharmaceuticals, Part 1: Overview of protein and peptide degradation pathways. *Bioprocess Int.* **9**, 20–31 (2011).
51. Karlsson, J. O. M. & Toner, M. Long-term storage of tissues by cryopreservation: critical issues. *Biomaterials* **17**, 243–256 (1996).
52. Ozkavukcu, S. & Erdemli, E. Cryopreservation: basic knowledge and biophysical effects. *J. Ankara Med. Sch.* **24**, 187–196 (2002).
53. Powrie, W. D. 1038_s4157.-018-0071-5. ri. Chemical effects during storage of frozen foods. *J. Chem. Educ.* **61**, 340 (1984).
54. Bischof, J. C. & He, X. Thermal Stability of Proteins. *Ann. N. Y. Acad. Sci.* **1066**, 12–33 (2006).
55. Dulloo, M. E. *et al.* Cost Efficiency of Cryopreservation as a Long-Term Conservation Method for Coffee Genetic Resources. *Crop Sci.* **49**, 2123–2138 (2009).
56. Franks, F. Freeze-drying of bioproducts: Putting principles into practice. *Eur. J. Pharm. Biopharm.* **45**, 221–229 (1998).
57. Ratti, C. Hot air and freeze-drying of high-value foods: a review. *J. Food Eng.* **49**, 311–319 (2001).
58. Liu, W., Zhang, M., Adhikari, B. & Chen, J. A novel strategy for improving drying efficiency and quality of cream mushroom soup based on microwave pre-gelatinization and infrared freeze-drying. *Innov. Food Sci. Emerg. Technol.* **66**, 102516 (2020).

59. Tran, P. H. L., Lee, B.-J. & Tran, T. T. D. Strategies and formulations of freeze-dried tablets for controlled drug delivery. *Int. J. Pharm.* **597**, 120373 (2021).
60. Jiang, H., Zhang, M. & Adhikari, B. Fruit and vegetable powders. in *Woodhead Publishing Series in Food Science, Technology and Nutrition* (eds. Bhandari, B., Bansal, N., Zhang, M. & Schuck, P. B. T.-H. of F. P.) 532–552 (Woodhead Publishing, 2013). doi:https://doi.org/10.1533/9780857098672.3.532
61. Carter, B., Patel, H., Barbano, D. M. & Drake, M. The effect of spray drying on the difference in flavor and functional properties of liquid and dried whey proteins, milk proteins, and micellar casein concentrates. *J. Dairy Sci.* **101**, 3900–3909 (2018).
62. Dulal, P. Investigation of sugar-membrane vaccine stabilisation for improved vaccine thermostability and delivery. *PhD thesis*
63. Dulal, P. *et al.* Potency of a thermostabilised chimpanzee adenovirus Rift Valley Fever vaccine in cattle. *Vaccine* **34**, 2296–2298 (2016).
64. Alcock, R. *et al.* Long-Term Thermostabilization of Live Poxviral and Adenoviral Vaccine Vectors at Supraphysiological Temperatures in Carbohydrate Glass. *Sci Transl Med.* **2**, 1–8 (2010).
65. Graber, K. M. *et al.* A rapid review of the impact of quarantine and restricted environments on children's play and the role of play in children's health. *Child. Care. Health Dev.* **47**, 143–153 (2021).
66. Lenzo, V., Quattropani, M. C., Sardella, A., Martino, G. & Bonanno, G. A. Depression, Anxiety, and Stress Among Healthcare Workers During the COVID-19 Outbreak and Relationships With Expressive Flexibility and Context Sensitivity . *Frontiers in Psychology* **12**, (2021).
67. Geraldi, M. S., Bavaresco, M. V, Triana, M. A., Melo, A. P. & Lamberts, R. Addressing the impact of COVID-19 lockdown on energy use in municipal buildings: A case study in Florianópolis, Brazil. *Sustain. Cities Soc.* **69**, 102823 (2021).
68. Chau, C. H., Strope, J. D. & Figg, W. D. COVID-19 Clinical Diagnostics and Testing Technology. *Pharmacother. J. Hum. Pharmacol. Drug Ther.* **40**, 857–868 (2020).
69. Xun, G., Lane, S. T., Petrov, V. A., Pepa, B. E. & Zhao, H. A rapid, accurate, scalable, and portable testing system for COVID-19 diagnosis. *Nat. Commun.* **12**, 2905 (2021).
70. Crozier, A., Rajan, S., Buchan, I. & McKee, M. Put to the test: use of rapid testing technologies for covid-19. *BMJ* **372**, n208 (2021).
71. Rai, P., Kumar, B. K., Deekshit, V. K., Karunasagar, I. & Karunasagar, I. Detection technologies and recent developments in the diagnosis of COVID-19 infection. *Appl. Microbiol. Biotechnol.* **105**, 441–455 (2021).
72. Huang, W. E. *et al.* RT-LAMP for rapid diagnosis of coronavirus SARS-CoV-2. *Microb. Biotechnol.* **13**, 950–961 (2020).
73. Aoki, M. N. *et al.* Colorimetric RT-LAMP SARS-CoV-2 diagnostic sensitivity relies on color interpretation and viral load. *Sci. Rep.* **11**, 9026 (2021).
74. Thompson, D. & Lei, Y. Mini review: Recent progress in RT-LAMP enabled COVID-19 detection. *Sensors and Actuators Reports* **2**, 100017 (2020).
75. Oatel, J. Stability Considerations fro Biopharmaceuticals: Overview of protein and Peptide Degradation Pathways. *Bioprocess Int.* (2011).
76. Mbanya, J. C., Sandow, J., Landgraf, W. & Owens, D. R. Recombinant

Human Insulin in Global Diabetes Management - Focus on Clinical Efficacy. *Eur. Endocrinol.* **13**, 21–25 (2017).
77. Krause, M. E. & Sahin, E. Chemical and physical instabilities in manufacturing and storage of therapeutic proteins. *Curr. Opin. Biotechnol.* **60**, 159–167 (2019).
78. Chang, L. L. & Pikal, M. J. Mechanisms of protein stabilization in the solid state. *J. Pharm. Sci.* **98**, 2886–2908 (2009).
79. Rabe, M., Verdes, D. & Seeger, S. Understanding protein adsorption phenomena at solid surfaces. *Adv. Colloid Interface Sci.* **162**, 87–106 (2011).
80. England, J. L. & Haran, G. Role of solvation effects in protein denaturation: from thermodynamics to single molecules and back. *Annu. Rev. Phys. Chem.* **62**, 257–277 (2011).
81. Jiang, L. *et al.* Relationship between surface hydrophobicity and structure of soy protein isolate subjected to different ionic strength. *Int. J. Food Prop.* **18**, 1059–1074 (2015).
82. Weiss, W. F., Young, T. M. & Roberts, C. J. Principles, approaches, and challenges for predicting protein aggregation rates and shelf life. *J. Pharm. Sci.* **98**, 1246–1277 (2009).
83. Crowe, J. H., Carpenter, J. F., Crowe, L. M. & Anchordoguy, T. J. Are freezing and dehydration similar stress vectors? A comparison of modes of interaction of stabilizing solutes with biomolecules. *Cryobiology* **27**, 219–231 (1990).
84. Crowe, J. H., Crowe, L. M. & Carpenter, J. F. Preserving Dry Biomaterials: The Water Replacement Hypothesis, Part 1, BIOPHARM -EUGENE-. *BIOPHARM -EUGENE-* **6**, 28 (1993).
85. Nicholls, A., Sharp, K. A. & Honig, B. Protein folding and association: insights from the interfacial and thermodynamic properties of hydrocarbons. *Proteins* **11**, 281–296 (1991).
86. Butreddy, A., Janga, K. Y., Ajjarapu, S., Sarabu, S. & Dudhipala, N. Instability of therapeutic proteins — An overview of stresses, stabilization mechanisms and analytical techniques involved in lyophilized proteins. *Int. J. Biol. Macromol.* **167**, 309–325 (2021).
87. Privalov, P. L. Cold Denaturation of Protein. *Crit. Rev. Biochem. Mol. Biol.* **25**, 281–306 (1990).
88. Franks, F. Protein Destabilization at Low Temperatures. in *Protein Stability* (eds. Anfinsen, C. B., Richards, F. M., Edsall, J. T. & Eisenberg, D. S. B. T.-A. in P. C.) **46**, 105–139 (Academic Press, 1995).
89. Narhi, L. O., Philo, J. S., Sun, B., Chang, B. S. & Arakawa, T. Reversibility of heat-induced denaturation of the recombinant human megakaryocyte growth and development factor. *Pharm. Res.* **16**, 799–807 (1999).
90. Jonas, J., Ballard, L. & Nash, D. High-Resolution, High-Pressure NMR Studies of Proteins. *Biophys. J.* **75**, 445–452 (1998).
91. Babu, C. R., Hilser, V. J. & Wand, A. J. Direct access to the cooperative substructure of proteins and the protein ensemble via cold denaturation. *Nat. Struct. Mol. Biol.* **11**, 352–357 (2004).
92. Davidovic, M., Mattea, C., Qvist, J. & Halle, B. Protein Cold Denaturation as Seen From the Solvent. *J. Am. Chem. Soc.* **131**, 1025–1036 (2009).
93. Dias, C. L., Ala-Nissila, T., Karttunen, M., Vattulainen, I. & Grant, M. Microscopic Mechanism for Cold Denaturation. *Phys. Rev. Lett.* **100**, 118101 (2008).

94. Matysiak, S., Debenedetti, P. G. & Rossky, P. J. Role of Hydrophobic Hydration in Protein Stability: A 3D Water-Explicit Protein Model Exhibiting Cold and Heat Denaturation. *J. Phys. Chem. B* **116**, 8095–8104 (2012).
95. Arsiccio, A., McCarty, J., Pisano, R. & Shea, J.-E. Heightened Cold-Denaturation of Proteins at the Ice–Water Interface. *J. Am. Chem. Soc.* **142**, 5722–5730 (2020).
96. Arsiccio, A. & Pisano, R. The Ice-Water Interface and Protein Stability: A Review. *J. Pharm. Sci.* **109**, 2116–2130 (2020).
97. Bhatnagar, B. S., Bogner, R. H. & Pikal, M. J. Protein stability during freezing: separation of stresses and mechanisms of protein stabilization. *Pharm. Dev. Technol.* **12**, 505–523 (2007).
98. Chang, B. S., Kendrick, B. S. & Carpenter, J. F. Surface-induced denaturation of proteins during freezing and its inhibition by surfactants. *J. Pharm. Sci.* **85**, 1325–1330 (1996).
99. Bhatnagar, B. S., Pikal, M. J. & Bogner, R. H. Study of the individual contributions of ice formation and freeze-concentration on isothermal stability of lactate dehydrogenase during freezing. *J. Pharm. Sci.* **97**, 798–814 (2008).
100. Nakanishi, K., Sakiyama, T. & Imamura, K. On the adsorption of proteins on solid surfaces, a common but very complicated phenomenon. *J. Biosci. Bioeng.* **91**, 233–244 (2001).
101. Kyriakides, T. R. Chapter 5 - Molecular Events at Tissue–Biomaterial Interface. in (ed. Badylak, S. F. B. T.-H. R. to B.) 81–116 (Academic Press, 2015). doi:https://doi.org/10.1016/B978-0-12-800196-7.00005-0
102. Roach, P., Farrar, D. & Perry, C. C. Interpretation of Protein Adsorption: Surface-Induced Conformational Changes. *J. Am. Chem. Soc.* **127**, 8168–8173 (2005).
103. Carpenter, J. F. *et al.* Overlooking subvisible particles in therapeutic protein products: gaps that may compromise product quality. *J. Pharm. Sci.* **98**, 1201–1205 (2009).
104. Mutlu, S., Çökeliler, D. & Mutlu, M. Modification of food contacting surfaces by plasma polymerization technique. Part II: Static and dynamic adsorption behavior of a model protein “bovine serum albumin” on stainless steel surface. *J. Food Eng.* **78**, 494–499 (2007).
105. Lum, K., Chandler, D. & Weeks, J. D. Hydrophobicity at Small and Large Length Scales. *J. Phys. Chem. B* **103**, 4570–4577 (1999).
106. Wallqvist, A. & Berne, B. J. Computer Simulation of Hydrophobic Hydration Forces on Stacked Plates at Short Range. *J. Phys. Chem.* **99**, 2893–2899 (1995).
107. Grigera, J. R. & McCarthy, A. N. The behavior of the hydrophobic effect under pressure and protein denaturation. *Biophys. J.* **98**, 1626–1631 (2010).
108. Lu, J. R. *et al.* The denaturation of lysozyme layers adsorbed at the hydrophobic solid/liquid surface studied by neutron reflection. *J. Colloid Interface Sci.* **206**, 212–223 (1998).
109. Wertz, C. F. & Santore, M. M. Adsorption and Relaxation Kinetics of Albumin and Fibrinogen on Hydrophobic Surfaces: Single-Species and Competitive Behavior. *Langmuir* **15**, 8884–8894 (1999).
110. Sethuraman, A. & Belfort, G. Protein structural perturbation and aggregation on homogeneous surfaces. *Biophys. J.* **88**, 1322–1333 (2005).
111. Norde, W. Driving forces for protein adsorption at solid surfaces. *Macromol.*

Symp. **103**, 5–18 (1996).
112. Norde, W. & Giacomelli, C. E. BSA structural changes during homomolecular exchange between the adsorbed and the dissolved states. *J. Biotechnol.* **79**, 259–268 (2000).
113. Norde, W. My voyage of discovery to proteins in flatland ...and beyond. *Colloids Surf. B. Biointerfaces* **61**, 1–9 (2008).
114. Mackenzie, C. D. *et al.* Ranaspumin-2: Structure and Function of a Surfactant Protein from the Foam Nests of a Tropical Frog. *Biophys. J.* **96**, 4984–4992 (2009).
115. Baujard-Lamotte, L., Noinville, S., Goubard, F., Marque, P. & Pauthe, E. Kinetics of conformational changes of fibronectin adsorbed onto model surfaces. *Colloids Surf. B. Biointerfaces* **63**, 129–137 (2008).
116. Vieira, E. P., Rocha, S., Carmo Pereira, M., Möhwald, H. & Coelho, M. A. N. Adsorption and Diffusion of Plasma Proteins on Hydrophilic and Hydrophobic Surfaces: Effect of Trifluoroethanol on Protein Structure. *Langmuir* **25**, 9879–9886 (2009).
117. Noinville, S., Bruston, F., El Amri, C., Baron, D. & Nicolas, P. Conformation, orientation, and adsorption kinetics of dermaseptin B2 onto synthetic supports at aqueous/solid interface. *Biophys. J.* **85**, 1196–1206 (2003).
118. Hlady, V. V & Buijs, J. Protein adsorption on solid surfaces. *Curr. Opin. Biotechnol.* **7**, 72–77 (1996).
119. Czeslik, C., Royer, C., Hazlett, T. & Mantulin, W. Reorientational Dynamics of Enzymes Adsorbed on Quartz: A Temperature-Dependent Time-Resolved TIRF Anisotropy Study. *Biophys. J.* **84**, 2533–2541 (2003).
120. Chen, V., Kim, K. J. & Fane, A. G. Effect of membrane morphology and operation on protein deposition in ultrafiltration membranes. *Biotechnol. Bioeng.* **47**, 174–180 (1995).
121. Maa, Y. F. & Hsu, C. C. Membrane fouling in sterile filtration of recombinant human growth hormone. *Biotechnol. Bioeng.* **50**, 319–328 (1996).
122. Roberts, C. J. Non-native protein aggregation kinetics. *Biotechnol. Bioeng.* **98**, 927–938 (2007).
123. Stefani, M. & Dobson, C. M. Protein aggregation and aggregate toxicity: new insights into protein folding, misfolding diseases and biological evolution. *J. Mol. Med. (Berl).* **81**, 678–699 (2003).
124. Cromwell, M. E. M., Hilario, E. & Jacobson, F. Protein aggregation and bioprocessing. *AAPS J.* **8**, E572-9 (2006).
125. Trevino, S. R., Scholtz, J. M. & Pace, C. N. Measuring and increasing protein solubility. *J. Pharm. Sci.* **97**, 4155–4166 (2008).
126. Matheus, S., Friess, W., Schwartz, D. & Mahler, H.-C. Liquid high concentration IgG1 antibody formulations by precipitation. *J. Pharm. Sci.* **98**, 3043–3057 (2009).
127. Reubsaet, J. L. E. *et al.* Analytical techniques used to study the degradation of proteins and peptides: chemical instability. *J. Pharm. Biomed. Anal.* **17**, 955–978 (1998).
128. Topp, E. M. *et al.* Chemical Instability in Peptide and Protein Pharmaceuticals. *Formulation and Process Development Strategies for Manufacturing Biopharmaceuticals* 41–67 (2010). doi:https://doi.org/10.1002/9780470595886.ch2
129. Nilsson, M. R., Driscoll, M. & Raleigh, D. P. Low levels of asparagine deamidation can have a dramatic effect on aggregation of amyloidogenic

peptides: implications for the study of amyloid formation. *Protein Sci.* **11**, 342–349 (2002).
130. Takata, T., Oxford, J. T., Demeler, B. & Lampi, K. J. Deamidation destabilizes and triggers aggregation of a lens protein, betaA3-crystallin. *Protein Sci.* **17**, 1565–1575 (2008).
131. Takata, T., Oxford, J. T., Brandon, T. R. & Lampi, K. J. Deamidation alters the structure and decreases the stability of human lens βA3-crystallin. *Biochemistry* **46**, 8861–8871 (2007).
132. Robinson, N. E. & Robinson, A. B. Deamidation of human proteins. *Proc. Natl. Acad. Sci.* **98**, 12409–12413 (2001).
133. Song, Y., Schowen, R. L., Borchardt, R. T. & Topp, E. M. Effect of 'pH' on the rate of asparagine deamidation in polymeric formulations: 'pH'–rate profile. *J. Pharm. Sci.* **90**, 141–156 (2001).
134. Liu, H., Gaza-Bulseco, G., Faldu, D., Chumsae, C. & Sun, J. Heterogeneity of monoclonal antibodies. *J. Pharm. Sci.* **97**, 2426–2447 (2008).
135. Wang, W., Singh, S., Zeng, D. L., King, K. & Nema, S. Antibody Structure, Instability, and Formulation. *J. Pharm. Sci.* **96**, 1–26 (2007).
136. Zheng, J. Y. & Janis, L. J. Influence of pH, buffer species, and storage temperature on physicochemical stability of a humanized monoclonal antibody LA298. *Int. J. Pharm.* **308**, 46–51 (2006).
137. Robinson, N. E. & Robinson, A. Molecular Clocks Deamidation of Asparaginyl and Glutaminyl Residues in Peptides and Proteins. *Althouse Press Cave Junction OR* (2004).
138. Ohtake, S., Feng, S. & Shalaev, E. Effect of Water on the Chemical Stability of Amorphous Pharmaceuticals: 2. Deamidation of Peptides and Proteins. *J. Pharm. Sci.* **107**, 42–56 (2018).
139. Pajares, M. *et al.* Redox control of protein degradation. *Redox Biol.* **6**, 409–420 (2015).
140. Reeg, S. & Grune, T. Protein Oxidation in Aging: Does It Play a Role in Aging Progression? *Antioxid. Redox Signal.* **23**, 239–255 (2014).
141. Manning, M. C., Chou, D. K., Murphy, B. M., Payne, R. W. & Katayama, D. S. Stability of protein pharmaceuticals: An update. *Pharm. Res.* **27**, 544–575 (2010).
142. Branca, C. *et al.* Tetrahedral order in homologous disaccharide-water mixtures. *J. Chem. Phys.* **122**, 174513 (2005).
143. Li, S., Schöneich, C. & Borchardt, R. T. Chemical instability of protein pharmaceuticals: Mechanisms of oxidation and strategies for stabilization. *Biotechnol. Bioeng.* **48**, 490–500 (1995).
144. Pikal, M. J., Dellerman, K. & Roy, M. L. Formulation and stability of freeze-dried proteins: effects of moisture and oxygen on the stability of freeze-dried formulations of human growth hormone. *Dev. Biol. Stand.* **74**, 21–28 (1992).
145. Hamburger, R., Azaz, E. & Donbrow, M. Autoxidation of polyoxyethylenic non-ionic surfactants and of polyethylene glycols. *Pharm. Acta Helv.* **50**, 10–17 (1975).
146. Li, S. *et al.* Effects of Reducing Sugars on the Chemical Stability of Human Relaxin in the Lyophilized State. *J. Pharm. Sci.* **85**, 873–877 (1996).
147. Chang, B. S., Randall, C. S. & Lee, Y. S. Stabilization of Lyophilized Porcine Pancreatic Elastase. *Pharm. Res.* **10**, 1478–1483 (1993).
148. Li, S., Schöneich, C., Wilson, G. S. & Borchardt, R. T. Chemical pathways of peptide degradation. V. Ascorbic acid promotes rather than inhibits the

oxidation of methionine to methionine sulfoxide in small model peptides. *Pharm. Res.* **10**, 1572–1579 (1993).
149. Li, S., Patapoff, T. W., Nguyen, T. H. & Borchardt, R. T. Inhibitory effect of sugars and polyols on the metal-catalyzed oxidation of human relaxin. *J. Pharm. Sci.* **85**, 868–872 (1996).
150. Trivedi, M. V, Laurence, J. S. & Siahaan, T. J. The role of thiols and disulfides on protein stability. *Curr. Protein Pept. Sci.* **10**, 614–625 (2009).
151. Rabdano, S. O. *et al.* Onset of disorder and protein aggregation due to oxidation-induced intermolecular disulfide bonds: case study of RRM2 domain from TDP-43. *Sci. Rep.* **7**, 11161 (2017).
152. Feige, M. J., Braakman, I. & Hendershot, L. M. CHAPTER 1.1 Disulfide Bonds in Protein Folding and Stability. in *Oxidative Folding of Proteins: Basic Principles, Cellular Regulation and Engineering* 1–33 (The Royal Society of Chemistry, 2018). doi:10.1039/9781788013253-00001
153. Costantino, H. R., Griebenow, K., Mishra, P., Langer, R. & Klibanov, A. M. Fourier-transform infrared spectroscopic investigation of protein stability in the lyophilized form. *Biochim. Biophys. Acta* **1253**, 69–74 (1995).
154. Liu, W. R., Langer, R. & Klibanov, A. M. Moisture-induced aggregation of lyophilized proteins in the solid state. *Biotechnol. Bioeng.* **37**, 177–184 (1991).
155. Costantino, H. R., Langer, R. & Klibanov, A. M. Solid-Phase Aggregation of Proteins under Pharmaceutically Relevant Conditions†. *J. Pharm. Sci.* **83**, 1662–1669 (1994).
156. Alegre-Cebollada, J., Kosuri, P., Rivas-Pardo, J. A. & Fernández, J. M. Direct observation of disulfide isomerization in a single protein. *Nat. Chem.* **3**, 882–887 (2011).
157. Shaked, Z., Szajewski, R. P. & Whitesides, G. M. Rates of thiol-disulfide interchange reactions involving proteins and kinetic measurements of thiol pKa values. *Biochemistry* **19**, 4156–4166 (1980).
158. Klibanov, A. M. & Schefiliti, J. A. On the relationship between conformation and stability in solid pharmaceutical protein formulations. *Biotechnol. Lett.* **26**, 1103–1106 (2004).
159. Rathore, N. & Rajan, R. S. Current Perspectives on Stability of Protein Drug Products during Formulation, Fill and Finish Operations. *Biotechnol. Prog.* **24**, 504–514 (2008).
160. Bye, J., Platts, L. & Falconer, R. Biopharmaceutical liquid formulation: A review of the science of protein stability and solubility in aqueous environments. *Biotechnol. Lett.* **36**, 869–875 (2014).
161. Singh, S. Storage considerations as part of the formulation development program for biologics. *Am. Pharm. Rev.* **10**, 26–33 (2007).
162. Webb, S. D., Webb, J., Hughes, T., Sesin, D. & Kincaid, A. Freezing bulk-scale biopharmaceuticals using common techniques - and the magnitude of freeze-concentration. *BioPharm* **15**, 22-+ (2002).
163. Singh, S., Kolhe, P., Wang, W. & Nema, S. Large-scale freezing of biologics: A Practitioner's review, part 2: Practical advice. *Bioprocess Int.* **7**, 34–42 (2009).
164. Kolhe, P., Holding, E., Lary, A., Chico, S. & Singh, S. K. Large-scale freezing of biologics: Understanding protein and solute concentration changes in a cryovessel - Part 2. *BioPharm Int.* **23**, 40–49 (2010).
165. Jang, T. H. *et al.* Cryopreservation and its clinical applications. *Integr. Med.*

Res. **6**, 12–18 (2017).
166. Graziano, G., Catanzano, F., Riccio, A. & Barone, G. A Reassessment of the Molecular Origin of Cold Denaturation. *J. Biochem.* **122**, 395–401 (1997).
167. Wang, W. *Lyophilization and development of solid protein pharmaceuticals*. *International Journal of Pharmaceutics* **203**, (2000).
168. Searles, J. A., Carpenter, J. F. & Randolph, T. W. The ice nucleation temperature determines the primary drying rate of lyophilization for samples frozen on a temperature-controlled shelf. *J. Pharm. Sci.* **90**, 860–871 (2001).
169. Shamlou, P. A., Breen, L. H., Bell, W. V, Pollo, M. & Thomas, B. A. A new scaleable freeze-thaw technology for bulk protein solutions. *Biotechnol. Appl. Biochem.* **46**, 13–26 (2007).
170. Mao, Y.-J., Sheng, X.-R. & Pan, X.-M. The effects of NaCl concentration and pH on the stability of hyperthermophilic protein Ssh10b. *BMC Biochem.* **8**, 28 (2007).
171. Arsiccio, A., Giorsello, P., Marenco, L. & Pisano, R. Considerations on Protein Stability During Freezing and Its Impact on the Freeze-Drying Cycle: A Design Space Approach. *J. Pharm. Sci.* **109**, 464–475 (2020).
172. Pikal-Cleland, K. A., Rodríguez-Hornedo, N., Amidon, G. L. & Carpenter, J. F. Protein denaturation during freezing and thawing in phosphate buffer systems: monomeric and tetrameric beta-galactosidase. *Arch. Biochem. Biophys.* **384**, 398–406 (2000).
173. Gómez, G., Pikal, M. J. & Rodríguez-Hornedo, N. Effect of initial buffer composition on pH changes during far-from-equilibrium freezing of sodium phosphate buffer solutions. *Pharm. Res.* **18**, 90–97 (2001).
174. Kilbride, P. & Morris, G. J. Viscosities encountered during the cryopreservation of dimethyl sulphoxide systems. *Cryobiology* **76**, 92–97 (2017).
175. Strambini, G. B. & Gabellieri, E. Proteins in frozen solutions: evidence of ice-induced partial unfolding. *Biophys. J.* **70**, 971–976 (1996).
176. Cao, E., Chen, Y., Cui, Z. & Foster, P. R. Effect of freezing and thawing rates on denaturation of proteins in aqueous solutions. *Biotechnol. Bioeng.* **82**, 684–690 (2003).
177. Wowk, B. Thermodynamic aspects of vitrification. *Cryobiology* **60**, 11–22 (2010).
178. Amorij, J.-P. *et al.* Rational design of an influenza subunit vaccine powder with sugar glass technology: Preventing conformational changes of haemagglutinin during freezing and freeze-drying. *Vaccine* **25**, 6447–6457 (2007).
179. Zhang, Y. & Ertbjerg, P. On the origin of thaw loss: Relationship between freezing rate and protein denaturation. *Food Chem.* **299**, 125104 (2019).
180. Miller, M. A. *et al.* Frozen-State Storage Stability of a Monoclonal Antibody: Aggregation is Impacted by Freezing Rate and Solute Distribution. *J. Pharm. Sci.* **102**, 1194–1208 (2013).
181. Hansen, L. J. J., Daoussi, R., Vervaet, C., Remon, J. P. & De Beer, T. R. M. Freeze-drying of live virus vaccines: A review. *Vaccine* **33**, 5507–5519 (2015).
182. Baboo, J. *et al.* The Impact of Varying Cooling and Thawing Rates on the Quality of Cryopreserved Human Peripheral Blood T Cells. *Sci. Rep.* **9**, 3417 (2019).
183. Thielmann, A., Viehmann, A. & Weltermann, B. M. Effectiveness of a web-

based education program to improve vaccine storage conditions in primary care (Keep Cool): study protocol for a randomized controlled trial. *Trials* **16**, 301 (2015).
184. Chesko, J., Fox, C., Dutill, T., Vedvick, T. & Reed, S. Lyophilization and Stabilization of Vaccines. in *Development of Vaccines* 385–397 (John Wiley & Sons, Inc., 2011). doi:10.1002/9781118023648.ch14
185. Kartoglu, U. & Milstien, J. Tools and approaches to ensure quality of vaccines throughout the cold chain. *Expert Rev. Vaccines* **13**, 843–854 (2014).
186. Kumru, O. S. *et al.* Vaccine instability in the cold chain: Mechanisms, analysis and formulation strategies. *Biologicals* **42**, 237–259 (2014).
187. Larena, I. *et al.* Vaccine cold chain interruption in a primary care centre and economic evaluation ☪. **27**, 44–48 (2017).
188. Wolfson, L. J. *et al.* Estimating the costs of achieving the WHO-UNICEF Global Immunization Vision and Strategy, 2006-2015. *Bull. World Health Organ.* **86**, 27–39 (2008).
189. Cheyne, J. Vaccine Delivery Management. *Rev. Infect. Dis.* **11**, S617–S622 (1989).
190. Bishai, D. M., Bhatt, S., Miller, L. T. & Hayden, G. F. Vaccine Storage Practices in Pediatric Offices. *Pediatrics* **89**, 193 LP – 196 (1992).
191. Zhang, J. *et al.* Stabilization of vaccines and antibiotics in silk and eliminating the cold chain. *Proc. Natl. Acad. Sci.* **109**, 11981 LP – 11986 (2012).
192. Schlehuber, L. D. *et al.* Towards ambient temperature-stable vaccines: The identification of thermally stabilizing liquid formulations for measles virus using an innovative high-throughput infectivity assay. *Vaccine* **29**, 5031–5039 (2011).
193. Ueberreiter, K. Change of water structure by solvents and polymers. *Colloid Polym. Sci.* **260**, 37–45 (1982).
194. Marcus, Y. Effect of Ions on the Structure of Water: Structure Making and Breaking. *Chem. Rev.* **109**, 1346–1370 (2009).
195. Capicciotti, C. J. *et al.* Small Molecule Ice Recrystallization Inhibitors Enable Freezing of Human Red Blood Cells with Reduced Glycerol Concentrations. *Sci. Rep.* **5**, 9692 (2015).
196. Patist, A. & Zoerb, H. Preservation mechanisms of trehalose in food and biosystems. *Colloids Surf. B. Biointerfaces* **40**, 107–113 (2005).
197. Skrabanja, A. T., de Meere, A. L., de Ruiter, R. A. & van den Oetelaar, P. J. Lyophilization of biotechnology products. *PDA J. Pharm. Sci. Technol.* **48**, 311–317 (1994).
198. Kar, M., Chourasiya, Y., Maheshwari, R. & Tekade, R. K. Chapter 2 - Current Developments in Excipient Science: Implication of Quantitative Selection of Each Excipient in Product Development. in *Advances in Pharmaceutical Product Development and Research* (ed. Tekade, R. K. B. T.-B. F. of D. D.) 29–83 (Academic Press, 2019). doi:https://doi.org/10.1016/B978-0-12-817909-3.00002-9
199. Piszkiewicz, S. & Pielak, G. J. Protecting Enzymes from Stress-Induced Inactivation. *Biochemistry* **58**, 3825–3833 (2019).
200. Carpenter, J. F., Prestrelski, S. J. & Arakawa, T. Separation of freezing- and drying-induced denaturation of lyophilized proteins using stress-specific stabilization. I. Enzyme activity and calorimetric studies. *Arch. Biochem. Biophys.* **303**, 456–464 (1993).
201. Saluja, V. *et al.* A comparison between spray drying and spray freeze drying

to produce an influenza subunit vaccine powder for inhalation. *J. Control. Release* **144**, 127–133 (2010).
202. Wathen, B. & Jia, Z. 25 - Controlling the Freezing Process with Antifreeze Proteins. in (ed. Sun, D.-W. B. T.-E. T. for F. P.) 653–674 (Academic Press, 2005). doi:https://doi.org/10.1016/B978-012676757-5/50027-X
203. DeVries, A. L. & Wohlschlag, D. E. Freezing resistance in some Antarctic fishes. *Science* **163**, 1073—1075 (1969).
204. Srivastava, L. M. CHAPTER 16 - Abscisic Acid and Stress Tolerance in Plants. in (ed. Srivastava, L. M. B. T.-P. G. and D.) 381–412 (Academic Press, 2002). doi:https://doi.org/10.1016/B978-012660570-9/50158-1
205. Kristiansen, E. & Zachariassen, K. E. The mechanism by which fish antifreeze proteins cause thermal hysteresis. *Cryobiology* **51**, 262–280 (2005).
206. Ustun, N. S. & Turhan, S. Antifreeze Proteins: Characteristics, Function, Mechanism of Action, Sources and Application to Foods. *J. Food Process. Preserv.* **39**, 3189–3197 (2015).
207. Emami, F., Vatanara, A., Park, E. J. & Na, D. H. Drying technologies for the stability and bioavailability of biopharmaceuticals. *Pharmaceutics* **10**, 1–22 (2018).
208. Grasmeijer, N., Tiraboschi, V., Woerdenbag, H. J., Frijlink, H. W. & Hinrichs, W. L. J. Identifying critical process steps to protein stability during spray drying using a vibrating mesh or a two-fluid nozzle. *Eur. J. Pharm. Sci.* **128**, 152–157 (2019).
209. Wang, S. H., Kirwan, S. M., Abraham, S. N., Staats, H. F. & Hickey, A. J. Stable dry powder formulation for nasal delivery of anthrax vaccine. *J. Pharm. Sci.* **101**, 31–47 (2012).
210. Garidel, P., Pevestorf, B. & Bahrenburg, S. Stability of buffer-free freeze-dried formulations: A feasibility study of a monoclonal antibody at high protein concentrations. *Eur. J. Pharm. Biopharm. Off. J. Arbeitsgemeinschaft fur Pharm. Verfahrenstechnik e.V* **97**, 125–139 (2015).
211. Liao, Y.-H., Brown, M. B. & Martin, G. P. Investigation of the stabilisation of freeze-dried lysozyme and the physical properties of the formulations. *Eur. J. Pharm. Biopharm. Off. J. Arbeitsgemeinschaft fur Pharm. Verfahrenstechnik e.V* **58**, 15–24 (2004).
212. Imamura, K., Ogawa, T., Sakiyama, T. & Nakanishi, K. Effects of types of sugar on the stabilization of protein in the dried state. *J. Pharm. Sci.* **92**, 266–274 (2003).
213. Tian, F., Sane, S. & Rytting, J. H. Calorimetric investigation of protein/amino acid interactions in the solid state. *Int. J. Pharm.* **310**, 175—186 (2006).
214. Wahl, V., Khinast, J. & Paudel, A. Lyophilized protein powders: A review of analytical tools for root cause analysis of lot-to-lot variability. *TrAC - Trends Anal. Chem.* **82**, 468–491 (2016).
215. Rival, J. M. *et al.* Understanding Lyophilization Formulation Development. *Phamaceutical Technol.* 10–18 (2004).
216. Kasper, J. C. & Friess, W. The freezing step in lyophilization: Physico-chemical fundamentals, freezing methods and consequences on process performance and quality attributes of biopharmaceuticals. *Eur. J. Pharm. Biopharm.* **78**, 248–263 (2011).
217. Chang, B. S. & Fischer, N. L. Development of an efficient single-step freeze-drying cycle for protein formulations. *Pharm. Res.* **12**, 831–837 (1995).

218. Peters, B.-H. *et al.* Effects of cooling rate in microscale and pilot scale freeze-drying–variations in excipient polymorphs and protein secondary structure. *Eur. J. Pharm. Sci.* **95**, 72–81 (2016).
219. Tang, X. & Pikal, M. J. Design of Freeze-Drying Processes for Pharmaceuticals: Practical Advice. *Pharm. Res.* **21**, 191–200 (2004).
220. Pikal, M. J. & Shah, S. R. The collapse temperature in freeze-drying: dependence on measurement methodology and rate of water removal from the glassy phase, Int. *J. Pharm.* **62**, 165–186 (1990).
221. Karathanos, V. T., Anglea, S. A. & Karel, M. Structural collapse of plant materials during freeze-drying. *J. Therm. Anal.* **47**, 1451–1461 (1996).
222. ITO, K. Freeze drying of pharmaceuticals. Eutectic temperature and collapse temperature of solute matrix upon freeze drying of three-component systems. *Chem. Pharm. Bull.* **19**, 1095–1102 (1971).
223. De Meyer, L. *et al.* Dual chamber cartridges in a continuous pharmaceutical freeze-drying concept: Determination of the optimal dynamic infrared heater temperature during primary drying. *Int. J. Pharm.* **570**, 118631 (2019).
224. Lu, X. & Pikal, M. J. Freeze-drying of mannitol–trehalose–sodium chloride-based formulations: The impact of annealing on dry layer resistance to mass transfer and cake structure. *Pharm. Dev. Technol.* **9**, 85–95 (2004).
225. Fonseca, F., Passot, S., Lieben, P. & Marin, M. Collapse temperature of bacterial suspensions: the effect of cell type and concentration. *Cryo Letters* **25**, 425–434 (2004).
226. Abdul-Fattah, A. M., Kalonia, D. S. & Pikal, M. J. The challenge of drying method selection for protein pharmaceuticals: product quality implications. *J. Pharm. Sci.* **96**, 1886–1916 (2007).
227. Bano, G. *et al.* Primary Drying Optimization in Pharmaceutical Freeze-Drying: A Multivial Stochastic Modeling Framework. *Ind. Eng. Chem. Res.* **59**, 5056–5071 (2020).
228. Kett, V., Mcmahon, D. & Ward, K. Freeze-drying of protein pharmaceuticals: The application of thermal analysis. *Cryo Letters* **25**, 389–404 (2004).
229. Hottot, A., Vessot, S. & Andrieu, J. Determination of mass and heat transfer parameters during freeze-drying cycles of pharmaceutical products. *PDA J. Pharm. Sci. Technol.* **59**, 138–153 (2005).
230. Horn, J. & Friess, W. Detection of Collapse and Crystallization of Saccharide, Protein, and Mannitol Formulations by Optical Fibers in Lyophilization . *Frontiers in Chemistry* **6**, 4 (2018).
231. Mehmood, Y. & Farooq, U. Excipients Use in Parenteral and Lyophilized Formulation Development. *Open Sci. J. Pharm. Pharmacol.* **3**, 19–27 (2015).
232. Herman, B. D., Sinclair, B. D., Milton, N. & Nail, S. L. The Effect of Bulking Agent on the Solid-State Stability of Freeze-Dried Methylprednisolone Sodium Succinate. *Pharm. Res.* **11**, 1467–1473 (1994).
233. Lu, E., Ewing, S., Gatlin, L., Suryanarayanan, R. & Shalaev, E. The effect of bulking agents on the chemical stability of acid-sensitive compounds in freeze-dried formulations: Sucrose inversion study. *J. Pharm. Sci.* **98**, 3387–3396 (2009).
234. Drake, A. C. *et al.* Effect of water content on the glass transition temperature of mixtures of sugars, polymers, and penetrating cryoprotectants in physiological buffer. *PLoS One* **13**, e0190713 (2018).
235. Ratti, C. 3 - Freeze drying for food powder production. in *Handbook of Food Powders* (eds. Bhandari, B., Bansal, N., Zhang, M. & Schuck, P.) 57–84

(Woodhead Publishing, 2013). doi:https://doi.org/10.1533/9780857098672.1.57
236. Telikepalli, S. *et al.* Characterization of the physical stability of a lyophilized IgG1 mAb after accelerated shipping-like stress. *J. Pharm. Sci.* **104**, 495–507 (2015).
237. Ameri, M. & Maa, Y.-F. Spray Drying of Biopharmaceuticals: Stability and Process Considerations. *Dry. Technol.* **24**, 763–768 (2006).
238. Gauvin, W. H. Spray drying handbook (third edition) by K. Masters, 687 pages, George Godwin Limited (London) (1979); *AIChE J.* **26**, 702 (1980).
239. Percy, S. R. Improvement in drying and concentrating liquid substances by atomizing. *United states Pat. Off.* 2 (1872).
240. Ameri, M. & Maa, Y. F. Spray drying of biopharmaceuticals: Stability and process considerations. *Dry. Technol.* **24**, 763–768 (2006).
241. Ziaee, A. *et al.* Spray drying of pharmaceuticals and biopharmaceuticals: Critical parameters and experimental process optimization approaches. *Eur. J. Pharm. Sci.* **127**, 300–318 (2019).
242. Vishali, D. A., Monisha, J., Sivakamasundari, S. K., Moses, J. A. & Anandharamakrishnan, C. Spray freeze drying: Emerging applications in drug delivery. *J. Control. Release* **300**, 93–101 (2019).
243. Adler, M. & Lee, G. Stability and surface activity of lactate dehydrogenase in spray-dried trehalose. *J. Pharm. Sci.* **88**, 199–208 (1999).
244. Lee, G. Spray-Drying of Proteins BT - Rational Design of Stable Protein Formulations: Theory and Practice. in *Rational Design of Stable Protein Formulations* (eds. Carpenter, J. F. & Manning, M. C.) 135–158 (Springer US, 2002). doi:10.1007/978-1-4615-0557-0_6
245. Mumenthaler, M., Hsu, C. C. & Pearlman, R. Feasibility study on spray-drying protein pharmaceuticals: recombinant human growth hormone and tissue-type plasminogen activator. *Pharm. Res.* **11**, 12–20 (1994).
246. Maa, Y.-F., Ameri, M., Shu, C., Payne, L. G. & Chen, D. Influenza vaccine powder formulation development: spray-freeze-drying and stability evaluation. *J. Pharm. Sci.* **93**, 1912–1923 (2004).
247. Parsian, A. R. *et al.* Inhalable budesonide porous microparticles tailored by spray freeze drying technique. *Powder Technol.* **260**, 36–41 (2014).
248. Rahmati, M. R. *et al.* Effect of formulation ingredients on the physical characteristics of salmeterol xinafoate microparticles tailored by spray freeze drying. *Adv. Powder Technol.* **24**, 36–42 (2013).
249. Poursina, N., Vatanara, A., Rouini, M. R., Gilani, K. & Najafabadi, A. R. The effect of excipients on the stability and aerosol performance of salmon calcitonin dry powder inhalers prepared via the spray freeze drying process. *Acta Pharm.* **66**, 207–218 (2016).
250. Rogers, T. L. *et al.* A novel particle engineering technology to enhance dissolution of poorly water soluble drugs: spray-freezing into liquid. *Eur. J. Pharm. Biopharm.* **54**, 271–280 (2002).
251. Wanning, S., Süverkrüp, R. & Lamprecht, A. Pharmaceutical spray freeze drying. *Int. J. Pharm.* **488**, 136–153 (2015).
252. Poursina, N., Vatanara, A., Rouini, M. R., Gilani, K. & Rouholamini Najafabadi, A. Systemic delivery of parathyroid hormone (1-34) using spray freeze-dried inhalable particles. *Pharm. Dev. Technol.* **22**, 733–739 (2017).
253. Anandharamakrishnan, C., Rielly, C. D. & Stapley, A. G. F. Spray-freeze-drying of whey proteins at sub-atmospheric pressures. *Dairy Sci. Technol.*

90, 321–334 (2010).
254. Jangle, R. D. & Pisal, S. S. Vacuum foam drying: an alternative to lyophilization for biomolecule preservation. *Indian J. Pharm. Sci.* **74**, 91–100 (2012).
255. Hajare, A., Pisal, S. S. & More, H. N. Vacuum foam drying: New technology for preservation of sensitive biomolecules. *Eur. Ind. Pharm* **2**, 16–18 (2009).
256. Pisal, S., Wawde, G., Salvankar, S., Lade, S. & Kadam, S. Vacuum foam drying for preservation of LaSota virus: effect of additives. *Aaps Pharmscitech* **7**, E30–E37 (2006).
257. Day, J. B., Nguyen, H., Sharma, S. K., Al-Khaldi, S. F. & Hao, Y.-Y. D. Effect of dehydrated storage on the survival of Francisella tularensis in infant formula. *Food Microbiol.* **26**, 932–935 (2009).
258. Ohtake, S. *et al.* Formulation and Stabilization of Francisella tularensis Live Vaccine Strain. *J. Pharm. Sci.* **100**, 3076–3087 (2011).
259. Abdul-Fattah, A. M. *et al.* Drying-Induced Variations in Physico-Chemical Properties of Amorphous Pharmaceuticals and Their Impact on Stability II: Stability of a Vaccine. *Pharm. Res.* **24**, 715 (2007).
260. Ohtake, S. *et al.* Room temperature stabilization of oral, live attenuated Salmonella enterica serovar Typhi-vectored vaccines. *Vaccine* **29**, 2761–2771 (2011).
261. Walters, R. H. *et al.* Next Generation Drying Technologies for Pharmaceutical Applications. *J. Pharm. Sci.* **103**, 2673–2695 (2014).
262. Okuzono, T., Ozawa, K. & Doi, M. Simple Model of Skin Formation Caused by Solvent Evaporation in Polymer Solutions. *Phys. Rev. Lett.* **97**, 136103 (2006).
263. Yu, Y., Yang, A., Ye, H., Dye, J. F. & Cui, Z. Numerical study of the formation and drying kinetics of a capillary bridge of trehalose solution between two parallel hydrophilic fibres. *Chem. Eng. Sci.* **226**, 115849 (2020).
264. Saye, R. I. & Sethian, J. A. Multiscale modeling of membrane rearrangement, drainage, and rupture in evolving foams. *Science* **340**, 720–724 (2013).
265. Zimmerman, J. Functional metabolism: Regulation and adaptation: Storey, K. B. (ed.). *Biochem. Mol. Biol. Educ.* **33**, 75 (2005).
266. Bianchi, G., Gamba, A., Murelli, C., Salamini, F. & Bartels, D. Novel carbohydrate metabolism in the resurrection plant Craterostigma plantagineum. *Plant J.* **1**, 355–359 (1991).
267. Crowe, J. H., Crowe, L. M., Carpenter, J. F. & Aurell Wistrom, C. Stabilization of dry phospholipid bilayers and proteins by sugars. *Biochem. J.* **242**, 1–10 (1987).
268. Cicerone, M. T., Pikal, M. J. & Qian, K. K. Stabilization of proteins in solid form. *Adv. Drug Deliv. Rev.* **93**, 14–24 (2015).
269. Vogt, G., Woell, S. & Argos, P. Protein thermal stability, hydrogen bonds, and ion pairs11Edited by F. E. Cohen. *J. Mol. Biol.* **269**, 631–643 (1997).
270. Wang, W. Instability, stabilization, and formulation of liquid protein pharmaceuticals. *Int. J. Pharm.* **185**, 129–188 (1999).
271. Craig, D. Q., Royall, P. G., Kett, V. L. & Hopton, M. L. The relevance of the amorphous state to pharmaceutical dosage forms: glassy drugs and freeze dried systems. *Int. J. Pharm.* **179**, 179–207 (1999).
272. Parker, R., Gunning, Y. M., Lalloué, B., Noel, T. R. & Ring, S. G. Glassy state dynamics, its significance for biostabilisation and the role of carbohydrates. in *Amorphous Food and Pharmaceutical Systems* (ed. Levine, H.) 73–87

(The Royal Society of Chemistry, 2002). doi:10.1039/9781847550118-00073
273. Duddu, S. P. & Dal Monte, P. R. Effect of glass transition temperature on the stability of lyophilized formulations containing a chimeric therapeutic monoclonal antibody. *Pharm. Res.* **14**, 591–595 (1997).
274. Genin, N. & René, F. Analyse du rôle de la transition vitreuse dans les procédés de conservation agro-alimentaires. *J. Food Eng.* **26**, 391–408 (1995).
275. Li, Q. Investigating the Glassy To Rubbery Transition of Polydextrose and. *dissertation* (2010).
276. Mitsuiki, M., Yamamoto, Y., Mizuno, A. & Motoki, M. Glass Transition Properties as a Function of Water Content for Various Low-Moisture Galactans. *J. Agric. Food Chem.* **46**, 3528–3534 (1998).
277. Schawe, J. E. K. & Hess, U. Influence of Moisture on the Glass Transition of A Spray-Dried Compound Using the Isosteptm Method. *J. Therm. Anal. Calorim.* **68**, 741–749 (2002).
278. Mauer, L. J., Smith, D. E. & Labuza, T. P. Effect of water content, temperature and storage on the glass transition, moisture sorption characteristics and stickiness of β-casein. *Int. J. Food Prop.* **3**, 233–248 (2000).
279. Towns, J. K. Moisture content in proteins: its effects and measurement. *J. Chromatogr. A* **705**, 115–127 (1995).
280. Croyle, M. A., Cheng, X. & Wilson, J. M. Development of formulations that enhance physical stability of viral vectors for gene therapy. *Gene Ther.* **8**, 1281–1290 (2001).
281. Grasmeijer, N., Stankovic, M., de Waard, H., Frijlink, H. W. & Hinrichs, W. L. J. Unraveling protein stabilization mechanisms: vitrification and water replacement in a glass transition temperature controlled system. *Biochim. Biophys. Acta* **1834**, 763–769 (2013).
282. Mensink, M. A. *et al.* In-line near infrared spectroscopy during freeze-drying as a tool to measure efficiency of hydrogen bond formation between protein and sugar, predictive of protein storage stability. *Int. J. Pharm.* **496**, 792–800 (2015).
283. Simperler, A. *et al.* Glass Transition Temperature of Glucose, Sucrose, and Trehalose: An Experimental and in Silico Study. *J. Phys. Chem. B* **110**, 19678–19684 (2006).
284. Forssell, P. M., Mikkilä, J. M., Moates, G. K. & Parker, R. Phase and glass transition behaviour of concentrated barley starch-glycerol-water mixtures, a model for thermoplastic starch. *Carbohydr. Polym.* **34**, 275–282 (1997).
285. Zhao, L.-S., Cao, Z.-X. & Wang, Q. Glass transition of aqueous solutions involving annealing-induced ice recrystallization resolves liquid-liquid transition puzzle of water. *Sci. Rep.* **5**, 15714 (2015).
286. Wongsasulak, S., Tongsin, P., Intasanta, N. & Yoovidhya, T. Effect of glycerol on solution properties governing morphology, glass transition temperature, and tensile properties of electrospun zein film. *J. Appl. Polym. Sci.* **118**, 910–919 (2010).
287. Tonnis, W. F. *et al.* Influence of size and molecular flexibility of sugars on the storage stability of proteins after freeze drying. *Mol. Pharm.* (2014).
288. Icoz, D., Moraru, C. & Kokini, J. Polymer–polymer interactions in dextran systems using thermal analysis. *Carbohydr. Polym.* 120–129 (2005). doi:10.1016/j.carbpol.2005.07.012

289. Asgreen, C., Knopp, M. M., Skytte, J. & Löbmann, K. Influence of the polymer glass transition temperature and molecular weight on drug amorphization kinetics using ball milling. *Pharmaceutics* **12**, (2020).
290. Septevani, A. A. & Bhakri, S. Plasticization of poly(lactic acid) using different molecular weight of Poly(ethylene glycol). *AIP Conf. Proc.* **1904**, (2017).
291. Starciuc, T. *et al.* Trehalose or Sucrose: Which of the Two Should be Used for Stabilizing Proteins in the Solid State? A Dilemma Investigated by In Situ Micro-Raman and Dielectric Relaxation Spectroscopies During and After Freeze-Drying. *J. Pharm. Sci.* **109**, 496–504 (2020).
292. Crowe, J. H., Carpenter, J. F. & Crowe, L. M. The role of vitrification in anhydrobiosis. *Annu. Rev. Physiol.* **60**, 73–103 (1998).
293. Singh, S. K. Sucrose and Trehalose in Therapeutic Protein Formulations BT - Challenges in Protein Product Development. in (eds. Warne, N. W. & Mahler, H.-C.) 63–95 (Springer International Publishing, 2018). doi:10.1007/978-3-319-90603-4_3
294. Jain, N. K. & Roy, I. Effect of trehalose on protein structure. *Protein Sci.* **18**, 24–36 (2009).
295. Cordone, L., Cottone, G., Cupane, A., Emanuele, A. & Levantino, S. G. and M. Proteins in Saccharides Matrices and the Trehalose Peculiarity: Biochemical and Biophysical Properties. *Current Organic Chemistry* **19**, 1684–1706 (2015).
296. Bellavia, G., Cottone, G., Giuffrida, S., Cupane, A. & Cordone, L. Thermal Denaturation of Myoglobin in Water−Disaccharide Matrixes: Relation with the Glass Transition of the System. *J. Phys. Chem. B* **113**, 11543–11549 (2009).
297. Olsson, C., Jansson, H. & Swenson, J. The Role of Trehalose for the Stabilization of Proteins. *J. Phys. Chem. B* **120**, 4723–4731 (2016).
298. Crowe, L. M., Reid, D. S. & Crowe, J. H. Is trehalose special for preserving dry biomaterials? *Biophys. J.* **71**, 2087–93 (1996).
299. Magazù, S., Migliardo, F. & Telling, M. T. F. Study of the dynamical properties of water in disaccharide solutions. *Eur. Biophys. J.* **36**, 163–171 (2007).
300. Magazù, S., Migliardo, F. & Telling, M. T. F. Structural and dynamical properties of water in sugar mixtures. *Food Chem.* **106**, 1460–1466 (2008).
301. Olsson, C. & Swenson, J. Structural Comparison between Sucrose and Trehalose in Aqueous Solution. *J. Phys. Chem. B* **124**, 3074–3082 (2020).
302. Longinotti, M. P. & Corti, H. R. Viscosity of concentrated sucrose and trehalose aqueous solutions including the supercooled regime. *J. Phys. Chem. Ref. Data* **37**, 1503–1515 (2008).
303. Bellavia, G., Cottone, G., Giuffrida, S., Cupane, A. & Cordone, L. Thermal Denaturation of Myoglobin in Water−Disaccharide Matrixes: Relation with the Glass Transition of the System. *J. Phys. Chem. B* **113**, 11543–11549 (2009).
304. Perić-Hassler, L., Hansen, H. S., Baron, R. & Hünenberger, P. H. Conformational properties of glucose-based disaccharides investigated using molecular dynamics simulations with local elevation umbrella sampling. *Carbohydr. Res.* **345**, 1781–1801 (2010).
305. Winther, L. R., Qvist, J. & Halle, B. Hydration and mobility of trehalose in aqueous solution. *J. Phys. Chem. B* **116**, 9196–9207 (2012).
306. Branca, C., Magazu', V., Maisano, G., Migliardo, F. & Soper, A. K. Study on

Destructuring effect of trehalose on water by neutron diffraction. *Appl. Phys. A* **74**, s450–s451 (2002).
307. Lammert, A. M., Schmidt, S. J. & Day, G. A. Water activity and solubility of trehalose. *Food Chem.* **61**, 139–144 (1998).
308. Roos, Y. Melting and glass transitions weight carbohydrates of low molecular. *Carbohydr. Res.* **238**, 39–48 (1993).
309. Galmarini, M. V., Baeza, R., Sanchez, V., Zamora, M. C. & Chirife, J. Comparison of the viscosity of trehalose and sucrose solutions at various temperatures: Effect of guar gum addition. *LWT - Food Sci. Technol.* **44**, 186–190 (2011).
310. Lerbret, A., Bordat, P., Affouard, F., Descamps, M. & Migliardo, F. How Homogeneous Are the Trehalose, Maltose, and Sucrose Water Solutions? An Insight from Molecular Dynamics Simulations. *J. Phys. Chem. B* **109**, 11046–11057 (2005).
311. Malferrari, M. *et al.* Structural and dynamical characteristics of trehalose and sucrose matrices at different hydration levels as probed by FTIR and high-field EPR. *Phys. Chem. Chem. Phys.* **16**, 9831–9848 (2014).
312. Tonnis, W. F. *et al.* Size and molecular flexibility of sugars determine the storage stability of freeze-dried proteins. *Mol. Pharm.* **12**, 684–694 (2015).
313. Davidson, T. *Vaccines: History, Science, and Issues*. (ABC-CLIO, 2017).
314. Leung, V. *et al.* Thermal Stabilization of Viral Vaccines in Low-Cost Sugar Films. *Sci. Rep.* **9**, 1–11 (2019).
315. Leung, V. *et al.* Long-Term Preservation of Bacteriophage Antimicrobials Using Sugar Glasses. *ACS Biomater. Sci. Eng.* **4**, 3802–3808 (2018).
316. Dulal, P. Investigation of sugar-membrane vaccine stabilisation for improved vaccine thermostability and delivery. (University of Oxford, 2016).
317. Abbate, C. *et al.* Changes induced by exposure of the human lung to glass fiber-reinforced plastic. *Environ. Health Perspect.* **114**, 1725–1729 (2006).
318. Morrow, N. R. Wettability and Its Effect on Oil Recovery. *J Pet Technol* **42**, 1476–1484 (1990).
319. Xu, J. *et al.* Self-Assembly of Gradient Concentric Rings via Solvent Evaporation from a Capillary Bridge. *Phys. Rev. Lett.* **96**, 66104 (2006).
320. Thomas, Y. An essay on the cohesion of fluids. *Phil. Trans. R. Soc.* **95**, (1805).
321. Dörmann, M. & Schmid, H. Simulation of Capillary Bridges between Particles. *Procedia Eng.* **102**, 14–23 (2015).
322. Wang, L. & McCarthy, T. J. Capillary-bridge derived particles with negative Gaussian curvature. *Proc. Natl. Acad. Sci.* **112**, 2664–2669 (2015).
323. Anjali, T. G. & Basavaraj, M. G. Shape-Induced Deformation, Capillary Bridging, and Self-Assembly of Cuboids at the Fluid − Fluid Interface. (2017). doi:10.1021/acs.langmuir.6b03866
324. Bezdenejnykh, N. A., Meseguer, J., Perales, J. M., Aerodinamica, L. De & Introduction, I. Experimental analysis of stability limits of capillary liquid bridges. **i**, (1991).
325. Chen, T.-Y., Tsamopoulos, J. A. & Good, R. J. Capillary bridges between parallel and non-parallel surfaces and their stability. *J. Colloid Interface Sci.* **151**, 49–69 (1992).
326. Bostwick, J. B. & Steen, P. H. Stability of Constrained Capillary Surfaces. *Annu. Rev. Fluid Mech.* **47**, 539–568 (2015).
327. Bezdenejnykh, N. A., Meseguer, J. & Perales, J. M. Experimental analysis of

stability limits of capillary liquid bridges. **677**, (2011).
328. Ruiter, R. De *et al.* Stability Limits of Capillary Bridges : How Contact Angle Hysteresis Affects Morphology Transitions of Liquid Microstructures. **234501**, 1–5 (2015).
329. Capillary, I. Capillary surfaces : stability from families of equilibria with application to the liquid bridge. 411–439 (1995).
330. Cooray, H., Huppert, H. E. & Neufeld, J. A. Maximal liquid bridges between horizontal cylinders. (2016).
331. Protiere, S., Duprat, C. & Stone, H. A. Wetting on two parallel fi bers : drop to column transitions. *Soft Matter* **m**, 271–276 (2013).
332. Virozub, A., Haimovich, N. & Brandon, S. Three-Dimensional Simulations of Liquid Bridges between Two Cylinders : Forces , Energies , and Torques. *Langmuir* **88**, 12837–12842 (2009).
333. Beebe, A. Y. & Stone, H. A. Wetting of flexible fibre arrays `. 5–8 (2012). doi:10.1038/nature10779
334. Bostwick, J. B. & Steen, P. H. Stability of Constrained Capillary Surfaces. **Annu. Rev.**,
335. Boulogne, F., Sauret, A., Soh, B., Dressaire, E. & Stone, H. A. Mechanical Tuning of the Evaporation Rate of Liquid on Crossed Fibers. *Langmuir* **31**, 3094–3100 (2015).
336. Cho, K. *et al.* Low internal pressure in femtoliter water capillary bridges reduces evaporation rates. *Nat. Publ. Gr.* 1–7 (2016). doi:10.1038/srep22232
337. Mielniczuk, B. & Hueckel, T. Rupture of an Evaporating Liquid Bridge between Two Grains. *Acta Geophys.* (2014). doi:10.2478/s11600-014-0225-6
338. Mielniczuk, B. *et al.* Effect of water on granular matter mechanics , local scale : evaporation , extension and rupture of liquid bridges To cite this version : HAL Id : hal-01102747 Effect of water on granular matter mechanics , local scale : evaporation , extension and ruptur. (2015).
339. Mastrangeli, M. The Fluid Joint : The Soft Spot of Micro- and Nanosystems. (2017). doi:10.1002/adma.201501260
340. Portuguez, E., Alzina, A., Michaud, P. & Smith, A. Evaporation Kinetics and Breaking of a Thin Water Liquid Bridge between Two Plates of Silicon Wafer. 157–166 (2016).
341. Aziz, H. & Tafreshi, H. V. Competing forces on a liquid bridge between parallel and orthogonal dissimilar fibers. *Soft Matter* **15**, 6967–6977 (2019).
342. Neeson, M. J., Dagastine, R. R., Chan, Y. C. & Tabor, R. F. Evaporation of a capillary bridge between a particle and a surface†. 8489–8499 (2014). doi:10.1039/c4sm01826e
343. Kralchevsky, P. & Nagayama, K. Capillary Bridges and Capillary-Bridge Forces. **7303**, (2017).
344. Do, M. & Schmid, H. Simulation of Capillary Bridges between Nanoscale Particles. (2014). doi:10.1021/la404409k
345. Rynhart, P. R., Mclachlan, R., Jones, J. R. & Mckibbin, R. Solution of the Young-Laplace equation for three particles. **5**, 119–127 (2003).
346. Nguyen, H. N. G., Millet, O. & Gagneux, G. On the capillary bridge between spherical particles of unequal size: analytical and experimental approaches. *Contin. Mech. Thermodyn.* **31**, 225–237 (2019).
347. Company, L. B., Division, D. & Jer, N. Capillary Phenomena in Assemblies

of Parallel Cylinders III . Liquid Columns between Horizontal Parallel Cylinders. **34**, (1970).
348. Cheong, B. H.-P., Lye, J. K. K., Backhous, S., Liew, O. W. & Ng, T. W. Microplates based on liquid bridges between glass rods. *J. Colloid Interface Sci.* **397**, 177–184 (2013).
349. Yang, L., Tu, Y. & Fang, H. Modeling the rupture of a capillary liquid bridge between a sphere and plane. *Soft Matter* **6**, 6178–6182 (2010).
350. De Lazzer, A., Dreyer, M. & Rath, H. J. Particle - Surface capillary forces. *Langmuir* **15**, 4551–4559 (1999).
351. Van Honschoten, J. W., Brunets, N. & Tas, N. R. Capillarity at the nanoscale. *Chem. Soc. Rev.* **39**, 1096–1114 (2010).
352. Weeks, B. L., Vaughn, M. W. & Deyoreo, J. J. Direct imaging of meniscus formation in atomic force microscopy using environmental scanning electron microscopy. *Langmuir* **21**, 8096–8098 (2005).
353. Kim, S., Kim, D., Kim, J., An, S. & Jhe, W. Direct Evidence for Curvature-Dependent Surface Tension in Capillary Condensation: Kelvin Equation at Molecular Scale. *Phys. Rev. X* **8**, (2018).
354. Craster, R. V, Matar, O. K. & Sefiane, K. Pinning, Retraction, and Terracing of Evaporating Droplets Containing Nanoparticles. *Langmuir* **25**, 3601–3609 (2009).
355. Karapetsas, G., Sahu, K. C. & Matar, O. K. Evaporation of Sessile Droplets Laden with Particles and Insoluble Surfactants. *Langmuir* **32**, 6871–6881 (2016).
356. Beattie, G. M. *et al.* Trehalose: a cryoprotectant that enhances recovery and preserves function of human pancreatic islets after long-term storage. *Diabetes* **46**, 519–523 (1997).
357. Martinetti, D. *et al.* Effect of trehalose on cryopreservation of pure peripheral blood stem cells. *Biomed. reports* **6**, 314–318 (2017).
358. Rodrigues, J. P. *et al.* Evaluation of trehalose and sucrose as cryoprotectants for hematopoietic stem cells of umbilical cord blood. *Cryobiology* **56**, 144–151 (2008).
359. Osman, A., Shahidzadeh, N., Stitt, H. & Shokri, N. Morphological transformations during drying of surfactant-nanofluid droplets. *J. Ind. Eng. Chem.* **67**, 92–98 (2018).
360. Trybala, A. Evaporation of sessile droplets Evaporation of sessile droplets. 0–22 (2017).
361. Colaço, C. A. L. S. & Roser, B. Trehalose-a multifunctional additive for food preservation. in *Food Packaging and Preservation* (ed. Mathlouthi, M.) 123–140 (Springer US, 1994). doi:10.1007/978-1-4615-2173-0_7
362. Grasmeijer, N., Frijlink, H. W. & Hinrichs, W. L. J. Model to predict inhomogeneous protein–sugar distribution in powders prepared by spray drying. *J. Aerosol Sci.* **101**, 22–33 (2016).
363. Brutin, D. Recent advances in droplet wetting and evaporation. *Chem Soc Rev* 558–585 (2018). doi:10.1039/c6cs00902f
364. Bhardwaj, R., Fang, X. & Attinger, D. Pattern formation during the evaporation of a colloidal nanoliter drop: a numerical and experimental study. *New J. Phys.* **11**, 75020 (2009).
365. Jensen, O. E. & Grotberg, J. B. The spreading of heat or soluble surfactant along a thin liquid film The spreading of heat or solluble surfactant along a thin liquid film. **58**, (2010).

366. Celaya, E. A., Aguirrezabala, J. J. A. & Chatzipantelidis, P. Implementation of an Adaptive BDF2 Formula and Comparison with the MATLAB Ode15s. *Procedia Comput. Sci.* **29**, 1014–1026 (2014).
367. Kohen, A., Cannio, R., Bartolucci, S., Klinman, J. P. & Klinman, J. P. Enzyme dynamics and hydrogen tunnelling in a thermophilic alcohol dehydrogenase . *Nature* **399**, 496–499 (1999).
368. Robinson, P. K. Enzymes: principles and biotechnological applications. *Essays Biochem.* **59**, 1–41 (2015).
369. Christopher, L. P., Hemanathan Kumar & Zambare, V. P. Enzymatic biodiesel: Challenges and opportunities. *Appl. Energy* **119**, 497–520 (2014).
370. Starnes, J. W. Effect of storage conditions on lactate dehydrogenase released from perfused hearts. *International journal of cardiology* **127**, 114–116 (2008).
371. Liu, Y., Bhandari, B. & Zhou, W. Glass Transition and Enthalpy Relaxation of Amorphous Food Saccharides: A Review. *J. Agric. Food Chem.* **54**, 5701–5717 (2006).
372. Buera, M. P., Rossi, S., Moreno, S. & Chirife, J. DSC confirmation that vitrification is not necessary for stabilization of the restriction enzyme EcoRI dried with saccharides. *Biotechnol. Prog.* **15**, 577–579 (1999).
373. Rossi, S., Buera, M. P., Moreno, S. & Chirife, J. Stabilization of the restriction enzyme EcoRI dried with trehalose and other selected glass-forming solutes. *Biotechnol. Prog.* **13**, 609–616 (1997).
374. Cicerone, M. T. & Douglas, J. F. β-Relaxation governs protein stability in sugar-glass matrices. *Soft Matter* **8**, 2983–2991 (2012).
375. Yoshioka, S. *et al.* Molecular mobility of protein in lyophilized formulations linked to the molecular mobility of polymer excipients, as determined by high resolution 13C solid-state NMR. *Pharm. Res.* **16**, 1621—1625 (1999).
376. Yoshioka, S., Miyazaki, T. & Aso, Y. Beta-relaxation of insulin molecule in lyophilized formulations containing trehalose or dextran as a determinant of chemical reactivity. *Pharm. Res.* **23**, 961–966 (2006).
377. Cicerone, M. T. & Soles, C. L. Fast dynamics and stabilization of proteins: binary glasses of trehalose and glycerol. *Biophys. J.* **86**, 3836–3845 (2004).
378. Yu, L. Amorphous pharmaceutical solids: preparation, characterization and stabilization. *Adv. Drug Deliv. Rev.* **48**, 27–42 (2001).
379. Liu, Y., Bhandari, B. & Zhou, W. Glass Transition and Enthalpy Relaxation of Amorphous Food Saccharides: A Review. *J. Agric. Food Chem.* **54**, 5701–5717 (2006).
380. Brawer, S. A. Theory of relaxation in viscous liquids and glasses. *J. Chem. Phys.* **81**, 954–975 (1984).
381. Surana, R., Pyne, A., Rani, M. & Suryanarayanan, R. Measurement of enthalpic relaxation by differential scanning calorimetry—effect of experimental conditions. *Thermochim. Acta* **433**, 173–182 (2005).
382. Meste, M. Le, Champion, D., Roudaut, G., Blond, G. & Simatos, D. Glass Transition and Food Technology: A Critical Appraisal. *J. Food Sci.* **67**, 2444–2458 (2002).
383. Abiad, M. G., Carvajal, M. T. & Campanella, O. H. A Review on Methods and Theories to Describe the Glass Transition Phenomenon: Applications in Food and Pharmaceutical Products. *Food Eng. Rev.* **1**, 105–132 (2009).
384. Yoshida, H. Relationship between enthalpy relaxation and dynamic mechanical relaxation of engineering plastics. *Thermochim. Acta* **266**, 119–

127 (1995).
385. Muñoz, E. & García-Manrique, J. A. Water Absorption Behaviour and Its Effect on the Mechanical Properties of Flax Fibre Reinforced Bioepoxy Composites. *Int. J. Polym. Sci.* **2015**, 390275 (2015).
386. Lai, M. C. & Topp, E. M. Solid-state chemical stability of proteins and peptides. *J. Pharm. Sci.* **88**, 489–500 (1999).
387. Rubert Pérez, C. M., Álvarez, Z., Chen, F., Aytun, T. & Stupp, S. I. Mimicking the Bioactivity of Fibroblast Growth Factor-2 Using Supramolecular Nanoribbons. *ACS Biomater. Sci. Eng.* **3**, 2166–2175 (2017).
388. Kottakis, F. *et al.* FGF-2 regulates cell proliferation, migration, and angiogenesis through an NDY1/KDM2B-miR-101-EZH2 pathway. *Mol. Cell* **43**, 285–298 (2011).
389. Ching, Y.-H., Sutton, T. L., Pierpont, Y. N., Robson, M. C. & Payne, W. G. The use of growth factors and other humoral agents to accelerate and enhance burn wound healing. *Eplasty* **11**, e41 (2011).
390. Cooper, M. L. & Spielvogel, R. L. Artificial skin for wound healing. *Clin. Dermatol.* **12**, 183–191 (1994).
391. Chen, W. Y., Rogers, A. A. & Lydon, M. J. Characterization of biologic properties of wound fluid collected during early stages of wound healing. *J. Invest. Dermatol.* **99**, 559–564 (1992).
392. Gu, T. M., Niu, X. T. & Guo, H. [Clinical observation on changes of fibroblast growth factor in burn wounds]. *Zhongguo xiu fu chong jian wai ke za zhi = Zhongguo xiufu chongjian waike zazhi = Chinese J. reparative Reconstr. Surg.* **14**, 261–263 (2000).
393. Vogt, P. M. *et al.* Determination of endogenous growth factors in human wound fluid: temporal presence and profiles of secretion. *Plast. Reconstr. Surg.* **102**, 117–123 (1998).
394. Akita, S., Akino, K., Imaizumi, T. & Hirano, A. Basic fibroblast growth factor accelerates and improves second-degree burn wound healing. *Wound repair Regen. Off. Publ. Wound Heal. Soc. [and] Eur. Tissue Repair Soc.* **16**, 635–641 (2008).
395. Montesano, R., Vassalli, J. D., Baird, A., Guillemin, R. & Orci, L. Basic fibroblast growth factor induces angiogenesis in vitro. *Proc. Natl. Acad. Sci. U. S. A.* **83**, 7297–7301 (1986).
396. Steed, D. L. THE ROLE OF GROWTH FACTORS IN WOUND HEALING. *Surg. Clin. North Am.* **77**, 575–586 (1997).
397. Nissen, N. N., Polverini, P. J., Gamelli, R. L. & DiPietro, L. A. Basic fibroblast growth factor mediates angiogenic activity in early surgical wounds. *Surgery* **119**, 457–465 (1996).
398. Nunes, Q. M., Li, Y., Sun, C., Kinnunen, T. K. & Fernig, D. G. Fibroblast growth factors as tissue repair and regeneration therapeutics. *PeerJ* **4**, e1535 (2016).
399. Shah, D. Effect of various additives on the stability of basic fibroblast growth factor and development of an intradermal injectable formulation. (1998).
400. Benington, L., Rajan, G., Locher, C. & Lim, L. Y. Fibroblast Growth Factor 2-A Review of Stabilisation Approaches for Clinical Applications. *Pharmaceutics* **12**, (2020).
401. Fang, H.Z; Zheng, Z.S; Zhu, A.T; Lan, X; Huang, X. . Recombinant Bovine Basic Fibroblast Growth Factor Freeze-Dried Formulation for External Application. CN Patent CN102389402B (2012).

402. Wei, Q. *et al.* Protein Interactions with Polymer Coatings and Biomaterials. *Angew. Chemie Int. Ed.* **53**, 8004–8031 (2014).
403. Sweryda-Krawiec, B., Devaraj, H., Jacob, G. & Hickman, J. J. A new interpretation of serum albumin surface passivation. *Langmuir : the ACS journal of surfaces and colloids* **20**, 2054–2056 (2004).
404. Man, Y. *et al.* Adsorptive BSA Coating Method for CE to Separate Basic Proteins. *Chromatographia* **76**, 59–65 (2013).
405. Ma, G. J., Ferhan, A. R., Jackman, J. A. & Cho, N.-J. Conformational flexibility of fatty acid-free bovine serum albumin proteins enables superior antifouling coatings. *Commun. Mater.* **1**, 45 (2020).
406. Steinitz, M. Quantitation of the blocking effect of tween 20 and bovine serum albumin in ELISA microwells. *Anal. Biochem.* **282**, 232–238 (2000).
407. Mahmood, T. & Yang, P.-C. Western blot: technique, theory, and trouble shooting. *N. Am. J. Med. Sci.* **4**, 429–434 (2012).
408. Stewart, A. A., Byron, C. R., Pondenis, H. & Stewart, M. C. Effect of fibroblast growth factor-2 on equine mesenchymal stem cell monolayer expansion and chondrogenesis. *Am. J. Vet. Res.* **68**, 941–945 (2007).
409. Fujimoto, Y., Yokozeki, T., Yokoyama, A. & Tabata, Y. Basic fibroblast growth factor enhances proliferation and hepatocyte growth factor expression of feline mesenchymal stem cells. *Regen. Ther.* **15**, 10–17 (2020).
410. An, K. *et al.* hTERT-Immortalized Bone Mesenchymal Stromal Cells Expressing Rat Galanin via a Single Tetracycline-Inducible Lentivirus System. *Stem Cells Int.* **2017**, 6082684 (2017).
411. te Booy, M. P., de Ruiter, R. A. & de Meere, A. L. Evaluation of the physical stability of freeze-dried sucrose-containing formulations by differential scanning calorimetry. *Pharm. Res.* **9**, 109–114 (1992).
412. Roe, K. D. & Labuza, T. P. Glass Transition and Crystallization of Amorphous Trehalose-sucrose Mixtures. *Int. J. Food Prop.* **8**, 559–574 (2005).
413. Zhang, Y., Jiang, B., Yuan, J. & Tao, Y. The impact of social distancing and epicenter lockdown on the COVID-19 epidemic in mainland China: A data-driven SEIQR model study. *medRxiv* 2020.03.04.20031187 (2020). doi:10.1101/2020.03.04.20031187
414. Palomino, J. C., Rodríguez, J. G. & Sebastian, R. Wage inequality and poverty effects of lockdown and social distancing in Europe. *Eur. Econ. Rev.* **129**, 103564 (2020).
415. Block, P. *et al.* Social network-based distancing strategies to flatten the COVID-19 curve in a post-lockdown world. *Nat. Hum. Behav.* **4**, 588–596 (2020).
416. Slavitt, A. The COVID-19 Pandemic Underscores the Need to Address Structural Challenges of the US Health Care System. *JAMA Heal. Forum* **1**, e200839–e200839 (2020).
417. Kringos, D. *et al.* Managing COVID-19 within and across health systems: why we need performance intelligence to coordinate a global response. *Heal. Res. Policy Syst.* **18**, 80 (2020).
418. Khalid, A. & Ali, S. COVID-19 and its Challenges for the Healthcare System in Pakistan. *Asian Bioeth. Rev.* **12**, 551–564 (2020).
419. Wei, M. Social Distancing and Lockdown – An Introvert's Paradise? An Empirical Investigation on the Association Between Introversion and the Psychological Impact of COVID19-Related Circumstantial Changes . *Frontiers in Psychology* **11**, 2440 (2020).

420. Carter, L. J. *et al.* Assay Techniques and Test Development for COVID-19 Diagnosis. *ACS Cent. Sci.* **6**, 591–605 (2020).
421. Notomi, T. *et al.* Loop-mediated isothermal amplification of DNA. *Nucleic Acids Res.* **28**, E63 (2000).
422. Tomita, N., Mori, Y., Kanda, H. & Notomi, T. Loop-mediated isothermal amplification (LAMP) of gene sequences and simple visual detection of products. *Nat. Protoc.* **3**, 877–882 (2008).
423. Tanner, N. A., Zhang, Y. & Evans, T. C. Visual detection of isothermal nucleic acid amplification using pH-sensitive dyes. *Biotechniques* **58**, 59–68 (2015).
424. Chen, S., Wang, F., Beaulieu, J. C., Stein, R. E. & Ge, B. Rapid detection of viable salmonellae in produce by coupling propidium monoazide with loop-mediated isothermal amplification. *Appl. Environ. Microbiol.* **77**, 4008–4016 (2011).
425. Brinkhof, B., Spee, B., Rothuizen, J. & Penning, L. C. Development and evaluation of canine reference genes for accurate quantification of gene expression. *Anal. Biochem.* **356**, 36–43 (2006).
426. Brinkhof, B. *et al.* Improving characterisation of human Multipotent Stromal Cells cultured in 2D and 3D: Design and evaluation of primer sets for accurate gene expression normalisation. *PLoS One* **13**, e0209772 (2019).
427. Duralliu, A. *et al.* The influence of moisture content and temperature on the long-term storage stability of freeze-dried high concentration immunoglobulin G (IgG). *Pharmaceutics* **12**, (2020).
428. Breen, E. D., Curley, J. G., Overcashier, D. E., Hsu, C. C. & Shire, S. J. Effect of Moisture on the Stability of a Lyophilized Humanized Monoclonal Antibody Formulation. *Pharm. Res.* **18**, 1345–1353 (2001).
429. Meagher, R. J., Priye, A., Light, Y. K., Huang, C. & Wang, E. Impact of primer dimers and self-amplifying hairpins on reverse transcription loop-mediated isothermal amplification detection of viral RNA. *Analyst* **143**, 1924–1933 (2018).
430. Dao Thi, V. L. *et al.* A colorimetric RT-LAMP assay and LAMP-sequencing for detecting SARS-CoV-2 RNA in clinical samples. *Sci. Transl. Med.* **12**, eabc7075 (2020).
431. Donbrow, M., Azaz, E. & Pillersdorf, A. Autoxidation of polysorbates. *J. Pharm. Sci.* **67**, 1676–1681 (1978).
432. Cao, X. *et al.* Free fatty acid particles in protein formulations, Part 1: Microspectroscopic identification. *J. Pharm. Sci.* **104**, 433–446 (2015).
433. Tomlinson, A., Demeule, B., Lin, B. & Yadav, S. Polysorbate 20 Degradation in Biopharmaceutical Formulations: Quantification of Free Fatty Acids, Characterization of Particulates, and Insights into the Degradation Mechanism. *Mol. Pharm.* **12**, 3805–3815 (2015).
434. Hardinge, P. & Murray, J. Reduced False Positives and Improved Reporting of Loop-Mediated Isothermal Amplification using Quenched Fluorescent Primers. *Sci. Rep.* **9**, (2019).
435. Oscorbin, I. P., Belousova, E. A., Zakabunin, A. I., Boyarskikh, U. A. & Filipenko, M. L. Comparison of fluorescent intercalating dyes for quantitative loop-mediated isothermal amplification (qLAMP). *Biotechniques* **61**, 20–25 (2016).
436. Quyen, T. L., Ngo, T. A., Bang, D. D., Madsen, M. & Wolff, A. Classification of Multiple DNA Dyes Based on Inhibition Effects on Real-Time Loop-Mediated Isothermal Amplification (LAMP): Prospect for Point of Care

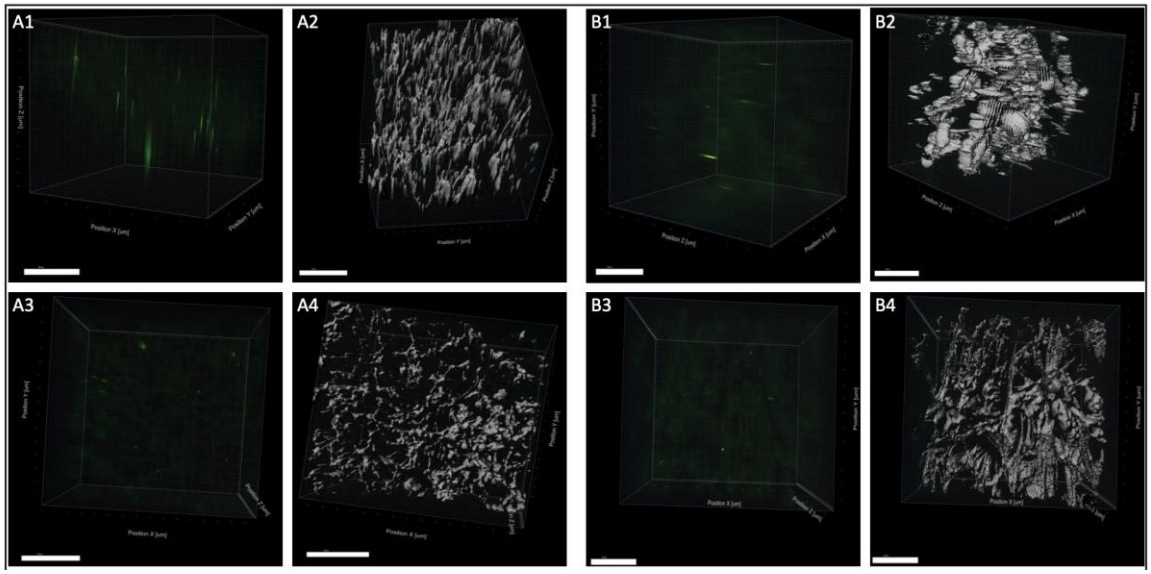
Setting . *Frontiers in Microbiology* **10**, 2234 (2019).
437. Coronaviros (COVID-19): getting tested. *GOV.UK* (2020). Available at: https://www.gov.uk/guidance/coronavirus-covid-19-getting-tested.
438. CDC. Information for Laboratories about Coronavirus (COVID-19). Centers for Disease Control and Prevention. (2020). Available at: https://www.cdc.gov/coronavirus/2019-ncov/lab/virus-requests.html (2020).
439. Babiker, A., Myers, C. W., Hill, C. E. & Guarner, J. SARS-CoV-2 Testing: Trials and Tribulations. *Am. J. Clin. Pathol.* **153**, 706–708 (2020).
440. Becherer, L. *et al.* Loop-mediated isothermal amplification (LAMP) – review and classification of methods for sequence-specific detection. *Anal. Methods* **12**, 717–746 (2020).
441. Cui, Z. *et al.* Development of a rapid test kit for SARS-CoV-2: an example of product design. *Bio-Design Manuf.* **3**, 83–86 (2020).
442. Yan, C. *et al.* Rapid and visual detection of 2019 novel coronavirus (SARS-CoV-2) by a reverse transcription loop-mediated isothermal amplification assay. *Clin. Microbiol. Infect.* **26**, 773–779 (2020).
443. Yu, L. *et al.* Rapid Detection of COVID-19 Coronavirus Using a Reverse Transcriptional Loop-Mediated Isothermal Amplification (RT-LAMP) Diagnostic Platform. *Clinical chemistry* **66**, 975–977 (2020).
444. Yang, W. *et al.* Rapid Detection of SARS-CoV-2 Using Reverse transcription RT-LAMP method. *medRxiv* 2020.03.02.20030130 (2020). doi:10.1101/2020.03.02.20030130
445. Park, G.-S. *et al.* Development of Reverse Transcription Loop-Mediated Isothermal Amplification Assays Targeting Severe Acute Respiratory Syndrome Coronavirus 2 (SARS-CoV-2). *J. Mol. Diagn.* **22**, 729–735 (2020).
446. Broughton, J. P. *et al.* CRISPR–Cas12-based detection of SARS-CoV-2. *Nat. Biotechnol.* **38**, 870–874 (2020).
447. Gaunt, E. R., Hardie, A., Claas, E. C. J., Simmonds, P. & Templeton, K. E. Epidemiology and clinical presentations of the four human coronaviruses 229E, HKU1, NL63, and OC43 detected over 3 years using a novel multiplex real-time PCR method. *J. Clin. Microbiol.* **48**, 2940–2947 (2010).
448. Hsieh, K., Mage, P. L., Csordas, A. T., Eisenstein, M. & Tom Soh, H. Simultaneous elimination of carryover contamination and detection of DNA with uracil-DNA-glycosylase-supplemented loop-mediated isothermal amplification (UDG-LAMP). *Chem. Commun.* **50**, 3747–3749 (2014).
449. Kim, E.-M. *et al.* Uracil-DNA glycosylase-treated reverse transcription loop-mediated isothermal amplification for rapid detection of avian influenza virus preventing carry-over contamination. *J. Vet. Sci.* **17**, 421–425 (2016).

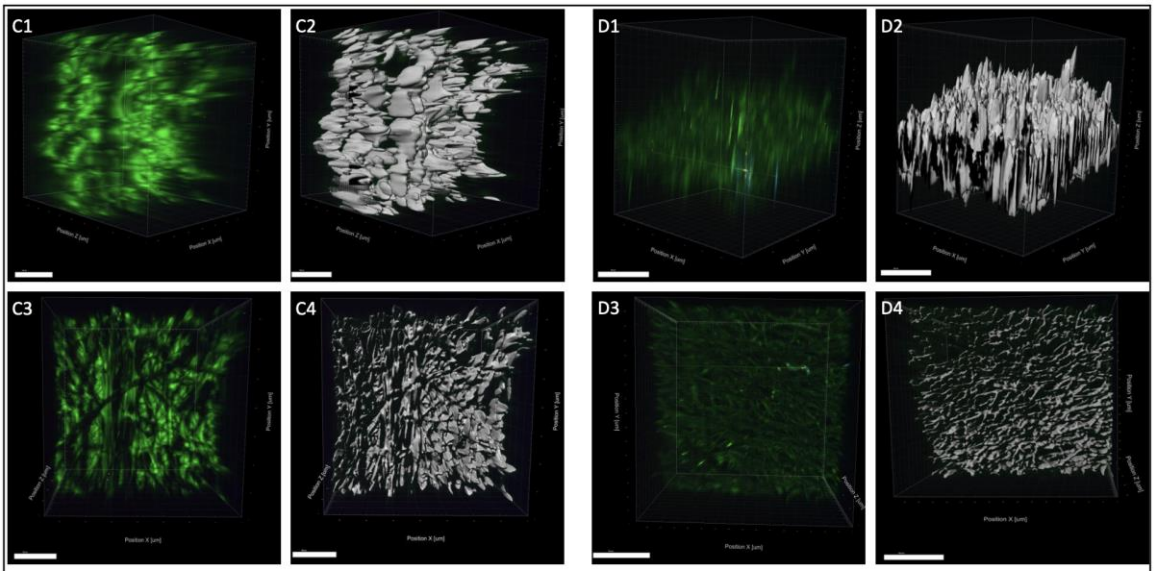
Appendices

Appendix 1: Distribution of Protein In the Membrane

Table A1: Selection of membranes

Reference	Material Type	Source
A	Polyester	Hollingsworth-vose
B	Polyamide	Hollingsworth-vose
C	Proprietary (Leu)	Pall
D	Polypropylene	Pall
E	Proprietary (CP)	Pall
F	Glass fibre	GE
G	Cellulose	GE


A1
A2
B1
B2
A3
A4
B3
B4


C1
C2
D1
D2
C3
C4
D3
D4

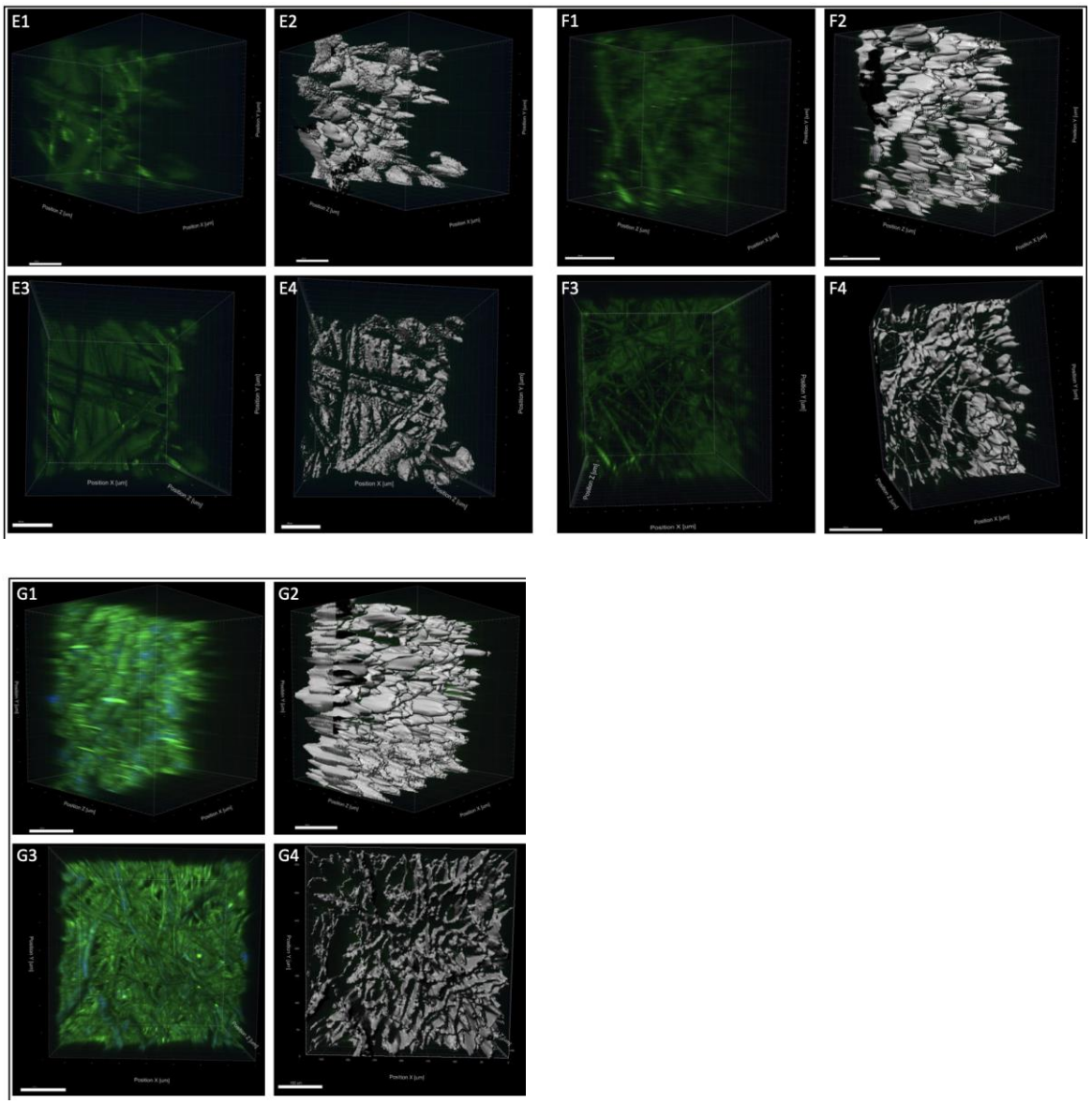


Figure A1:Multiphoton microscopy images of dried FITC-labelled antibody on the membranes (listed in Table A1). FITC-labelled antibody was formulated with sugar solution and dried on the membranes before taking images by multi-photon microscope (Bio-Rad Radiance 2100). Images number 1 and 3 presented the distribution of FITC-labelled antibody in z-plane and xy-plane, respectively. Images number 2 and 4 are isosurface rending of MPM images for 3D reconstruction using Imaris Software. Scare bar indicates a length of 100 µm.

Appendix 2: Determination of Trehalose Viscosity Equation

The relationship between trehalose concentration and viscosity needs to be determined before the numerical solution.

Material and Methods

Materials and Method

D- (+)-Trehalose dehydrate (Sigma Aldrich, $\geq 99\%$) has been dissolved in Milli-Q water to configure different weight percentage sugar solutions gravimetrically. The range of Trehalose concentrations was from 0% to 62%. When over 40%wt, trehalose could not dissolve easily in water at room temperature. In that case, the solutions were prepared by heating and mixing in sealed glass vials.

Viscosity

Viscosities of Trehalose solutions were measured by optical Rheometer (DWS RheoLabs from LS Instruments). Firstly, all the solutions were mixed with 500 nm nanoparticles in 2% weight percentage, which was referred to the calculation provided by LS Instruments to ensure the turbidity index (I) was located between 5 and 30. Otherwise, the results were invalid. Then, each mixture was transferred into a 2mm cuvette and placed into the machine. The measuring temperature was set to 9 ℃ by the software on the computer, which is the wet-bulb temperature of room temperature (25 ℃) with 5% relative humidity. When the temperature became constant, software was run, and the results were recorded.

Results

The dynamic viscosities (in units cp) of several different weight percentage Trehalose solutions have been determined by Rheometer. In this work, the dilution of adding nanoparticles was neglected.

Those two empirical numbers could be determined by rearranging the Eq. 3.19

$$\ln(\mu) = \mathrm{A}_1\psi + \ln(\mathrm{A}_0) \qquad \textit{Eq. 0.1}$$

Substituting all the data into Eq. 0.1, the tendency equation could be obtained from Figure A2.

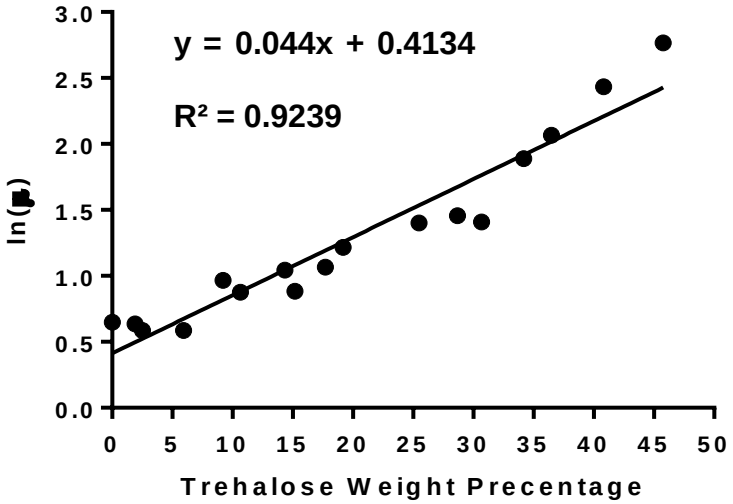


Figure A2: The calibration of viscosities with different trehalose weight percentages. The slope and intercept are related to the above two empirical parameters A_0 and A_1.

Two empirical numbers A_0 and A_1 are read based on tendency equation, which are 1.2932×10^{-3} and 0.0471, respectively. However, the exponential approximation is valid when the trehalose weight is lower than 50%. If fitting the data over 50%, the R Square number drops sharply, which considerably increases the error of approximation.

Appendix 3: The Correlation of BSA to LDH in BCA Assay

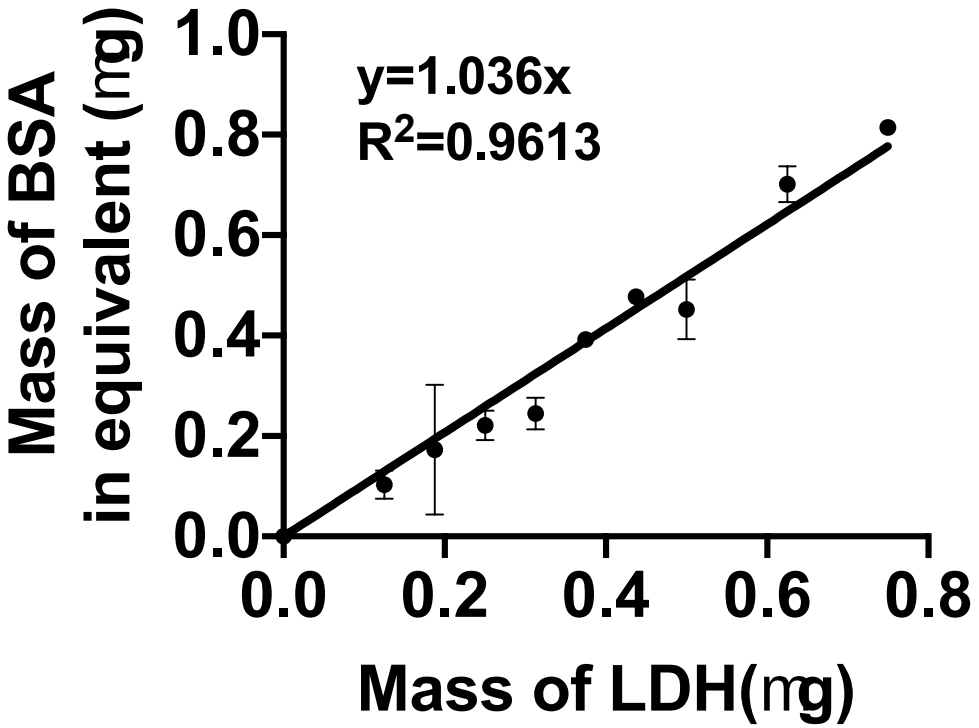


Figure A3: The relationship of LDH with the corresponding BSA in BCA assay. Results are presented as Mean ±SD. The original LDH of 5mg/ml was serial diluted into 0 to 0.75 mg/ml. After mixing 50μl of LDH solutions with 2ml MilliQ water, 50 μl of diluted solution was transfer into 96-well plate. The amount of proteins was varied from 0 to 0.8 μg. Then, using QuantiPro Bicinchoninic Acid (BCA) protein assay kit to measure the protein concentration by following the manufacture's protocol. Bovine serum albumin solutions with the concentration of 0 to 0.8 mg/ml was added as standards.

Appendix 4: The Influence of LDH Activity by Adding Excipients

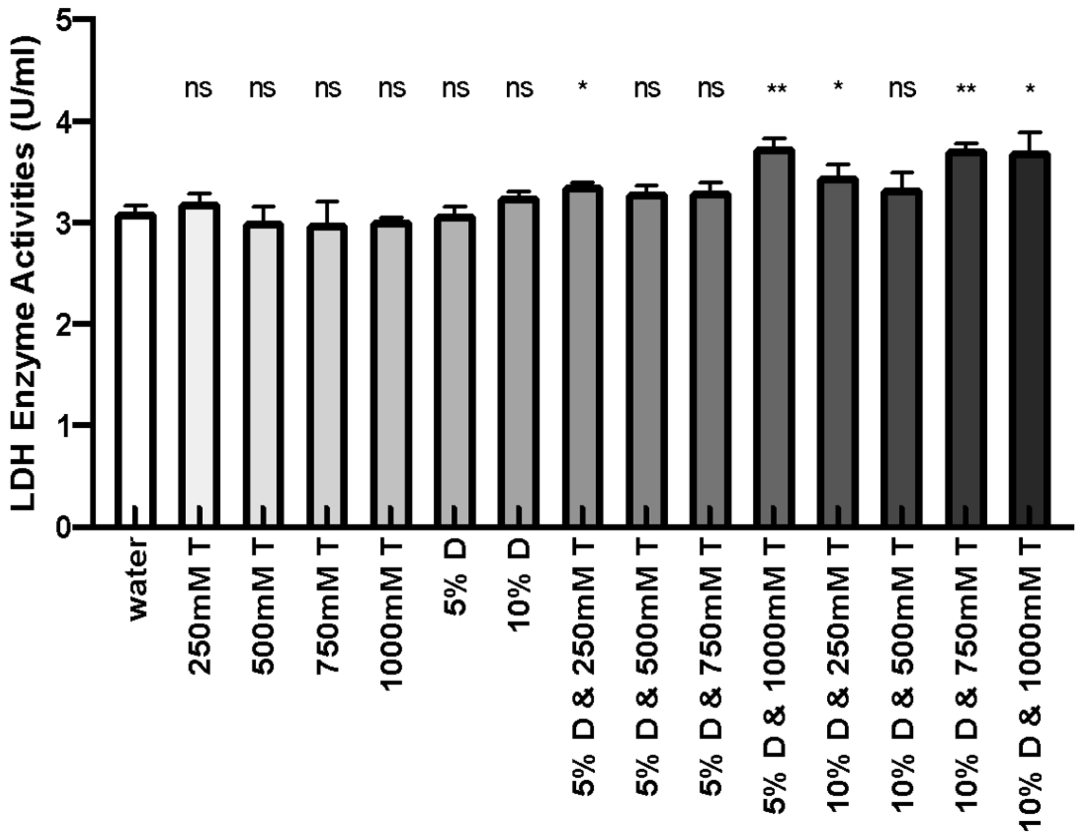


*Figure A4:The effect of LDH activities by formulated with water or different excipients in various concentrations. 'T' denotes for trehalose and 'D' stands for dextran. results are presented as Mean ±SEM, n=3. 'ns' = no significant difference (P>0.05), *=P<0.05, and **=P<0.01.*

Appendix 5: Effect of Using Diluted UTM and VTM

Four different transport media have been diluted by water as negative sample or Twist RNA solution as positive sample.

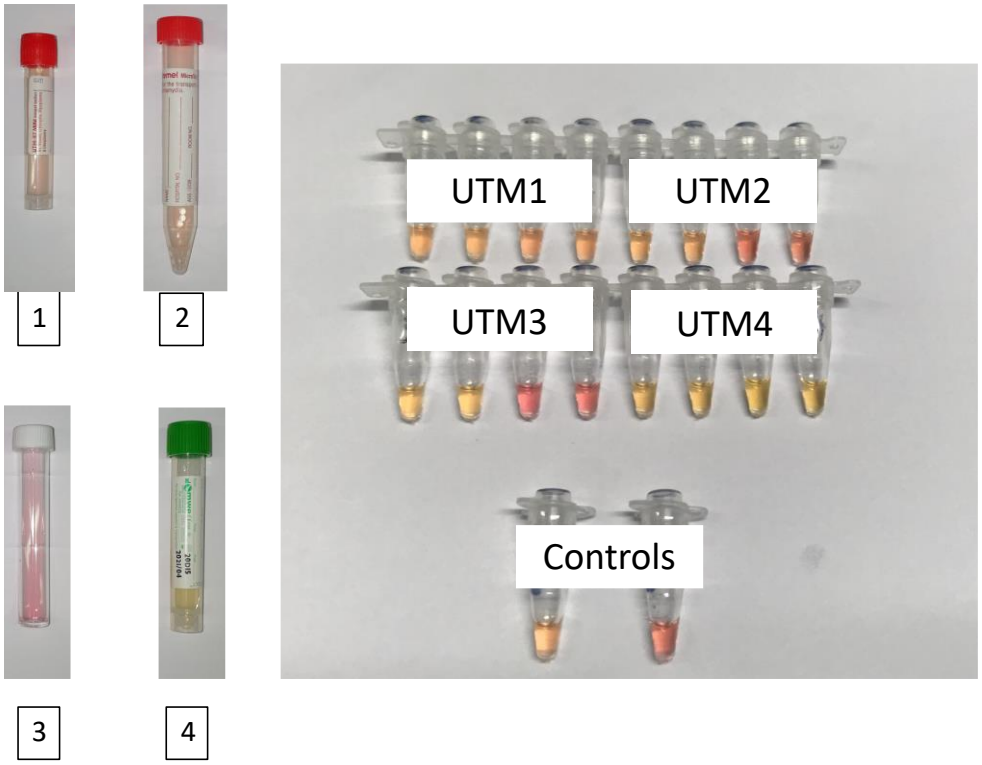
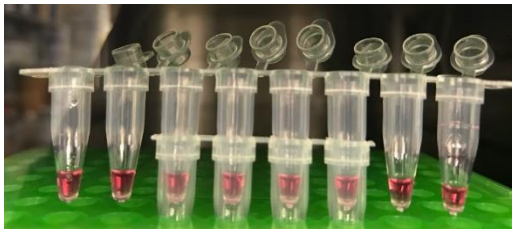
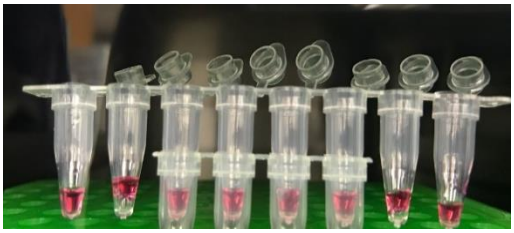


Figure A5: The impact of diluted universal and viral transport media to the reading of RT-LAMP results. 3 universal transport media (UTM) and 1 viral transport medium (VTM) were diluted by water as negative samples and by Twist RNA solution as positive samples. Tube 1 is UTM -RT MINI from COPAN, Tube 2 is Universal Kits from ThermoFisher, and Tube 4 is Viral Transport Medium from mWe. 10 μl of diluted UTM or VTM samples was added into each tube containing 15 μl reagent (12.5μl master mix and 2.5 μl primers).All tubes contain O117 primers and WarmStart Colorimetric Lamp Master Mix. The tubes were incubated at 65 ^{o}C for 30 min. Positive samples containing Twist RNA was added into first two tube and negative samples in last two tubes.

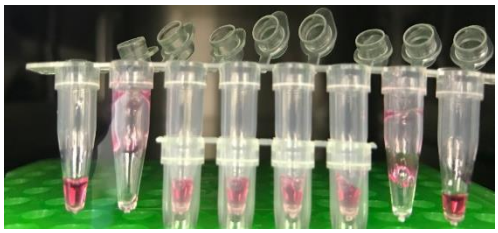
Appendix 6: Vacuum Foam Drying Process



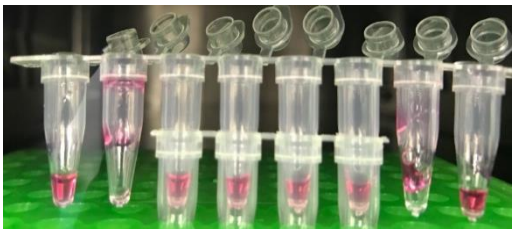
760 Torr



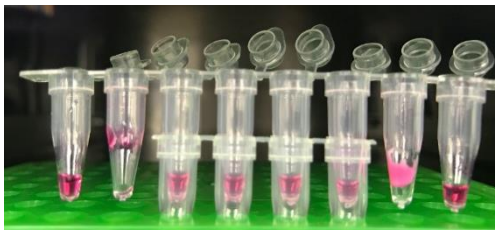
59.9 Torr



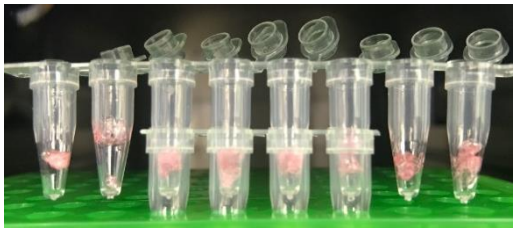
28.2 Torr



6.399 Torr



935 mTorr

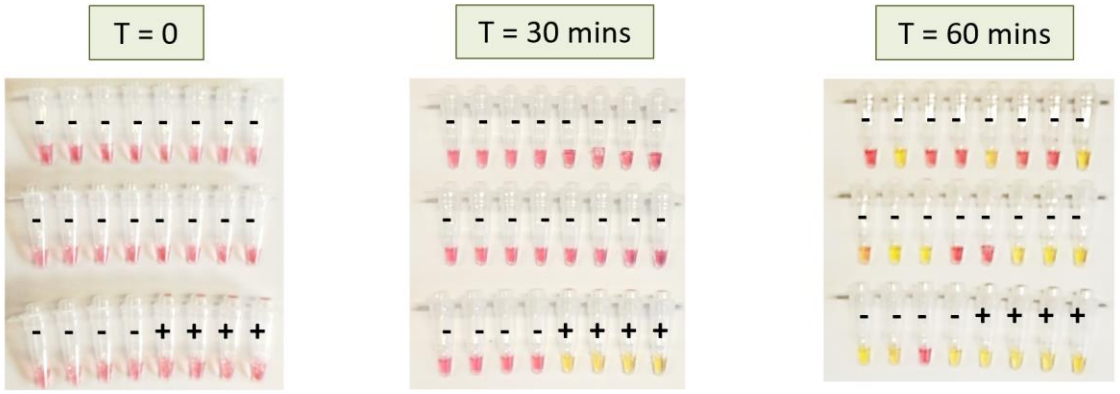


50 mTorr

Figure A6: Vacuum Foam Drying process of reagent in SARS-CoV-2 detection kit. The morphology of reagents in different pressure conditions.

Appendix 7: The Switch can Stabilise RT-LAMP Performance

(a)



(b)

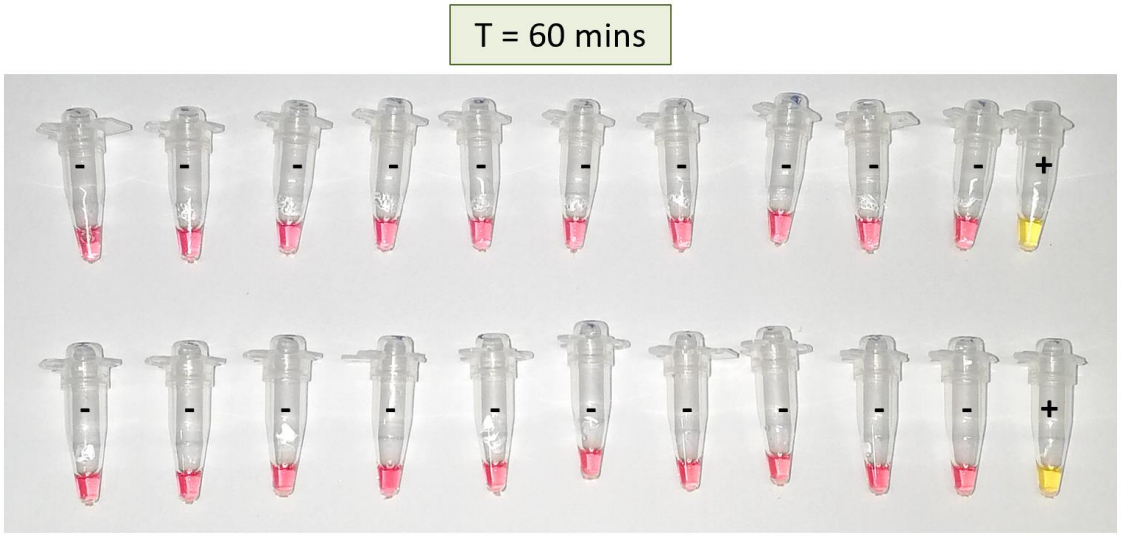


Figure A7: O117_N generated 60% false positive results (12/20 reactions) due to self- and off-target amplification in human RNA control sample after incubating at 65°C for 60 min. O117_Q still shows negative to human RNA control as long as 60 min at 65°C reaction.

Appendix 8: Sensitivity Analysis of Improved RT-LAMP Assay

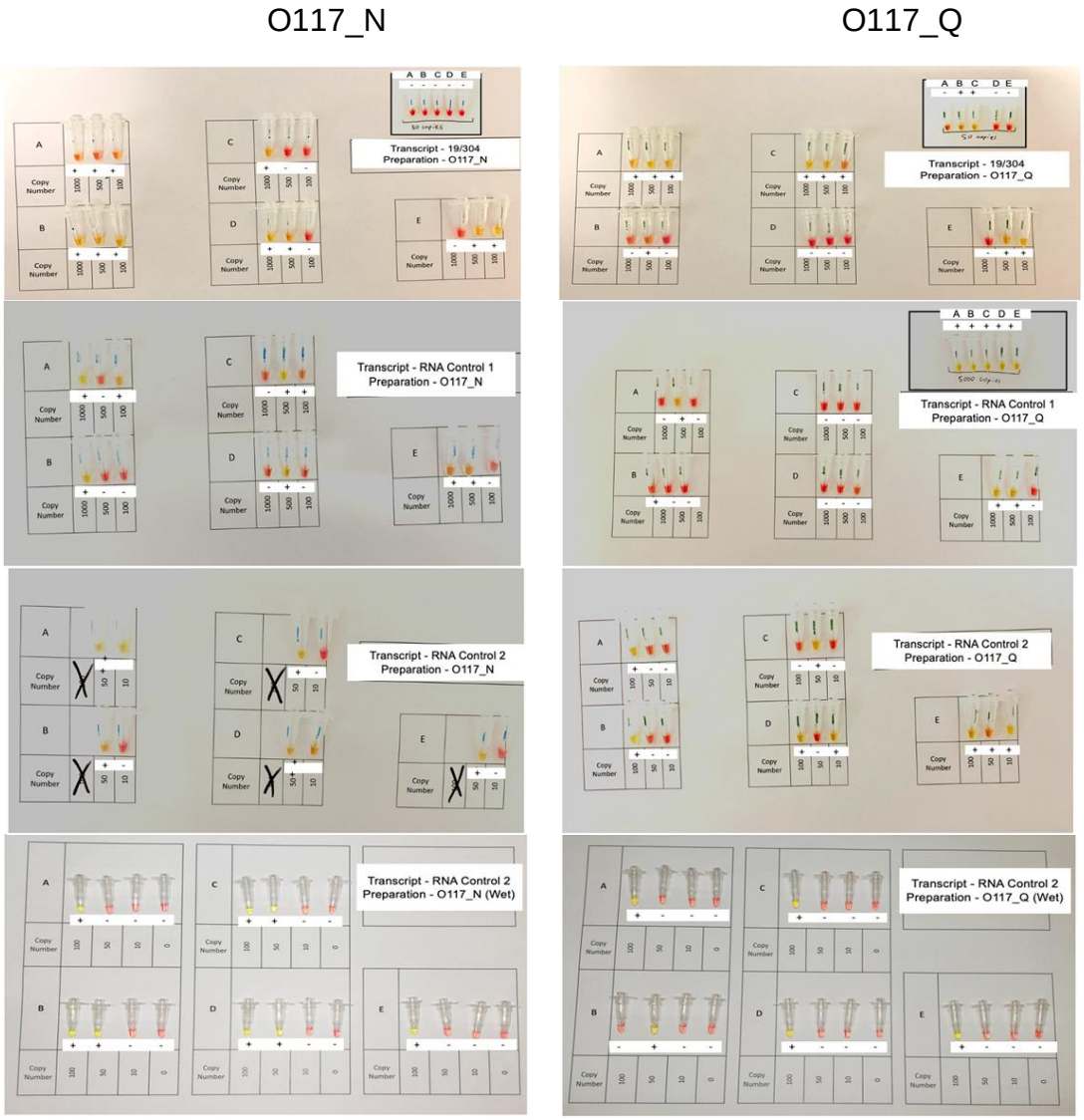


Figure A8: SARS-CoV-2 RNA transcript and reaction mix used in each experiment are labelled on the top right white box of each image. '+' indicates a positive result while '-' indicates a negative result. A, B, C, D, E represents five technical replicates.